

PHASE TRANSFORMATION KINETICS IN MEDIUM-MN THIRD-  
GENERATION ADVANCED HIGH STRENGTH STEELS

PHASE TRANSFORMATION KINETICS IN MEDIUM-MN THIRD-GENERATION  
ADVANCED HIGH STRENGTH STEELS

By: Azin Mehrabi, B.Sc., M.A.Sc

A Thesis

Submitted to the School of Graduate Studies in Partial Fulfilment of the  
Requirements for the Degree

Doctor of Philosophy

McMaster University

© Copyright by Azin Mehrabi, April 2024

Doctor of Philosophy (2024)

McMaster University

(Materials Science and Engineering)

Hamilton, Ontario, Canada

TITLE: Phase transformation kinetics in medium-Mn third  
generation advanced high strength steels

AUTHOR: Azin Mehrabi, B.Sc. (University of Tehran), M.A.Sc  
(University of Tehran)

SUPERVISORS: Professors Hatem Saif Zurob and Joseph Robert McDermid

NUMBER OF PAGES: xxv, 158

## Lay Abstract

Development of medium-Mn third-generation advanced high strength steels (3G AHSS) with desirable combination of specific strength and ductility has received significant attention from the automotive industry to reduce vehicle weight and fuel consumption as well as improve passenger safety. However, the mechanical properties of medium-Mn steels are strongly influenced by the amount and stability of any retained austenite present. It is, therefore, crucial to understand the effect of the initial microstructure and heat treatment on the amount of retained austenite. In this study, the effects of starting microstructure and intercritical annealing temperature on the phase transformation kinetics and microstructural evolution of a prototype Fe-0.15C-5.56Mn-1.1Si-1.89Al medium-Mn third-generation advanced high strength steel were determined. The starting microstructures comprise i) an as-received cold rolled (CR) microstructure containing a significant fraction of ferrite, tempered martensite, and cementite and ii) an austenitized and quenched martensite and ferrite microstructure. The studies were interpreted using the DICTRA module of Thermo-Calc.

## Abstract

Medium-Mn third-generation advanced high strength steels (3G AHSS) are promising candidates for vehicle lightweighting due to their desirable combination of specific strength and ductility. However, the mechanical properties of medium-Mn (med-Mn) steels are strongly influenced by the amount and stability of any retained austenite present. It is, therefore, crucial to understand the effect of the initial microstructure and heat treatment on the amount of retained austenite. In the current study, the effects of starting microstructure and intercritical annealing temperature (IAT) on the phase transformation kinetics in a prototype Fe-0.15C-5.56Mn-1.1Si-1.89Al med-Mn third-generation advanced high strength steel (3G AHSS) were determined.

The growth kinetics of intercritical austenite were simulated using DICTRA for both cold-rolled (CR) and martensite–ferrite (MF) starting microstructure during intercritical annealing. In the CR microstructure, austenite nucleates at ferrite grain boundaries apart from cementite, while in the MF microstructure, it directly grows from pre-existing inter-lath retained austenite (RA). Accelerated austenite reversion kinetics were observed for the MF microstructure due to the direct growth of intercritical austenite from pre-existing inter-lath RA films and rapid partitioning of C from the martensitic matrix. The difference in growth kinetics is more significant at 665 °C IAT due to the presence of cementite. The slow dissolution of cementite effectively reduces the growth rate of austenite.

To further develop and validate the modeling approach, this study conducted *in situ* measurements of austenite transformation kinetics using *in situ* High-Energy X-ray Diffraction (HEXRD) and dilatometry. Additionally, *ex situ* microstructural analysis was performed using Atom Probe Tomography (APT) to characterize elemental partitioning, and Electron Backscatter Diffraction (EBSD) was used to determine morphology and phase distribution in intercritically annealed samples at room temperature. The HEXRD experiments, combined with microstructural characterization, verified the austenite growth model. The overall kinetics at 665 °C and 710 °C were determined through HEXRD and dilatometry, aligning well with DICTRA results. These kinetics can be effectively modeled using the simple diffusion model outlined in DICTRA. The partitioning of substitutional alloying elements at the interface, as measured by APT, aligns with thermodynamic predictions, with the exception of Si. While DICTRA predicted Si enrichment in austenite, experimental data revealed a flat Si profile between ferrite and austenite. A comparison between intercritical austenite and RA based on HEXRD results

revealed that ~1% of austenite transformed into martensite during quenching in the MF, compared to ~5% in the CR sample. These results support the argument that the lath-shaped RA in the MF sample is more chemically stable.

A set of process maps were developed for a prototype med-Mn steel with the generic composition of 0.2C-xMn-1.0Si-1.5Al wt.% ( $x = 4 - 12$  wt.%). These maps predict the intercritical austenite vol.% formed during IA, as a function of the intercritical annealing parameters and starting microstructure employing a combination of microstructural analysis and DICTRA-based modeling. The maps cover an intercritical annealing temperature (IAT) range of 600 °C to 740 °C and an IA holding time of 120 s, suitable for industrial continuous galvanizing lines. The DICTRA-based model, in conjunction with the modified Koistinen–Marburger model was employed to enhance the estimation of RA vol.% in med-Mn steels. In situ HEXRD experiments, along with complementary microstructural characterization verified the intercritical austenite growth model during IA. However, the calculated results represent the austenite vol.% before cooling to room temperature, where a portion is expected to transform into martensite. To address this limitation, RA maps have been computed using the Koistinen–Marburger model considering both starting microstructures. To validate this method, the experimentally determined RA fractions obtained through XRD for various prototype med-Mn steels were considered. The values predicted by the model closely correspond with the experimentally measured RA vol.% reported in the literature. A comparison between process maps of both starting microstructures (M and TM) also highlighted the role of martensite starting microstructure in enhancing the mechanical properties of med-Mn steels. This enhancement is attributed to its ability to promote a higher vol.% of intercritical austenite during IA and results in a higher RA fraction after cooling to room temperature.

## Acknowledgements

First and foremost, I would like to thank my amazing supervisor Dr. Hatem Zurob for his tremendous mentorship and encouragement throughout this project. I was extremely lucky to get to know Hatem, as he helped me to be more confident and believe more in myself every day. I would also like to express my deepest appreciation towards my co-supervisor Dr. Joseph McDermid, for his wonderful guidance all time of my Ph.D. His support, encouragement, and patience throughout my graduate studies is greatly appreciated. It has been an absolute honor to work for them and perform many interesting analyses under their supervision. I would also like to sincerely thank my supervisory committee member, Dr. Gary Purdy, for his insightful comments and invaluable discussions throughout these past few years.

I would like to express my appreciation for technical support provided by:

- Dr. Beth McNally, Dr. Mike Bruhis, and my colleagues at the Centre for Automotive Materials and Corrosion
- The staff of the Canadian Centre for Electron Microscopy, especially Mr. Chris Butcher and Mr. Jhoynner Martinez (SEM); Dr. Xiang Wang (TEM); and Dr. Brian Langelier (APT)
- Dr. Jim Britten, and Ms. Victoria Jarvis, (McMaster Analytical X-Ray Diffraction Facility)
- Dr. Fateh Fazeli and Ms. Marta Aniolek (CanmetMATERIALS)
- Dr. Imed-Eddine Benrabah (Data analysis of high energy XRD test)
- Dr. Graham King and Dr. Al Rahemtulla (Canadian Light Source-HEXRD)

I would also like to thank all members of the phase transformation group, past and present, for their support throughout this journey. Many thanks to my groupmates and friends from the Department of Materials Science and Engineering at McMaster for so many good memories, nice friendships, and their support. I would like to extend my thankfulness to my friends at the CAMC for their encouragement and the countless cherished memories we have made together.

I would like to express my immense gratitude to my supportive family, my parents, Irandokht and Hossein, and sister, Ayda, for all their love and inspiration even being far away; without them none of this would indeed be possible – I sincerely say *thank you*. Thanks to my best friend, Atefeh (Dr. Azizi), for her emotional support throughout all the ups and downs. Lastly, a big thanks to Ashkan for being an incredibly supportive partner and always encouraging me to pursue my passions, no matter which direction they may lead.

## Table of Contents

Lay Abstract.....	iii
Abstract.....	iv
Acknowledgements.....	vi
Table of Contents.....	vii
List of Figures.....	xii
List of Tables.....	xviii
Abbreviations and Symbols.....	xix
Declaration of Academic Achievement.....	xxv
1 Introduction.....	1
1.1 Overall Context.....	1
1.2 Research Objectives.....	3
1.3 Thesis Layout.....	4
1.4 References.....	6
2 Literature Review.....	10
2.1 Third-Generation Advanced High Strength Steels.....	10
2.2 Medium Mn TRIP Steels.....	12
2.2.1 Microstructures and Chemical Composition of Medium Mn TRIP Steels.....	12
2.2.2 Effect of Intercritical Annealing Conditions.....	17
2.3 Phase Transformations in Medium-Mn TRIP-Assisted Steels.....	19
2.3.1 Austenite Growth from Martensite or Martensite-Austenite Mixture.....	26
2.3.2 Role of Cementite Dissolution on the Austenite Formation.....	30
2.3.3 Austenite Decomposition.....	33
2.4 Summary.....	35

2.5	References.....	36
3	Austenite Nucleation and Growth as a Function of Starting Microstructure for a Fe-0.15C-5.56Mn-1.1Si-1.89Al Medium-Mn Steel.....	44
3.1	Abstract.....	44
3.2	Introduction.....	45
3.3	Experimental.....	47
3.3.1	Steel Chemistry, Fabrication, and Thermal Process.....	47
3.3.2	X-ray Diffraction.....	50
3.3.3	DICTRA Simulations.....	50
3.4	Results.....	52
3.4.1	TEM Microstructural Characterization.....	52
3.4.2	Extraction Replica.....	56
3.5	Discussion.....	58
3.5.1	Austenite Nucleation.....	58
3.5.2	DICTRA Simulations of Austenite Formation.....	58
3.6	Conclusions.....	63
3.7	Acknowledgements.....	64
3.8	Reference.....	64
4	Austenite Formation in a Medium-Mn Steel During Intercritical Annealing via <i>in situ</i> High-Energy X-ray Diffraction.....	70
4.1	Abstract.....	70
4.2	Introduction.....	70
4.3	Materials and Methods.....	73
4.3.1	Starting Material and Heat Treatment Parameters.....	73

4.3.2	Microstructural Analysis.....	74
4.3.3	Dilatometry .....	75
4.3.4	High Energy X-ray Diffraction (HEXRD) .....	76
4.3.5	DICTRA Simulations.....	77
4.4	Results.....	78
4.4.1	Microstructural Analysis.....	78
4.4.2	Dilatometry .....	80
4.4.3	HEXRD.....	81
4.4.4	Concentration Profile Simulations by DICTRA.....	85
4.5	Discussion.....	87
4.6	Conclusions.....	90
4.7	Acknowledgements.....	91
4.8	References.....	92
5	An <i>in situ</i> Study of Austenite Formation During Intercritical Annealing of a Medium-Manganese Steel with Cold-Rolled Starting Microstructure .....	98
5.1	Abstract.....	98
5.2	Introduction.....	98
5.3	Materials and Methods.....	99
5.3.1	Starting Material and Heat Treatment Parameters.....	99
5.3.2	Microstructure Analysis.....	100
5.3.3	Dilatometry .....	101
5.3.4	High Energy X-ray Diffraction (HEXRD) .....	101
5.3.5	DICTRA Simulations.....	102
5.4	Results.....	103

5.4.1	Microstructural Analysis.....	103
5.4.2	Dilatometry .....	105
5.4.3	HEXRD.....	106
5.4.4	Concentration Profile Simulations by DICTRA.....	110
5.5	Discussion.....	114
5.6	Conclusions.....	116
5.7	Acknowledgements.....	117
5.8	References.....	117
6	Process Maps for Predicting Austenite Fraction in Medium-Mn Third-Generation Advanced High Strength Steels .....	121
6.1	Abstract.....	121
6.2	Introduction.....	121
6.3	Overview of Models .....	123
6.3.1	DICTRA-Based Model.....	123
6.3.2	Koistinen–Marburger Model .....	125
6.4	Results.....	126
6.4.1	Tempered Martensite Starting Microstructure.....	127
6.4.2	Martensite Starting Microstructure .....	130
6.4.3	Comparing the Model with the Literature .....	132
6.5	Discussion.....	133
6.6	Conclusions.....	136
6.7	Acknowledgements.....	137
6.8	References.....	137

7	Global Discussion .....	144
7.1	Phase Transformation Kinetics and Microstructural Evolution.....	144
7.2	Process Map .....	149
7.3	References.....	151
8	Conclusions and Future Research Directions .....	155
8.1	Conclusions.....	155
8.2	Future Research Directions .....	156
8.3	References.....	158

## List of Figures

Figure 1.1: Schematic of different materials used in the construction of different generations of the Acura TLX body-in-white [5].....	1
Figure 1.2: Classification of the AHSS based on their mechanical properties [20–22]. .....	3
Figure 2.1: Schematic of TRIP effect during plastic deformation [2]. .....	11
Figure 2.2: (a) Chemical free energies and (b) applied stress for martensitic transformation versus temperature [2,4]. $U'$ represents the mechanical driving force resulting from applied stress, $\Delta G_{T_1}^{\gamma \rightarrow \alpha'}$ denotes the chemical driving force at $T_1$ , and $\Delta G_{M_s}^{\gamma \rightarrow \alpha'}$ indicates the chemical driving force necessary to initiate the transformation from austenite to martensite at the $M_s$ temperature. ....	12
Figure 2.3: Typical microstructures of (a) hot-rolled and (b) cold-rolled medium Mn steels intercritically annealed at 640 °C for 30 minutes [11].....	13
Figure 2.4: The effect of alloying elements on the phase diagram of medium Mn steels. (a) Fe-xC-5 Mn; (b) Fe-0.2C-xMn; (c) Fe-0.2C-5 Mn-xSi; (d) Fe-0.2C-5 Mn-xAl [6].....	14
Figure 2.5: Schematic of ART annealing process for medium Mn steels [2].....	15
Figure 2.6: (a) cementite dissolution regime based on amount of Mn in cementite and temperature, (b) chemical potential of C at the cementite/austenite and austenite/ferrite interfaces vs. temperature [26].....	17
Figure 2.7: Intercritical annealing temperature influence on (a) the volume fraction of austenite and (b) the UTS and elongation of a Fe–0.20C– 3.12Al–8.56Mn (wt.%) medium-Mn steel for an intercritical annealing time of 1 hour [30]. .....	18
Figure 2.8: (a) Engineering stress-strain curves of Fe–0.17C-5.6Mn–1.2Al medium-Mn steel and (b) the volume fraction of austenite [33]. .....	19
Figure 2.9: Initial state: the concentration profile of (a) carbon and (b) Mn [39]. .....	20

Figure 2.10: Illustration of carbon diffusion-controlled growth. (a) C gradient, (b) Mn gradient. (c) the tie line of C on the isotherm [39]. ..... 21

Figure 2.11: (a) Overlapping of carbon diffusion profiles in  $\gamma$  results in logarithmic carbon diffusion-controlled growth. (b) carbon concentration profile at the end of this stage [39]. ..... 22

Figure 2.12: (a) Carbon concentration profile (b) Mn concentration profile (c) shift in tie line in growth with Mn partition stage (d) the exaggerated carbon profile [39]. ..... 24

Figure 2.13: Predicted, convoluted and observed micro-probe traces for Fe-0.08 C-1Mn (wt.%) annealed for 6 days at 800 °C. The probe function was convoluted with the concentration profile predicted for a planar geometry [39]. ..... 25

Figure 2.14: (a) The estimated and measured thickness of austenite lath during intercritical annealing at 650 °C in an Fe-0.2C-5 Mn steel. It was assumed that austenite lath and martensite lath have thicknesses of 4 nm and 100–300 nm, respectively. As the interface mobility of martensite/austenite was limited, the measured interface mobility by Krielaart and Van der Zwaag [50] for the  $\gamma$ -to- $\alpha$  transformation was applied. Variations of (b) C and (c) Mn profiles during intercritical annealing, corresponding to curve No. 3 in (a) for the interface position. (Modified version of [41]) ..... 27

Figure 2.15: Comparison between model and experimental kinetics of austenite growth during holding at three different temperature in Fe-0.1C-3Mn-1.5Si steel alloy modified, from [40]. .... 28

Figure 2.16: The impacts of interface mobility on the austenite growth kinetics at (a) 750 °C and (b) 775 °C. Solid circles in (a) and (b) show the thickness of acicular austenite experimentally measured at different holding time. Mn and Si profiles at  $\gamma/\alpha$  interface at 775 °C for the interface mobility of (c)  $M_0$  and (d)  $0.001M_0$  [53]. ..... 29

Figure 2.17: TEM images of the microstructures in an Fe-0.2C-5Mn steel after IA at 650 °C for 5 min, showing (a) cementite precipitated in martensite, and (b) a cementite particle within reverted austenite. Cementite particles are indicated by arrows in (a) [19]. ..... 31

Figure 2.18: (a) Schematic illustration indicating the microstructures during IA. Simulation of austenite nucleation on (b) martensite laths (Setup A) and (c) cementite/ martensite interface

(Setup B). (d) The kinetics of austenite growth under different setups simulated using DICTRA. Setup O is related to austenite nucleated on the martensite lath with no cementite precipitation. Setup A + M is related to the effect of martensite/austenite interface mobility [58]..... 33

Figure 2.19: Experimental and calculated retained austenite fraction as a function of IA temperature [29]..... 35

Figure 3.1: (a) Phase fractions vs. temperature of the Fe-5.56Mn-0.15C -1.1Si-1.89Al generated using the Thermo-Calc TCFE12 database (b) thermal profile of Steel E during annealing..... 49

Figure 3.2: TEM images from the CR × 60s condition. For the CR 665 °C × 60s sample: (a) BF; (b) DF image obtained by using spot from  $\gamma$ . For the CR 710 °C × 60s sample: (c) BF; (d) DF corresponding to  $\langle 110 \rangle \gamma$ . Ferrite, cementite, and retained austenite are denoted by  $\alpha$ ,  $\theta$ , and RA respectively. Schematic of initial configuration indicating austenite formation during heating (e) on a ferrite phase boundary at some distance from cementite at 665 °C (f) on ferrite without cementite at 710 °C for the CR case. The dotted line shows a schematic of the carbon concentration during the simulation. .... 53

Figure 3.3: TEM images of the MF starting microstructure. (a) BF; (b) DF image obtained by using spot from  $\gamma$ . white ellipses show thin film of RA. Ferrite and martensite are denoted by  $\alpha$  and  $\alpha'$  respectively. (c) Schematic of initial configuration indicating austenite formation on ferrite lath boundaries ( $\gamma$  = austenite,  $\alpha$  = ferrite) for the MF starting microstructure case. .... 54

Figure 3.4: TEM images from the MF × 60s condition. For the MF 665 °C × 60s sample. (a) BF; (b) DF image obtained by using spot from  $\gamma$ . For MF 710 °C × 60s sample: (c) BF; (d) DF corresponding to  $\langle 110 \rangle \gamma$ . Retained austenite is denoted by RA..... 54

Figure 3.5: EDS elemental mappings from (a) the frame of the HAADF image of (b) Fe, (c) C, and (d) Mn at CR 665 °C × 0s sample. Tempered martensite, cementite, and retained austenite are denoted by TM,  $\theta$ , and RA respectively. .... 55

Figure 3.6: Particle size distribution of (a) the as-received CR, CR 665 °C × 120s, and CR 710 °C × 120s samples and (b) MF, MF 665 °C × 120s, and MF 710 °C × 120s samples. .... 57

Figure 3.7: Cementite extraction replica TEM micrographs in (a) the as received, (b) CR 665 °C × 120s, and (c) CR 710 °C × 120s samples. ....	57
Figure 3.8: Cementite distribution in the (a) MF, (b) MF 665 °C × 120s, and (c) and MF 710 °C × 120s samples. ....	57
Figure 3.9: Austenite volume fraction during isothermal holding at 665 °C, 710 °C for the CR starting microstructure with cementite. Error bars for austenite volume fraction measurement indicate maximum and minimum values among six measurements.....	60
Figure 3.10: Austenite volume fraction during isothermal holding at 665 °C and 710 °C for the MF starting microstructure. ....	61
Figure 3.11: Comparing CR and MF cases for austenite volume fraction during (a) 665 °C and (b) 710 °C isothermal holding. ....	63
Figure 4.1: Experimental thermal cycle for annealing treatment [2].....	74
Figure 4.2: Microstructural overview of an intercritically annealed sample after 710 °C for 120s. (a) an EBSD image showing retained austenite in red and ferrite in green. (b) atomic map section showing ferrite and austenite laths, where C atoms are given in green and Mn atoms in blue. The purple iso-surface indicates 6.5 at. % Mn, (c) experimental APT results show two interfaces through the APT reconstruction with C atoms (green) and Mn atoms (blue) are enriched in austenite, while Al (brown) and Si (red) are depleted in austenite and enriched in ferrite. Black dotted lines indicate the suggested crystallographic positions of the phase boundaries between ferrite and austenite, (d) concentration profiles for all elements across the ferrite/austenite phase boundaries Note that EBSD and APT were not taken at the same place.....	79
Figure 4.3: Dilatometric strain variations in austenite after a 240 s intercritical annealing at (a) 665 °C and (b) 710 °C.....	80
Figure 4.4: The 1-D diffractograms obtained at the selected times during heating (time=15 s), at the start of isothermal holding, end of isothermal holding, cooling (just above the $M_s$ temperature of 300 °C) for intercritical annealing at 710 °C for 120 s. ....	81

Figure 4.5: Measured HEXRD austenite vol % as a function of (a) temperature and (b) time. The arrows indicate data obtained through the thermal cycle from heating, isothermal holding, and cooling. Dotted lines in (b) show the equilibrium vol % of austenite during IA at 665 °C and 710 °C. .... 83

Figure 4.6: Austenite vol % during isothermal holding at 665 °C and 710 °C as determined using *in situ* HEXRD (solid lines) compared to DICTRA simulations (dotted lines) and dilatometry results (dashed lines) up to 240 s. .... 84

Figure 4.7: Normalized lattice parameter of austenite as a function of time during the heating and isothermal holding at 665 °C and 710 °C. The rescaled versions are added to the plots to show a clearer trend of lattice constant change during isothermal holding. .... 85

Figure 4.8: Concentration profiles of (a) C, (b) Mn, (c) Si, and (d) Al at various time-steps during isothermal holding at 665 °C. .... 86

Figure 4.9: Concentration profiles of (a) carbon, (b) Mn, (c) Si, and (d) Al at various time-steps during isothermal holding at 710 °C. .... 87

Figure 4.10: EDS elemental mappings from (a) the frame of the high-angle annular dark-field (HAADF) image and (b) concentration profile of Mn, Al, and Si at 710 °C for one year. .... 90

Figure 5.1: EBSD phase maps of the reference steel intercritically annealed during isothermal holding up to 120 s at (a) 665 °C and (b) 710 °C. .... 103

Figure 5.2: Experimental APT of an intercritically annealed sample after 665 °C for 120s. (a) atomic map section showing ferrite, austenite, and cementite regions, where C atoms are given in green and Mn atoms in blue. The orange and purple iso-surfaces indicated 3 at. % C and 8.5 at. % Mn, respectively. (b) experimental APT results show an interface through the APT reconstruction. C atoms (green) are enriched in precipitates in the ferrite. Precipitate-free austenite is bordered by a plate-like zone that is characterized by strong C and Mn enrichment (blue) and Al (brown) and Si (red) depletion. Black dotted lines indicate the suggested position of the phase boundary between ferrite and austenite. (c) concentration profiles for all elements across the ferrite/austenite phase boundaries. .... 105

Figure 5.3: Dilatometric strain variations in austenite after a 240 s intercritical annealing at (a) 665 °C and (b) 710 °C.....	106
Figure 5.4: The changes over time of (a) experimental thermal cycle (b) and 1D diffractograms obtained at the selected times during heating (time=11 s), at the start of isothermal holding, end of isothermal holding, cooling (just above the $M_s$ temperature of 300 °C) for intercritical annealing at 710 °C for 120 s. ....	107
Figure 5.5: Measured HEXRD austenite vol % as a function of (a) temperature and (b) time. The arrows indicate data obtained through the thermal cycle from heating, isothermal holding, and cooling. Dotted lines in (b) show the equilibrium vol % of austenite during IA at 665 °C and 710 °C. ....	108
Figure 5.6: Austenite vol % during isothermal holding at 665 °C and 710 °C as determined using <i>in situ</i> HEXRD (solid lines) compared to DICTRA simulations (dotted lines) and dilatometry results (dashed lines) up to 240 s. ....	109
Figure 5.7: Normalized lattice parameters as a function of time during the heating and isothermal holdings at 665 °C and 710 °C: (a) austenite and (b) ferrite/ martensite. The rescaled versions are added to the plots to show a clearer trend of lattice constant change during holding. ....	110
Figure 5.8: Concentration profiles of (a) C, (b) Mn, (c) Si, and (d) Al at various time-steps during isothermal holding at 665 °C. ....	111
Figure 5.9: Wide distribution of (a) C in $\alpha$ and (d) C in $\gamma$ , and (c) Mn near the $\theta$ - $\alpha$ interface and (d) Mn near the $\alpha$ - $\gamma$ interface at different time-steps at 655 °C.....	112
Figure 5.10: Concentration profiles of (a) C, (b) Mn, (c) Si, and (d) Al at various time-steps during isothermal holding at 710 °C. ....	114
Figure 6.1: Schematic of initial microstructural configuration and resultant DICTRA geometry for austenite formation during heating: (a) TM starting microstructure—austenite nucleation on ferrite with dissolved cementite; and (b) M starting microstructure—austenite growth on ferrite (martensite) lath boundaries ( $\gamma$ = austenite, $\alpha$ = ferrite). The arrows indicate regions containing	

high and low Mn contents. Dashed lines surrounding the  $\gamma$  phase represent the growth of austenite.  
..... 125

Figure 6.2: Section of the Fe-0.2C-xMn-1.0Si-1.50Al (wt.%) phase diagram, where Mn is varied from 0 – 12 wt.%. Diagram generated using the Thermo-Calc TCFE12 database. .... 128

Figure 6.3: (a) Equilibrium austenite vol.%, (b) intercritical austenite, and (c) calculated RA fraction (vol.%) for Fe-0.2C-xMn-1.5Al-1Si wt.% steels ( $x = 4-12$  wt.%) as a function of IAT from 680 °C to 740 °C for the TM starting microstructure, and assuming an austenite grain size of 1  $\mu$ m. Note that the dotted lines are related to higher Mn contents as the starting microstructures may be duplex. .... 130

Figure 6.4: Effects of chemical composition on (a) the intercritical austenite and (b) calculated RA fraction (vol.%) for Fe-0.2C-xMn-1.5Al-1Si wt.% steels ( $x = 4-12$  wt.%) as a function of IATs from 600 °C to 740 °C for the M starting microstructure, and assuming an austenite grain size of 1  $\mu$ m. Note that the dotted lines are related to higher Mn contents as the starting microstructures may be duplex. .... 132

Figure 7.1: Austenite vol. % during isothermal holding at 665 °C and 710 °C for up to 240 s, as determined using *in situ* HEXRD, for the CR and MF starting microstructures. .... 147

## List of Tables

Table 2.1: Summary of the effect of starting microstructure on RA ..... 16

Table 3.1: Summary of heat treatment parameters for CR and MF starting microstructures..... 49

Table 3.2: Average cementite, austenite, and tempered martensite (matrix) composition from EDS spot analysis (wt.%) for CR 665 °C  $\times$  0s sample..... 55

Table 6.1: Comparison of experimental measurements with calculated values for intercritical annealing austenite vol.% versus the final vol.% of retained austenite for several med-Mn steels. Note that all intercritical annealing treatments are for 120 s at the stated IAT. .... 129

## Abbreviations and Symbols

### List of Abbreviations

AHSS	Advanced High Strength Steels
APT	Atom Probe Tomography
ART	Austenite Reversion Transformation
BCT	Body-Centered Tetragonal
BF	Bright Field
BIW	Body-in-White
BXDS	Brockhouse X-ray Diffraction Sector
C	Carbon
CFB	Carbide-Free Bainitic
CGL	Continuous Galvanizing Line
CLS	Canadian Light Source
CP	Complex Phase
CR	Cold-Rolled
DF	Dark Field
DICTRA	Diffusion Controlled Transformation
DP	Dual Phase
dp	Dew point
EBSD	Electron Backscatter Diffraction
EELS	Electron Energy Loss Spectroscopy

EDM	Electric Discharge Machining
EDS	Energy-Dispersive X-Ray Spectroscopy
FCC	Face-Centered Cubic
FIB	Focused-Ion Beam
FE	Full Equilibrium
FEG-SEM	Field Emission Scanning Electron Microscope
HAADF	High-Angle Annular Dark-Field
HEXRD	High Energy X-ray Diffraction
IA	Intercritical Annealing
IAT	Intercritical Annealing Temperature
K-M	Koistinen–Marburger
LE	Local Equilibrium
L-IP	Lightweight Steels with Induced Plasticity
LVDT	linear Voltage Displacement Transducer
M	Martensite
M/A	Martensite/Austenite
Med-Mn	Medium-Manganese
MF	Martensite-Ferritic

NPLE	Negligible Partitioning Local Equilibrium
OM	Optical Microscope/Microscopy
OT	Overaging Temperature
PE	Para Equilibrium
PLE	Partitioning Local Equilibrium
PYFAI	Python Library
Q&P	Quenched and Partitioned Steel
RA	Retained Austenite
SAD	Selected Area Diffraction
SAMT	Stress-Assisted Martensitic Transformation
SEM	Scanning Electron Microscope/Microscopy
SIMT	Strain-Induced Martensitic Transformation
STEM	Scanning Transmission Electron Microscope/Microscopy
TD	Transverse Direction
TE	Total Elongation
TEM	Transmission Electron Microscopy
TM	Tempered Martensite
TRIP	Transformation-Induced Plasticity
TT	Through-Thickness Direction

TWIP	Twinning-Induced Plasticity
UTS	Ultimate Tensile Strength
XRD	X-Ray Diffraction
YS	Yield Strength
1D	One-Dimensional
2D	Two-Dimensional
3D	Three-Dimensional
1G	First-Generation
2G	Second-Generation
3G	Third-Generation

## List of Symbols

at. %	Atomic Percent
$C_{Mn}^{\gamma}$	Manganese Concentration in Austenite
$C_{Mn}^{\alpha}$	Manganese Concentration in Ferrite
$C_{Mn}^0$	Initial Manganese Concentration in Ferrite and Austenite
$C_c^E$	Eutectoid Composition
$C_c^S$	Carbon Concentration at the Interface
$k_0$	Distribution Coefficient of Iron
$k_1$	Distribution Coefficient of Carbon
$K_2$	Distribution Coefficient of Manganese
$f_{D\gamma}$	Austenite Volume Fraction at the IA Temperature
$f_{ret\ \gamma}$	Retained Austenite Volume Fraction
$f_{\gamma}$	Volume Fraction of Austenite After Quenching
$\Delta G$	Driving Force
$\Delta G_{TI}^{\gamma \rightarrow \alpha}$	Chemical Driving Force
$\Delta G_{Ms}^{\gamma \rightarrow \alpha}$	Chemical Driving Force Required for Initiating the Transformation of Austenite to Martensite
$M$	Interface Mobility
$M_s$	Martensite Start Temperature
$M_s^{\sigma}$	Deformation-Induced Martensite Start Temperature
$M_d$	highest temperature at which deformation is able to trigger austenite to martensite
$U'$	Mechanical Driving Force
$\mu_i^{\alpha}$	Chemical Potential of Element i in Ferrite
$\mu_i^{\gamma}$	Chemical Potential of Element i in Austenite
$D_c^{\gamma}$	Diffusion Coefficient of Carbon in Austenite

$D_{Mn}^{\alpha}$	Diffusion Coefficient of Manganese in Ferrite
R	Ratio of the Off-diagonal to On-diagonal Diffusion Coefficients
Vol.%	Volume Percent
$V_{\gamma}$	Average Grain Volume of Austenite
v	Velocity
wt.%	Weight Percent
$\alpha$	Ferrite
$\alpha'$	Martensite (Body-Centered Tetragonal Structure)
$\gamma$	Austenite
$\gamma_{ret}$	Retained Austenite
$\theta$	Cementite
T	Temperature
n	Transformation Kinetics Coefficients
m	Transformation Kinetics Coefficients

## Declaration of Academic Achievement

This thesis was prepared in partial fulfillment of the degree *Doctor of Philosophy* at McMaster University. The research was performed from September 2019 to December 2023 and studied phase transformation kinetics of a prototype grade of third-generation advanced high strength steel during intercritical annealing.

The author performed the experiments, analyzed the results, and prepared all manuscripts under the supervision of Professors Hatem Zurob and Joseph McDermid. The major results of this research have been published in three peer-review journal publications, and one draft manuscript for submission to a peer-review journal. The published articles are reused in the author's theses/dissertations.

1. A. Mehrabi, J. R. McDermid, X. Wang, and H. Zurob, "Austenite Nucleation and Growth as a Function of Starting Microstructure for a Fe-0.15C-5.56Mn-1.1Si-1.89Al Medium-Mn Steel," *Steel Res. Int.*, 94 (2023) 2200952. <https://doi.org/10.1002/srin.202200952>.
2. A. Mehrabi, H. Zurob, J. R. McDermid, "Process Maps for Predicting Austenite Fraction (vol.%) in Medium-Mn Third-Generation Advanced High Strength Steels," *Materials*, 17 (2024) 993. <https://doi.org/10.3390/ma17050993>.
3. A. Mehrabi, H. Zurob, I-E. Benrabah, J. R. McDermid, "Austenite formation in a medium-Mn steel during intercritical annealing via *in situ* high-energy X-ray diffraction," *J. Mat. Res. Tech.*, 30, (2024) pp. 2158-2167. <https://doi.org/10.1016/j.jmrt.2024.03.241>.
4. A. Mehrabi, H. Zurob, J. R. McDermid, "An *in situ* study of austenite formation during intercritical annealing of a medium-manganese steel with cold-rolled starting microstructure," Draft Manuscript.

# 1 Introduction

## 1.1 Overall Context

The most recent trends in the automotive industry have mostly focused on decreasing greenhouse gas emissions through increased fuel efficiency and the extension of electric vehicle battery range while enhancing the safety and performance of vehicles [1]. This has led to the development and use of advanced high strength steels (AHSS) [2]. The high strength and excellent formability balance of AHSSs offers the advantage of reducing sheet thickness, which results in weight reduction of the car body [3,4]. Therefore, AHSSs comprise a significant percentage of the vehicle body-in-white (BIW), as shown in Figure 1.1.

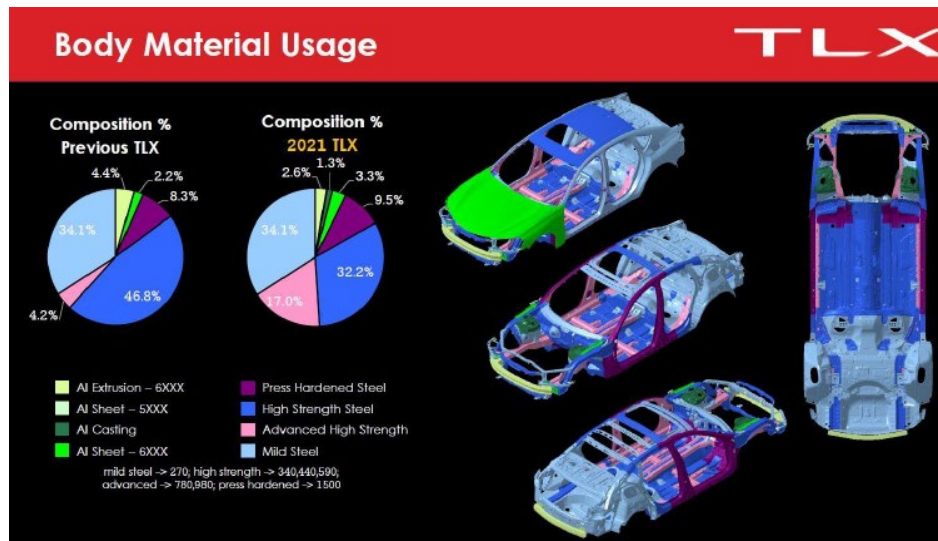


Figure 1.1: Schematic of different materials used in the construction of different generations of the Acura TLX body-in-white [5].

Advanced high strength steels are divided into three generations and their tensile strength vs. total elongation is shown in Figure 1.2 [4,6]. Dual phase (DP) steels, transformation induced plasticity (TRIP) steels, complex-phase (CP), and martensitic (MART) steels with  $UTS \times TE$  of approximately 10,000-15,000 MPa% are referred to as first-generation (1G) AHSS by the automotive industry. The microstructures of the 1G steels contains a soft ferritic matrix embedded with a hard second phase resulting in the high strength of these multiphase steels [7–9]. In particular, the microstructure of TRIP steels contains metastable retained austenite which transforms to martensite upon deformation, resulting in the improvement of both strength and ductility [7].

The second-generation (2G) of AHSS includes high Mn TRIP and twinning induced plasticity steels, with a transformable austenitic microstructure. These steels contain 15-30 wt.% Mn and 0-1wt.% C. In addition, some of the 2G AHSS steels may contain Al (0-3%), Si (0-3%) and other alloying elements, such as Cr, Cu, N, Nb, Ti, and V [10–12]. The intercritical annealing temperature and the room temperature SFE of austenite determine the deformation mechanism: TRIP, TWIP, or a combination of both (TRIP + TWIP) [13]. The TRIP/TWIP effect is pronounced at low SFE values, typically between 15 and 20 mJ/m<sup>2</sup> [13]. The effect of mechanical twins in the austenite phase or the formation of strain induced martensite during plastic deformation on the mechanical properties of 2G AHSS steels provides a superior balance of strength and elongation of approximately 50,000-100,000 MPa%. However, their engineering application is restricted owing to their high Mn and other alloying element contents, which leads to high alloying costs and production problems [14].

The third generation (3G) of AHSS includes quench and partition (Q&P), carbide-free bainitic (CFB), and medium-Mn TRIP-assisted steels. These steels are being developed based on their superior balance of strength and ductility compared to 1G AHSSs and can also be manufactured at reasonable cost compared to the 2G AHSSs. Third generation steels with significant volume fractions of retained austenite, which can be chemically stabilized in the final as-annealed microstructure, enable the activation of the TRIP (and possibly TWIP) mechanism(s) upon deformation. This allows the steel to maintain high work hardening rates and result in the desired balance of strength and ductility in the range of 24,000-40,000 MPa% [6,15,16]. The different generations of advanced high strength steels with their respective mechanical property ranges are shown in Figure 1.2.

Medium-Mn TRIP steels are one of the promising candidates to use in the automotive industry due to their superior mechanical properties and lower cost compared to other steel grades [10]. The microstructure of medium-Mn TRIP steels with 4-12 wt.% Mn with significant amounts of solute-enriched retained austenite which transforms to hard martensite during deformation, resulting in the desirable strength-ductility balances [7,8,17,18]. It has been found that several factors influence the volume fraction and stability of retained austenite, such as intercritical annealing parameters, initial microstructure (grain size and morphology) of the steel and the austenite chemical composition. Therefore, adjusting the heat treatment to control the

volume fraction and combination of both chemical and mechanical stability of retained austenite plays a crucial role in achieving the mechanical properties of these alloys [19,20].

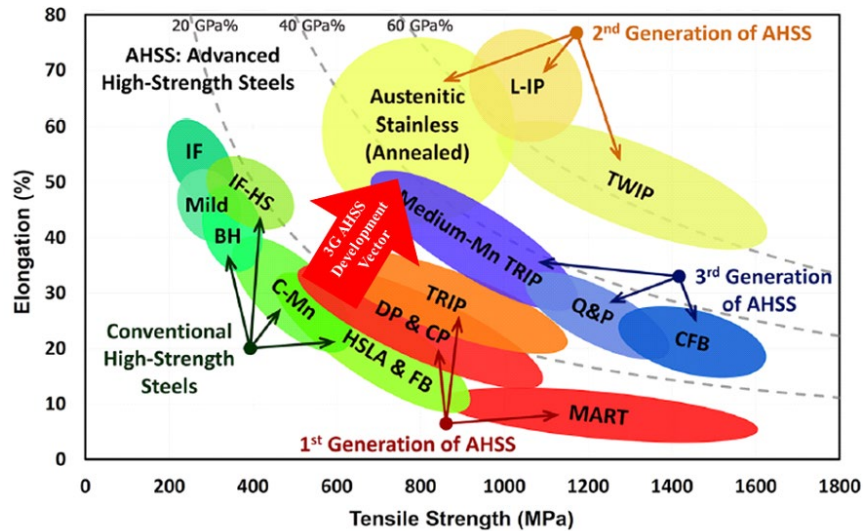


Figure 1.2: Classification of the AHSS based on their mechanical properties [20–22].

## 1.2 Research Objectives

Considerable research has been dedicated to studying the phase transformation kinetics of med-Mn steels as a function of intercritical annealing parameters, starting microstructure, and steel composition [23–29]. However, there is an insufficiency of studies focusing on the phase transformation kinetics, including both modeling and comprehensive characterization methods, for med-Mn steels with CGL-compatible processing parameters.

Consequently, the main objective of this Ph.D. research is to provide a comprehensive understanding of the phase transformation kinetics and microstructural evolution in a prototype Fe-0.15C-5.56Mn-1.1Si-1.89Al med-Mn third-generation advanced high strength steel (3G AHSS). The study focused on the effects of starting microstructure and intercritical annealing parameters on the development of austenite and its subsequent transformation kinetics during quenching. In that regard, the research objectives of this Ph.D. can be divided into:

- 1) Determining the effects of starting microstructure and intercritical annealing temperature on the phase transformation kinetics and microstructural evolution of the prototype med-Mn steel, with a focus on simulating the growth kinetics of austenite from as-received cold-rolled

(CR) tempered martensite and austenitized and quenched martensite–ferrite (MF) starting microstructures during intercritical annealing.

- 2) Determining the austenite formation sites during intercritical annealing for the CR and MF starting microstructure through the microstructural observations (SEM, TEM, EBSD, carbon replica).
- 3) Validating the DICTRA modeling of the austenite growth during intercritical annealing in a med-Mn steel with MF and CR starting microstructures, utilizing advanced microstructural characterization methods, such as HEXRD, dilatometry, and APT.
- 4) Developing process maps for a prototype medium-Mn steel with a generic composition of 0.2C-xMn-1.0Si-1.5Al wt.% ( $x = 4 - 12$  wt.%) to predict the intercritical austenite vol.% and retained austenite vol.% as a function of intercritical annealing parameters and starting microstructure, utilizing a combination of microstructural analysis and DICTRA-based modeling.

### 1.3 Thesis Layout

This thesis has been prepared in a sandwich format, with the layout as follows:

- Chapter 2 – Literature Review: This section presents a comprehensive overview of the design strategy and physical metallurgy of medium-Mn 3G AHSS. The discussion encompasses key aspects such as microstructure and chemical composition, effect of starting microstructure and intercritical annealing conditions on the volume fraction and stability of retained austenite in medium-Mn steels. Additionally, the chapter explores the modeling of austenite formation and stability during annealing treatments. Within this context, the literature review introduces experimental methods employed to study phase transformations, including Electron Backscatter Diffraction (EBSD), Transmission Electron Microscopy (TEM), Atom Probe Tomography (APT), and High-Energy X-ray Diffraction (HEXRD). The inclusion of these methods adds depth to the understanding of medium-Mn 3G AHSS behavior. This chapter serves as a foundational exploration of the existing knowledge in the field, setting the stage for the subsequent research and findings presented in the thesis.
- Chapter 3 – Austenite Nucleation and Growth as a Function of Starting Microstructure: This

chapter is a reproduction of the journal article entitled “Austenite Nucleation and Growth as a Function of Starting Microstructure for a Fe-0.15C-5.56Mn-1.1Si-1.89Al Medium-Mn Steel” published in *Steel Research international* in 2023. In this article, the effects of starting microstructure and intercritical annealing temperature on the phase transformation kinetics and microstructural evolution of a prototype Fe-0.15C-5.56Mn-1.1Si-1.89Al medium-Mn third-generation advanced high strength steel are examined. Based on the microstructural observations, two different scenarios for austenite formation during intercritical annealing have been proposed. For the cold-rolled starting microstructure, austenite can nucleate at ferrite/cementite interfaces, and at ferrite grain boundaries. In the case of the martensite-ferrite (MF) starting microstructure, which contains thin films of inter-lath retained austenite, austenite forms on the martensite lath boundaries or grows directly from the existing inter-lath retained austenite. The studies are interpreted using the DICTRA module of Thermo-Calc.

- Chapter 4 –*In Situ* Observation of Phase Transformations in MF Starting Microstructures: This chapter is a reproduction of the manuscript entitled “Austenite formation in a medium-Mn steel during intercritical annealing via *in situ* high energy X-ray diffraction” published in *Journal of Materials Research and Technology* in 2024. In this paper, *in situ* austenite transformation kinetics measurements were conducted in order to further develop and validate the modelling approach discussed in Chapter 3.
- Chapter 5 –*In Situ* Observation of Phase Transformations in CR Starting Microstructures: This chapter is a reproduction of the draft manuscript entitled “An *in situ* study of austenite formation during intercritical annealing of a medium-manganese steel with cold-rolled starting microstructure” In this work, the modeling approach discussed in Chapter 3 was validated through the *in situ* measurement of austenite transformation kinetics.
- Chapter 6 – Process maps: This chapter is a reproduction of the manuscript entitled “Process maps for predicting austenite fraction (vol.%) in medium-Mn third-generation advanced high strength steels, published in *Materials* in 2024. This article outlines a model-based approach to develop a robust process window for further development of the medium-Mn steels with compositions of 0.2C-xMn-1.0Si-1.5Al wt.% (x = 4 – 12 wt.%).
- Chapter 7 – Global Discussion: This chapter presents the major findings from Chapters 3 to 6. The effects of starting microstructure and intercritical annealing temperature on the phase

transformation kinetics and microstructural evolution will be discussed first and then lead into the development of the process map to predict the intercritical austenite vol.% and retained austenite vol.%.

- Chapter 8 – Conclusions and Future Research Directions: This chapter summarizes the primary findings of this research. Moreover, this chapter includes some recommendations for future study in the areas of simulation and phase transformation kinetics of medium-Mn 3G AHSS.

#### 1.4 References

- [1] Z. Xu, X. Jin, Ultra-high Strength Steel Treated by Using Quenching–Partitioning–Tempering Process, in: *Adv. Steels*, Springer Berlin Heidelberg, Berlin, Heidelberg, 2011: pp. 67–73. [https://doi.org/10.1007/978-3-642-17665-4\\_8](https://doi.org/10.1007/978-3-642-17665-4_8).
- [2] S. Lee, K. Lee, B.C. De Cooman, Ultra fine-grained 6wt% manganese TRIP steel, *Mater. Sci. Forum.* 654–656 (2010) 286–289.
- [3] D.K. Matlock, J.G. Speer, E. De Moor, P.J. Gibbs, Recent Developments in Advanced High Strength Sheet Steels for Automotive Applications: an Overview, *JESTECH.* 15 (2012) 1–12.
- [4] D.K. Matlock, J.G. Speer, Third Generation of AHSS: Microstructure Design Concepts, in: Springer, 2009: pp. 185–203.
- [5] J. Lucas, 2021 Acura TLX, Great Designs in Steel, Novi, Michigan, USA, 2021.
- [6] J. Zhao, Z. Jiang, Thermomechanical processing of advanced high strength steels, *Prog. Mater. Sci.* 94 (2018) 174–242. <https://doi.org/10.1016/j.pmatsci.2018.01.006>.
- [7] W. Bleck, X. Guo, Y. Ma, The TRIP Effect and Its Application in Cold Formable Sheet Steels, *Steel Res. Int.* 88 (2017) 1700218.
- [8] L. Liu, B. He, M. Huang, The Role of Transformation-Induced Plasticity in the Development of Advanced High Strength Steels, *Adv. Eng. Mater.* 20 (2018) 1701083. <https://doi.org/10.1002/adem.201701083>.

- [9] G.R. Speich, V.A. Demarest, R.L. Miller, Formation of Austenite During Intercritical Annealing of Dual-Phase Steels, *Metall. Trans. A.* 12A (1981) 1419–1428. <https://doi.org/10.1007/bf02643686>.
- [10] Y.K. Lee, J. Han, Current opinion in medium manganese steel, *Mater. Sci. Technol.* 31 (2015) 843–856. <https://doi.org/10.1179/1743284714Y.0000000722>.
- [11] B. Hu, H. Luo, F. Yang, H. Dong, Recent progress in medium-Mn steels made with new designing strategies, a review, *J. Mater. Sci. Technol.* 33 (2017) 1457–1464. <https://doi.org/10.1016/j.jmst.2017.06.017>.
- [12] Y. Ma, Medium-manganese steels processed by austenite-reverted-transformation annealing for automotive applications, *Mater. Sci. Technol.* 33 (2017) 1713–1727. <https://doi.org/10.1080/02670836.2017.1312208>.
- [13] S. Lee, B.C. De Cooman, Annealing Temperature Dependence of the Tensile Behavior of 10 pct Mn Multi-phase TWIP-TRIP Steel, *Metall. Mater. Trans. A.* 45A (2014) 6039–6052. <https://doi.org/10.1007/s11661-014-2540-6>.
- [14] B.C. De Cooman, Y. Estrin, S.K. Kim, Twinning-induced plasticity (TWIP) steels, *Acta Mater.* 142 (2018) 283–362. <https://doi.org/10.1016/j.actamat.2017.06.046>.
- [15] D.W. Suh, S.J. Kim, Medium Mn transformation-induced plasticity steels: Recent progress and challenges, *Scr. Mater.* 126 (2017) 63–67.
- [16] D.K. Matlock and J.G. Speer, Design considerations for the next generation of advanced high strength steel sheets, *Proc. 3rd Inter. Conf. Adv. High Strength Steels.* (2006) 774–781.
- [17] J.M. Jang, S.J. Kim, N.H. Kang, K.M. Cho, D.W. Suh, Effects of annealing conditions on microstructure and mechanical properties of low carbon, manganese transformation-induced plasticity steel, *Met. Mater. Int.* 15 (2009) 909–916. <https://doi.org/10.1007/s12540-009-0909-7>.
- [18] C. Liu, Q. Peng, Z. Xue, S. Wang, C. Yang, Microstructure and mechanical properties of hot-rolled and cold-rolled medium-Mn TRIP steels, *Materials (Basel)*. 11 (2018) 2242. <https://doi.org/10.3390/ma11112242>.

- [19] S. Lee, B.C. De Cooman, On the selection of the optimal intercritical annealing temperature for medium Mn TRIP steel, *Metall. Mater. Trans. A.* 44A (2013) 5018–5024. <https://doi.org/10.1007/s11661-013-1860-2>.
- [20] M. Soleimani, A. Kalhor, H. Mirzadeh, Transformation-induced plasticity (TRIP) in advanced steels: A review, *Mater. Sci. Eng. A.* 795 (2020) 140023. <https://doi.org/10.1016/j.msea.2020.140023>.
- [21] V. Savic, L. Hector, H. Singh, M. Paramasuwoom, U. Basu, A. Basudhar, N. Stander, Development of a Lightweight Third-Generation Advanced High-Strength Steel (3GAHSS) Vehicle Body Structure, *SAE Int. J. Mater. Manuf.* 11 (2018). <https://doi.org/10.4271/2018-01-1026>.
- [22] Z. Dai, H. Chen, R. Ding, Q. Lu, C. Zhang, Z. Yang, S. van der Zwaag, Fundamentals and application of solid-state phase transformations for advanced high strength steels containing metastable retained austenite, *Mater. Sci. Eng. R.* 143 (2021) 100590. <https://doi.org/10.1016/j.mser.2020.100590>.
- [23] J.J. Mueller, X. Hu, X. Sun, Y. Ren, K. Choi, E. Barker, J.G. Speer, D.K. Matlock, E. De Moor, Austenite formation and cementite dissolution during intercritical annealing of a medium-manganese steel from a martensitic condition, *Mater. Des.* 203 (2021) 109598. <https://doi.org/10.1016/j.matdes.2021.109598>.
- [24] K. Steineder, R. Schneider, D. Krizan, C. Béal, C. Sommitsch, Comparative investigation of phase transformation behavior as a function of annealing temperature and cooling rate of two medium-mn steels, *Steel Res. Int.* 86 (2015) 1179–1186. <https://doi.org/10.1002/srin.201400551>.
- [25] P.J. Gibbs, E. De Moor, M.J. Merwin, B. Clausen, J.G. Speer, D.K. Matlock, Austenite stability effects on tensile behavior of manganese-enriched- austenite transformation-induced plasticity steel, *Metall. Mater. Trans. A.* 42A (2011) 3691–3702. <https://doi.org/10.1007/s11661-011-0687-y>.

- [26] S. Lee, S.J. Lee, B.C. De Cooman, Austenite stability of ultrafine-grained transformation-induced plasticity steel with Mn partitioning, *Scr. Mater.* 65 (2011) 225–228. <https://doi.org/10.1016/j.scriptamat.2011.04.010>.
- [27] E. De Moor, D.K. Matlock, J.G. Speera, M.J. Merwin, Austenite stabilization through manganese enrichment, *Scr. Mater.* 64 (2011) 185–188. <https://doi.org/10.1016/j.scriptamat.2010.09.040>.
- [28] H. Luo, J. Shi, C. Wang, W. Cao, X. Sun, H. Dong, Experimental and numerical analysis on formation of stable austenite during the intercritical annealing of 5Mn steel, *Acta Mater.* 59 (2011) 4002–4014. <https://doi.org/10.1016/j.actamat.2011.03.025>.
- [29] H. Farahani, W. Xu, S. van der Zwaag, Prediction and Validation of the Austenite Phase Fraction upon Intercritical Annealing of Medium Mn Steels, *Metall. Mater. Trans. A.* 46A (2015) 4978–4985. <https://doi.org/10.1007/s11661-015-3081-3>.

## 2 Literature Review

### 2.1 Third-Generation Advanced High Strength Steels

The automotive industry is looking for lightweight advanced steels with superior combination of strength and ductility. Advanced high-strength steels can reach the desired mechanical properties by engineering the volume fractions of ferrite, austenite, bainite, and martensite. Thermomechanical processing and alloy additions can be used to adjust the microstructure and meet the target mechanical properties. The combination of high strength and high elongation can be obtained by controlling the intercritical annealing process and targeting an ultrafine-grained alloy [1].

There are different approaches to develop steels with the desired mechanical properties of the 3G-AHSSs. One of the most important approaches is using the TRIP effect as used for the 1<sup>st</sup> generation of AHSSs. Recently, low alloy transformation-induced plasticity (TRIP)-assisted steels with complex microstructures containing polygonal ferrite, retained austenite, carbide free bainite, and a small fraction of martensite have been receiving increasing attention, due to their high strength and ductility. The transformation of retained austenite to martensite during deformation can delay the onset of necking during plastic deformation, which results in the great combination of strength and ductility [2]. This is illustrated in Figure 2.1. The main purpose of TRIP/TWIP approach is to form stable retained austenite which can be transformed to martensite during plastic deformation leading to the desired mechanical properties of 3rd generation AHSSs. The red vector in Figure 1.2 shows this approach. The martensitic transformation of the retained austenite is the basis of the TRIP effect. Therefore, it will be explained in more detail in the following section.

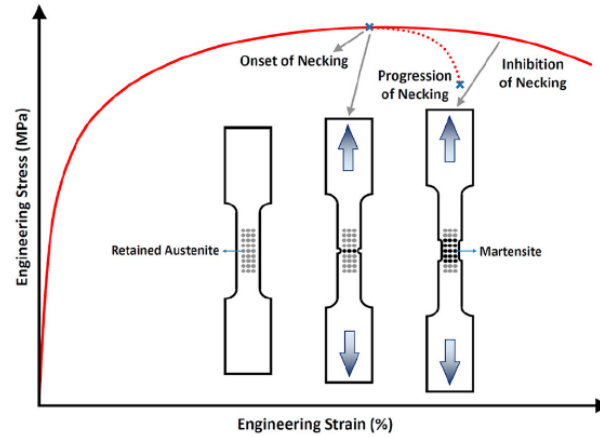


Figure 2.1: Schematic of TRIP effect during plastic deformation [2].

The martensitic transformation in steels can be stress or strain activated depending on the transformation temperature as shown in Figure 2.2 [3]. At  $T_0$ , the Gibbs free energy of martensite and austenite are equal. As a result, phase transformation is possible without composition changes below this temperature. For the martensitic transformation, the free energy is opposed by the surface energy and elastic strain energy related to martensite formation. Therefore, martensitic transformation cannot occur at  $T_0$ . At a temperature  $M_s$  ( $<T_0$ ), a sufficient chemical driving force (the critical driving force) is available to form martensite. A spontaneous transformation of austenite to martensite is possible below  $M_s$ . Above the  $M_s$  temperature ( $T_1$ ), the chemical driving force is not sufficient to initiate the martensite transformation. A Mechanical driving force ( $U'$ ) might therefore be used to trigger the martensitic transformation at these temperatures (above  $M_s$ ) [2,4]. Figure 2.2b shows that the required transformation stress linearly rises by increasing the temperature from  $M_s$  to  $M_s^\sigma$ . When the temperature is between  $M_s$  and  $M_s^\sigma$ , the austenite to martensite transformation occurs when the total of mechanical energy owing to an applied stress and the chemical driving force overcomes the critical activation energy. This is called stress-assisted martensitic transformation (SAMT) [2,4]. On the other hand, between  $M_s^\sigma$  and  $M_d$ , the required applied stress to overcome the critical driving force exceeds yield stress (YS) of austenite [3,4]. As a result, martensite forms from plastically deformed austenite, this is called the strain-induced martensitic transformation (SIMT).

At temperatures higher than  $M_d$ , martensitic transformation is not possible since the chemical driving force is too small and the mechanical energy cannot trigger the phase transformation [4].

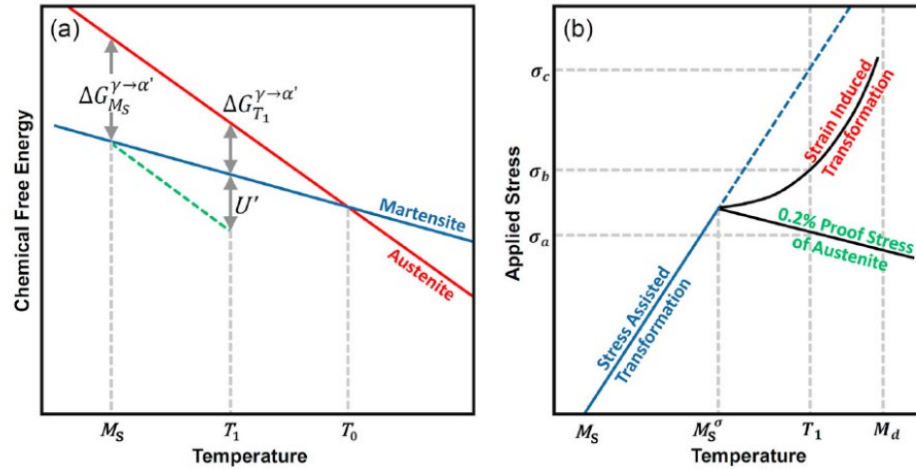


Figure 2.2: (a) Chemical free energies and (b) applied stress for martensitic transformation versus temperature [2,4].  $U'$  represents the mechanical driving force resulting from applied stress,  $\Delta G_{T_1}^{\gamma \rightarrow \alpha'}$  denotes the chemical driving force at  $T_1$ , and  $\Delta G_{M_s}^{\gamma \rightarrow \alpha'}$  indicates the chemical driving force necessary to initiate the transformation from austenite to martensite at the  $M_s$  temperature.

## 2.2 Medium Mn TRIP Steels

### 2.2.1 Microstructures and Chemical Composition of Medium Mn TRIP Steels

Recently, due to increasing demand for strong automotive steel, a new family of TRIP steels with medium concentration of Mn (4-12 wt.%) has been drawing significant attention. Medium-Mn steel microstructure is a dual-phase or tri-phase structure containing retained austenite, ferrite and/or martensite. In addition, the TRIP effect has also been used to target high mechanical properties for medium Mn TRIP steels. In these steels, the higher amount of Mn results in retaining a considerable fraction of austenite and by consequence a desirable strength-ductility balance as illustrated in Figure 1.2 [2,5–7]. The first idea of the increasing Mn concentration was offered by Miller in 1970s [8]. It was reported that a high strength of 1150 MPa with a uniform elongation over 25% could be achieved in cold rolled 0.1C-6Mn alloy after

annealing at 640 °C for 1 hour. This was attributed to the high amount of retained austenite in the alloy resulting in martensitic transformation during deformation.

It should be noted that strength-ductility balance in AHSSs are relative to the amount and stability of retained austenite [5]. Both C and Mn are austenite stabilizing elements. Therefore, by increasing their amount in the AHSS steels, it is possible to increase retained austenite volume fraction. Since good weldability is also a desired property for vehicle body structure, there is a limitation on C content in AHSS steels. Hence, increasing the amount of Mn is the main option to enhance the volume fraction of retained austenite and this has resulted in the well-known medium Mn steels [6]. Figure 2.3a, and Figure 2.3b show the hot-rolled and cold-rolled microstructures of a Fe-7Mn-0.1C-0.5Si (wt.%) medium Mn steel, respectively, that were intercritically annealed at 640 °C for 30 minutes. The hot-rolled intercritically annealed samples contain lath-shaped ferrite and austenite grains since the martensite matrix did not recrystallize before reverse transformation. Cold-rolled intercritical annealed samples contain globular-shaped ferrite and austenite grains because martensite matrix recrystallization occurred before reverse transformation. Medium Mn steels generally contain a dual-phase microstructure, with 20-50 vol. % of retained austenite enriched by C and Mn and a fine ferrite matrix. In order to achieve the excellent strength/elongation balance, some researches have also been focused on producing a mixed microstructure of martensite and retained austenite in medium Mn steels [9,10].

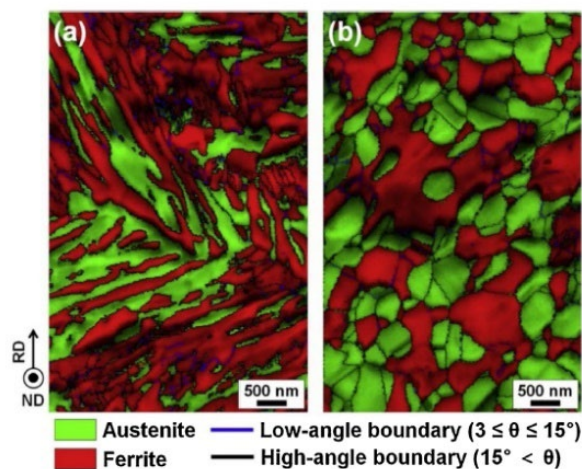


Figure 2.3: Typical microstructures of (a) hot-rolled and (b) cold-rolled medium Mn steels intercritically annealed at 640 °C for 30 minutes [11].

Medium Mn steels generally consist of 0.05-0.4 wt.% C and 4-12 wt.% Mn, 0.5-3 wt.% Al, 0.5-2 wt.% Si and small amount of micro-alloying elements, such as Mo, Ti, V and Nb. Si and/or Al are added to delay cementite formation and therefore to enhance C enrichment in austenite [12–14]. Suppressing cementite formation is due to the low diffusivity of Si in cementite at low temperatures. Furthermore, these alloying elements have an effect on the phase diagram of these steels, as indicated in Figure 2.4. Adding C makes narrower the IA (intercritical annealing) temperature range and promotes carbide formation at lower temperatures as illustrated in Figure 2.4a. Mn is added to shift the IA range to a lower temperatures, as shown in Figure 2.4b. Figure 2.4c and d indicate that both Si and Al raise the  $A_{e1}$  (the equilibrium temperature at which austenite starts to form) and  $A_{e3}$  (the equilibrium temperature at which the steel becomes fully austenitic) temperatures [6,15]. Adding Si improves the steel’s strength through solid solution strengthening, while it decreases the surface quality owing to the formation of  $\text{SiO}_2$ , which has unfavorable effect on the Zn coating process. Finally, Mo addition enhances hardenability and trace amounts of Ti, Nb and V additions are effective for grain refinement of prior austenite [16–18].

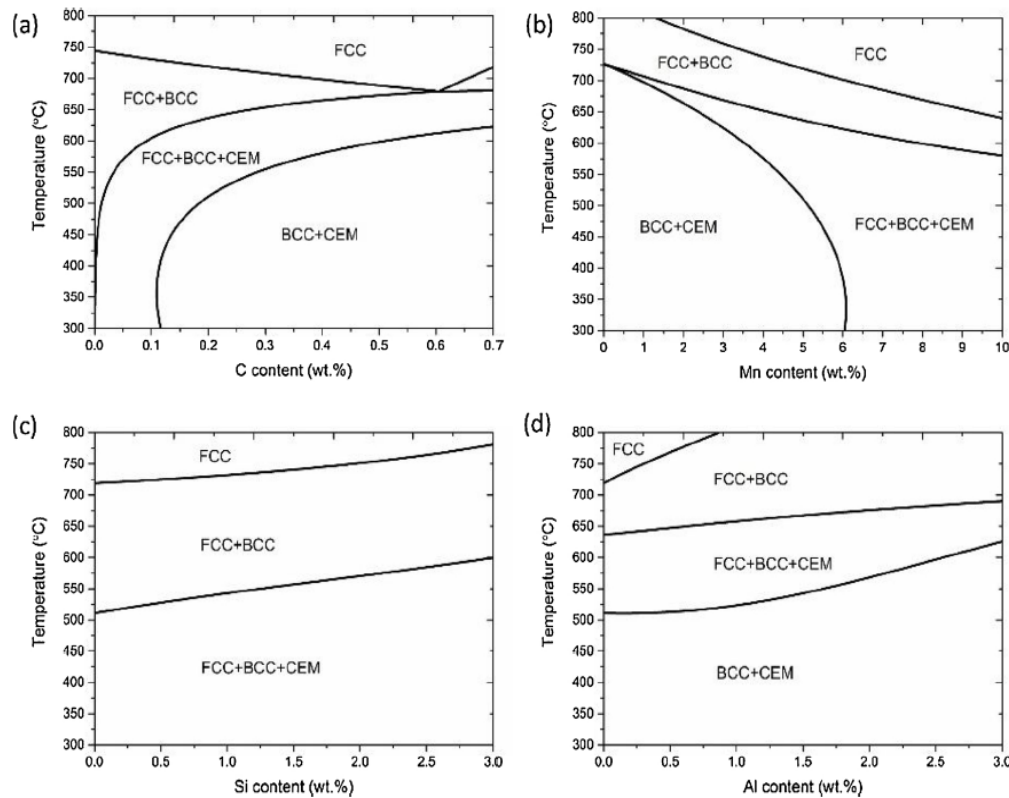


Figure 2.4: The effect of alloying elements on the phase diagram of medium Mn steels. (a) Fe-xC-5 Mn; (b) Fe-0.2C-xMn; (c) Fe-0.2C-5 Mn-xSi; (d) Fe-0.2C-5 Mn-xAl [6].

### 2.2.1.1 Starting Microstructure Effect

Medium Mn steels usually contain fully martensitic initial microstructure but some of them with higher Mn content have a slight amount of austenite in the martensite matrix [19]. Medium Mn steels can be intercritically annealed to obtain a mixture of fine ferrite and 20-50 vol.% retained austenite. The austenite is stabilized by both C and Mn partitioning from martensite or ferrite, during intercritical annealing. This reaction is called the austenite reversion treatment (ART) and was suggested the first time in 1970s [8]. Figure 2.5 indicates a schematic of the production route for medium-Mn steels. Medium Mn steels can obtain two different microstructures as a result of ART annealing, (a) ultrafine-grain duplex microstructures with austenite and ferrite lamella (b) equiaxed microstructures with ferrite and retained austenite [20].

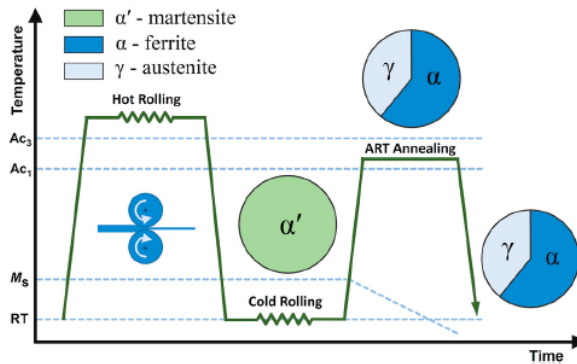


Figure 2.5: Schematic of ART annealing process for medium Mn steels [2].

The initial microstructure of medium-Mn TRIP steels strongly affects the volume fraction of retained austenite and then their mechanical properties. Two different starting martensitic microstructures are identified: (a) hot-rolled and (b) cold-rolled microstructures, which have an effect on the final microstructure and mechanical properties (see Figure 2.3) [21]. The fine lath martensite starting microstructure is generated after quenching from the austenitic region, which results in the formation of fine and stable reverted austenite after the ART process. The advantages of forming lath martensite are to form more nucleation sites in order to form very fine austenite and ferrite laths after annealing (see Figure 2.3a) [22]. It is important to note that tempered cold-rolled initial microstructure has a higher density of grain boundaries compared to the as-quenched martensite and thus, a higher number of nucleation sites for ferrite, resulting in an ultrafine globular austenite and ferrite microstructure (see Figure 2.3b) [23,24]. Prior austenite boundaries, martensite block boundaries, and martensite lath boundaries are all possible

nucleation sites for austenite during ART. Generally, there are two types of reverted austenite microstructures, i.e. lath and globular [21], and the final microstructure is affected by the initial morphology. The initial microstructure of medium-Mn TRIP steels strongly affects the volume fraction of retained austenite and then their mechanical properties. The hot-rolled samples with the martensitic initial microstructure can have higher volume fractions of retained austenite than the cold-rolled samples [22,25]. The effect of the starting microstructure of medium-Mn steels on the RA is summarized in Table 2.1.

Table 2.1: Summary of the effect of starting microstructure on RA

	<b>Martensitic Starting Microstructure</b>	<b>Cold Rolled (TM) Starting Microstructure</b>
<b>R.A. Morphology</b>	Lamellar	Globular
<b>Austenite nucleation</b>	Martensite laths	PAGB

Apart from the effect of initial microstructure on the growth kinetics and austenite stability, another important parameter is cementite precipitation and dissolution in tempered cold-rolled ferrite-cementite microstructures. The amount of Mn in cementite and its partitioning behavior plays a key role in the cementite dissolution driving force and austenite growth kinetics. Also, undissolved cementite in the microstructure could have an effect on the TRIP effect because the amount of C in RA can be significantly decreased since C is captured in cementite. Lower C results in a lower amount of RA. Thus, cementite dissolution kinetics is a very important process in medium-Mn steels. Gouné et. al. [26] studied the influence of Mn on cementite dissolution and austenite growth kinetics. The authors mentioned that adding alloying elements such as Mn can significantly slow down the cementite dissolution kinetics. Figure 2.6a shows the effect of Mn in cementite (6.7 wt.% and 15.5 wt.%) and temperature on the cementite dissolution regime. It is obvious that the shift from slow to fast cementite dissolution depends on Mn composition and temperature. When the amount of Mn in cementite is 15.5 wt.% (globular cementite) at a temperature of 750 °C, the austenite growth kinetics is slow due to the slow cementite dissolution kinetics. This is related to the slow diffusion of Mn and Si between cementite and the martensite, and the retardation is enhanced by increasing the Mn content in

cementite (see Figure 2.6b). Therefore, the dissolution of cementite and the growth of austenite are controlled by Mn diffusion and are slow at these conditions (see Figure 2.6). On the other hand, at higher temperature such as 790 °C, austenite growth kinetics is much faster because the cementite dissolution is controlled by C diffusion and the driving force of cementite dissolution is high at this temperature (see Figure 2.6b) [26].

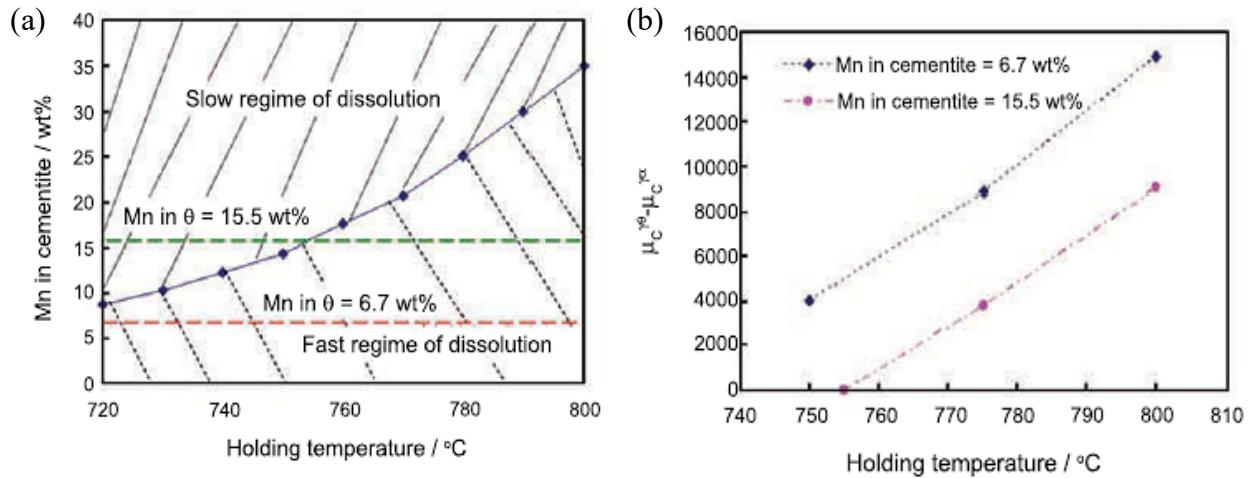


Figure 2.6: (a) cementite dissolution regime based on amount of Mn in cementite and temperature, (b) chemical potential of C at the cementite/austenite and austenite/ferrite interfaces vs. temperature [26].

### 2.2.2 Effect of Intercritical Annealing Conditions

Intercritical annealing temperature and time strongly affect the volume fraction and stability of retained austenite in medium-Mn steels. The volume fraction of retained austenite increases with increasing annealing temperature, and after reaching the highest value, it decreases at higher temperature. While the volume fraction of retained austenite at the intercritical annealing temperature increases, its stability decreases. The lower chemical stability (i.e. C and Mn concentrations in larger grains are diluted) and mechanical stability (i.e. the grain size increased, the hydrostatic pressure from surrounding phases decreased) might account for the transformation of the intercritical austenite to martensite [22,27,28]. The optimum annealing temperature allows maximizing the retained austenite volume fraction and provides a balance between austenite stability and its volume fraction [29].

The influence of the intercritical annealing temperature on the amount of retained austenite and mechanical properties of Fe–0.2C–8.5Mn–3Al medium-Mn TRIP steel is indicated in Figure 2.7. The highest elongation occurs at the intercritical annealing temperature corresponding to the maximum volume fraction of retained austenite (750 °C) owing to the TRIP effect. On the other hand, the tensile strength increases constantly because of the martensite formation at high intercritical annealing temperatures [30].

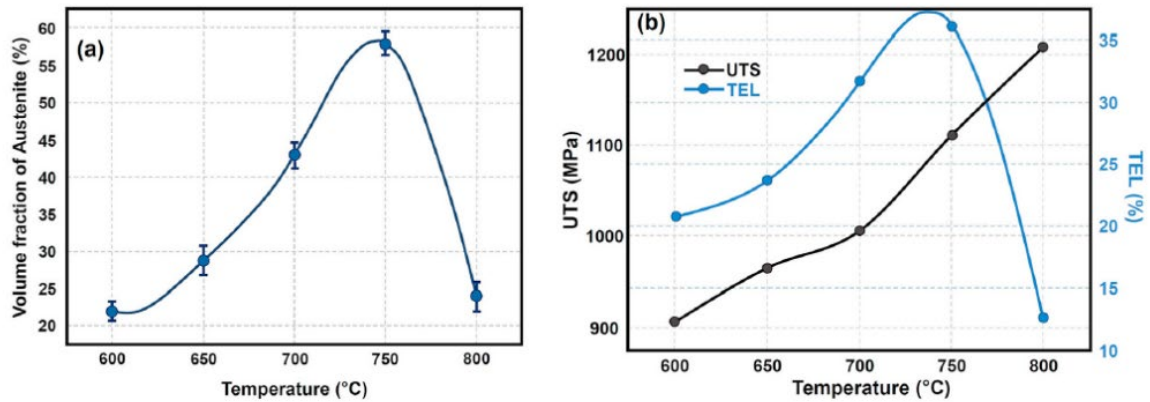


Figure 2.7: Intercritical annealing temperature influence on (a) the volume fraction of austenite and (b) the UTS and elongation of a Fe–0.20C– 3.12Al–8.56Mn (wt.%) medium-Mn steel for an intercritical annealing time of 1 hour [30].

It should be mentioned that annealing time has the same effect on the microstructure and mechanical properties of medium Mn steels [31]. Short annealing time may not be sufficient to form the required volume fraction of reverted austenite with the proper mechanical stability [32]. Conversely, a long annealing time may result in extreme enrichment of Mn and C in retained austenite, causing the stabilization of austenite and a weak TRIP effect. It was found that the amount of retained austenite increases with increasing annealing duration and then decreases again after a maximum value. This can be related to the volume fraction/phase stability balance of retained austenite formed during IA. Hence, annealing time significantly affect the mechanical properties of medium-Mn steels [33]. Figure 2.8 shows stress-strain curves and volume fraction of retained austenite of Fe–0.17C–5.6Mn–1.2Al medium Mn steel annealed at a temperature of 650 °C for the wide range holding times (5 min–48 hr.). The optimum annealing time for achieving the desired strength/ductility balance relates to the maximum amount of the retained austenite, which is obtained at 30 min of annealing for this steel [33].

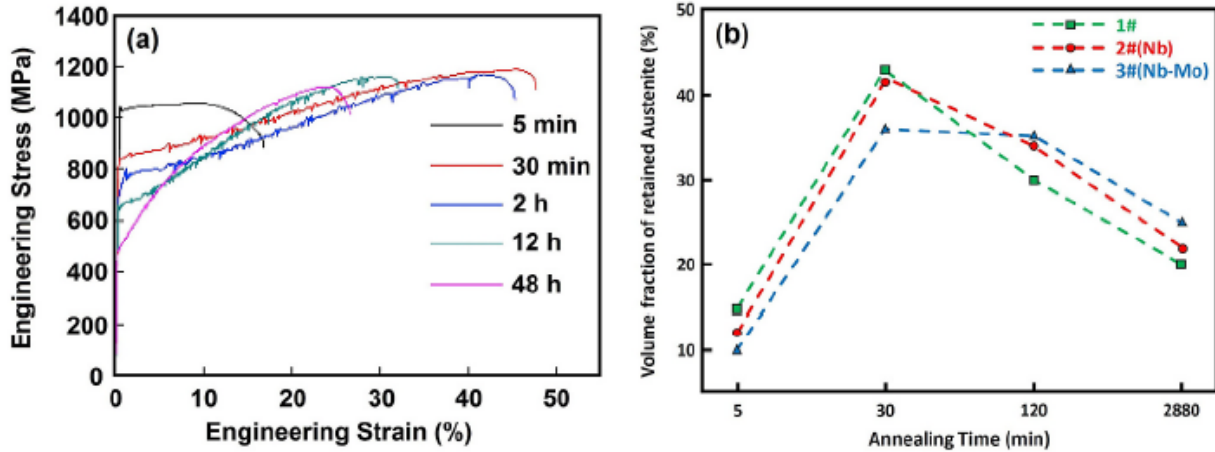


Figure 2.8: (a) Engineering stress-strain curves of Fe-0.17C-5.6Mn-1.2Al medium-Mn steel and (b) the volume fraction of austenite [33].

### 2.3 Phase Transformations in Medium-Mn TRIP-Assisted Steels

Diffusion-controlled phase transformations play an essential role in controlling mechanical properties and microstructures of medium-Mn steels. Thus, modeling these phase transformations is very important. In diffusion-controlled model, phase transformation relies only on the diffusivity of alloying elements in the bulk phases [34]. In multicomponent systems, modeling is much more complicated than the ternary due to two reasons. Firstly, the thermodynamic properties of the system are changed by adding alloying elements. Secondly, there is a large difference between the diffusivity of the interstitial element C and the substitutional element x [35]. Austenite growth in these systems can be described using the local equilibrium (LE) model [35]. LE model is based on the equilibrium condition across the interface. All elements have equal chemical potential at the interface,  $\mu_i^\alpha = \mu_i^\gamma$ .  $\mu_i^\gamma$  and  $\mu_i^\alpha$  are chemical potential of element  $i$  (Fe, C, M) in austenite and ferrite phase, respectively.

The growth of austenite has been described by various researchers [35–38], and one notable model is provided by Wycliffe [39]. Wycliffe et. al [39] analyze the austenite growth during IA of a ternary Fe-C-Mn alloy using a local equilibrium model. The initial microstructure of the material is a ferrite-pearlite mixture, which upon heating into the intercritical range, transforms into a combination of  $\alpha$  and  $\gamma$ . The composition profiles are considered locally

linearized. In the  $\alpha$  phase, the C content is considered negligible, whereas in the  $\gamma$  phase, it adopts the eutectoid composition (Figure 2.9a). Additionally, the Mn concentration is initially assumed to be uniform in both the  $\alpha$  and  $\gamma$  phases, denoted as  $C_{Mn}^0$  (Figure 2.9b). Under the assumption of local equilibrium, the compositions at the interface are determined by the equilibrium tie lines on the phase diagram. The interface concentration is expressed as a function of carbon content in  $\gamma$ ,  $C_c$ :

$$C_{Mn}^{\gamma} = a + bC_c \quad [1a]$$

$$C_{Mn}^{\alpha} = k_2(a + bC_c) \quad [1b]$$

$$a = \frac{1-k_0}{k_2-k_0} \quad b = \frac{k_0-k_1}{k_2-k_0}$$

where  $k_0$ ,  $k_1$ , and  $k_2$  are the distribution coefficient of Fe, C, and Mn, respectively.

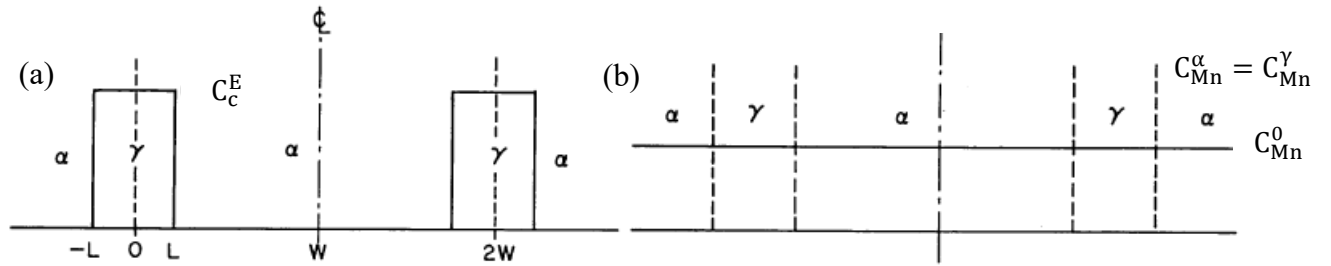


Figure 2.9: Initial state: the concentration profile of (a) carbon and (b) Mn [39].

The process contains three stages: the first two stages are controlled by carbon diffusion and negligible Mn partitioning to  $\gamma$ . In the last stage, Mn partition from  $\alpha$  happens and the growth is controlled by Mn diffusion. The first stage is parabolic growth. Considering a bulk mass balance for carbon (Figure 2.10a), with the carbon content of the  $\alpha$  phase neglected, the equation is formulated as follows:

$$C_c^E L = C_c^E x_0 - 1/2d(C_c^E - C_c^S) \quad [2]$$

The interface mass balance, accounting for the carbon flux to the interface, can be expressed as:

$$C_c^S \frac{dx_0}{dt} = D_c^{\gamma} \frac{C_c^E - C_c^S}{d} \quad [3]$$

replacing the value of  $d$  obtained from Eq. [2], yields:

$$\frac{dx_0}{dt} = D_c^{\gamma} \frac{(C_c^E - C_c^S)L}{2C_c^E C_c^S (x_0 - L)} \quad [4]$$

separating the variables and then integrating, it provides the parabolic growth rate.

The interface tie line, which determines  $C_c^s$  in the above equations, must be established by equating interface velocities derived from the fluxes of both carbon and Mn. Figure 2.10b shows Mn concentration profile. The interface concentration of Mn in the  $\gamma$  phase, denoted as  $C_{Mn}^Y$ , is assumed to remain constant as the interface advances, due to the significantly lower diffusivity rate of Mn in the  $\gamma$  phase compared to the  $\alpha$  phase.

A bulk mass balance for Mn:

$$(x_0 - L)(C_{Mn}^Y - C_{Mn}^0) = 1/2e(C_{Mn}^0 - C_{Mn}^\alpha) \quad [5]$$

while the interface mass balance is:

$$(C_{Mn}^Y - C_{Mn}^\alpha) \frac{dx}{dt} = D_{Mn}^\alpha \frac{C_{Mn}^0 - C_{Mn}^\alpha}{e} \quad [6]$$

Combining Eqs. [5] and [6] to eliminate the variable  $e$  (marked on Figure 2.10b), results in a velocity expression:

$$\frac{dx_0}{dt} = \frac{D_{Mn}^\alpha (C_{Mn}^0 - C_{Mn}^\alpha)^2}{2(x_0 - L)(C_{Mn}^Y - C_{Mn}^0)(C_{Mn}^Y - C_{Mn}^\alpha)} \quad [7]$$

Equating the interface velocities described in Eqs. [7] and [4] yields:

$$(C_{Mn}^Y - C_{Mn}^0) = \frac{D_{Mn}^\alpha (C_{Mn}^0 - C_{Mn}^\alpha) C_c^E C_c^s}{D_c^Y (C_c^E - C_c^s) (C_{Mn}^Y - C_{Mn}^\alpha)} \quad [8]$$

Hence, the growth of  $\gamma$  phase occurs with negligible Mn partitioning. The tie line, denoted as  $s$ , determines the interface carbon concentration in the  $\gamma$  phase,  $C_c^s$  where  $C_{Mn}^{Ys} \approx C_{Mn}^0$ .

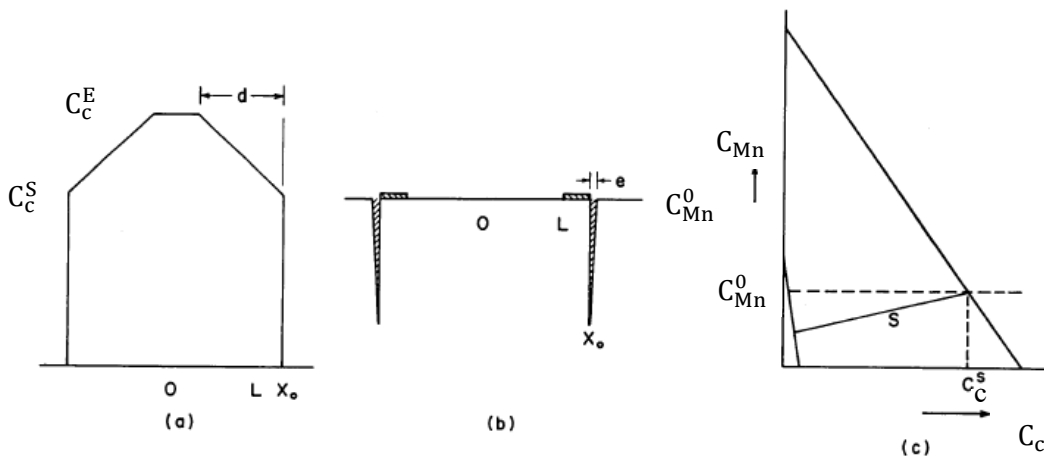


Figure 2.10: Illustration of carbon diffusion-controlled growth. (a) C gradient, (b) Mn gradient. (c) the tie line of C on the isotherm [39].

Carbon diffusion in  $\gamma$  results in logarithmic growth. In the second stage, carbon diffusion fields within the  $\gamma$  phase overlap with each other. The overlapping of carbon diffusion profiles in the  $\gamma$  results in the concentration profile depicted in Figure 2.11. A carbon mass balance yield:

$$C_c^* = \frac{2LC_c^E}{x_0} - C_c^S \quad [9]$$

The interface mass balance gives:

$$C_c^S \frac{dx_0}{dt} = D_c^\gamma \frac{C_c^* - C_c^S}{x_0} \quad [10]$$

which results in:

$$2D_c^\gamma = -1/2(A - x_0)^2 + 2A(A - x_0) - A^2 \ln(A - x_0) \quad [11]$$

where  $A = L \frac{C_c^E}{C_c^S}$

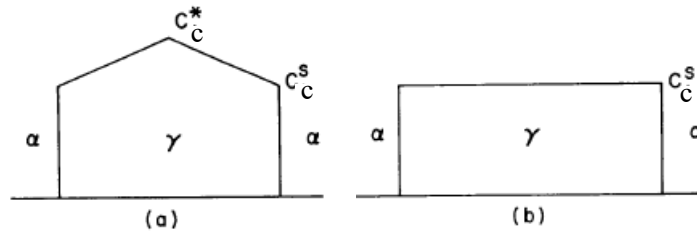


Figure 2.11: (a) Overlapping of carbon diffusion profiles in  $\gamma$  results in logarithmic carbon diffusion-controlled growth. (b) carbon concentration profile at the end of this stage [39].

Once carbon concentration profile becomes uniform, as shown in b, the growth is controlled by Mn diffusion. Further growth of the  $\gamma$  phase cannot occur unless the carbon concentration within the  $\gamma$  phase decreases from the level shown as  $C_c^S$  in a. This necessitates a change in the interface composition, represented by the tie line moving from s towards p in c, resulting in a reduction of the carbon content of austenite, denoted as  $C_1$ . Due to slower diffusion in the  $\gamma$  phase compared to the  $\alpha$  phase, it is assumed that the interface leaves behind a Mn profile representing equilibrium compositions of the  $\gamma$  phase versus distance, as depicted in b. This Mn concentration profile is accompanied by a slight variation in carbon concentration, ensuring uniform carbon activity. An exaggerated carbon profile is illustrated in d. No carbon flux will occur if:

$$\bar{C}_c = C_c + R(C_{Mn}^\gamma - C_{Mn}^0) \quad [12]$$

R represents the ratio of the off-diagonal to on-diagonal diffusion coefficients.

The carbon concentration profile from  $x_0^s$  to  $x_0$  is assumed to be linear, allowing for the derivation of a carbon mass balance equation.

$$C_c^0 = \bar{C}_c x_0 + 1/2(C_c - \bar{C}_c)(x_0 - x_0^s) \quad [13]$$

The interface position as a function of the interface carbon concentration,  $C_c$ , is derived by combining Eqs. [8] and [1]. Then, by inserting Eqs. [8] and [1] into Eq. [13] and differentiating one obtains:

$$dx_0 = \frac{2C_c^0 L(DE/C_c^s - F)}{(FC_c + DE)^2} dC_c \quad [14]$$

where  $E = a - C_{Mn}^0$ ,  $F = Rb + 2$ .

By approximating the diffusion profile of Mn in the  $\alpha$  phase to that of a triangle, the bulk mass balance equation for Mn can be formulated as

$$1/2(C_{Mn}^0 - C_{Mn}^\alpha)e = \int_{x_s}^{x_0} (C_{Mn}^\gamma[x] - C_{Mn}^0) dx \quad [15]$$

$C_{Mn}^\gamma[x]$  is Mn content of the  $\gamma$  as a function of distance. By combining Eqs. [14] and [1] and integration:

$$e = \frac{4C_c^0 L}{F^2(C_{Mn}^0 + C_{Mn}^\alpha)} \left( \frac{RE}{C_c^s} - F \right) \left( \frac{2E}{G} - \frac{2E}{H} + b \ln \frac{H}{G} \right) \quad [16]$$

where  $G = FC_c^s + RE$ ,  $H = FC_c + RE$ .

The interface mass balance for Mn is:

$$D_{Mn}^\alpha \frac{C_{Mn}^0 - C_{Mn}^\alpha}{e} = (C_{Mn}^\gamma - C_{Mn}^\alpha) \frac{dx_0}{dt} \quad [17]$$

Separating variables results in

$$\frac{(C_{Mn}^\gamma - C_{Mn}^\alpha)}{C_{Mn}^0 - C_{Mn}^\alpha} e dx_0 = D_{Mn}^\alpha dt \quad [18]$$

Eqs. [14], [18], and [1] lead to an expression in  $C_c$ , which can be numerically integrated to determine  $C_c$  in phase  $\gamma$  (the shift in the tie line) as a function of time. Eq. [13] correlates an

interface position with each tie line position, while Eq. [17] provides the interface velocity. The growth of austenite is controlled by Mn diffusion in  $\alpha$  phase.

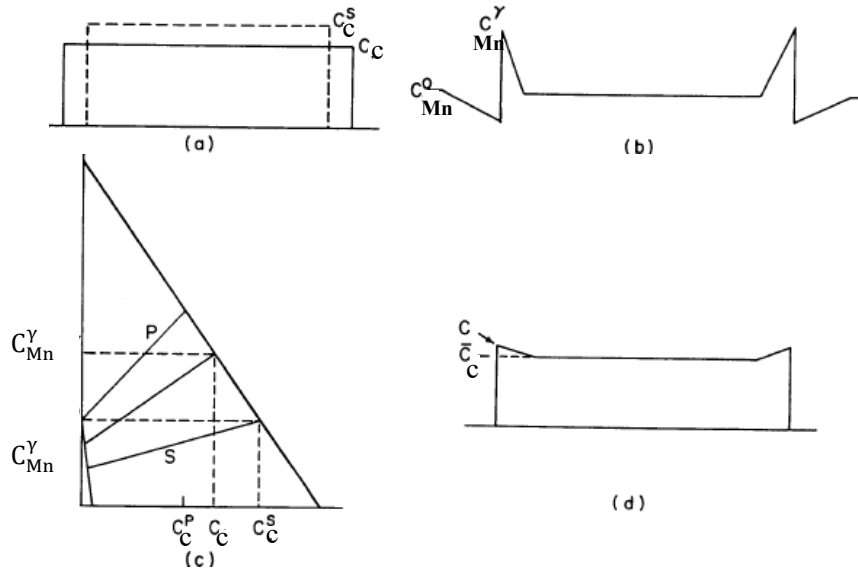


Figure 2.12: (a) Carbon concentration profile (b) Mn concentration profile (c) shift in tie line in growth with Mn partition stage (d) the exaggerated carbon profile [39].

In the final stage of  $\gamma$  growth, the Mn partitions to  $\gamma$ , resulting in a reduction of Mn in the  $\alpha$  phase. The growth of  $\gamma$  will persist until the flux of Mn in the  $\gamma$  phase equals that in the  $\alpha$  phase.

In summary, during annealing in the intercritical range, an Fe-C-Mn alloy rapidly achieves uniform C activity within a short period (i.e., on the order of 1-10 s) through C diffusion control. Subsequent growth of austenite occurs at a significantly slower rate through diffusion of substitutional alloying elements, resulting in noticeable growth over timescales of approximately 10 hours. This growth process creates a region within the  $\gamma$  phase enriched with Mn, while depleting Mn in the  $\alpha$  phase [39]. The model, which is supported by experimental data commonly accepted in the literature [40,41] suggests that the transformation follows the three stages described in this model. Figure 2.13 shows predicted and observed micro-probe for Fe-0.08 C-1Mn (wt.%) annealed for 6 days at 800 °C. The comparison reveals a notable alignment between the predicted and observed Mn concentration profiles. The probe function was convoluted with the concentration profile predicted for a planar geometry.

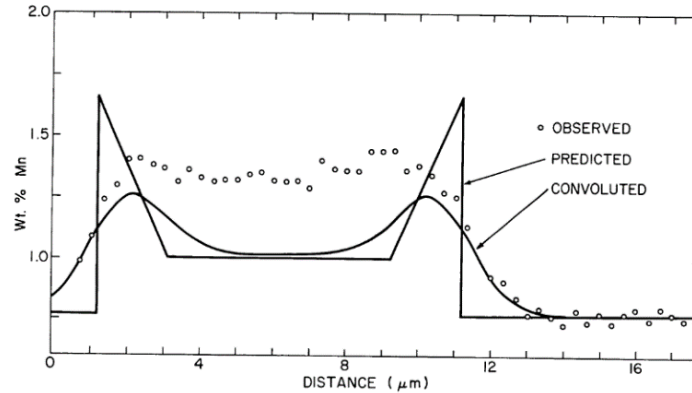


Figure 2.13: Predicted, convoluted and observed micro-probe traces for Fe-0.08 C-1Mn (wt.%) annealed for 6 days at 800 °C. The probe function was convoluted with the concentration profile predicted for a planar geometry [39].

Furthermore, the model results are in agreement with the available experimental data on austenite growth [42]. Speich et. al [42] studied the formation of austenite during intercritical annealing within a temperature range of 740 °C to 900 °C. This study involved a series of 1.5 wt.% Mn steels containing 0.06 to 0.20 wt.% carbon, with a ferrite-pearlite starting microstructure. The experimental findings reveal continued significant austenite growth for durations of up to 24 hours.

The Wycliffe's model [39] provides time-dependent tie-line, interface position, and velocity, along with simplified composition profiles calculated at each time step. The model differs from numerical models like DICTRA [34]. DICTRA provides a comprehensive numerical treatment of diffusion equations in one dimension, employing planar, cylindrical, or spherical geometry. Unlike DICTRA, which provides a full diffusion profile in the  $\gamma$  phase, the Wycliffe model assumes straight-line diffusion profiles. Wycliffe also assumes an ideal phase diagram with straight phase boundaries [39].

In DICTRA, the chemical potentials of species are determined using Thermo-Calc databases. The diffusion coefficients are computed by utilizing mobility databases and considering cross-terms and local composition, thereby enabling the study of multi-component systems. However, it is noteworthy that most systems investigated using DICTRA in the literature are ternary [43–45] or quaternary [40,46]. Dealing with multi-constituent systems can be complex and often poses challenges for numerical convergence.

It should be noted that Wycliffe's model is effective in illustrating the various stages of phase transformation. However, it does have certain limitations. For instance, it does not adequately account for the kinetics of cementite dissolution. Additionally, modifications are necessary when dealing with scenarios involving ferrite/martensite microstructures. These aspects will be further explored in the subsequent section, with reference to DICTRA simulations found in the literature.

### 2.3.1 Austenite Growth from Martensite or Martensite-Austenite Mixture

The growth of austenite and associated alloying elements partitioning in medium Mn steels have been modeled using the local equilibrium (LE) model [35,37,40,41,46–49]. Luo et al. [41] studied the growth of austenite during intercritical annealing at 650 °C in a 5 wt.% Mn-containing steel by assuming LE conditions. It was shown (as depicted in Figure 2.14) that the austenite formation consists of three stages:

- a) Negligible partitioning growth (NPLE-( $\alpha' \rightarrow \gamma$ )) controlled by C diffusion in martensite while there is a Mn spike ahead of the interface. At this first stage, the interface migration rate is very rapid (b). While this stage is very short (around 0.001 second), it significantly increases the size of the austenite phase.
- b) Partitioning growth (PLE-( $\alpha' \rightarrow \gamma$ )) controlled by substitutional alloying elements (Mn and/or Si) diffusion in martensite. During this stage, the concentration of Mn in the austenite phase is slowly increased (c). The austenite growth kinetic was predicted to occur much slower due to the NPLE/PLE transition [40,41].
- c) Very slow partitioning growth (PLE-( $\gamma \rightarrow \alpha'$ )) controlled by diffusion of substitutional elements in austenite to reach final equilibrium, and the interface between martensite and austenite moves back to the austenite side (a and c). First, the reverted austenite volume fraction exceeds the equilibrium amount and then reaches it by shrinkage. The amount of excess may be affected by the diffusion rate of alloying elements in the parent and growing phases, the composition of the steel alloy and the IA temperature.

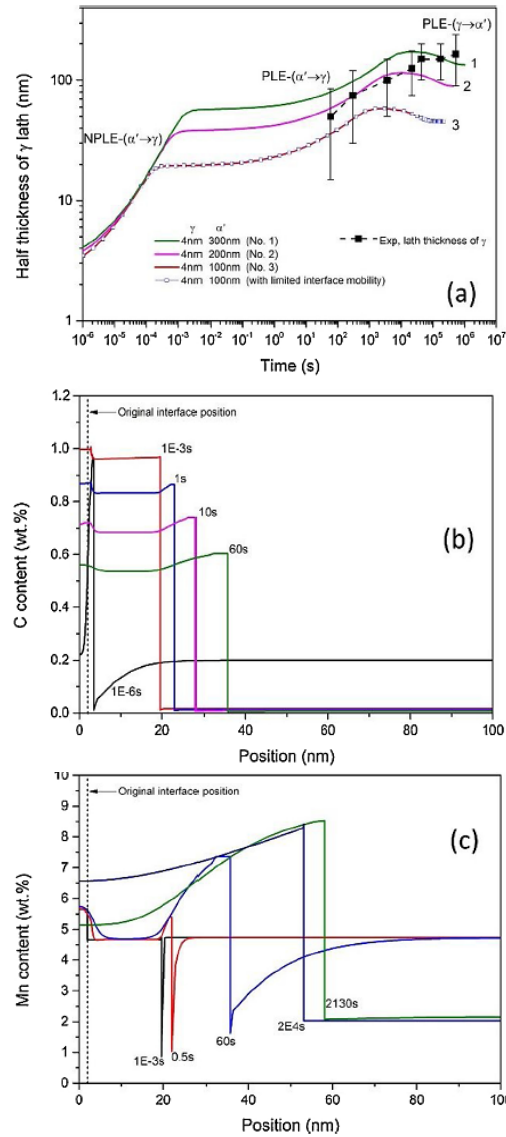


Figure 2.14: (a) The estimated and measured thickness of austenite lath during intercritical annealing at 650 °C in an Fe-0.2C-5 Mn steel. It was assumed that austenite lath and martensite lath have thicknesses of 4 nm and 100–300 nm, respectively. As the interface mobility of martensite/austenite was limited, the measured interface mobility by Krielaart and Van der Zwaag [50] for the  $\gamma$ -to- $\alpha$  transformation was applied. Variations of (b) C and (c) Mn profiles during intercritical annealing, corresponding to curve No. 3 in (a) for the interface position. (Modified version of [41])

Furthermore, Wei et al. [40] conducted a study on austenite growth from martensite microstructure after annealing at various temperatures (690 °C, 720 °C, 790 °C) in Fe-0.1C-

3Mn–1.5Si steel. They identified different stages of austenite growth (see Figure 2.15), including stages controlled by C diffusion in austenite (under  $10^{-2}$  s), diffusion of Mn in ferrite (between  $10^{-2}$  s and  $10^3$  s), and diffusion of Mn in austenite (between  $10^3$  s and  $10^5$  s) [35].

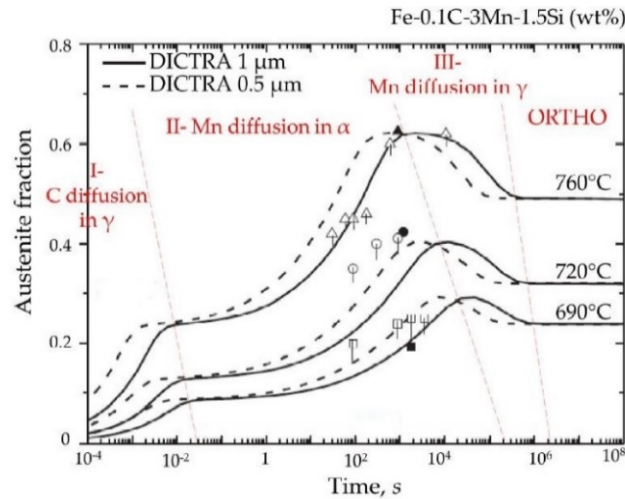


Figure 2.15: Comparison between model and experimental kinetics of austenite growth during holding at three different temperature in Fe-0.1C-3Mn-1.5Si steel alloy modified, from [40].

It worth mentioning that the LE model predictions were in qualitative agreement with the experiment, while the full equilibrium (FE) and para equilibrium (PE) calculations deviated remarkably, as shown in [43,51]. On the other hand, the austenite growth kinetics simulated by LE model are typically more rapid at the initial stage of austenite formation compared to in the experimental observations. It might be related to the interface mobility of martensite/austenite interface assumed to be infinite in this model.

Diffusion-controlled phase transformation can be simulated by mixed-mode approach which accounts for a finite interface mobility [52]. In the case where bulk diffusion does not completely control the transition, this approach is extremely useful. If this is the case, the condition of local chemical equilibrium cannot be met. As a result, the Gibbs energy required to move the interface is provided by the difference in chemical potentials at the interface. If the interface mobility serves as a limiting factor in the kinetic process, then it should be taken into consideration in the corresponding predictions. Zhang et al. [53] studied the simulation of kinetics and the partitioning behavior of alloying elements during reverse transformation of austenite in an Fe-0.3C-2Mn-1.5Si alloy using a mixed-mode model with finite interface

mobility. Different values of the interface mobility were considered in this study ( $M_0 = x * 4 \times 10^{-7} \exp(-140000/RT) \text{ m}^4/\text{Js}$ , where  $x$  is between 0.001 and 1). Figure 2.16a and b show both measured and predicted thickness of acicular-shaped austenite during annealing at 750 °C and 775 °C. It can be seen that the rate of austenite reversion becomes slower by reducing the mobility of interface. Mn and Si content profiles through the interface at 775 °C assuming  $M_0$  and  $0.001 M_0$  are illustrated in Figure 2.16c and d, respectively. At slow interface mobility ( $0.001 M_0$ ), calculation results were in acceptable agreement with experimental observations. Si and Mn more significantly partitioned through  $\alpha/\gamma$  interface for the smaller interface mobility ( $0.001 M_0$ ) (see Figure 2.16d). When the interface mobility is low, Mn and Si atoms have enough time for redistribution across the interface. Although the studied steel is not a grade of medium Mn steels, the whole concept of austenite growth should be similar to that of a medium Mn steel.

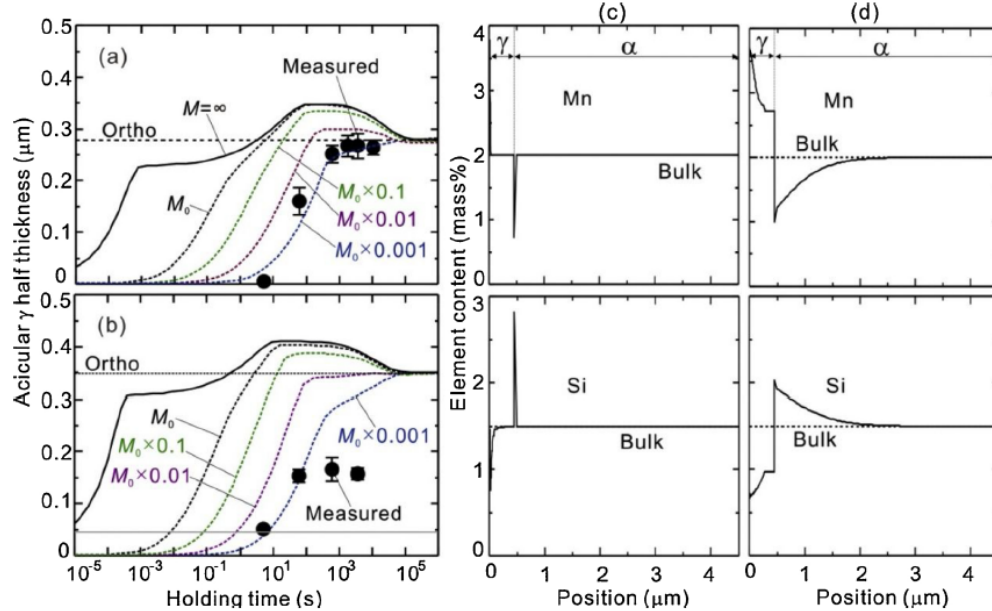


Figure 2.16: The impacts of interface mobility on the austenite growth kinetics at (a) 750 °C and (b) 775 °C. Solid circles in (a) and (b) show the thickness of acicular austenite experimentally measured at different holding time. Mn and Si profiles at  $\gamma/\alpha$  interface at 775 °C for the interface mobility of (c)  $M_0$  and (d)  $0.001 M_0$  [53].

A study on an Fe-0.1C-5 Mn-1.2Si-0.02Al alloy was performed by Tsuchiyama et al. [54] to create a microstructure containing tempered martensite, retained austenite, and fresh martensite after quenching the alloy to a temperature between  $M_s$  and  $M_f$  temperatures, followed by an intercritical annealing (IA). The growth of initial austenite was simulated by DICTRA

assuming LE conditions. Results showed that C and Mn partitioning occurred between martensite and austenite. A gradient of Mn was predicted in austenite due to the slow Mn diffusion coefficient in austenite and the fast  $\alpha'/\gamma$  interface migration. During quenching to ambient temperature, the Mn rich area in the austenite was retained whereas the Mn lean part was transformed to fresh martensite. Ding et al. [55] studied the influence of pre-existing austenite on austenite reversion from an austenite and martensite mixture. It was concluded that a slight amount of pre-existing austenite accelerated austenite reversion kinetics but when its fraction was more than 10%, it decelerated the kinetics by decreasing the austenite nucleation sites.

### 2.3.2 Role of Cementite Dissolution on the Austenite Formation

The intercritical austenite can nucleate at the ferrite/cementite interface and grow accompanied by cementite dissolution since significant amount of cementite particles have been formed and are assumed to precipitate during heating or at the beginning of the IA. These cementite particles could play a significant role in the following austenitization kinetics during IA. Cementite particles are nucleation sites of the austenite grains. Moreover, their dissolution during IA could provide C for austenite growth. However, if these particles do not dissolve, the stability of austenite decreases. The former case results in a higher austenite fraction with a finer grain size formed during IA. The latter case leads to a lower retained austenite fraction owing to the low chemical stability of austenite [41]. Heterogeneous formation of austenite at the ferrite/cementite interface during IA in tempered ferrite and dispersed cementite microstructure was studied by Grujicic et al. [56]. They concluded that incomplete Mn partitioning during IA accelerates nucleation of austenite at the ferrite/cementite interface as well as the following cementite transformation into austenite.

Luo et al. [19,41,57] studied the effect of heating rate on carbide precipitation/dissolution and austenite reversion during IA at 650 °C in a Fe-0.2C-5 Mn steel. It was concluded that a slow heating rate of 1 °C/s provides enough time for cementite precipitation and partitioning of alloying elements from martensite into cementite. Cementite particles served as nucleation sites for the following austenite reversion, whereas the reversion driving force was decreased due to Mn enrichment in cementite and a low C content in martensite. Thus, it was indicated that the rate of austenite reversion was reduced by cementite precipitation. By increasing the heating rate

from 1 ° C/s to 10- 100 ° C/s, cementite still formed in martensite, although there was no Mn partitioning into cementite due to the short available time. Consequently, the austenite reversion at 650 °C was faster at higher heating rates. During a rapid heating rate, carbide formation is delayed to the isothermal IA [19]. Indeed, Luo et al. indicated that cementite precipitation could still occur at the primary stage of isothermal IA after fast heating rate of 300 °C/s. Figure 2.17a and b show rod-like cementite having a diameter of 15 to 35 nm that precipitated in martensite and some austenite nucleated at cementite/martensite interface after IA at 650 °C for 5 min. It was explained that cementite precipitates faster than austenite in martensite matrixes with high levels of defects and supersaturated C during the early intercritical annealing stage, however cementite does not remain stable in the intercritical annealing two phases ( $\alpha + \gamma$ ) region.

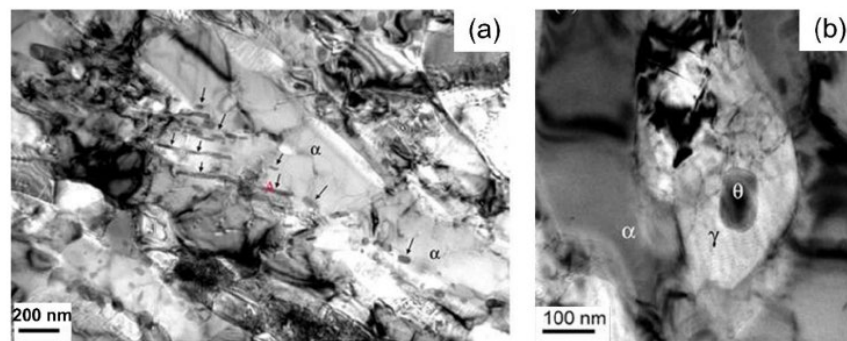


Figure 2.17: TEM images of the microstructures in an Fe-0.2C-5Mn steel after IA at 650 °C for 5 min, showing (a) cementite precipitated in martensite, and (b) a cementite particle within reverted austenite. Cementite particles are indicated by arrows in (a) [19].

As mentioned before, precipitation and dissolution of carbides depend on many factors and are very complex. Many researchers attempted to simulate carbide precipitation/dissolution and austenite reversion via DICTRA to understand this complicated concept [45,58–60]. The simulation of growth kinetics of austenite in an as-quenched Fe-0.2C-5 Mn medium Mn steel was performed by Huyan et al. [58]. Different setups have been used in this simulation (see Figure 2.18.). Figure 2.18 a shows two different setups for austenite growth simulation from martensite and cementite:

- a) Set up A consists of austenite, martensite, and cementite regions, as shown in Figure 2.18 b. This setup shows that austenite forms on martensite lath boundaries and grows into martensite laths and that cementite precipitation-dissolution in martensite has an effect on the austenite growth.

As mentioned in 2.3.1 section, the influence of martensite and austenite interface mobility on the growth kinetics of austenite could be considered.

- b) Set up B contains cementite, austenite, and martensite regions, as shown in Figure 2.18c. This setup shows that cementite precipitates in martensite at the first stage of annealing and then austenite nucleates on the martensite/cementite interfaces. Because of the DICTRA software limitations, the influence of martensite/austenite interface mobility on the growth kinetics of austenite could not be considered.

Austenite growth from martensite without precipitation of cementite was named as setup O (Figure 2.18d). According to setup A simulation (Figure 2.18d), growth kinetics of austenite consists of three stages, a plateau related to the NP/PE transition was also shown. The rate of austenite growth was predicted to be reduced by cementite precipitation. It was also suggested that when the martensite/austenite interface mobility is finite in the simulations setup A (Setup A + M), the predicted growth kinetics of austenite is in qualitative agreement with experimental results.

It was indicated that austenite can nucleate at a cementite/ martensite interface and surround the cementite at a next stage [19,57]. The suitable setup for this case is setup B. Setup B simulations by Huan et al [58] showed that cementite precipitates under NP/PE mode before dissolving. It was observed in the setup B simulations that austenite formation and growth occur only once cementite dissolution starts, although in setup A, austenite growth starts in the beginning. Precipitation of cementite is mostly under NP/PE mode in DICTRA. Nevertheless, Mn-enriched cementite can form before austenite growth in many cases [61]. Zhang et al. [53] simulated the growth kinetics of austenite from cementite/martensite matrix with considerable alloying elements redistribution and indicated that austenite growth kinetics is delayed due to cementite enrichment with Mn. Moreover, Lee et al. [61] reported that cementite dissolution controls the austenite growth and that the average amount of Mn and C in cementite plays an essential role in the growth kinetics of austenite.

In summary, precipitation and dissolution of carbides play a complicated role in the austenite growth process. In many cases, austenite growth rate was decreased by carbide precipitations, because of the reduced driving force for austenite growth due to the C and Mn enrichment in carbides. However, it has also been indicated by Luo et al. [57] and Liu et al. [62]

that the rate of austenite growth can be increased by precipitation of carbides or para-cementite without Mn enrichment at lower pre-tempering temperatures. This suggests that the providing of sufficient nucleation sites would be very crucial. The carbide precipitation-dissolution mechanism and its influence on austenite growth still needs more studies.

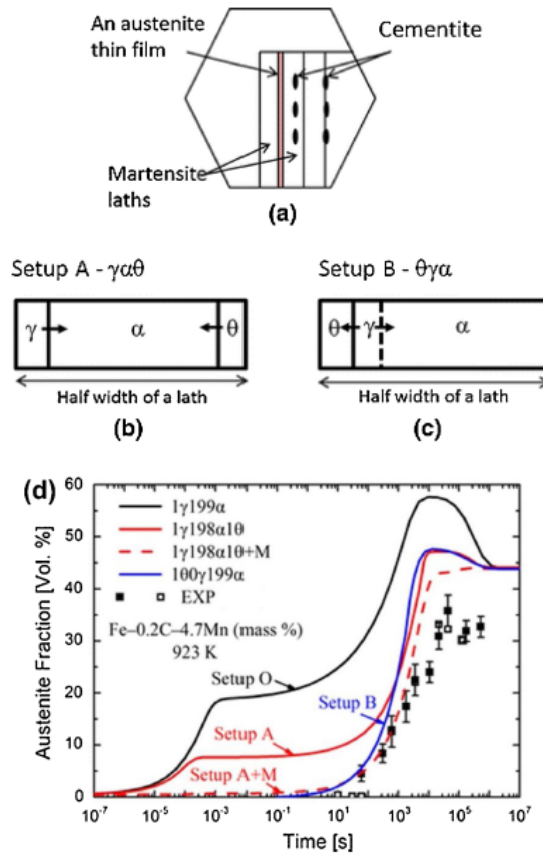


Figure 2.18: (a) Schematic illustration indicating the microstructures during IA. Simulation of austenite nucleation on (b) martensite laths (Setup A) and (c) cementite/ martensite interface (Setup B). (d) The kinetics of austenite growth under different setups simulated using DICTRA. Setup O is related to austenite nucleated on the martensite lath with no cementite precipitation. Setup A + M is related to the effect of martensite/austenite interface mobility [58].

### 2.3.3 Austenite Decomposition

Thermal stability of the retained austenite considerably increases during ART annealing process when C and Mn partition into austenite from the starting martensite. Therefore, some amount of austenite is retained after quenching to room temperature. It can be concluded that for a specific composition, the retained austenite volume fraction that can be obtained is strongly

related to the ART temperature. De Moor et al. [29] presented a simplified thermodynamic model to calculate the fraction of retained austenite as a function of IA temperature. By assuming full equilibrium, firstly, the amount of retained austenite and its composition after IA was approximated. After that, the fraction of austenite that can be retained to ambient temperature was calculated by the Koistinen–Marburger (K-M) equation taking the composition of the retained austenite into account. Figure 2.19 indicates the predicted fraction of retained austenite reaching a peak value at an optimum IA temperature, which is in qualitative agreement with experiments. Based on this thermodynamic model, many calculations were carried out to study the alloying effects of C, Mn, Si, Al and Cr partitioning on the amount of retained austenite [63]. It was reported that Mn has a greater effect than C on increasing the final fraction of retained austenite. By adding Mn, the Mn content of intercritical austenite increases, but its C content is diluted by increased austenite fraction. Conversely, the addition of C increases the austenite's C content, while reducing its Mn content. Adding Al and Si, which are ferrite stabilizers results in decreasing the maximum fraction of retained austenite and increasing the optimum IA temperature. On the other hand, Cr considerably decreases the dependence of retained austenite fraction on the annealing temperature. Many researches have used this thermodynamic model to predict processing variables for medium Mn steels [51,64,65].

Generally, thermodynamic models are in good agreement with experiments when the ART time is long enough to obtain the full equilibrium condition. Prolonged ART times are not possible in industry, therefore, kinetic factors become important to be taken into account. In addition to austenite formation, carbide dissolution during ART plays an important role on the austenite formation kinetics and the alloy microstructure. Thus, the phase transformation kinetics in medium Mn steels during ART is still very complicated and there is still lack of fundamental knowledge [6]. In several studies, the interface migration kinetics of martensite-austenite, alloying elements partitioning, carbide precipitation-dissolution and their influences on austenite formation have been studied. All of them are main subjects playing crucial roles in controlling the microstructure of medium Mn steels.

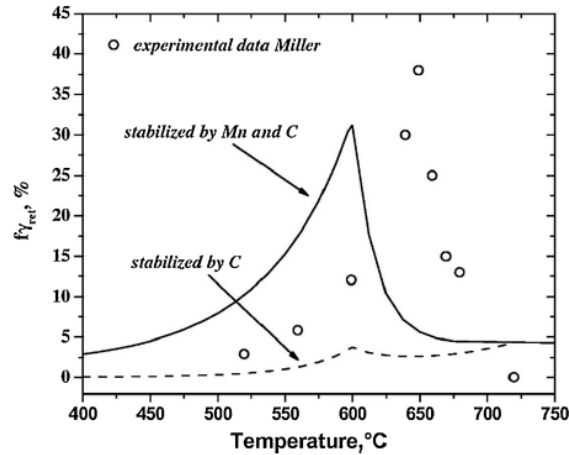


Figure 2.19: Experimental and calculated retained austenite fraction as a function of IA temperature [29].

## 2.4 Summary

To summarize this chapter, considerable efforts have been dedicated to the development of medium-Mn 3G AHSS, with a focus primarily on ternary alloys. Additionally, the thermal processing parameters used in these investigations often do not align with CGL processing windows. Many studies employ longer annealing times at higher temperatures than those practical in conventional industrial CGLs. There is an insufficient body of literature on the phase transformation kinetics, including both modeling and comprehensive characterization methods, for med-Mn steels at short time. Obtaining reliable data within a short timeframe (1-2 minutes) is challenging. In-situ techniques play a key role in enhancing reliability within this limited window. In this study, *in situ* HEXRD has been effectively utilized to examine the austenite volume fraction during intercritical annealing of a medium-Mn steel. Furthermore, recent studies have indicated that the martensitic starting microstructure exhibits enhanced capability in achieving the target mechanical properties for medium-Mn 3G AHSS steels with CGL-compatible processing parameters. Nevertheless, a more in-depth investigation is required to understand the effect of starting microstructure and intercritical annealing parameters on the austenite growth kinetics of medium-Mn steels.

## 2.5 References

- [1] M.Y. Demeri, *Advanced High-Strength Steels: Science, Technology, and Application*, (2013).
- [2] M. Soleimani, A. Kalhor, H. Mirzadeh, Transformation-induced plasticity (TRIP) in advanced steels: A review, *Mater. Sci. Eng. A.* 795 (2020) 140023. <https://doi.org/10.1016/j.msea.2020.140023>.
- [3] G.B. Olson, M. Cohen, A mechanism for the strain-induced martensitic transformations, *J. Less-Common Met.* 28 (1972) 107–118.
- [4] M. Mukherjee, S.B. Singh, O.N. Mohanty, Deformation-induced transformation of retained austenite in transformation induced plasticity-aided steels: A thermodynamic model, *Metall. Mater. Trans. A.* 39A (2008) 2319–2328. <https://doi.org/10.1007/s11661-008-9599-x>.
- [5] D.W. Suh, S.J. Kim, Medium Mn transformation-induced plasticity steels: Recent progress and challenges, *Scr. Mater.* 126 (2017) 63–67.
- [6] Z. Dai, H. Chen, R. Ding, Q. Lu, C. Zhang, Z. Yang, S. van der Zwaag, Fundamentals and application of solid-state phase transformations for advanced high strength steels containing metastable retained austenite, *Mater. Sci. Eng. R.* 143 (2021) 100590. <https://doi.org/10.1016/j.mser.2020.100590>.
- [7] Y. Chang, C.Y. Wang, K.M. Zhao, H. Dong, J.W. Yan, An introduction to medium-Mn steel: Metallurgy, mechanical properties and warm stamping process, *Mater. Des.* 94 (2016) 424–432. <https://doi.org/10.1016/j.matdes.2016.01.048>.
- [8] R.L. Miller, Ultrafine-grained microstructures and mechanical properties of alloy steels, *Met Trans.* 3 (1972) 905–912. <https://doi.org/10.1007/bf02647665>.
- [9] H. Lee, M.C. Jo, S.S. Sohn, A. Zargaran, J.H. Ryu, N.J. Kim, S. Lee, Novel medium-Mn (austenite + martensite) duplex hot-rolled steel achieving 1.6 GPa strength with 20 % ductility by Mn-segregation-induced TRIP mechanism, *Acta Mater.* 147 (2018) 247–260. <https://doi.org/10.1016/j.actamat.2018.01.033>.

- [10] R. Ding, Y. Yao, B. Sun, G. Liu, J. He, T. Li, X. Wan, Z. Dai, D. Ponge, D. Raabe, C. Zhang, A. Godfrey, G. Miyamoto, T. Furuhashi, Z. Yang, S. van der Zwaag, H. Chen, Chemical boundary engineering: A new route toward lean, ultrastrong yet ductile steels, *Sci. Adv.* 6 (2020) 1–8. <https://doi.org/10.1126/sciadv.aay1430>.
- [11] J. Han, A.K. da Silva, D. Ponge, D. Raabe, S.M. Lee, Y.K. Lee, S.I. Lee, B. Hwang, The effects of prior austenite grain boundaries and microstructural morphology on the impact toughness of intercritically annealed medium Mn steel, *Acta Mater.* 122 (2017) 199–206. <https://doi.org/10.1016/j.actamat.2016.09.048>.
- [12] Y.K. Lee, J. Han, Current opinion in medium manganese steel, *Mater. Sci. Technol.* 31 (2015) 843–856. <https://doi.org/10.1179/1743284714Y.0000000722>.
- [13] B. Hu, H. Luo, F. Yang, H. Dong, Recent progress in medium-Mn steels made with new designing strategies, a review, *J. Mater. Sci. Technol.* 33 (2017) 1457–1464. <https://doi.org/10.1016/j.jmst.2017.06.017>.
- [14] Y. Ma, Medium-manganese steels processed by austenite-reverted-transformation annealing for automotive applications, *Mater. Sci. Technol.* 33 (2017) 1713–1727. <https://doi.org/10.1080/02670836.2017.1312208>.
- [15] B. Sun, F. Fazeli, C. Scott, N. Brodusch, R. Gauvin, S. Yue, The influence of silicon additions on the deformation behavior of austenite-ferrite duplex medium manganese steels, *Acta Mater.* 148 (2018) 249–262. <https://doi.org/10.1016/j.actamat.2018.02.005>.
- [16] B.B. He, M.X. Huang, Simultaneous Increase of Both Strength and Ductility of Medium Mn Transformation-Induced Plasticity Steel by Vanadium Alloying, *Metall. Mater. Trans. A.* 49 (2018) 1433–1438. <https://doi.org/10.1007/s11661-018-4517-3>.
- [17] M. Cai, Z. Li, Q. Chao, P.D. Hodgson, A Novel Mo and Nb Microalloyed Medium Mn TRIP Steel with Maximal Ultimate Strength and Moderate Ductility, *Metall. Mater. Trans. A.* 45 (2014) 5624–5634. <https://doi.org/10.1007/s11661-014-2504-x>.

- [18] D. Lee, J.K. Kim, S. Lee, K. Lee, B.C. De Cooman, Microstructures and mechanical properties of Ti and Mo micro-alloyed medium Mn steel, *Mater. Sci. Eng. A.* 706 (2017) 1–14. <https://doi.org/10.1016/j.msea.2017.08.110>.
- [19] H. Luo, J. Liu, H. Dong, A Novel Observation on Cementite Formed During Intercritical Annealing of Medium Mn Steel, *Metall. Mater. Trans. A.* 47A (2016) 3119–3124. <https://doi.org/10.1007/s11661-016-3448-0>.
- [20] W. Bleck, X. Guo, Y. Ma, The TRIP Effect and Its Application in Cold Formable Sheet Steels, *Steel Res. Int.* 88 (2017) 1700218.
- [21] J. Han, S.J. Lee, J.G. Jung, Y.K. Lee, The effects of the initial martensite microstructure on the microstructure and tensile properties of intercritically annealed Fe-9Mn-0.05C steel, *Acta Mater.* 78 (2014) 369–377. <https://doi.org/10.1016/j.actamat.2014.07.005>.
- [22] H. Luo, H. Dong, M. Huang, Effect of intercritical annealing on the Lüders strains of medium Mn transformation-induced plasticity steels, *Mater. Des.* 83 (2015) 42–48. <https://doi.org/10.1016/j.matdes.2015.05.085>.
- [23] M.M. Wang, C.C. Tasan, D. Ponge, D. Raabe, Spectral TRIP enables ductile 1.1 GPa martensite, *Acta Mater.* 111 (2016) 262–272. <https://doi.org/10.1016/j.actamat.2016.03.070>.
- [24] M. Nouroozi, H. Mirzadeh, M. Zamani, Effect of microstructural refinement and intercritical annealing time on mechanical properties of high-formability dual phase steel, *Mater. Sci. Eng. A.* 736 (2018) 22–26. <https://doi.org/10.1016/j.msea.2018.08.088>.
- [25] S. Zhang, K.O. Findley, Quantitative assessment of the effects of microstructure on the stability of retained austenite in TRIP steels, *Acta Mater.* 61 (2013) 1895–1903. <https://doi.org/10.1016/j.actamat.2012.12.010>.
- [26] M. Goun'e, P. Maugis, J. Drillet, A Criterion for the Change from Fast to Slow Regime of Cementite Dissolution in Fe – C – Mn Steels, *J. Mater. Sci. Technol.* 28 (2012) 728–736. [https://doi.org/10.1016/S1005-0302\(12\)60122-4](https://doi.org/10.1016/S1005-0302(12)60122-4).

- [27] D.W. Suh, J.H. Ryu, M.S. Joo, H.S. Yang, K.Y. Lee, Medium – Alloy Manganese – Rich Transformation – Induced Plasticity Steels, *Metall. Mater. Trans. A*. 46A (2013) 286–293.
- [28] R. Schneider, K. Steineder, D. Krizan, C. Sommitsch, Effect of the heat treatment on the microstructure and mechanical properties of medium-Mn-steels, *Mater. Sci. Technol.* 35 (2019) 2045–2053. <https://doi.org/10.1080/02670836.2018.1548957>.
- [29] E. De Moor, D.K. Matlock, J.G. Speera, M.J. Merwin, Austenite stabilization through manganese enrichment, *Scr. Mater.* 64 (2011) 185–188. <https://doi.org/10.1016/j.scriptamat.2010.09.040>.
- [30] Z. Li, Y. Mou, X. Li, D. Misra, H. Ding, L. He, H. Li, The Significance of Microstructure Evolution on Governing Impact Toughness of Fe–0.2C–8.5Mn–3Al Medium-Mn TRIP Steel Studied by a Novel Heat Treatment, *Steel Res. Int.* 91 (2020) 1–8. <https://doi.org/10.1002/srin.202000029>.
- [31] H. Huang, O. Matsumura, T. Furukawa, Retained austenite in low carbon, manganese steel after intercritical heat treatment H., *Mater. Sci. Technol.* July. 10 (1994) 621–626.
- [32] J. Hu, L.X. Du, H. Liu, G.S. Sun, H. Xie, H.L. Yi, R.D.K. Misra, Structure-mechanical property relationship in a low-C medium-Mn ultrahigh strength heavy plate steel with austenite-martensite submicro-laminate structure, *Mater. Sci. Eng. A*. 647 (2015) 144–151. <https://doi.org/10.1016/j.msea.2015.09.008>.
- [33] H. Pan, H. Ding, M. Cai, Microstructural evolution and precipitation behavior of the warm-rolled medium Mn steels containing Nb or Nb-Mo during intercritical annealing, *Mater. Sci. Eng. A*. 736 (2018) 375–382. <https://doi.org/10.1016/j.msea.2018.08.055>.
- [34] A. Borgenstam, A. Engström, L. Höglund, J. Ågren, DICTRA, a tool for simulation of diffusional transformations in alloys, *J. Phase Equilibria*. 21 (2000) 269–280. <https://doi.org/10.1361/105497100770340057>.
- [35] Z. Dai, R. Ding, Z. Yang, C. Zhang, H. Chen, Elucidating the effect of Mn partitioning on interface migration and carbon partitioning during Quenching and Partitioning of the Fe-C-Mn-Si

steels: Modeling and experiments, *Acta Mater.* 144 (2018) 666–678. <https://doi.org/10.1016/j.actamat.2017.11.025>.

[36] H. Chen, X. Xu, W. Xu, S. Van Der Zwaag, Predicting the austenite fraction after intercritical annealing in lean steels as a function of the initial microstructure, *Metall. Mater. Trans. A.* 45A (2014) 1675–1679. <https://doi.org/10.1007/s11661-014-2186-4>.

[37] Z. Dai, R. Ding, Z. Yang, C. Zhang, H. Chen, Thermo-kinetic design of retained austenite in advanced high strength steels, *Acta Mater.* 152 (2018) 288–299. <https://doi.org/10.1016/j.actamat.2018.04.040>.

[38] G. Ghosh, G.B. Olson, Simulation of paraequilibrium growth in multicomponent systems, *Metall. Mater. Trans. A.* 32 (2001) 455–467. <https://doi.org/10.1007/s11661-001-0062-5>.

[39] P.A. Wycliffe, G.R. Purdy, J.D. Embury, Growth of austenite in the intercritical annealing of Fe-C-Mn dual phase steels, *Can. Metall. Q.* 20 (1981) 339–350. <https://doi.org/10.1179/cm.1981.20.3.339>.

[40] R. Wei, M. Enomoto, R. Hadian, H.S. Zurob, G.R. Purdy, Growth of austenite from as-quenched martensite during intercritical annealing in an Fe-0.1C-3Mn-1.5Si alloy, *Acta Mater.* 61 (2013) 697–707. <https://doi.org/10.1016/j.actamat.2012.10.019>.

[41] H. Luo, J. Shi, C. Wang, W. Cao, X. Sun, H. Dong, Experimental and numerical analysis on formation of stable austenite during the intercritical annealing of 5Mn steel, *Acta Mater.* 59 (2011) 4002–4014. <https://doi.org/10.1016/j.actamat.2011.03.025>.

[42] G.R. Speich, V.A. Demarest, R.L. Miller, Formation of Austenite in 1.5 Pct Mn Steels, *Metall. Trans. A.* 12A (1981) 1419–1428. <https://doi.org/10.1007/bf02643686>.

[43] H. Chen, X. Xu, W. Xu, S. Van Der Zwaag, Predicting the austenite fraction after intercritical annealing in lean steels as a function of the initial microstructure, *Metall. Mater. Trans. A.* 45A (2014) 1675–1679. <https://doi.org/10.1007/s11661-014-2186-4>.

[44] Z. Dai, R. Ding, Z. Yang, C. Zhang, H. Chen, Elucidating the effect of Mn partitioning on interface migration and carbon partitioning during Quenching and Partitioning of the Fe-C- Mn-

Si steels: Modeling and experiments, *Acta Mater.* 144 (2018) 666–678. <https://doi.org/10.1016/j.actamat.2017.11.025>.

[45] Q. Lai, M. Gouné, A. Perlade, T. Pardoën, P. Jacques, O. Bouaziz, Y. Bréchet, Mechanism of Austenite Formation from Spheroidized Microstructure in an Intermediate Fe-0.1C-3.5Mn Steel, *Metall. Mater. Trans. A.* 47A (2016) 3375–3386. <https://doi.org/10.1007/s11661-016-3547-y>.

[46] H. Farahani, W. Xu, S. van der Zwaag, Prediction and Validation of the Austenite Phase Fraction upon Intercritical Annealing of Medium Mn Steels, *Metall. Mater. Trans. A.* 46A (2015) 4978–4985. <https://doi.org/10.1007/s11661-015-3081-3>.

[47] D.E. Coates, Diffusion-Controlled Precipitate Growth in Ternary Systems I, *Metall. Trans.* 3 (1972) 1203–1212.

[48] D.E. Coates, Diffusion Controlled Precipitate Growth in Ternary Systems: II, *Metall. Trans.* 4 (1973) 1077–1086.

[49] Z.J. Xie, C.J. Shang, S. V. Subramanian, X.P. Ma, R.D.K. Misra, Atom probe tomography and numerical study of austenite stabilization in a low carbon low alloy steel processed by two-step intercritical heat treatment, *Scr. Mater.* 137 (2017) 36–40. <https://doi.org/10.1016/j.scriptamat.2017.05.002>.

[50] G.P. Krielaart, S. Van Der Zwaag, Simulations of pro-eutectoid ferrite formation using a mixed control growth model, *Mater. Sci. Eng. A.* 246 (1998) 104–116. [https://doi.org/10.1016/s0921-5093\(97\)00752-1](https://doi.org/10.1016/s0921-5093(97)00752-1).

[51] G.K. Bansal, D.A. Madhukar, A.K. Chandan, K. Ashok, G.K. Mandal, V.C. Srivastava, On the intercritical annealing parameters and ensuing mechanical properties of low-carbon medium-Mn steel, *Mater. Sci. Eng. A.* 733 (2018) 246–256. <https://doi.org/10.1016/j.msea.2018.07.055>.

[52] C. Bos, J. Sietsma, A mixed-mode model for partitioning phase transformations, *Scr. Mater.* 57 (2007) 1085–1088. <https://doi.org/10.1016/j.scriptamat.2007.08.030>.

- [53] X. Zhang, G. Miyamoto, T. Kaneshita, Y. Yoshida, Y. Toji, T. Furuhashi, Growth mode of austenite during reversion from martensite in Fe-2Mn-1.5Si-0.3C alloy: A transition in kinetics and morphology, *Acta Mater.* 154 (2018) 1–13. <https://doi.org/10.1016/j.actamat.2018.05.035>.
- [54] T. Tsuchiyama, T. Inoue, J. Tobata, D. Akama, S. Takaki, Microstructure and mechanical properties of a medium manganese steel treated with interrupted quenching and intercritical annealing, *Scr. Mater.* 122 (2016) 36–39. <https://doi.org/10.1016/j.scriptamat.2016.05.019>.
- [55] R. Ding, Z. Dai, M. Huang, Z. Yang, C. Zhang, H. Chen, Effect of pre-existed austenite on austenite reversion and mechanical behavior of an Fe-0.2C-8Mn-2Al medium Mn steel, *Acta Mater.* 147 (2018) 59–69. <https://doi.org/10.1016/j.actamat.2018.01.009>.
- [56] M. Grujicic, Stabilization of precipitated austenite in tempered FeMnC steels, *Mater. Sci. Eng. A.* 127 (1990) 79–84. [https://doi.org/10.1016/0921-5093\(90\)90192-6](https://doi.org/10.1016/0921-5093(90)90192-6).
- [57] H.W. Luo, C.H. Qiu, H. Dong, J. Shi, Experimental and numerical analysis of influence of carbide on austenitisation kinetics in 5Mn TRIP steel, *Mater. Sci. Technol.* 30 (2014) 1367–1377. <https://doi.org/10.1179/1743284713Y.00000000447>.
- [58] F. Huyan, J.Y. Yan, L. Höglund, J. Ågren, A. Borgenstam, Simulation of the Growth of Austenite from As-Quenched Martensite in Medium Mn Steels, *Metall. Mater. Trans. A.* 49A (2018) 1053–1060. <https://doi.org/10.1007/s11661-018-4497-3>.
- [59] N. Yan, H. Di, R.D.K. Misra, H. Huang, Y. Li, Enhancing austenite stability in a new medium-Mn steel by combining deep cryogenic treatment and intercritical annealing: An experimental and theoretical study, *Mater. Sci. Eng. A.* 753 (2019) 11–21. <https://doi.org/10.1016/j.msea.2019.01.026>.
- [60] X. Zhang, G. Miyamoto, Y. Toji, T. Furuhashi, Effects of heating rate on formation of globular and acicular austenite during reversion from martensite, *Metals (Basel)*. 9 (2019) 266. <https://doi.org/10.3390/met9020266>.

- [61] S. Lee, B.C. De Cooman, Influence of Carbide Precipitation and Dissolution on the Microstructure of Ultra-Fine-Grained Intercritically Annealed Medium Manganese Steel, *Metall. Mater. Trans. A.* 47A (2016) 3263–3270. <https://doi.org/10.1007/s11661-016-3507-6>.
- [62] Z.Q. Liu, G. Miyamoto, Z.G. Yang, C. Zhang, T. Furuhashi, Effects of Pre-tempering on Intercritical Annealing in Fe-2Mn-0.3C Alloy, *Metall. Mater. Trans. A.* 45 (2014) 5290–5294. <https://doi.org/10.1007/s11661-014-2519-3>.
- [63] S. Kang, E. De Moor, J.G. Speer, Retained Austenite Stabilization Through Solute Partitioning During Intercritical Annealing in C-, Mn-, Al-, Si-, and Cr-Alloyed Steels, *Metall. Mater. Trans. A.* 46A (2015) 1005–1011. <https://doi.org/10.1007/s11661-014-2708-0>.
- [64] S. Kang, R.W. Hofer, J.G. Speer, D. Krizan, D.K. Matlock, E. De Moor, Intercritical Annealing Response of Medium Manganese Steels Having Different Carbon Concentrations, *Steel Res. Int.* 89 (2018) 1800069. <https://doi.org/10.1002/srin.201800069>.
- [65] S. Lee, B.C. De Cooman, Tensile behavior of intercritically annealed 10 pct Mn Multi-phase Steel, *Metall. Mater. Trans. A.* 45A (2014) 709–716. <https://doi.org/10.1007/s11661-013-2047-6>.

### **3 Austenite Nucleation and Growth as a Function of Starting Microstructure for a Fe-0.15C-5.56Mn-1.1Si-1.89Al Medium-Mn Steel**

Azin Mehrabi, Joseph R. McDermid, Xiang Wang, and Hatem Zurob

Department of Materials Science and Engineering, McMaster University, 1280 Main Street West, Hamilton, Ontario, Canada, L8S 4L8

Steel Research International, 2023, vol. 94, 2200952.

#### **3.1 Abstract**

The effects of starting microstructure and intercritical annealing temperature on the phase transformation kinetics and microstructural evolution of a prototype Fe-0.15C-5.56Mn-1.1Si-1.89Al medium-Mn third-generation advanced high strength steel are examined. The starting microstructures comprise 1) an as-received cold-rolled (CR) microstructure containing a significant fraction of ferrite and tempered martensite and 2) an austenitized and quenched martensite-ferrite (MF) microstructure. Based on the microstructural observations, two different scenarios for austenite formation during intercritical annealing are proposed. For the CR starting microstructure, austenite can nucleate at ferrite/cementite interfaces, and at ferrite grain boundaries. In the case of the MF starting microstructure, which contains thin films of interlath retained austenite (RA), austenite forms on the martensite lath boundaries or grows directly from the existing interlath RA. The studies are interpreted using the DICTRA module of Thermo-Calc. At 665 °C, the austenite reversion kinetics of the MF samples are faster than the transformation kinetics in the CR structure. At higher temperatures where most of the cementite has dissolved, the austenite fraction in both starting microstructures is very similar. The effects of starting microstructure and intercritical annealing temperature on the phase transformation kinetics and microstructural evolution of a prototype Fe-0.15C-5.56Mn-1.1Si-1.89Al medium-Mn third-generation advanced high strength steel are examined. The starting microstructures comprise i) an as-received cold rolled (CR) microstructure containing a significant fraction of ferrite and tempered martensite and ii) an austenitized and quenched martensite – ferrite microstructure. Based on the microstructural observations, two different scenarios for austenite formation during

intercritical annealing have been proposed. For the cold-rolled starting microstructure, austenite can nucleate at ferrite/cementite interfaces, and at ferrite grain boundaries. In the case of the martensite-ferrite (MF) starting microstructure, which contains thin films of inter-lath retained austenite, austenite forms on the martensite lath boundaries or grows directly from the existing inter-lath retained austenite. The studies are interpreted using the DICTRA module of Thermo-Calc. At 665 °C, the austenite reversion kinetics of the martensite-ferrite samples are faster than the transformation kinetics in the cold-rolled structure. At higher temperatures where most of the cementite has dissolved, the austenite fraction in both starting microstructures is very similar.

### **3.2 Introduction**

Recent trends in the automotive industry have focused on decreasing greenhouse gas emissions through increased fuel efficiency and the extension of electric vehicle battery range whilst enhancing vehicle safety and performance [1,2]. This has led to the development of advanced high strength steels (AHSS) with excellent strength/formability characteristics [3,4]. Medium-manganese (med-Mn) steels, which are strong third-generation advanced high strength steels (3G AHSS) candidates, have significant potential for enhanced structural applications in the automotive industry [5,6]. Since the mechanical properties of med-Mn steels are strongly influenced by the amount and stability of Retained Austenite (RA), it is crucial to control the RA through alloy design, including thermo-mechanical processing [7,8]. The microstructure of med-Mn Transformation Induced Plasticity (TRIP) steels with 4-12 wt.% Mn generally consists of a fine martensitic matrix with significant fractions of solute-enriched RA from Intercritical Annealing (IA) thermal treatments, where the partitioning of carbon into the austenite, in particular, improves its chemical and mechanical stability. Austenite Reversion Treatment (ART) is the name generally applies to this process [9,10]. The amount of RA and its stability are influenced by several factors, including the IA parameters, the initial microstructure (grain size and morphology) of the alloy, and the chemical composition of the austenite [11]. Thus, controlling the volume fraction and stability of RA plays a key role in achieving the target mechanical properties of these alloys [11–13].

The starting microstructure is one of the most important factors affecting the volume fraction, stability, morphology, and reversion kinetics of the RA and the resultant mechanical

properties of med-Mn TRIP steels. The retained austenite can exhibit a variety of morphologies, depending on the initial microstructure. In case of a martensitic starting microstructure, the RA tends to be lamellar, because the martensitic matrix does not recrystallize before the austenite reversion transformation, whereas equiaxed RA is observed in cold-rolled starting microstructures because the martensitic matrix recrystallizes before the reversion transformation [13,14]. As a result, of this processing history, the lath shaped RA is usually present in smaller volume fractions and contains higher C and Mn than the equiaxed or globular RA. In addition, the lath-shaped retained austenite tends to be surrounded by martensite, imposing a local hydrostatic stress which resists the shape change associated with the  $\gamma \rightarrow \alpha'$  transformation. As a result, lath shaped retained austenite is generally found to be more stable during subsequent deformation [15,16]. Furthermore, a martensitic starting microstructure accelerates austenite reversion kinetics because less energy is needed for the nucleation and growth of intercritical austenite at martensite (i.e.  $\alpha'$ ) lath boundaries during IA [17]. Austenite growth from a martensitic starting microstructure might also occur from pre-existing interlath retained austenite [18,19]. In contrast, cementite particles and ferrite grain boundaries are the preferred nucleation sites in cold-rolled medium Mn steels [20,21]. For this reason, it is important to consider cementite precipitation and dissolution in cold-rolled ferrite-cementite microstructures. The amount of Mn in cementite and its partitioning behavior plays a key role in the cementite dissolution kinetics and consequently austenite formation kinetics [22]. Undissolved cementite in the microstructure may also affect the TRIP kinetics because the amount of carbon in the RA can be significantly decreased if carbon is captured in cementite. A lower carbon content in RA translates into lower stability and can result in lower volume fractions of RA and poor RA mechanical stability [23]. Many researchers have simulated carbide precipitation/dissolution and austenite reversion using DICTRA [21,24–26]. For example, Gouné et. al. [27] studied the influence of Mn on cementite dissolution and austenite growth kinetics and showed that a significant decrease in cementite dissolution kinetics occurs if the cementite Mn content exceeds a temperature-dependent critical value (e.g., 15 wt% at 750°C). Similarly, Zhang et al. [28] used DICTRA to simulate the growth kinetics of austenite at the cementite/martensite interface with considerable alloying element redistribution. It was determined that the presence of cementite

and partitioning of Mn and Si between cementite and the martensite matrix retards austenite growth and the retardation is enhanced by increasing the Mn content in cementite.

DICTRA has been used by a number of investigators in an attempt to predict austenite transformation kinetics in ternary Fe-C-Mn [21,23,24,29,30] and quaternary Fe-C-Mn-Si [19,25,31] and Fe-C-Mn-Al [32] systems under particular conditions of temperature and composition. It has been reported that austenite growth consists of three stages. The first stage involves negligible partitioning local equilibrium (NPLE-( $\alpha' \rightarrow \gamma$ )) growth controlled by carbon diffusion in ferrite without significant substitutional alloying element (M=Mn, Al, Si) partitioning. During this first stage, the interface migration rate is very rapid. The second stage involves partitioning local equilibrium (PLE-( $\alpha' \rightarrow \gamma$ )) growth of the austenite controlled by substitutional alloying element (M=Mn, Al, Si) diffusion in ferrite. During this stage, the concentration of Mn in the austenite phase is slowly increased. In the last stage, the austenite volume fraction decreases (PLE-( $\gamma \rightarrow \alpha$ )) as a result of the relaxation of the diffusion profiles of the substitutional elements in austenite. As the final equilibrium concentration is approached, the interface between ferrite and austenite moves back to the austenite side.

The objective of this work is to measure and simulate the growth kinetics of RA from (i) an as-quenched martensitic microstructure and (ii) a cold rolled tempered martensite starting microstructure in a model med-Mn 3G steel during intercritical annealing. The processes of cementite dissolution and austenite formation have been studied, focusing on the evolution of alloying element partitioning during intercritical annealing. Fine scale microstructural analysis has been performed using transmission electron microscopy (TEM) for determining the phase distribution and morphology in annealed samples. In addition, extraction replicas were used to examine the cementite particle distribution. The experimental results were critical in terms of making reasonable assumptions for the simulations, such as the growth geometry and the size and composition of the phases and particles present.

### **3.3 Experimental**

#### **3.3.1 Steel Chemistry, Fabrication, and Thermal Process**

The chemical composition of the prototype medium-Mn 3G-AHSS (designated “Steel E”) is 0.15 C- 5.56 Mn- 1.1 Si- 1.89 Al- 0.08 Mo- 0.01 Ti (wt.%). The steel was made at U.S. Steel R&D (Munhall, Pennsylvania) using vacuum melting, casting, hot rolling, coiling, edge trimming, surface grinding and cold rolling to a final thickness of 1.2 mm, similar to the work carried out in [8].

Two starting microstructures were investigated. The as-received cold rolled (CR) starting microstructure consists of 70% cold-rolled tempered martensite and 30% cold-rolled ferrite. Ferrite was present owing to the relatively high Al content in the alloy which resulted in a high A3 temperature. Based on X-ray diffraction (XRD) results, a negligible amount of RA was detected in the as-received microstructure [8]. The second starting microstructure consisting of 80% martensite – 20% ferrite (MF) was made by austenitizing the as-received CR steel at 890 °C for 600 s, followed by quenched at –10 °C/s to room temperature.

Samples were intercritically annealed at 665 °C, and 710 °C for 0, 60, and 120 s in a N<sub>2</sub>-5vol% H<sub>2</sub> atmosphere at a dew point of –30 °C. Samples were then cooled at –10°C/s to an overaging temperature (OT) of 460 °C. Following a short holding of 30s, the samples were cooled to room temperature at –20 °C/s. The IA temperatures were chosen based on the Ae1 and Ae3 temperatures derived from the phase diagram, in order to obtain various volume fractions of intercritical austenite. The predicted phase fractions of ferrite, austenite, and cementite as a function of temperature are shown in Figure 3.1a, from which it can be seen that cementite dissolves completely at 647 °C. This information is used as input to the model. Figure 3.1b shows a schematic of the annealing cycle. Table 3.1 summarizes the IA parameters for both the CR and MF starting microstructures.

The choice of the intercritical annealing temperatures was designed to highlight the role of cementite on austenite formation. The lower temperature (665 °C) is slightly above the cementite dissolution temperature and would therefore lead to slow dissolution of the cementite. In contrast, the higher intercritical temperature (710 °C) is well-above the cementite dissolution temperature and as a result, cementite is not expected to strongly influence austenite formation at this temperature.

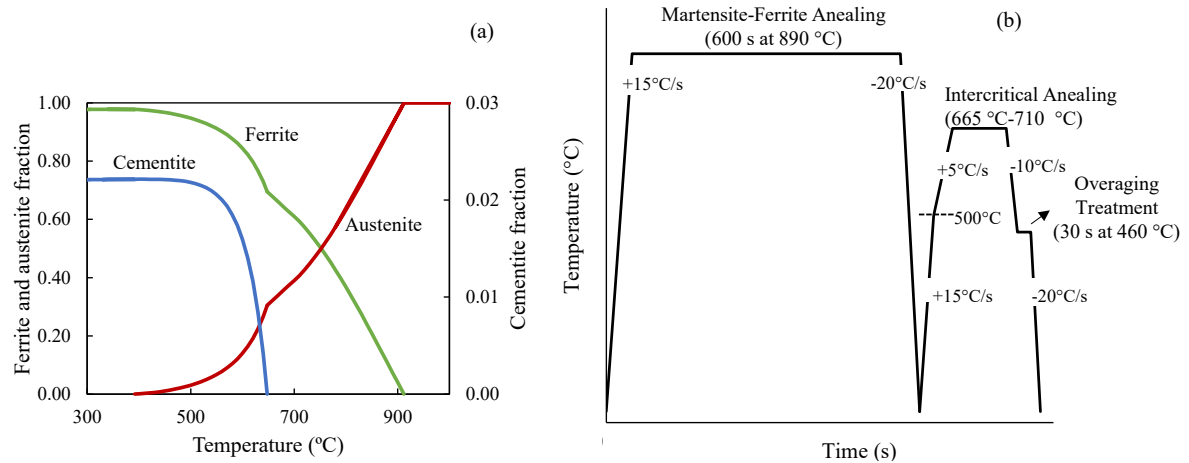


Figure 3.1: (a) Phase fractions vs. temperature of the Fe-5.56Mn-0.15C -1.1Si-1.89Al generated using the Thermo-Calc TCFE12 database (b) thermal profile of Steel E during annealing.

Table 3.1: Summary of heat treatment parameters for CR and MF starting microstructures

<b>IAT (°C)</b>	<b>Holding Time (s)</b>	<b>OT(°C)</b>	<b>Holding Time (s)</b>
<b>665</b>	0, 60, 120	460	30
<b>710</b>	0, 60, 120	460	30

### 3.3.1.1 *Transmission Electron Microscopy (TEM)*

Fine scale microstructural analysis was carried out using transmission electron microscopy (TEM) in order to determine phase distribution and morphology. Thin foils for TEM were prepared by mechanical thinning of sheet samples down to 100  $\mu\text{m}$ , punching 3 mm diameter discs and twinjet electropolishing the discs using a 10 pct perchloric acid – methanol solution at  $-40$  °C and an applied voltage of 15 V. The Talos L120C electron microscope was used for microstructural analysis using an acceleration voltage of 120 kV. The Talos 200X TEM/STEM was used for EDX analysis in scanning transmission (STEM) mode with a probe size of 1 nm and an acceleration voltage of 200 kV. Quantitative point analyses were performed to characterize the chemistry of the various phases.

In addition, the extraction replica technique was used to examine the particles present in the samples. Specimens were first mounted, ground, and polished to a mirror finish before being lightly etched using 2% nital to expose the particles. After carbon coating the etched samples, the carbon film was lightly scored into small squares, stripped by etching with a 4% nital solution and floating the films on a water-methanol mixture. Finally, sections of the film were captured on copper TEM grids. The replicas were examined in the Talos L120 TEM operating at 120 kV.

### 3.3.2 X-ray Diffraction

X-Ray Diffraction (XRD) was carried out on the cross-section of the intercritically annealed samples using a Bruker D8 DISCOVER with a DAVINCI.DESIGN diffractometer equipped with a Vantec 500 (MiKroGap™ technology) area detector and Co K $\alpha$  radiation ( $\lambda = 1.79026 \text{ \AA}$ ). The sample cross-sections in the through thickness-transverse direction (i.e., TT-TD) orientation were mounted in epoxy resin and ground with SiC paper (1200 grit being the final polishing step) to remove approximately 500  $\mu\text{m}$  from the cross-sections to eliminate any stress-induced transformations caused by the cutting of the sample. ASTM E975-13 [33] was used to determine the volume fraction of RA present using the austenite (111), (200), and (220) peaks whilst the ferrite (110), (200) and (211) peaks were used to calculate the ferrite volume fraction. The resident TOPAS software (Bruker AXS) was used to plot the intensity vs.  $2\theta$ . After normalizing the measured intensity to the calculated structure factor for each phase, the diffractogram was used to determine the volume fractions of each phase. Based on the calculated and measured diffraction patterns, the analytical error was determined.

### 3.3.3 DICTRA Simulations

The DICTRA module of Thermo-Calc was used to model the austenite growth kinetics with and without cementite in the CR and MF starting microstructures. The models used the TCFE12 and MOBFE5 databases [34]. The diffusion of C, Mn, Si and Al was considered in the simulation. The size of the simulation cell was based on the observed length scales within the TEM micrographs. Closed-cell boundary conditions were used to conserve mass.

Three initial configurations were considered for the simulation. In the case of the CR starting microstructure, austenite nucleated at ferrite grain boundaries with the presence of cementite at 665 °C and without cementite at 710 °C (Figure 3.2e, f). In the case of the MF starting microstructure, austenite nucleated at the lath-martensite (Figure 3.3c). The DICTRA simulations were therefore, configured as follows:

- MF starting microstructure: A one-dimensional cell containing austenite ( $\gamma$ ) and martensite/ferrite ( $\alpha$ ) was used to simulate the growth of austenite. This type of simulation cell configuration has been reported in many studies [19,29,35] and represents a starting microstructure of martensite with interlath RA. The interface is assumed to be planar. The initial composition of the martensite is assumed to be essentially the same as the nominal alloy composition. The simulation cell has been chosen based on the half-width of a martensite lath representative of the initial microstructure.
- CR starting microstructure at 665 °C: Based on the literature [36] and the microstructural observations, cementite dissolution plays an important role under these conditions. Spherical coordinates were used with a cementite particle at the center of a ferrite sphere. The austenite was introduced as an inactive phase on the outer shell of the ferrite sphere. Austenite is formed when the driving force for precipitation is about  $10^{-5}$  J mol<sup>-1</sup>[24]. The width of the initial cementite and ferrite regions in the simulation was selected based on the volume fraction of cementite, estimated to be 0.02 using the TCFE12 database of Thermo-Calc when  $\gamma$  is not present (suspended). The size of the cementite was selected based on TEM observations (30 nm) and the size of ferrite was set based on the mass balance. The C concentration in ferrite was determined to be 0.015 wt. pct, whereas that of cementite was 6.7 wt. pct.
- CR starting microstructure at 710 °C: In this case cementite dissolution takes place rapidly. As a result, the cementite particles were not considered in the simulation. The simulation was based on a spherical austenite nucleus within a ferrite matrix. (Additional details are in section 4.2.1).

In all simulations, each phase was discretized using a one-dimensional grid. Austenite and ferrite had linear grid spacing in the case of the MF starting microstructure. In the case of the CR starting microstructure, the mesh nodes were distributed geometrically in ferrite and cementite such that the mesh was finer near the moving phase boundaries. The computational

time was reduced without affecting accuracy when the time and spatial discretization were optimized.

Martensite is not considered a separate phase in DICTRA. As a result, martensite is represented as ferrite in the following calculations. Both phases will be called  $\alpha$  in this study.

### 3.4 Results

#### 3.4.1 TEM Microstructural Characterization

In order to determine the austenite nucleation sites, fine scale microstructural analysis was performed for the starting MF and CR microstructures using TEM. TEM images of the CR starting microstructure annealed at 665 °C and 710 °C for 60s are presented in Figure 3.2 and show a series of multiphase microstructures consisting of fine equiaxed ferrite that has a relatively low dislocation density alongside martensite/austenite (M/A) phases that were also equiaxed. DF images of the RA microstructure were obtained using the  $\langle 110 \rangle_{\gamma}$  austenite diffraction spot. Figure 3.2a also shows that the microstructure contains spherical cementite particles at 665 °C. For the CR microstructure intercritically annealed at 665 °C for 60 s, austenite nucleated at the ferrite/cementite interface, and at ferrite grain boundaries. In contrast, Figure 3.2c shows that most cementite was dissolved at 710 °C. Figure 3.2e, f shows a schematic of the initial configuration for austenite growth in CR starting microstructure. Figure 3.2e shows that at 665 °C, cementite dissolution provides the carbon needed for austenite growth. The carbon diffuses from the cementite/ferrite interface to the ferrite/austenite interface. In contrast, for the CR microstructure, which is annealed at 710 °C, Figure 3.2f schematically shows austenite directly growing into ferrite without the presence of cementite.

Figure 3.3 shows TEM BF and austenite DF micrographs of the MF starting microstructure along with the appropriate austenite Selected Area Diffraction (SAD) pattern. The DF image shows that the austenite was largely located on the martensite lath boundaries. Based on these microstructural observations (Figure 3.3), could directly grow from existing inter-lath RA. The initial configuration for austenite growth in MF is shown schematically in Figure 3.3c. BF and DF images and corresponding SAD patterns of the MF starting microstructure annealed at 665 °C and 710 °C for 60s are presented in Figure 3.4 and shows a series of

multiphase microstructures consisting of ultrafine ferrite, austenite, and lath martensite. Phase identification was carried out using DF TEM imaging and SAD. DF images of the lamellar RA microstructure were obtained using the  $\langle 110 \rangle_{\gamma}$  austenite diffraction spot. It can be seen that, in Figure 3.4 b and d, the thickness of austenite increased with temperature, resulting in increased volume fractions of austenite at 710 °C.

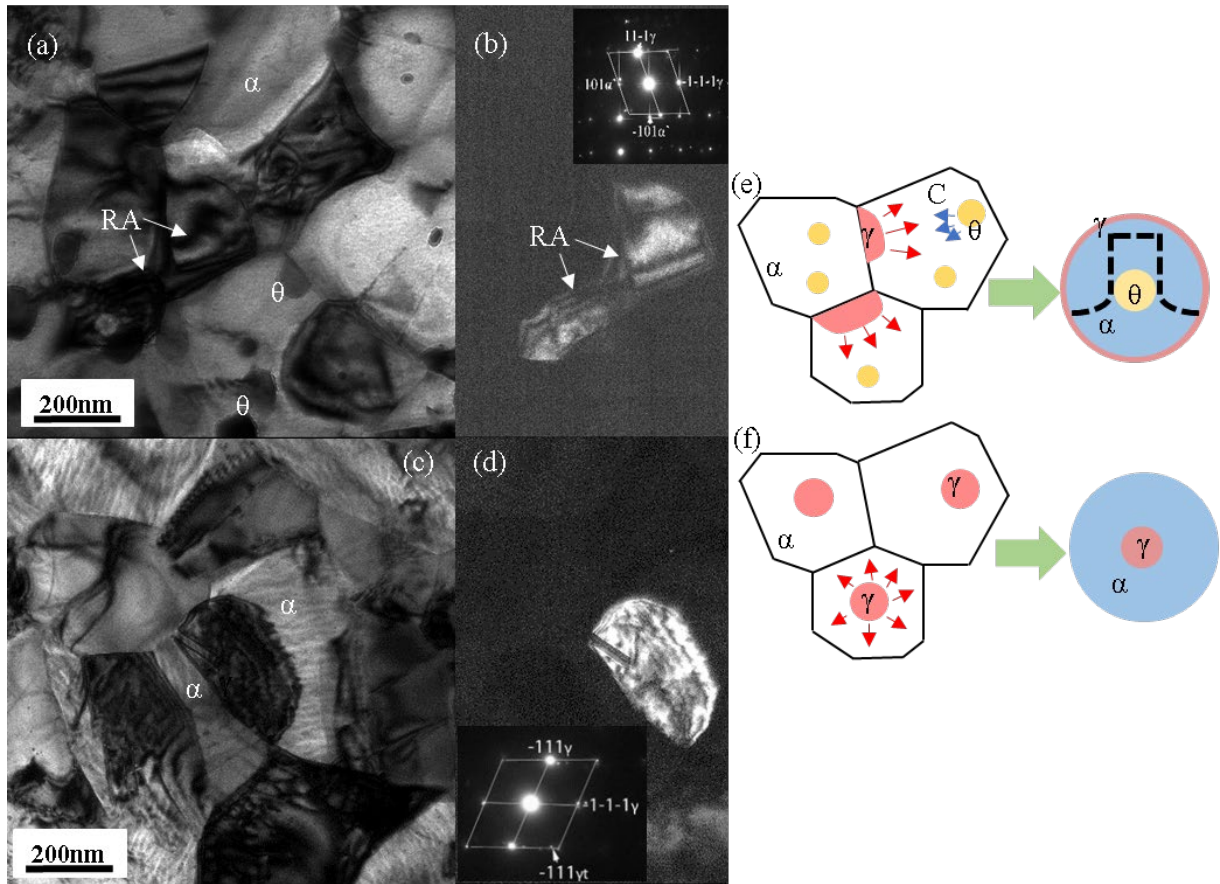


Figure 3.2: TEM images from the CR  $\times$  60s condition. For the CR 665 °C  $\times$  60s sample: (a) BF; (b) DF image obtained by using spot from  $\gamma$ . For the CR 710 °C  $\times$  60s sample: (c) BF; (d) DF corresponding to  $\langle 110 \rangle_{\gamma}$ . Ferrite, cementite, and retained austenite are denoted by  $\alpha$ ,  $\theta$ , and RA respectively. Schematic of initial configuration indicating austenite formation during heating (e) on a ferrite phase boundary at some distance from cementite at 665 °C (f) on ferrite without cementite at 710 °C for the CR case. The dotted line shows a schematic of the carbon concentration during the simulation.

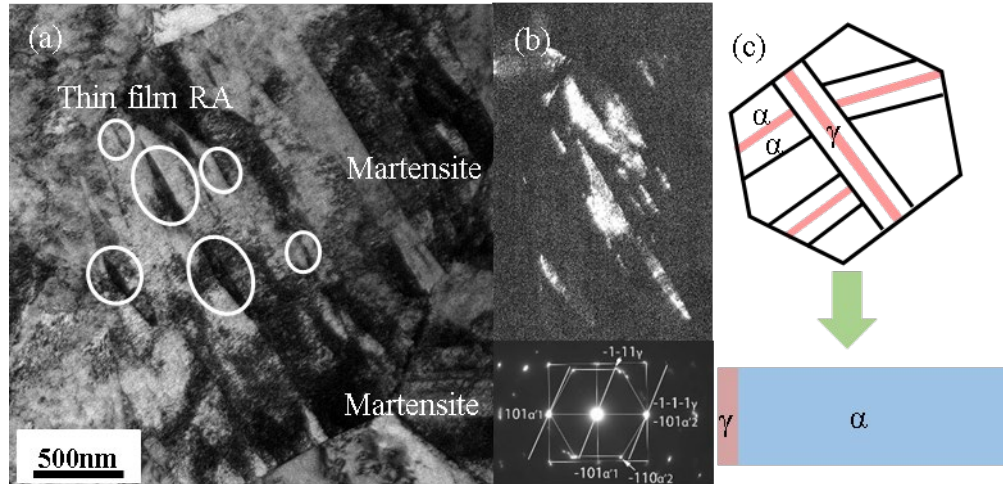


Figure 3.3: TEM images of the MF starting microstructure. (a) BF; (b) DF image obtained by using spot from  $\gamma$ . white ellipses show thin film of RA. Ferrite and martensite are denoted by  $\alpha$  and  $\alpha'$  respectively. (c) Schematic of initial configuration indicating austenite formation on ferrite lath boundaries ( $\gamma$  = austenite,  $\alpha$  = ferrite) for the MF starting microstructure case.

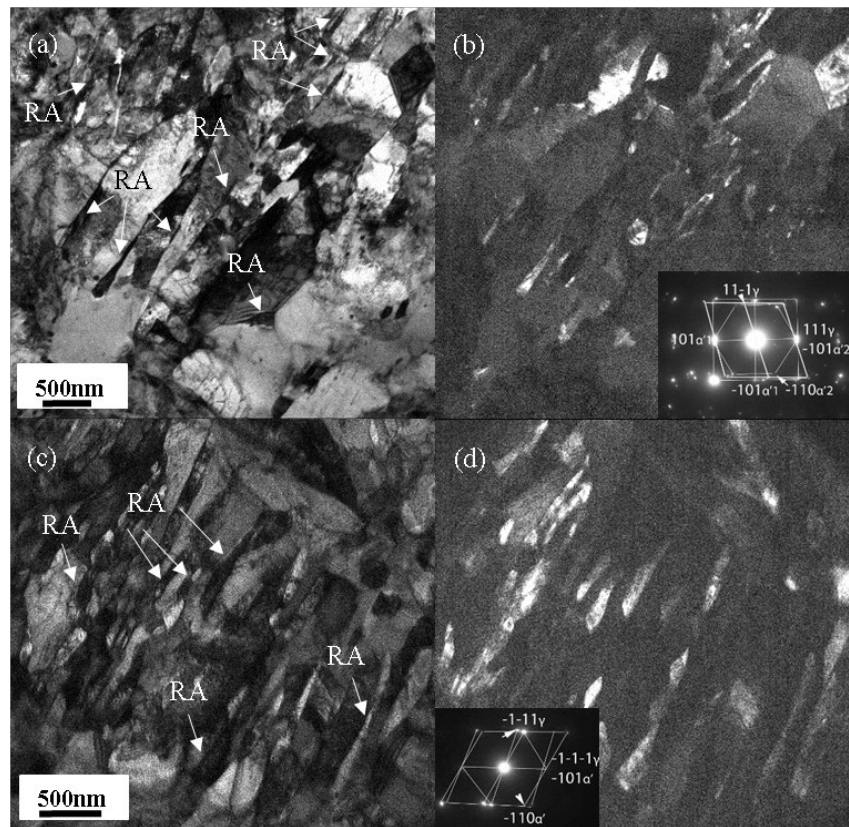


Figure 3.4: TEM images from the MF  $\times$  60s condition. For the MF 665 °C  $\times$  60s sample: (a) BF; (b) DF image obtained by using spot from  $\gamma$ . For MF 710 °C  $\times$  60s sample: (c) BF; (d) DF corresponding to  $\langle 110 \rangle$   $\gamma$ . Retained austenite is denoted by RA.

Given the importance of cementite dissolution for the kinetics in the CR samples at 665 °C, multiple (at least eight) particles were analyzed to determine an average composition of the cementite. EDS results revealed that the particles were C- and Mn-rich. Figure 3.5 shows the EDS elemental mappings of Fe, C, and Mn (Figure 3.5b,c, and d) from the frame of the High Angle Annual Dark Field (HAADF) image (Figure 3.5a), to highlight the cementite particles, austenite, and tempered martensite for the CR sample annealed at 665 °C for 0 s. Cementite particles had a spherical morphology. The composition of the cementite, austenite, and ferrite (matrix) are listed in Table 3.2. For austenite and ferrite, the Mn content was 6 and 4 wt.%, respectively, while for cementite, it ranged from 7 to 15 wt.%.

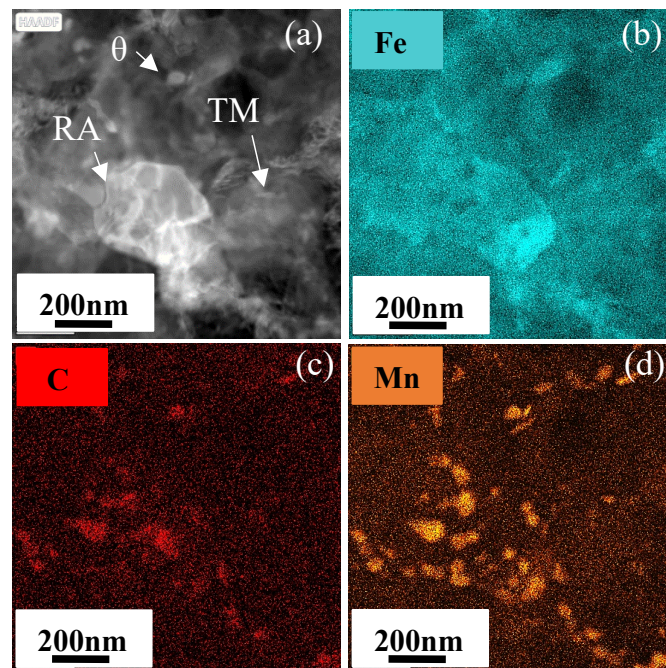


Figure 3.5: EDS elemental mappings from (a) the frame of the HAADF image of (b) Fe, (c) C, and (d) Mn at CR 665 °C  $\times$  0s sample. Tempered martensite, cementite, and retained austenite are denoted by TM,  $\theta$ , and RA respectively.

Table 3.2: Average cementite, austenite, and tempered martensite (matrix) composition from EDS spot analysis (wt.%) for CR 665 °C  $\times$  0s sample

<b>Chemical content, wt. %</b>	<b>Tempered martensite (Matrix)</b>	<b>Austenite</b>	<b>Cementite</b>
Al	1.7	1.5	1.5
Si	0.9	0.8	0.8
Mn	4.1	6.7	9.9

### 3.4.2 Extraction Replica

Carbide particle size distributions were measured for selected samples using carbon extraction replicas. A montage of multiple micrographs for the as-received CR sample is shown in Figure 3.6a. It can be seen that, in the as-received-CR sample, cementite particles are present, mainly along the boundaries. Figure 3.6b and c show the carbides in CR samples intercritically annealed at 665 °C, and 710 °C for 120s. Both coarse (> 100 nm) and fine (< 100 nm) particles were observed in the CR sample annealed at 665 °C for 120s, suggesting that some cementite formed during heating. It appears that all the cementite particles were enriched in Mn (Figure 3.5d). On the other hand, very little cementite is present at 710 °C, suggesting that the cementite particles dissolve quickly at this temperature. The corresponding particle size distributions are shown in Figure 3.8a. The particle size evolution is consistent with cementite precipitation during heating followed by dissolution during holding at 710 °C for 120s treatment.

Figure 3.7 shows typical extraction replicas taken from the as received MF samples, as well as, MF intercritically annealed at 665 °C, and 710 °C for 120s. As can be seen in comparison to the as-received CR sample documented in Figure 3.6a, the initial MF microstructure had very few carbide particles. Accordingly, the carbon remained supersaturated in the martensite. During heating, the cementite started to precipitate out and a large number of cementite particles was still present after 120 s at 665 °C. Nonetheless, there were significantly fewer carbides present in the MF microstructure annealed at 665 °C for 120s than in the CR microstructure annealed at 665 °C for 120s, indicating that more carbon was in solution. Cementite particle size distribution analysis revealed that cementite particles dissolved rapidly during the IA treatment at 710 °C for the MF and CR samples (Figure 3.7).

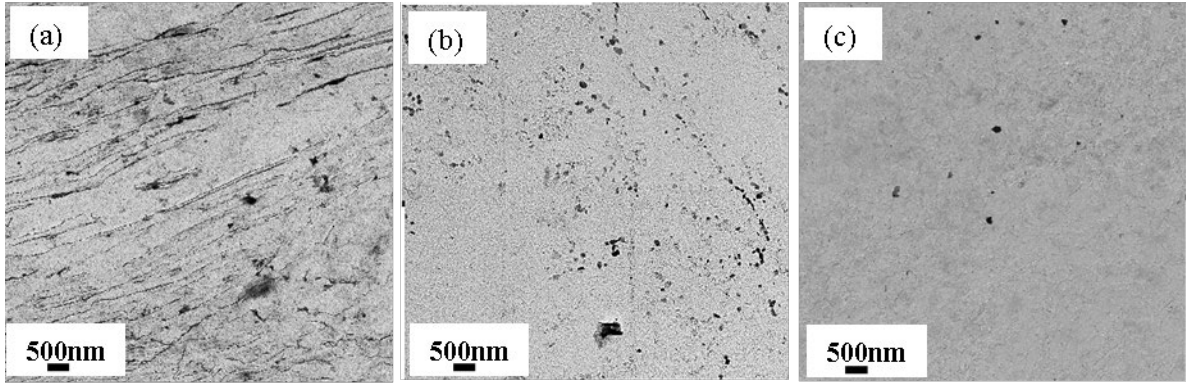


Figure 3.6: Particle size distribution of (a) the as-received CR, CR 665 °C × 120s, and CR 710 °C × 120s samples and (b) MF, MF 665 °C × 120s, and MF 710 °C × 120s samples.

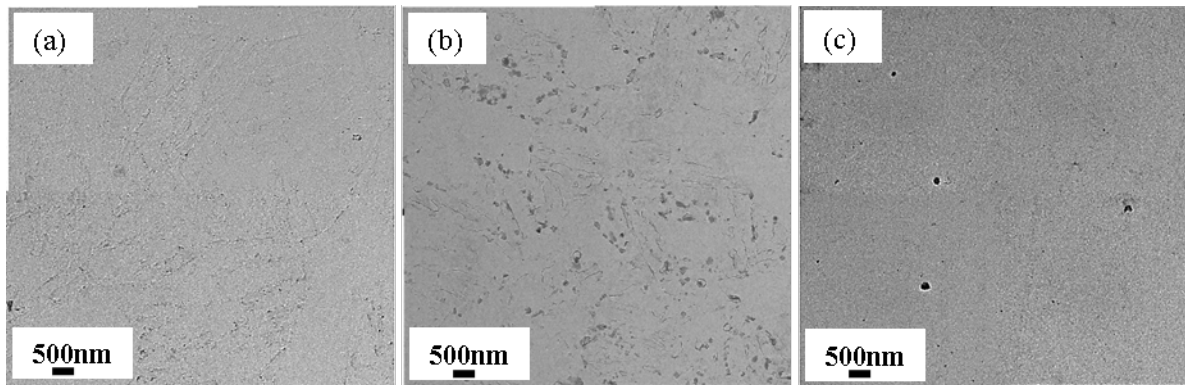


Figure 3.7: Cementite extraction replica TEM micrographs in (a) the as received, (b) CR 665 °C × 120s, and (c) CR 710 °C × 120s samples.

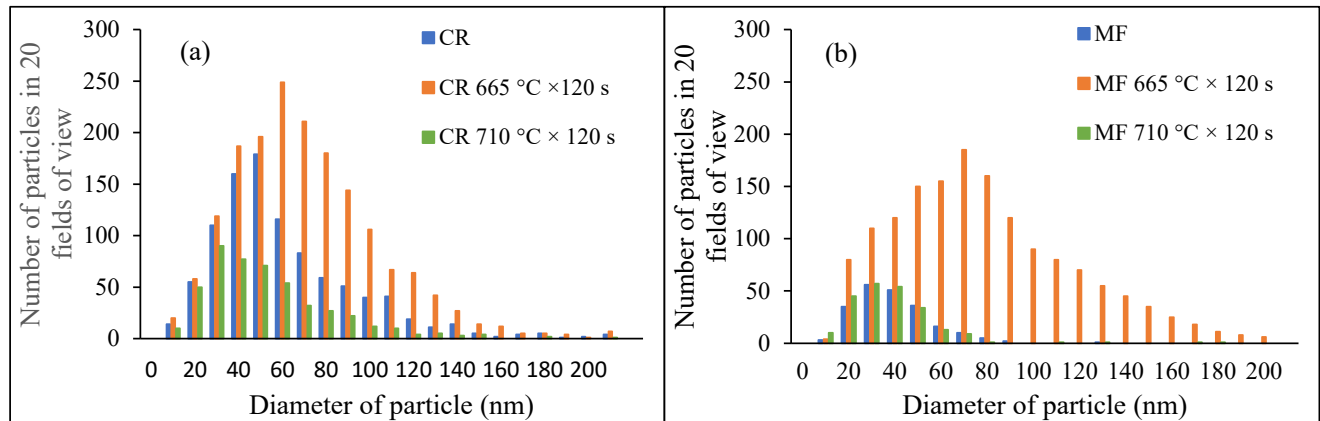


Figure 3.8: Cementite distribution in the (a) MF, (b) MF 665 °C × 120s, and (c) and MF 710 °C × 120s samples.

### 3.5 Discussion

#### 3.5.1 Austenite Nucleation

Nucleation is the initial stage of solid-state phase transformations. The distribution, density, morphology, and size of RA is controlled by the nucleation sites in med-Mn steels. The starting microstructures and IA conditions can determine the nucleation sites [28,37,38].

The microstructural observations (Figure 3.2a) support the finding that cementite precipitation influences the final austenite characteristics. Granular austenite was found in the CR starting microstructure [8], while lath-like austenite was observed in the samples with the MF starting microstructure (Figure 3.4). This is due to the presence of different nucleation sites in the two starting microstructures. In the case of the MF microstructure, austenite grows from pre-existing films of RA between the martensite laths, and this leads to lamellar austenite morphology. In contrast, cementite and ferrite grain boundaries are preferred nucleation sites for austenite in the cold-rolled ferrite and tempered martensite microstructure [27,39,40]. Globular austenite grains are formed at these nucleation sites. Interestingly, even after the nucleation of austenite, cementite particles are still present in the CR microstructure which was annealed at 665 °C. Mn enrichment within the cementite particles led to the slow dissolution of cementite and this reduced the growth rate of austenite.

#### 3.5.2 DICTRA Simulations of Austenite Formation

The DICTRA module of the Thermo-Calc software (using the TCFE12 and MOBFE5 databases) was used to model austenite growth kinetics for the CR and MF starting microstructures.

##### 3.5.2.1 *CR Starting Microstructure*

The CR starting microstructure model simulates austenite growth in a globular microstructure (Figure 3.2e, f). Based on the microstructure of spherical cementite in ferrite and equiaxed microstructure, spherical geometry was considered. According to the carbon replica results in Figure 3.6, cementite was present in the CR starting microstructure, and more cementite precipitated out during heating. The dissolution of cementite was slow the 665 °C. As result, cementite dissolution had to be considered when modelling the growth of austenite at this

temperature. Thus, at 665 °C The geometry employed is that of a single cementite particle which dissolves into ferrite to provide carbon to a growing austenite grain (Figure 3.2e). Based on TEM observation the cell size was set to 110 nm. The Mn content in cementite was set to 10 wt pct, which was the average value measured by TEM-EDX (Table 3.2). In contrast, at 710 °C, a large fraction of the cementite dissolved quick, as was shown in the extraction replica study presented in Figure 3.6. For this reason, the geometry used was that shown in Figure 3.2f, consisting only of ferrite and inactive austenite. The total cell size was 440 nm.

Figure 3.9 shows the calculated austenite volume fraction during isothermal holding of the CR microstructure at 665 °C and 710 °C. Figure 3.9 also includes experimental XRD results. It can be seen that the measured fractions of RA agree well with those simulated by DICTRA at 665 °C. At this temperature, austenite is only in contact with ferrite. Based on the DICTRA simulations, the transformation is almost immediately controlled by the diffusion of the substitutional elements in ferrite. Nonetheless, the transformation proceeds relatively quickly due to the fast diffusion of the substitutional elements in ferrite and short diffusion distances. At 710 °C, it was assumed that cementite dissolution had already taken place. The simulations simply involved the growth of austenite into supersaturated ferrite. The calculated evolution of the austenite fraction clearly shows an initial stage which is controlled by carbon diffusion, followed by a second stage which is controlled by the diffusion of the substitutional elements in ferrite. As shown in Figure 3.9, the measured volume fractions of austenite at 710 °C are lower than those predicted by DICTRA. This might be because the RA is less stable in the CR microstructure annealed at 710 °C, resulting in significant martensite phase transformation during quenching. As a result, the volume fractions measured by XRD at room temperature may underestimate the amount of austenite that was present during intercritical annealing at 710 °C.

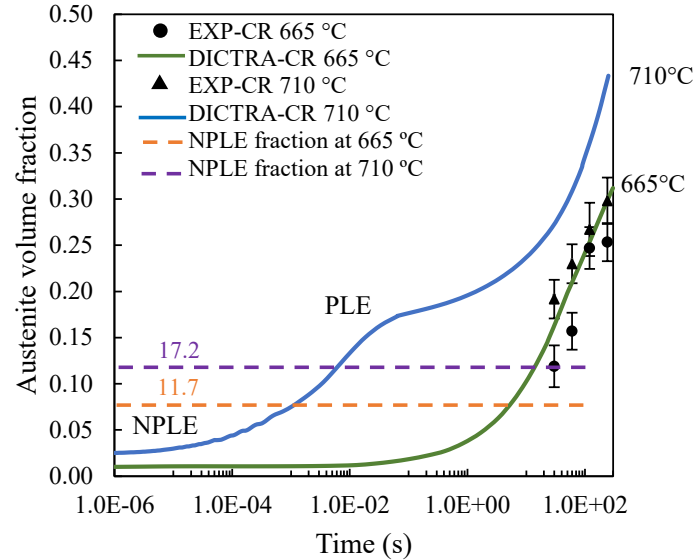


Figure 3.9: Austenite volume fraction during isothermal holding at 665 °C, 710 °C for the CR starting microstructure with cementite. Error bars for austenite volume fraction measurement indicate maximum and minimum values among six measurements.

### 3.5.2.2 MF Starting Microstructure

A simplified geometry is considered for austenite formation in DICTRA. The MF starting microstructure model simulates austenite growth in a lamellar geometry (Figure 3.3c). The cell size for simulation at 665 °C and 710 °C were approximated as 120 nm and 300 nm, respectively. The larger value at 710 °C reflects the coarsening of the microstructure at this higher temperature. Figure 3.10 shows the modelled austenite volume fraction during isothermal holding at 665 °C and 710 °C for the MF starting microstructure. Experimental results based on XRD data are plotted in Figure 3.10 as individual points. In this simulation, as well as in other papers [19,29], rapid initial NPLE growth of austenite followed by a more gradual PLE growth mode is predicted. The initial stage of carbon-controlled growth leads to a rapid increase in the austenite volume fraction to approximately 0.12 at 665 °C and 0.18 at 710 °C in 0.001s, well before significant Mn partitioning can take place. As is also shown in Figure 3.10, the MF simulation predicts 0.22 and 0.40 austenite volume fraction at approximately 120 s at 665 °C and 710 °C, respectively. By way of comparison, Pallisco and McDermid [8] reported as-annealed RA volume fractions of 0.21 and 0.31, for MF starting microstructures annealed at 665 °C for 120s and at 710 °C for 120s, respectively.

As the temperature drops from 710 °C to 665 °C, austenite formation becomes much slower. Austenite growth kinetics are influenced by temperature because it affects the driving forces and solute diffusivities. In fact, a decrease in temperature of 45 °C leads to a drop in the diffusivity of Mn in ferrite by a factor of 87% and the equilibrium amount of austenite from 0.41 at 710 °C to 0.34 at 665 °C. The DICTRA results are also reflective of the volume fractions of austenite before quenching to room temperature. After quenching to room temperature, the transformation of some fraction of intercritical austenite to martensite is expected. After quenching to room temperature, the Mn-depleted region of reverted austenite transformed into martensite, but the Mn-enriched region was retained [41]. The results are also in good agreement with the experiments conducted at 665 °C. Furthermore, a higher volume fraction of stable retained austenite was reported in the literature for 650 °C and 675 °C IA treatments for martensitic starting microstructures [42]. On the other hand, it is possible that the small difference in the results at 710 °C are due to the faster transformation kinetics of RA into martensite, leading to a lower stability of RA for the MF microstructure annealed at 710 °C for 120s.

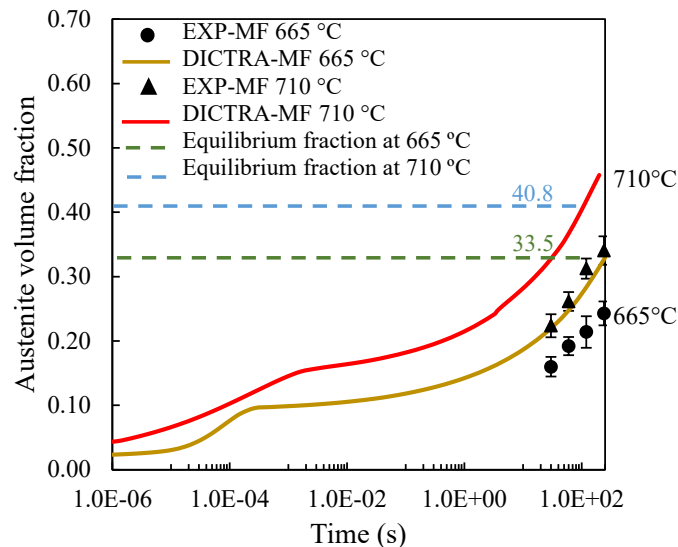


Figure 3.10: Austenite volume fraction during isothermal holding at 665 °C and 710 °C for the MF starting microstructure.

Simulations comparing the austenite volume fractions for the 665 °C and 710 °C intercritical anneal from the CR and MF starting microstructures are shown in Figure 3.11. It can be seen that, with the presence of cementite in the CR starting microstructure, longer times are needed to obtain the same volume fraction of intercritical austenite compared to the MF starting

microstructure without cementite. At 665 °C, the initial growth of austenite in the MF starting microstructure is controlled by carbon diffusion in ferrite, whereas austenite growth in the CR starting microstructure is controlled by Mn diffusion in ferrite since there is not a detectable stage that is controlled by C diffusion. The significant difference between the diffusion rates of C and Mn, thus, explains the difference in austenite growth kinetics in the two starting microstructures. The present results are in agreement with earlier work [21] which has shown that when austenite forms at cementite particles in medium Mn steel, the growth of austenite is controlled by Mn diffusion due to the high Mn content in cementite. It is worth pointing out that the Mn content of cementite was determined by TEM-EDX to be high (10-15%). As a result, Mn diffusion in ferrite is very important. The difference in austenite growth kinetics in both starting microstructure is also reported to be due to the absence of a nucleation barrier for intercritical austenite formation from existing inter-lath RA, along with the rapid partitioning of C from supersaturated martensite [42]. It was found that the austenite fraction in both starting microstructures became the same at 710 °C, when most of the cementite had dissolved. To conclude this discussion, it is useful to consider the different factors that contribute to the discrepancy between the experimental and calculated austenite volume fractions. In general, the calculated volume fractions are larger than the experimental reported ones. This can be attributed to:

- 1- The XRD measurements were made at room temperature. As a result, some of the less stable austenite present at the intercritical temperature may have transformed during quenching.
- 2- Both initial microstructures contained ~ 20% ferrite. The present simulation is only based on what happens in the martensite (MF) and tempered martensite (CR) microstructure. The presence of ferrite within the initial microstructures was not accounted for and as a result the calculated austenite volume fractions are probably overestimated.
- 3- Based on the microstructure observations, the microstructure got significantly coarser after holding at 710 °C. The present simulations do not capture the coarsening of the microstructure which would have to be accounted for by increasing the cell size as a function of holding time. The use of a constant cell size would lead to the calculated kinetics being overestimated at long times.
- 4- The simulations were limited to a one-dimensional model, which may not accurately reflect the complexities of the actual microstructure.

- 5- The simulations considered only one size and composition for the cementite, whilst the experiments (TEM-EDS and extraction replica) revealed a wide range of cementite sizes and compositions.

In spite of these potential issues, the simulation provides a good first order description of the austenite transformation kinetics.

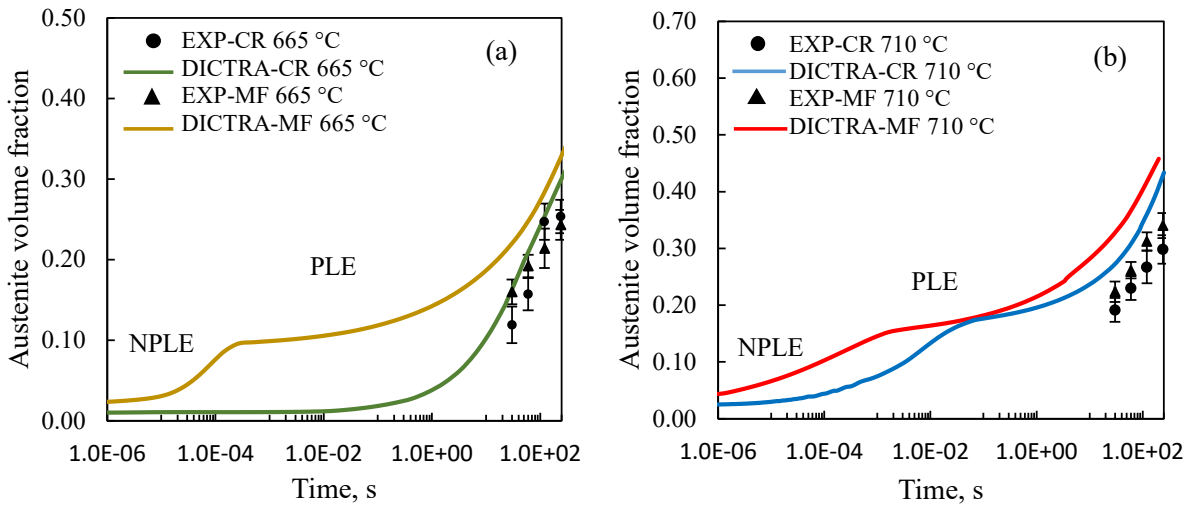


Figure 3.11: Comparing CR and MF cases for austenite volume fraction during (a) 665 °C and (b) 710 °C isothermal holding.

### 3.6 Conclusions

The effects of starting microstructure and intercritical annealing temperature on the phase transformation kinetics in a prototype Fe-0.15C-5.56Mn-1.1Si-1.89Al med-Mn third-generation advanced high strength steel (3G AHSS) were determined. From the results of this study, it can be concluded that:

- 1- Simulations indicate that the time for obtaining the same volume fraction of austenite is longer in the presence of cementite, as the dissolution of cementite is required to support austenite growth.
- 2- Accelerated austenite reversion kinetics were observed for the MF starting microstructure samples annealed at 665 °C. This was due to the direct growth of intercritical RA from pre-existing interlath RA films and the relatively rapid partitioning of C from the surrounding supersaturated martensitic matrix.

- 3- At higher temperatures, when most of the cementite had dissolved, the austenite fraction in both starting microstructures were similar.
- 4- The DICTRA results are at the isothermal annealing temperature before quenching. For this reason, the DICTRA results may differ from XRD-based retained austenite measurements after quenching to room temperature. These results are in qualitative agreement with experimental results at 665 °C. Otherwise, the retained austenite results of the experiment are significantly lower than the DICTRA simulations at higher intercritical annealing temperatures. In these cases, the RA is likely to be less stable at 710 °C, resulting in significant transformation to martensite upon quenching.

### **3.7 Acknowledgements**

This work was financially supported by the International Zinc Association Galvanized Autobody Partnership (IZA-GAP), and the Natural Sciences and Engineering Research Council of Canada (NSERC grant CRDPJ 522309 – 17). The experimental steel was provided by U.S. Steel Research (Munhall). Electron microscopy was performed at the Canadian Centre for Electron Microscopy (CCEM), a core research facility of McMaster University (also supported by NSERC and other government agencies).

### **3.8 Reference**

- [1] C. Lesch, N. Kwiaton, F.B. Klose, Advanced High Strength Steels (AHSS) for Automotive Applications – Tailored Properties by Smart Microstructural Adjustments, *Steel Res. Int.* 88 (2017) 1–21. <https://doi.org/10.1002/srin.201700210>.
- [2] Z. Xu, X. Jin, Ultra-high Strength Steel Treated by Using Quenching–Partitioning–Tempering Process, in: *Adv. Steels*, Springer Berlin Heidelberg, Berlin, Heidelberg, 2011: pp. 67–73. [https://doi.org/10.1007/978-3-642-17665-4\\_8](https://doi.org/10.1007/978-3-642-17665-4_8).
- [3] V. Savic, L. Hector, H. Singh, M. Paramasuwom, U. Basu, A. Basudhar, N. Stander, Development of a Lightweight Third-Generation Advanced High-Strength Steel (3GAHSS) Vehicle Body Structure, *SAE Int. J. Mater. Manuf.* 11 (2018). <https://doi.org/10.4271/2018-01-1026>.

- [4] S. Lee, K. Lee, B.C. De Cooman, Ultra fine-grained 6wt% manganese TRIP steel, *Mater. Sci. Forum.* 654–656 (2010) 286–289.
- [5] B. Hu, H. Luo, F. Yang, H. Dong, Recent progress in medium-Mn steels made with new designing strategies, a review, *J. Mater. Sci. Technol.* 33 (2017) 1457–1464. <https://doi.org/10.1016/j.jmst.2017.06.017>.
- [6] Y.K. Lee, J. Han, Current opinion in medium manganese steel, *Mater. Sci. Technol.* 31 (2015) 843–856. <https://doi.org/10.1179/1743284714Y.0000000722>.
- [7] D.W. Suh, S.J. Kim, Medium Mn transformation-induced plasticity steels: Recent progress and challenges, *Scr. Mater.* 126 (2017) 63–67.
- [8] D.M. Pallisco, J.R. McDermid, Mechanical property development of a 0.15C–6Mn–2Al–1Si third-generation advanced high strength steel using continuous galvanizing heat treatments, *Mater. Sci. Eng. A.* 778 (2020) 139111. <https://doi.org/10.1016/j.msea.2020.139111>.
- [9] W. Bleck, X. Guo, Y. Ma, The TRIP Effect and Its Application in Cold Formable Sheet Steels, *Steel Res. Int.* 88 (2017) 1700218.
- [10] L. Liu, B. He, M. Huang, The Role of Transformation-Induced Plasticity in the Development of Advanced High Strength Steels, *Adv. Eng. Mater.* 20 (2018) 1701083. <https://doi.org/10.1002/adem.201701083>.
- [11] S. Lee, B.C. De Cooman, On the selection of the optimal intercritical annealing temperature for medium Mn TRIP steel, *Metall. Mater. Trans. A.* 44A (2013) 5018–5024. <https://doi.org/10.1007/s11661-013-1860-2>.
- [12] M. Soleimani, A. Kalhor, H. Mirzadeh, Transformation-induced plasticity (TRIP) in advanced steels: A review, *Mater. Sci. Eng. A.* 795 (2020) 140023. <https://doi.org/10.1016/j.msea.2020.140023>.
- [13] J. Han, S.J. Lee, J.G. Jung, Y.K. Lee, The effects of the initial martensite microstructure on the microstructure and tensile properties of intercritically annealed Fe-9Mn-0.05C steel, *Acta Mater.* 78 (2014) 369–377. <https://doi.org/10.1016/j.actamat.2014.07.005>.

- [14] J. Han, A.K. da Silva, D. Ponge, D. Raabe, S.M. Lee, Y.K. Lee, S.I. Lee, B. Hwang, The effects of prior austenite grain boundaries and microstructural morphology on the impact toughness of intercritically annealed medium Mn steel, *Acta Mater.* 122 (2017) 199–206. <https://doi.org/10.1016/j.actamat.2016.09.048>.
- [15] H. Luo, H. Dong, M. Huang, Effect of intercritical annealing on the Lüders strains of medium Mn transformation-induced plasticity steels, *Mater. Des.* 83 (2015) 42–48. <https://doi.org/10.1016/j.matdes.2015.05.085>.
- [16] S. Zhang, K.O. Findley, Quantitative assessment of the effects of microstructure on the stability of retained austenite in TRIP steels, *Acta Mater.* 61 (2013) 1895–1903. <https://doi.org/10.1016/j.actamat.2012.12.010>.
- [17] H. Luo, H. Dong, New ultrahigh-strength Mn-alloyed TRIP steels with improved formability manufactured by intercritical annealing, *Mater. Sci. Eng. A.* 626 (2015) 207–212. <https://doi.org/10.1016/j.msea.2014.12.049>.
- [18] A.K. Chandan, G.K. Bansal, J. Kundu, J. Chakraborty, S.G. Chowdhury, Effect of prior austenite grain size on the evolution of microstructure and mechanical properties of an intercritically annealed medium manganese steel, *Mater. Sci. Eng. A.* 768 (2019) 138458. <https://doi.org/10.1016/j.msea.2019.138458>.
- [19] R. Wei, M. Enomoto, R. Hadian, H.S. Zurob, G.R. Purdy, Growth of austenite from as-quenched martensite during intercritical annealing in an Fe-0.1C-3Mn-1.5Si alloy, *Acta Mater.* 61 (2013) 697–707. <https://doi.org/10.1016/j.actamat.2012.10.019>.
- [20] D.Z. Yang, E.L. Brown, D.K. Matlock, G. Krauss, Ferrite recrystallization and austenite formation in cold-rolled intercritically annealed steel, *Metall. Trans. A.* 16A (1985) 1385–1392. <https://doi.org/10.1007/BF02658671>.
- [21] Q. Lai, M. Gouné, A. Perlade, T. Pardoën, P. Jacques, O. Bouaziz, Y. Bréchet, Mechanism of Austenite Formation from Spheroidized Microstructure in an Intermediate Fe-0.1C-3.5Mn Steel, *Metall. Mater. Trans. A.* 47A (2016) 3375–3386. <https://doi.org/10.1007/s11661-016-3547-y>.

- [22] Z. Dai, H. Chen, R. Ding, Q. Lu, C. Zhang, Z. Yang, S. van der Zwaag, Fundamentals and application of solid-state phase transformations for advanced high strength steels containing metastable retained austenite, *Mater. Sci. Eng. R.* 143 (2021) 100590. <https://doi.org/10.1016/j.mser.2020.100590>.
- [23] H. Luo, J. Liu, H. Dong, A Novel Observation on Cementite Formed During Intercritical Annealing of Medium Mn Steel, *Metall. Mater. Trans. A.* 47A (2016) 3119–3124. <https://doi.org/10.1007/s11661-016-3448-0>.
- [24] F. Huyan, J.Y. Yan, L. Höglund, J. Ågren, A. Borgenstam, Simulation of the Growth of Austenite from As-Quenched Martensite in Medium Mn Steels, *Metall. Mater. Trans. A.* 49A (2018) 1053–1060. <https://doi.org/10.1007/s11661-018-4497-3>.
- [25] N. Yan, H. Di, R.D.K. Misra, H. Huang, Y. Li, Enhancing austenite stability in a new medium-Mn steel by combining deep cryogenic treatment and intercritical annealing: An experimental and theoretical study, *Mater. Sci. Eng. A.* 753 (2019) 11–21. <https://doi.org/10.1016/j.msea.2019.01.026>.
- [26] X. Zhang, G. Miyamoto, Y. Toji, T. Furuhashi, Effects of heating rate on formation of globular and acicular austenite during reversion from martensite, *Metals (Basel)*. 9 (2019) 266. <https://doi.org/10.3390/met9020266>.
- [27] M. Goun' e, P. Maugis, J. Drillet, A Criterion for the Change from Fast to Slow Regime of Cementite Dissolution in Fe – C – Mn Steels, *J. Mater. Sci. Technol.* 28 (2012) 728–736. [https://doi.org/10.1016/S1005-0302\(12\)60122-4](https://doi.org/10.1016/S1005-0302(12)60122-4).
- [28] X. Zhang, G. Miyamoto, T. Kaneshita, Y. Yoshida, Y. Toji, T. Furuhashi, Growth mode of austenite during reversion from martensite in Fe-2Mn-1.5Si-0.3C alloy: A transition in kinetics and morphology, *Acta Mater.* 154 (2018) 1–13. <https://doi.org/10.1016/j.actamat.2018.05.035>.
- [29] J.J. Mueller, X. Hu, X. Sun, Y. Ren, K. Choi, E. Barker, J.G. Speer, D.K. Matlock, E. De Moor, Austenite formation and cementite dissolution during intercritical annealing of a medium-manganese steel from a martensitic condition, *Mater. Des.* 203 (2021) 109598. <https://doi.org/10.1016/j.matdes.2021.109598>.

- [30] H.W. Luo, C.H. Qiu, H. Dong, J. Shi, Experimental and numerical analysis of influence of carbide on austenitisation kinetics in 5Mn TRIP steel, *Mater. Sci. Technol.* 30 (2014) 1367–1377. <https://doi.org/10.1179/1743284713Y.0000000447>.
- [31] H. Farahani, W. Xu, S. van der Zwaag, Prediction and Validation of the Austenite Phase Fraction upon Intercritical Annealing of Medium Mn Steels, *Metall. Mater. Trans. A.* 46A (2015) 4978–4985. <https://doi.org/10.1007/s11661-015-3081-3>.
- [32] R. Ding, Z. Dai, M. Huang, Z. Yang, C. Zhang, H. Chen, Effect of pre-existed austenite on austenite reversion and mechanical behavior of an Fe-0.2C-8Mn-2Al medium Mn steel, *Acta Mater.* 147 (2018) 59–69. <https://doi.org/10.1016/j.actamat.2018.01.009>.
- [33] W. Conshohocken, ASTM E975-13. Standard Practice for X-Ray Determination of Retained Austenite in Steel with Near Random Crystallographic Orientation, *ASTM Int.* (2013). <https://doi.org/10.1520/E0975-13.necessary>.
- [34] J.O. Andersson, T. Helander, L. Höglund, P. Shi, B. Sundman, Thermo-Calc & DICTRA, computational tools for materials science, *Calphad.* 26 (2002) 273–312. [https://doi.org/10.1016/S0364-5916\(02\)00037-8](https://doi.org/10.1016/S0364-5916(02)00037-8).
- [35] O. Dmitrieva, D. Ponge, G. Inden, J. Millán, P. Choi, J. Sietsma, D. Raabe, Chemical gradients across phase boundaries between martensite and austenite in steel studied by atom probe tomography and simulation, *Acta Mater.* 59 (2011) 364–374. <https://doi.org/10.1016/j.actamat.2010.09.042>.
- [36] D. Han, Y. Xu, R. Liu, F. Peng, Y. Zou, W. Sun, Improving Mn partitioning and mechanical properties through carbides-enhancing pre-annealing in Mn-reduced transformation-induced plasticity steel, *Scr. Mater.* 187 (2020) 274–279. <https://doi.org/10.1016/j.scriptamat.2020.06.027>.
- [37] K.M.H. Bhadhon, X. Wang, E.A. McNally, J.R. McDermid, Effect of Intercritical Annealing Parameters and Starting Microstructure on the Microstructural Evolution and Mechanical Properties of a Medium-Mn Third Generation Advanced High Strength Steel, *Metals (Basel)*. 12 (2022) 356. <https://doi.org/10.3390/met12020356>.

- [38] A. Mehrabi, J.R. McDermid, H.S. Zurob, F.E. Goodwin, Austenite Nucleation and Growth as a Function of Starting Microstructure in a Fe-0.15C-5.56Mn-1.1Si-1.89Al Medium-Mn Steel, in: 5th International High Manganese Steel Conference, Vienna, 2022.
- [39] M. Kulakov, W.J. Poole, M. Militzer, The effect of the initial microstructure on recrystallization and austenite formation in a DP600 steel, *Metall. Mater. Trans. A.* 44A (2013) 3564–3576. <https://doi.org/10.1007/s11661-013-1721-z>.
- [40] H. Azizi-Alizamini, M. Militzer, W.J. Poole, Austenite formation in plain low-carbon steels, *Metall. Mater. Trans. A.* 42A (2011) 1544–1557. <https://doi.org/10.1007/s11661-010-0551-5>.
- [41] F. Moszner, E. Povoden-Karadeniz, S. Pogatscher, P.J. Uggowitzer, Y. Estrin, S.S.A. Gerstl, E. Kozeschnik, J.F. Löffler, Reverse  $\alpha' \rightarrow \gamma$  transformation mechanisms of martensitic Fe-Mn and age-hardenable Fe-Mn-Pd alloys upon fast and slow continuous heating, *Acta Mater.* 72 (2014) 99–109. <https://doi.org/10.1016/j.actamat.2014.03.032>.
- [42] K.M.H. Bhadhon, X. Wang, J.R. McDermid, Effects of CGL-compatible thermal processing, starting microstructure, and Sn micro-alloying on the mechanical properties of a medium-Mn third generation advanced high strength steel, *Mater. Sci. Eng. A.* 833 (2022) 142563. <https://doi.org/10.1016/j.msea.2021.142563>.

## **4 Austenite Formation in a Medium-Mn Steel During Intercritical Annealing via *in situ* High-Energy X-ray Diffraction**

Azin Mehrabi<sup>1</sup>, Hatem Zurob<sup>\*1</sup>, Imed-Eddine Benrabah<sup>1,2</sup>, and Joseph R. McDermid<sup>1</sup>

<sup>1</sup> Department of Materials Science and Engineering, McMaster University, 1280 Main Street West, Hamilton, Ontario, Canada, L8S 4L8

<sup>2</sup> Université de Lorraine, CNRS, IJL, F-54000 Nancy, France

*Journal of Materials Research and Technology*, 2024, vol. 30, 2158-2167.

### **4.1 Abstract**

The microstructural evolution of a prototype Fe-0.15C-5.56Mn-1.1Si-1.89Al medium-Mn third-generation advanced high strength steel (3G AHSS) with a martensite-ferrite (MF) starting microstructure during intercritical annealing was determined in situ using high energy X-ray diffraction (HEXRD). Intercritical annealing was carried out at 665 °C and 710 °C for 120 s and 240 s, followed by cooling to room temperature. HEXRD data were analyzed to monitor the austenite fraction and lattice parameters throughout the thermal cycle. During isothermal holding, the austenite fraction increased, up to 31% and 45% for the samples annealed for 120 s, and up to 33% and 46% for the samples annealed for 240 s at 665 °C and 710 °C, respectively. Observed changes in lattice parameters during isothermal holding were attributed to composition changes due to the partitioning of C between austenite and ferrite. Diffusion simulations using DICTRA were used to calculate solute partitioning during intercritical annealing, providing further insights into both austenite growth and the distribution of alloying elements within the austenite.

### **4.2 Introduction**

Intercritically annealed (med-Mn ) third generation advanced high strength steels (3G AHSS), have been shown to exhibit high strength and ductility due to the transformation induced plasticity (TRIP) effect in which retained austenite (RA) transforms to martensite (M) under the action of applied stress/strain [1–4]. It has been suggested that the transformation of RA maintains the instantaneous work hardening rate at high values, thereby delaying the onset of necking and resulting in high ultimate tensile

strengths and uniform elongations [5–7]. The partitioning of austenite stabilizing solutes, such as C and Mn, during intercritical annealing enables the retention of significant volume fractions of austenite – as much as 30 – 40 vol % [2,3,8]– at ambient temperatures. The key to achieving a high-volume fraction of retained austenite is to control the chemistry of the austenite formed during intercritical annealing. Upon cooling, the intercritical austenite is either retained at room temperature – forming the desired RA – or undergoes partial transformation into martensite, leading to the formation of complex microstructures comprising austenite-ferrite or austenite-ferrite-martensite [4,9].

Successful austenite reversion treatments for med-Mn steels are known to consist of two steps: the first is austenitization and quenching to produce martensite, and the second is intercritical annealing in the ferrite-austenite region, promoting the reversion of martensite to austenite [2,10–13]. The initial austenitization treatment can be carried out on various initial microstructures, including as cold-rolled, as-quenched, or tempered martensite. A fine lath martensitic microstructure is generated after quenching from the austenite region. In med-Mn steels, fine and chemically stable inter-lath austenite is frequently retained at room temperature [2]. The lath martensite structure offers several advantages, such as providing numerous nucleation sites for the formation of fine austenite and ferrite laths during subsequent intercritical annealing [14]. The inter-lath retained austenite exhibits greater stability due to its enriched composition of C and Mn, which is facilitated by the short diffusion distances within the lath-shaped austenite grains as compared to equiaxed or globular-shaped austenite [10]. For example, an experimental med-Mn steel with a composition of 0.15C–6Mn–1.5Al–1Si (wt.%) achieved 3G AHSS mechanical property targets (UTS × TE of 24,000–40,000 MPa%) when it was intercritically annealed at 710 °C for 120s from a martensite-ferrite (MF) starting microstructure [2]. The excellent mechanical properties were attributed to the gradual transformation of retained austenite during deformation, resulting in a sustained high work hardening and delayed necking [2]. In comparison to cold-rolled samples, the martensitic initial microstructure exhibits more rapid austenite reversion kinetics and higher volume fractions of retained austenite after cooling [2,3,10,14,15].

In order to determine the effects of intercritical annealing temperature and holding time on microstructure development of candidate med-Mn steels, *ex situ* microstructural analyses are commonly conducted at room temperature. These analyses involve the utilization of different characterization techniques such as light optical microscopy, scanning electron microscopy (SEM) [2,3,10], transmission electron microscopy (TEM) [2,3,10,16], and low energy X-ray diffraction (XRD) using lab scale Cu K $\alpha$  or Co K $\alpha$  radiation [2,3,10]. However, there is a growing interest in incorporating alternative, *in situ* techniques, to enable a more comprehensive observation of the microstructural development of these materials through the whole thermal cycle [17–19].

Synchrotron-based high energy X-ray diffraction (HEXRD) is an advanced characterization method with advantages such as a high penetration depth, exceptional time resolution, and high accuracy due to the observation of numerous diffraction peaks as a result of the small wavelength of the X-rays. It provides valuable data for calculating crucial properties such as phase volume fractions, lattice distortions, and variations in lattice parameters, which are directly linked to individual phase compositions during an IA thermal cycle. The advancement of *in situ* HEXRD techniques has enabled the measurement of microstructural changes during heating/cooling or isothermal holding [17,20]. By employing *in situ* HEXRD characterization during the intercritical annealing of med-Mn steels, valuable insights can be gained regarding phase transformations kinetics and microstructural development throughout thermal processing. Another significant feature is HEXRD's ability to determine the C content of phases by precisely measuring lattice parameters, which is crucial in studying austenite growth kinetics and its chemical stability [21,22].

The purpose of this paper is to clarify certain details of microstructural development from an as-quenched martensitic microstructure in a med-Mn 3G steel during intercritical annealing. A simulation of austenite formation from a martensite/ferrite initial microstructure was performed by Mehrabi et al. [10] using Thermo-Calc's diffusion module, DICTRA. The study reported the evolution of the austenite volume fraction during intercritical annealing at 665 °C and 710 °C. The Simulations were compared with *ex situ* XRD results obtained at room temperature. A key disadvantage of this approach is the

potential transformation of intercritical austenite to martensite during quenching. In order to further develop and validate the modelling approach discussed in [10], *in situ* austenite transformation kinetics measurements were conducted as part of this study. *In situ* HEXRD [17] and dilatometry [23–26] have been used to examine the austenite volume fraction during intercritical annealing of a med-Mn steel. In addition to the HEXRD analysis, *Ex situ* microstructural analysis has been performed using Atom probe tomography (APT) for characterizing the elemental partitioning and EBSD for determining morphology and phase distribution in intercritical annealed samples at room temperature. The HEXRD experiments and complementary microstructural characterization were used to verify an austenite growth model during intercritical annealing.

### 4.3 Materials and Methods

#### 4.3.1 Starting Material and Heat Treatment Parameters

The steel was provided by U.S. Steel R&D (Munhall, Pennsylvania) and had a composition of 0.15 C-5.56 Mn-1.1 Si-1.89 Al-0.08 Mo-0.01 Ti (wt.%). The processing steps included vacuum melting, casting, hot rolling, coiling at 665 °C for 2 h, edge trimming, surface grinding and cold rolling to a final thickness of 1.2 mm. Full details of the steel manufacture and thermomechanical processing, including the mechanical properties resulting from the two-stage thermal treatments used herein, are provided elsewhere [2].

The starting microstructure consisting of 80% martensite and 20% ferrite (MF) was made by austenitizing the as-received cold-rolled steel at 890 °C for 600 s, followed by quenching at  $-20\text{ °C s}^{-1}$  to room temperature. Samples for microstructural examination were intercritically annealed at 665 °C and 710 °C for 120 s and 240 s in an instrumented dilatometer (BÄHR DIL 805). Both dilatometry and *in situ* HEXRD experiments were conducted to study phase transformation kinetics in a prototype steel with a MF starting microstructure. The heat treatment conditions in the dilatometer were consistent with those used in the *in situ* HEXRD experiments, except for the cooling rates, which were set at  $10\text{ °C s}^{-1}$ . The IA temperatures were chosen between the  $A_{e1}$  (625 °C) and  $A_{e3}$  (900 °C) temperatures calculated using Thermo-Calc and the TCFE12 database, with the goal of

achieving various volume fractions of intercritical austenite. These temperatures were determined based on the findings from Pallisco and McDermid [2], which demonstrated high strength and ductility for the alloy. The thermal path is schematically shown in Figure 4.1.

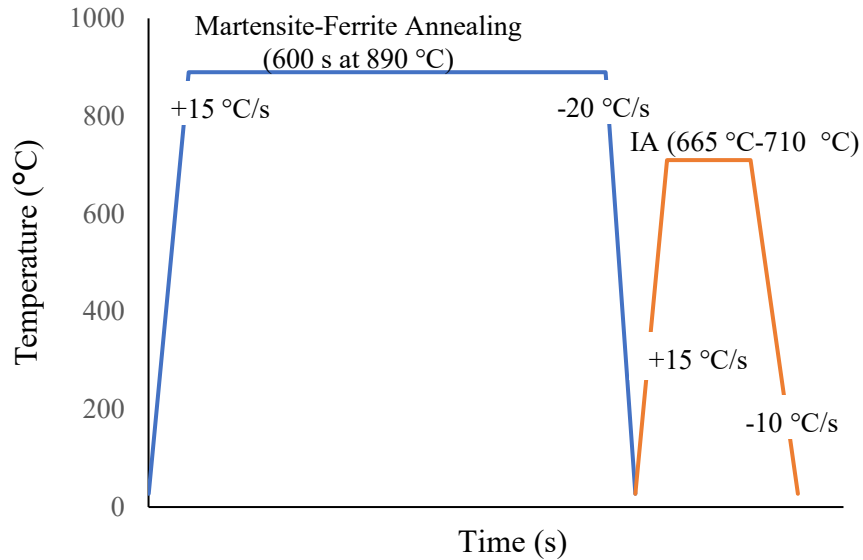


Figure 4.1: Experimental thermal cycle for annealing treatment [2].

#### 4.3.2 Microstructural Analysis

Microstructures and the distribution of phases during intercritical annealing were characterized by electron backscatter diffraction (EBSD) using a JEOL 7000F field emission scanning electron microscope (FEG-SEM) using an acceleration voltage of 20 kV and step size of 50 nm. A  $15 \times 12 \mu\text{m}$  area was scanned to ensure representative results. The data was collected and analyzed using Aztec software. The specimens were metallographically prepared using standard procedures, followed by colloidal silica oxide polishing for 5 min and then cleaning in an ultrasonic bath. The mounted samples were coated with a thin layer of carbon in order to prevent charging. The small scale of the retained austenite at room temperature made it very difficult to be detected by EBSD since most austenite films were below the resolution limit for the present step size used here.

In order to characterize elemental partitioning between the various phases present, 3D atom probe tomography (3D APT) was conducted using a Cameca LEAP 4000X HR

atom probe (Cameca Instruments). To prepare the tips, samples were cut as matchsticks (dimensions: 0.5 mm × 0.5 mm × 20 mm) using a precision cutter and were then electropolished. Electropolishing consisted of two stages: a rough-stage and a fine-stage. During the rough stage, the matchstick was submerged into an electrolyte composed of 25 vol % perchloric acid in acetic acid. During the fine stage, the sample was placed in a Cu tube and electropolished under an optical microscope using a single droplet of 2% perchloric acid in 1-butoxyethanol. A DC voltage range of 10–25 V was used. The tips were analyzed using APT, operating in laser pulsing mode ( $\lambda = 355$  nm, 50 pJ/pulse) with a stage temperature of  $\sim 60$  K and chamber vacuum of  $\sim 3\text{--}4 \times 10^{-11}$  Torr. The target detection rate was set to 0.005 ions/pulse (0.5 %) which was maintained by an applied DC voltage. The laser pulsing rate was 250 kHz. IVAS v3.8.2 software was used for reconstruction and analysis of the data. Only the sample that was intercritically annealed at 710 °C for 120 s was examined using APT. This condition was selected because it provided the optimal mechanical properties based on [2].

For compositional analysis, the Talos 200X TEM/STEM was used in scanning transmission (STEM) mode for energy-dispersive spectroscopy (EDS) with a probe size of 1 nm and an acceleration voltage of 200 kV. TEM samples were prepared by FIB-SEM using a Thermo Scientific Helios 5 UC. The targeted phase boundaries from a polished specimen surface were covered by a tungsten protection layer, lifted out in cross-section, attached to a Cu FIB grid, and thinned for TEM by conventional FIB-SEM methods.

#### 4.3.3 Dilatometry

Dilatometry was carried out using Quench/Deformation BÄHR Dilatometer DIL 805A/D, which was configured in Quench mode. To heat the specimens, an induction Cu coil was employed. Measuring the length change of the specimen was accomplished using a linear voltage displacement transducer (LVDT) connected to quartz push rods attached to the specimen ends. For temperature measurements, K-type thermocouples with a diameter of 0.1 mm were spot-welded at the center of the specimens. The specimens were flat rectangular pieces of approximately 1.2 mm thickness, 5 mm width, and a length of 10 mm, cut from the industrial sheet via EDM (electric discharge machining) in order to avoid

possible sample deformation effects on the austenite to martensite transformation. Sample dimensions were measured using a Mitutoyo micrometer with a resolution of  $\pm 0.001$  mm, where five measurements were taken for each specimen to obtain an average. The volume fraction of austenite present in the samples annealed at 665 °C and 710 °C for 120 s and 240 s was estimated by applying the method reported in [12,23].

#### 4.3.4 High Energy X-ray Diffraction (HEXRD)

*In situ* HEXRD experiments were carried out at the Canadian light source (CLS) on the BXDS (Brockhouse X-ray Diffraction Sector) beamline operated in transmission mode under powder diffraction conditions. High energy X-rays with 60 keV energy and 0.0206641 nm wavelength originating from the central portion of the wiggler radiation fan were reflected inboard by a Si (111), (422), or (533) single crystal monochromator in Laue mode. The X-ray beam penetrates over a  $100 \mu\text{m} \times 100 \mu\text{m}$  area, so that the analyzed volume contained a sufficient number of austenite grains at the start of each experiment. Cylindrical specimens with a diameter of 0.7 mm, and a length of 10 mm were directly machined from the plates. They were cut with the cylindrical axis parallel to the transverse direction (TD). *In situ* heat treatments were performed using a high temperature furnace. The samples were inserted in quartz tubes and the heat treatments were conducted under argon flow to limit decarburization and oxidation during annealing. The temperature was monitored using a type-S thermocouple positioned as closely as possible to the sample. The intercritical thermal treatment consisted of annealing at 665 °C and 710 °C for 120 s and 240 s (Figure 4.1). A 2-D Perkin-Elmer area detector was positioned 77 cm behind the sample, giving access to full Debye-Scherrer rings with a maximum  $2\theta$  angle of  $13^\circ$ . The distance between the sample and the detector was calibrated by diffraction of pure Ni powder.

The 2D images were radially integrated to provide 1D diffractograms using PYFAI (Python library). The 1D diffractograms were then analyzed utilizing a full Rietveld refinement procedure. The diffraction peaks were fitted by a pseudo-Voigt functions using the FullProf code [27] with 16 degrees of freedom to determine the phase fractions and the lattice parameters. Two phases were determined to comprise the bulk of the microstructure:

a face-centered cubic phase, which corresponds to austenite, and a body-centered phase. The latter could be either body-centered cubic corresponding to ferrite (BCC-ferrite) or body-centered tetragonal, corresponding to martensite (BCT-martensite). For low carbon contents, the tetragonality of martensite is not sufficient to allow differentiation between martensite and ferrite [28–30]. Thus, the two phases' lattices were assumed to be cubic during the Rietveld refinement processes (i.e. the  $Fm\bar{3}m$  space group for austenite and  $Im\bar{3}m$  for martensite/ferrite).

#### 4.3.5 DICTRA Simulations

The developed DICTRA module of Thermo-Calc [31] was utilized to model the kinetics of austenite growth for a fully austenitized and as-quenched martensite/ferrite (MF) starting microstructure, known for its more rapid austenite reversion kinetics [2,3]. The models employed the TCFE12 and MOBFE5 databases [31], taking into account the diffusion of C, Mn, Si, and Al in the simulation. Austenite growth from the existing inter-lath RA in martensite was considered as an initial configuration in the DICTRA simulations [10]. The model simulates austenite growth from the planar geometry, which originates from the inter-lath RA geometry observed in previous studies on this family of alloys [2,3,8,10]. The width of the initial austenite and ferrite simulation was selected based on the initial amount of austenite, estimated to be 2% using the HEXRD results. The cell size for the DICTRA simulations for the 665 °C and 710 °C IATs were approximated as 200 nm and 300 nm, respectively [10]. The larger cell size at the higher IA temperatures reflects the coarsening of the microstructure with higher IA temperatures. The simulation cell sizes were chosen based on the microstructural observations that have previously been made [2,3,10]. Based on experimental results, the concentration of C and Mn in austenite was determined to be 1.5 wt% and 10 wt%, respectively [10]. The Al and Si content in austenite was assumed to be essentially the same as the nominal alloy composition. The composition of ferrite was set based on the mass balance. It's important to note that, given the initial microstructure containing 20% ferrite while DICTRA assumed a fully martensitic starting microstructure, the total carbon content was considered as 0.19 wt%, whereas the nominal carbon content is 0.15 wt%. This calculation was based on the phase diagram at the austenization temperature of 890 °C (Figure 4.1).

## 4.4 Results

### 4.4.1 Microstructural Analysis

Figure 4.2 shows a composite SEM-EBSD and APT characterization result after intercritical annealing at 710 °C for 120 s. In Figure 4.2a, the EBSD image indicates cubic ferrite in green and retained austenite in red. Based on area fraction analysis of the EBSD maps the retained austenite vol % was estimated to be 26 %, which is less than that the 31 vol % determined by XRD measurement at room temperature using the standard ASTM E975-13 approach employed by [2]. The reason for this discrepancy is due to a small probe area in EBSD technique [32]. Figure 4.2b shows an APT reproduction of the needle microstructure, including ferrite and austenite. C atoms are shown in green and Mn atoms in blue. The purple iso-surfaces were set at 6.5 at. % Mn. Figure 4.2c shows two interfaces. The region between the two interfaces is believed to be retained austenite because C and Mn are enriched whilst Al, Si are depleted. This is expected to be due to the partitioning of C and Mn from ferrite to austenite. Similarly, Al and Si partition from austenite to ferrite. From these results, it can be concluded that the area investigated by APT comprised a lath-like austenitic grain with ferritic grains on each side (Figure 4.2c). It should be mentioned that the APT tip was not obtained from the same region analyzed by EBSD. Figure 4.2d shows the alloying element distribution in the austenite layer and surrounding ferrite. Chemical characterization of the austenite/ferrite interface was carried out using one-dimensional concentration profiles extracted perpendicular to the interface, along the arrow marked in Figure 4.2b, by using the proxigram technique. An increase in Mn of up to 10 at. % was observed at the interface. The concentration of Mn in the austenite far from interface was slightly less than 9 at. %. Within the ferritic matrix the concentration of Mn was approximately 5 at. % which is close to the nominal composition of the alloy. Also, other elements show a significant partitioning between the ferrite and austenite phases.

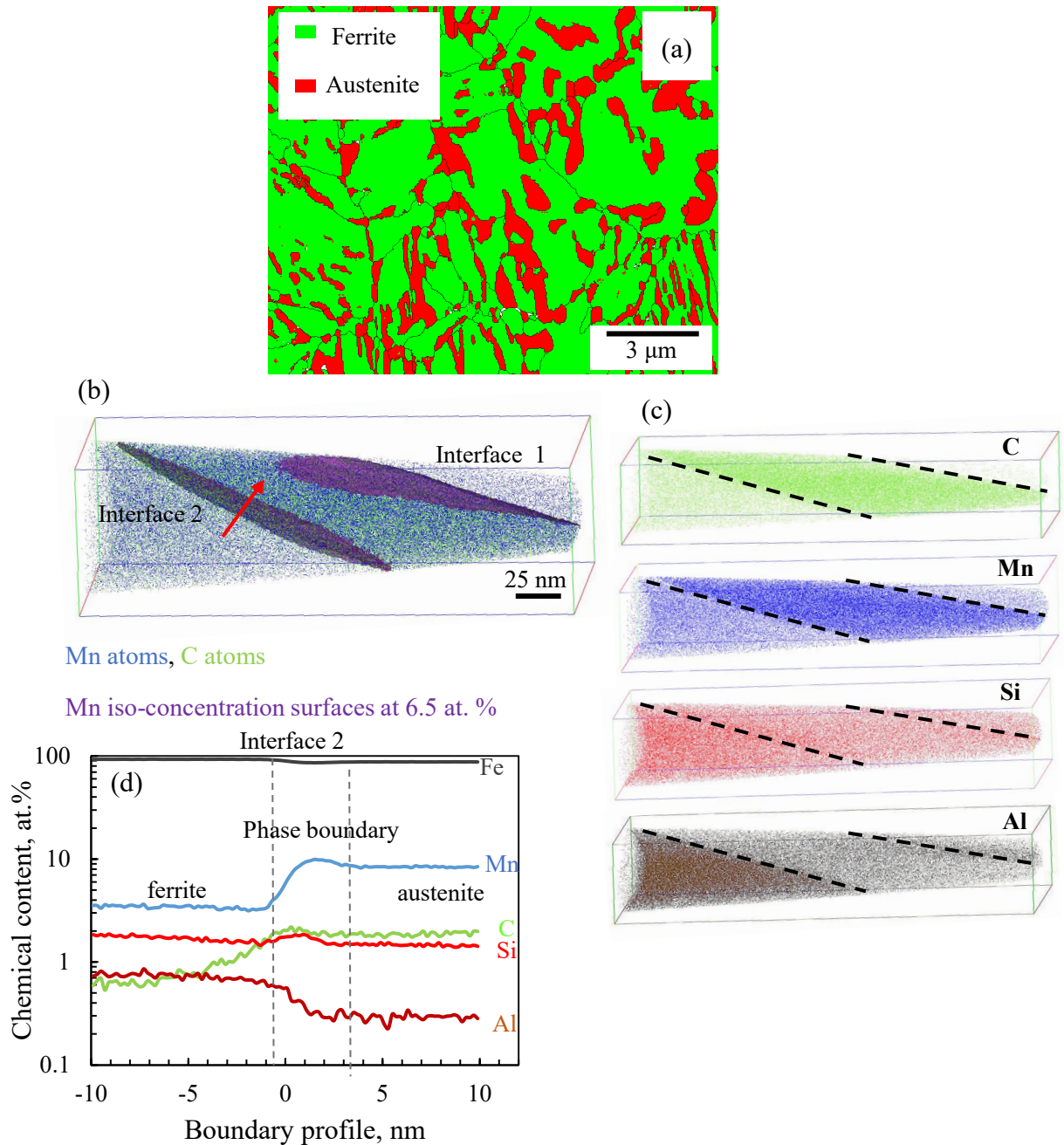


Figure 4.2: Microstructural overview of an intercritically annealed sample after 710 °C for 120s. (a) an EBSD image showing retained austenite in red and ferrite in green. (b) atomic map section showing ferrite and austenite laths, where C atoms are given in green and Mn atoms in blue. The purple iso-surface indicates 6.5 at. % Mn, (c) experimental APT results show two interfaces through the APT reconstruction with C atoms (green) and Mn atoms (blue) are enriched in austenite, while Al (brown) and Si (red) are depleted in austenite and enriched in ferrite. Black dotted lines indicate the suggested crystallographic positions of the phase boundaries between

ferrite and austenite, (d) concentration profiles for all elements across the ferrite/austenite phase boundaries Note that EBSD and APT were not taken at the same place.

#### 4.4.2 Dilatometry

The dilatometric plots for the two IA treatments at 665 °C and 710 °C for 240 s are shown in Figure 4.3. The observed strain contraction in the intercritical region signifies the formation of intercritical austenite in the martensitic matrix during isothermal holding. It should be noted that this contraction becomes more pronounced as the IAT increases. Upon analyzing Figure 4.3a and b, it becomes evident that austenite formation takes place during heating as illustrated by the significant deviations from linear behavior in the heating range. This is understood in terms of the thin films of retained austenite growing without encountering a nucleation barrier. Consequently, the austenite vol % has been calculated based on the extrapolated dashed lines originating from lower-temperature segments. This approach aimed to provide a closer estimation of the total austenite volume fraction [12]. After the isothermal hold, the sample was quenched at 10 °Cs<sup>-1</sup> to 30 °C. *In situ* measured austenite vol % during isothermal holding at 665 °C and 710 °C are shown in § 4.4.3 along with the predicted amount of austenite by DICTRA.

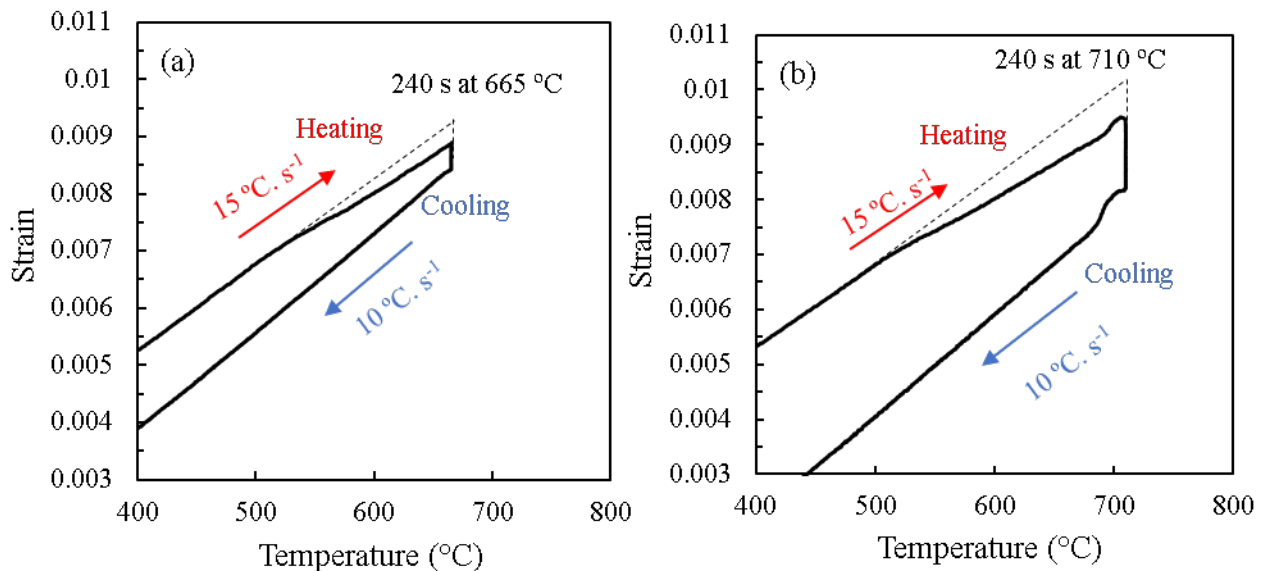


Figure 4.3: Dilatometric strain variations in austenite after a 240 s intercritical annealing at (a) 665 °C and (b) 710 °C.

### 4.4.3 HEXRD

#### 4.4.3.1 *Austenite Transformation Kinetics*

Examples of diffraction patterns obtained during the thermal cycle are presented in Figure 4.4. In all the experiments only two phases were detected in the diffraction patterns: a face-centered cubic phase, corresponding to austenite; and a body-centered phase, which, as discussed earlier, can be either BCT-martensite or BCC-ferrite due to the relatively small c-axis distortion associated with low C steels. As shown in Figure 4.4, the austenite fraction is relatively small during heating, whereas it significantly increases during isothermal holding. Conversely, a considerable amount of austenite remains during cooling, highlighting the chemical stability of the RA.

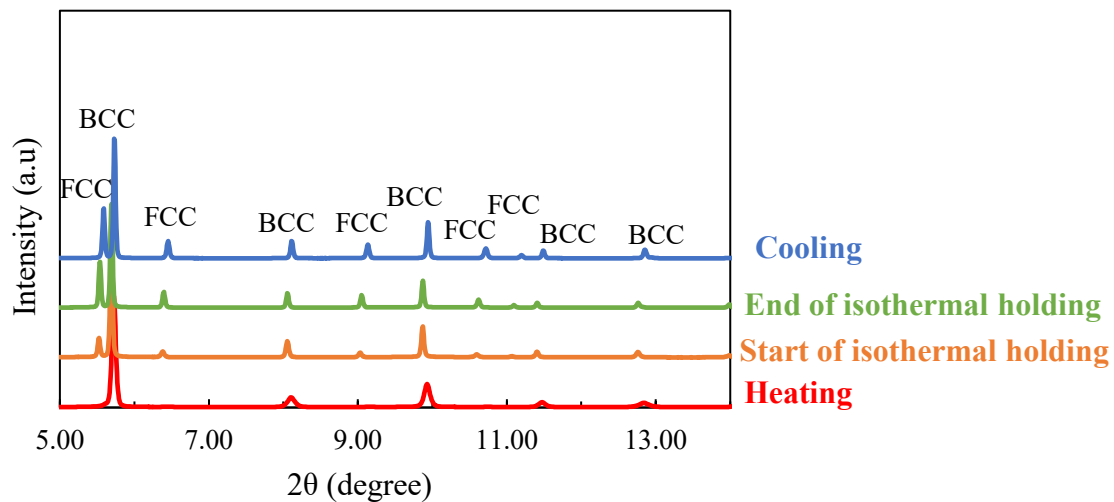


Figure 4.4: The 1-D diffractograms obtained at the selected times during heating (time=15 s), at the start of isothermal holding, end of isothermal holding, cooling (just above the  $M_s$  temperature of 300 °C) for intercritical annealing at 710 °C for 120 s.

Figure 4.5 shows the change in austenite vol % with temperature and time for samples subjected to IATs of 665 °C and 710 °C. Each figure shows a comprehensive thermal cycle, commencing from room temperature at the start time of 0 s, progressing through heating towards the isothermal hold temperatures, and ending with cooling to room temperature. This thermal cycle is highlighted by arrows in Figure 4.5a. As can also be seen in Figure 4.5b, the cooling rate was not constant due to furnace limitations. From IAT

to 400 °C, the cooling rate was close to 10 °Cs<sup>-1</sup> and then gradually decreased. Upon observing Figure 4.5a and b, it is evident that continuous heating to the IAT did not result in a significant increase in austenite vol %. The austenite vol % exhibits a rise during intercritical annealing (IA), reaching a maximum value of 33% at 665 °C and 46% at 710 °C after isothermal holding for 240 s (Figure 4.5). For the 665 °C IAT, the austenite fraction steadily increases with time, whereas at 710 °C, it reaches a plateau at approximately 180 s, displaying saturation (Figure 4.5b). After cooling to room temperature (temperature of about 100 °C on the x-axis of Figure 4.5a), the amount of austenite was reduced to approximately 28% and 45% after the IA at 665 °C and 710 °C, respectively. It's important to highlight that the anticipated equilibrium fractions, represented by the dotted lines in Figure 4.5b, are 34% for the 665 °C IAT and 41% for the 710 °C IAT, as determined using Thermo-Calc and the TCFE12 database. Interestingly, while the calculated equilibrium value at 665 °C aligns closely with the measured result at 240 s, the situation differs for the 710 °C IAT, where the measured value significantly surpasses the predicted one in this study. This is consistent with previous literature that austenite grows beyond equilibrium because substitutional diffusion is significantly slower within austenite than ferrite. At longer times, beyond those studied in this work, the diffusion of substitutional elements in austenite at the final stages of austenite growth determines its kinetics, which will lead to reverse motion of the interface and shrinkage of the austenite [12]. At 665 °C, the system achieves thermodynamic equilibrium following the same holding duration.

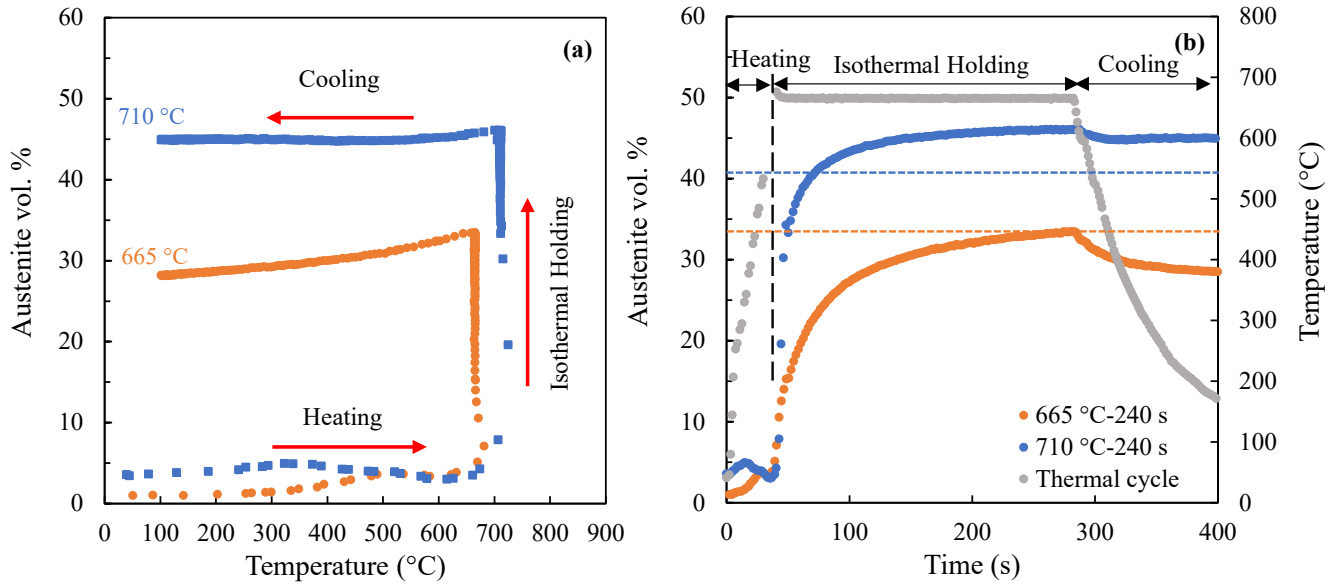


Figure 4.5: Measured HEXRD austenite vol % as a function of (a) temperature and (b) time. The arrows indicate data obtained through the thermal cycle from heating, isothermal holding, and cooling. Dotted lines in (b) show the equilibrium vol % of austenite during IA at 665 °C and 710 °C.

Figure 4.6 compares the predicted austenite vol % (dotted lines) as a function of time at 665 °C (orange) and 710 °C (blue), with the experimentally determined austenite vol % determined by HEXRD (solid lines) and dilatometry (dashed lines). The experimental observations demonstrate a similar pattern in the amount of austenite relative to the isothermal holding time. As depicted in the Figure 4.6, the DICTRA simulation results are within 5% of the measured values. Furthermore, both dilatometry-measured and DICTRA-calculated values exhibit similar trends (shape of the curve) for the austenite vol % at 665 °C and 710 °C IATs with respect to isothermal holding time. However, there is a slight discrepancy between the dilatometry and HEXRD analyses performed at 710 °C regarding the level of austenite present. Nevertheless, both experimental methods show similar trends for the austenite vol % with respect to isothermal holding time. The austenite vol % predictions are in relatively good agreement with the experimental results. The measured and calculated volume fractions both show an initial rapid austenite growth followed by gradual growth for the remainder of the holding time.

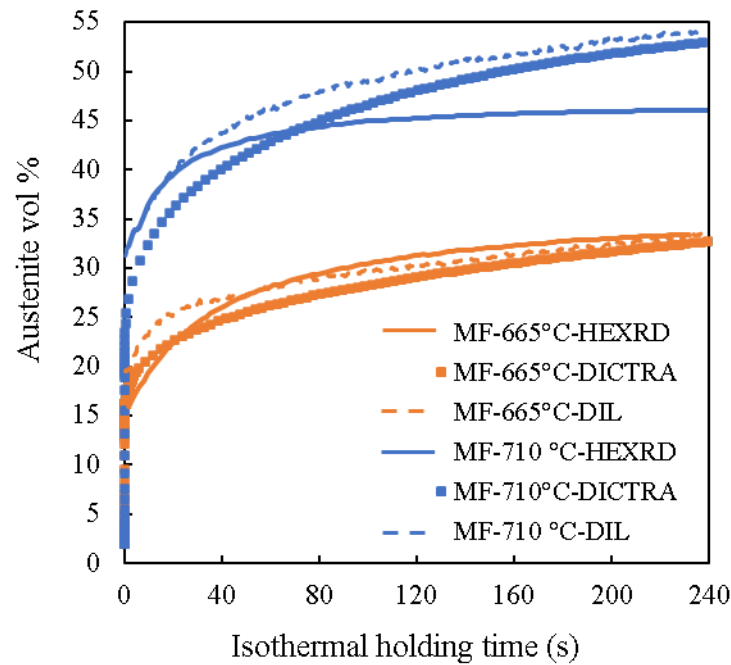


Figure 4.6: Austenite vol % during isothermal holding at 665 °C and 710 °C as determined using *in situ* HEXRD (solid lines) compared to DICTRA simulations (dotted lines) and dilatometry results (dashed lines) up to 240 s.

#### 4.4.3.2 Austenite Lattice Parameter

Figure 4.7 represents the measured austenite lattice parameter normalized by the value determined at the beginning of heating as a function of time at 665 °C and 710 °C. It shows that, during heating, the lattice constant of austenite increases approximately linearly due to thermal expansion. The lattice parameter of austenite exhibits a decrease throughout the holding period at 665 °C and 710 °C. The decrease in lattice parameter during holding is particularly noticeable at 710 °C. The normalized lattice parameter of austenite decreases from 1.020 at the beginning of the isothermal hold to 1.018 during the 665 °C hold and from 1.023 to 1.019 during isothermal holding at 710 °C. Upon cooling to room temperature, the lattice parameter decreases as a result of thermal contraction. At 665 °C, the austenite lattice parameter does not exhibit a saturated value by the end of holding, aligning with the transformation kinetics (Figure 4.5b). Transformations persist throughout the entire duration without attaining a real stasis. In contrast, for the 710 °C

IAT, saturation becomes evident as the austenite lattice parameter becomes constant at approximately 180 s.

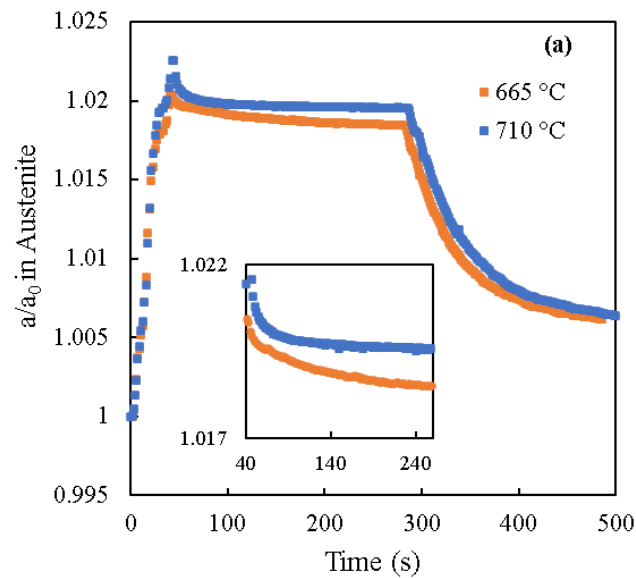


Figure 4.7: Normalized lattice parameter of austenite as a function of time during the heating and isothermal holding at 665 °C and 710 °C. The rescaled versions are added to the plots to show a clearer trend of lattice constant change during isothermal holding.

#### 4.4.4 Concentration Profile Simulations by DICTRA

Concentration profiles for the different alloying elements across the austenite ferrite interface, after annealing at 665 °C and 710 °C for time increments of 0.1 s, 1 s, 10 s, 120 s and 240 s are shown in Figure 4.8 and Figure 4.9, respectively. The enrichment of C and Mn and the depletion of Al at the austenite interface (Figure 4.8 and Figure 4.9) are in good quantitative agreement with the experimentally measured APT concentration profiles presented in Figure 4.2d. The Mn profile (Figure 4.8b and Figure 4.9b) at 0.1 s shows negligible partitioning of Mn in the austenite associated with non-partitioning local equilibrium (NPLE) austenite growth. Under NPLE, the concentration spike of Mn can be seen across the interface. As a result of the negligible partitioning of Mn, the Mn concentration in austenite and ferrite is constant, apart from Mn spike caused by the local equilibrium conditions. These Mn spikes have been observed [33,34] in steels with 2 and 5 wt % Mn, respectively. The Al and Si profiles show negative spike/solute depletion at 665 °C, as shown in Figure 4.8c, d.

At longer times ( $\geq 1$  s) austenite growth is controlled by the diffusion of the substitutional elements in ferrite/martensite. As shown in Figure 4.8, Mn partitions from ferrite to austenite and Al partitions from austenite to ferrite as expected. Surprisingly, however, Si appears to be enriched in austenite. This strange result is due to the thermodynamic database (TCFE12) which predicts that Si partitions to austenite for this alloy composition and temperature.

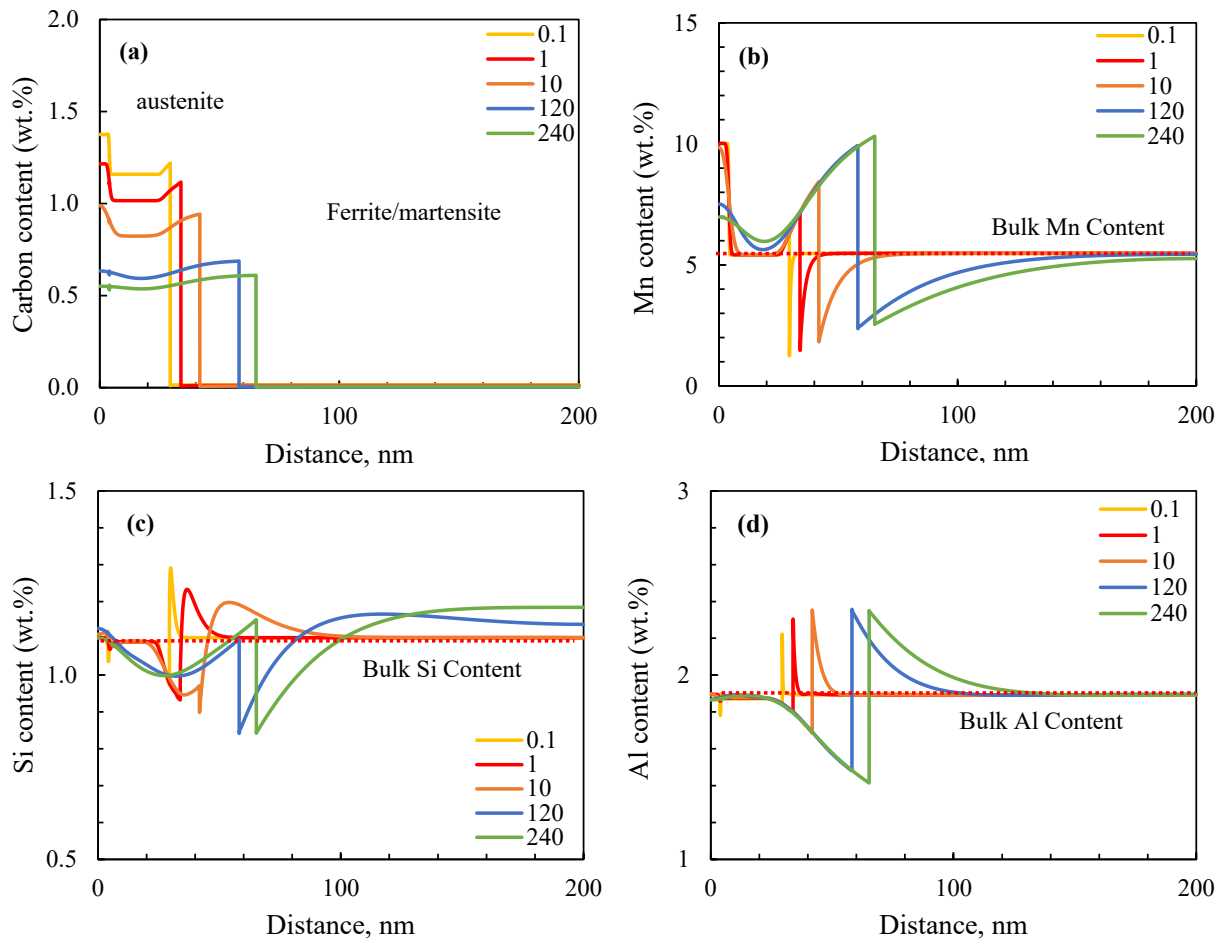


Figure 4.8: Concentration profiles of (a) C, (b) Mn, (c) Si, and (d) Al at various time-steps during isothermal holding at 665 °C.

Similar trends are observed during intercritical annealing at 710 °C. At the longest time (240 s) the substitutional solute profiles in austenite overlap. If intercritical annealing is continued for even longer times, the overlap of the solute profiles in ferrite would lead to a third stage in which the austenite phase begins to shrink. The transformation during this stage would

be controlled by the diffusion of the substitutional elements in austenite and it would allow the austenite fraction to decrease back to the equilibrium level at 710 °C.

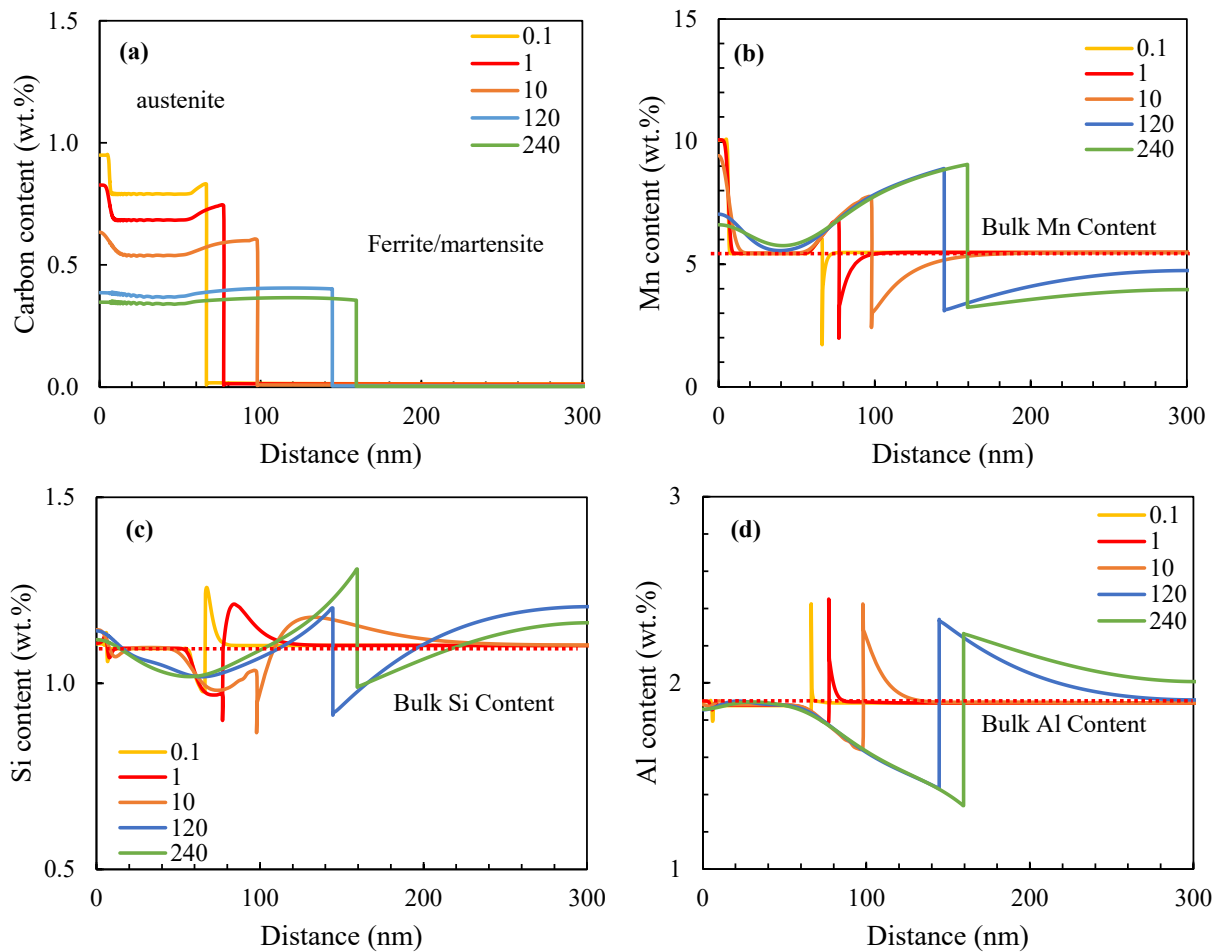


Figure 4.9: Concentration profiles of (a) carbon, (b) Mn, (c) Si, and (d) Al at various time-steps during isothermal holding at 710 °C.

#### 4.5 Discussion

The *in situ* HEXRD technique was utilized to determine the austenite fraction during isothermal holding at 665 °C and 710 °C, and the results were compared to DICTRA simulations (represented as dashed lines) and dilatometer results (represented as dotted lines) in Figure 4.6. Figure 4.6 illustrates that the overall kinetics obtained from HEXRD, dilatometry, and DICTRA are in good agreement at 665 °C and 710 °C. The simple diffusion model in DICTRA has been utilized to predict the overall kinetics without modifying the diffusion coefficient of substitutional alloying elements in ferrite. The

mobility factor of substitutional alloying elements remained unchanged. However, in other studies comparing DICTRA simulations to experimental results [35], a mobility factor of 45 was found to provide good agreement between simulation and experimental data. The slight discrepancy observed between the model and experimental analyses (dilatometry and HEXRD) regarding the vol % austenite present could be attributed to the limitations of 1D simulation, which may not precisely capture the complexities in the actual microstructure [10]. Furthermore, a few percent differences exist in data obtained through HEXRD (local analysis) and dilatometric measurements (global analysis). The differences are expected given the uncertainty associated with the HEXRD method, such as constant chemical composition of the phases, potential peak asymmetries, chemical heterogeneities inside a sample, errors in temperature readings by the thermocouple ( $\pm 5$  °C) [36,37]. The effect of temperature is particularly important. DICTRA simulations indicate that a  $\pm 5$  °C change in temperature can lead to  $\pm 5\%$  change in the vol % of austenite.

The dilatometer data suggests an increase in the austenite volume fraction during heating (Figure 4.3), while the HEXRD measurements (Figure 4.5) showed an essentially constant amount of austenite during heating. This discrepancy could be attributed to the unsuitability of Rietveld refinement for low volume fractions (<10%) observed at the beginning or end of the transformation [36]. Hence, the increase in austenite vol % during intercritical annealing could be interpreted in terms of the growth of the existing retained austenite films, thus enabling austenite to form without fresh nucleation. There is also a possibility that new austenite grains nucleated at martensite lath boundaries [14].

From Figure 4.7, it can be seen that the lattice parameter of austenite decreases during holding at 665 °C and 710 °C. Another study on Fe-0.19C-4.39 Mn (wt%) med-Mn steel reported a consistent trend of decreasing lattice parameter during holding at 650 °C [18]. This was explained by equilibrium calculations of chemical composition changes versus temperature for C and Mn in austenite [18]. Figure 4.8a and Figure 4.9a clearly show a decrease in the C content of austenite with increasing holding time. As the average C content of austenite decreases, the lattice parameter would decrease as well.

In Figure 4.7, comparing the austenite lattice constants between the initial states (T=0 s) and the final states (T=500 s) at room temperature shows an increase in the lattice

parameter at the final state. This increase is attributed to the formation of new austenite with higher carbon content. Consequently, intercritical annealing led to elevated concentrations of carbon within the austenite, enhancing its chemical and mechanical stability upon quenching. At the end of the intercritical annealing cycle, the vol % of RA in the microstructures was measured as 28% and 45%, at 665 °C and 710 °C IAT, respectively. Before cooling, the volume fraction of austenite stood at 33% and 46% at 240 s for the 665 °C and 710 °C IATs, respectively. This suggests that only ~5% and ~1% of the austenite transformed during quenching for the above conditions. The presence of retained austenite, with appropriate stability, plays a crucial role in maintaining a sustained TRIP effect. Various factors influence the stability of austenite, including its morphology, size, and elemental enrichment [38]. Pallisco and McDermid [2] found that the best combination of ultimate tensile strength (UTS) and total elongation (TE) occurred with the IA treatment at 710 °C. Their study revealed an increase in both the volume fraction and stability of austenite with increasing annealing temperature from 665 °C to 710 °C, followed by a decrease in stability for annealing at 740 °C. This reduction in stability could be attributed to lower chemical stability (caused by the dilution of carbon and manganese concentrations in larger grains) and reduced mechanical stability (resulting from increased grain size and decreased hydrostatic pressure from surrounding phases) [14,39,40]. Selecting the optimal annealing temperature is crucial for maximizing the volume fraction of retained austenite while maintaining its stability [41]. As a result, 710 °C is the optimum temperature for intercritical annealing, as it provides a balance between austenite stability and its volume fraction [2].

Finally, it is worth commenting on the Si concentration profiles that were calculated using DICTRA. Figure 4.9c indicates that the Si profile, at 710 °C, shows Si depletion in ferrite. Although Si is known to be a ferrite stabilizer [4,35,42], the TCFE12 database predicts that for some conditions and temperatures, Si can partition to austenite. To assess the accuracy of the database, direct experimental measurements of the Si profile were carried out. Experimental results from a TEM-EDS elemental mapping after intercritical annealing at 710 °C for nearly a year are shown in Figure 4.10. The concentration profile through the austenite and ferrite phases is shown in Figure 4.10b. The concentration profile shows Mn enrichment and Al depletion in austenite, while Si (light blue line) exhibited

negligible enrichment in ferrite. This would suggest that Si does not have a significant effect on austenite growth kinetics, as there was no significant gradient of Si in either ferrite or austenite. When comparing the equilibrium experiment (Figure 4.10b) with the calculated data (Figure 4.9c), there is a discrepancy in the Si profile, suggesting the need to revisit the thermodynamic assessment of the Fe-Mn-Al-Si-C system.

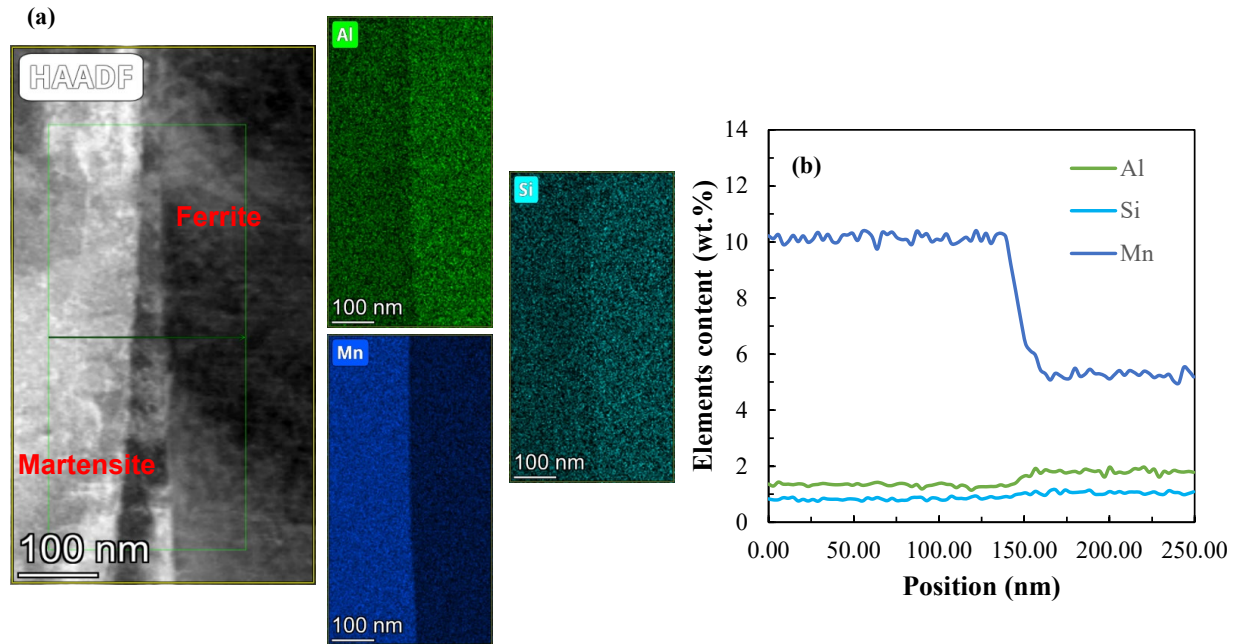


Figure 4.10: EDS elemental mappings from (a) the frame of the high-angle annular dark-field (HAADF) image and (b) concentration profile of Mn, Al, and Si at 710 °C for one year.

## 4.6 Conclusions

In the present study, advanced *in situ* HEXRD observation of the austenite growth during intercritical annealing of a med-Mn steel with a martensite-ferrite starting microstructure has been performed. DICTRA™ simulations were employed to model austenite growth and solute partitioning during intercritical annealing, and the results were compared with experimental analyses from *in situ* HEXRD and dilatometry. From the results of this study, it can be concluded that:

- 1) The experimental results confirm that austenite growth primarily occurs from pre-existing RA films.

- 2) Austenite growth exhibits two stages: initially controlled by rapid carbon diffusion, followed by Mn diffusion in ferrite.
- 3) The partitioning of the substitutional alloying elements at the interface, as measured by APT, aligns with thermodynamic predictions, except in the case of Si. DICTRA predicted Si enrichment in austenite, while experimental data revealed a flat Si profile between ferrite and austenite.
- 4) The overall kinetics can be effectively modeled using the simple diffusion model outlined in DICTRA.
- 5) The overall kinetics obtained from HEXRD, dilatometry, and DICTRA are in good agreement at 665 °C and 710 °C. The slight difference observed between the model and experimental analyses regarding the austenite vol % can be attributed to the limitations of the 1D simulation, which may not precisely capture the complexities in the microstructure.
- 6) At the end of the intercritical annealing cycle, the vol % of RA in the microstructures was measured as 28% and 45% for the 665 °C and 710 °C IAT, respectively. Before cooling, the vol % of austenite stood at 33% and 46% at 240 s for the 665 °C and 710 °C IATs, respectively. This suggests that only ~5 vol % and ~1 vol % of the intercritical austenite transformed to fresh martensite during quenching.

#### **4.7 Acknowledgements**

The authors gratefully acknowledge the Canadian Light Source (CLS), Canada's national synchrotron light source facility in Saskatoon, Saskatchewan, and Drs. King and Rahemtulla, scientists at the Brockhouse Diffraction Sector, for their assistance with HEXRD experiments.

This work was financially supported by the International Zinc Association Galvanized Autobody Partnership (IZA-GAP), and the Natural Sciences and Engineering Research Council of Canada (NSERC grant CRDPJ 522309 – 17). The experimental steel was provided by U.S. Steel Research and Development (Munhall, PA, USA). Atom prob tomography was performed at the Canadian Centre for Electron Microscopy (CCEM), a core research facility of McMaster University (also supported by NSERC and other government agencies).

#### 4.8 References

- [1] D.W. Suh, S.J. Kim, Medium Mn transformation-induced plasticity steels: Recent progress and challenges, *Scr. Mater.* 126 (2017) 63–67. <https://doi.org/10.1016/j.scriptamat.2016.07.013>.
- [2] D.M. Pallisco, J.R. McDermid, Mechanical property development of a 0.15C–6Mn–2Al–1Si third-generation advanced high strength steel using continuous galvanizing heat treatments, *Mater. Sci. Eng. A.* 778 (2020) 139111. <https://doi.org/10.1016/j.msea.2020.139111>.
- [3] K.M.H. Bhadhon, X. Wang, J.R. McDermid, Effects of CGL-compatible thermal processing, starting microstructure, and Sn micro-alloying on the mechanical properties of a medium-Mn third generation advanced high strength steel, *Mater. Sci. Eng. A.* 833 (2022) 142563. <https://doi.org/10.1016/j.msea.2021.142563>.
- [4] Z. Dai, H. Chen, R. Ding, Q. Lu, C. Zhang, Z. Yang, S. van der Zwaag, Fundamentals and application of solid-state phase transformations for advanced high strength steels containing metastable retained austenite, *Mater. Sci. Eng. R.* 143 (2021) 100590. <https://doi.org/10.1016/j.mser.2020.100590>.
- [5] D.W. Suh, S.J. Kim, Medium Mn transformation-induced plasticity steels: Recent progress and challenges, *Scr. Mater.* 126 (2017) 63–67.
- [6] J. Zhao, Z. Jiang, Thermomechanical processing of advanced high strength steels, *Prog. Mater. Sci.* 94 (2018) 174–242. <https://doi.org/10.1016/j.pmatsci.2018.01.006>.
- [7] D.K. Matlock and J.G. Speer, Design considerations for the next generation of advanced high strength steel sheets, *Proc. 3rd Inter. Conf. Adv. High Strength Steels.* (2006) 774–781.
- [8] K.M.H. Bhadhon, X. Wang, E.A. McNally, J.R. McDermid, Effect of Intercritical Annealing Parameters and Starting Microstructure on the Microstructural Evolution and Mechanical Properties of a Medium-Mn Third Generation Advanced High Strength Steel, *Metals (Basel)*. 12 (2022) 356. <https://doi.org/10.3390/met12020356>.

- [9] B. Hu, H. Luo, F. Yang, H. Dong, Recent progress in medium-Mn steels made with new designing strategies, a review, *J. Mater. Sci. Technol.* 33 (2017) 1457–1464. <https://doi.org/10.1016/j.jmst.2017.06.017>.
- [10] A. Mehrabi, J.R. McDermid, X. Wang, H. Zurob, Austenite Nucleation and Growth as a Function of Starting Microstructure for a Fe–0.15C–5.56Mn–1.1Si–1.89Al Medium-Mn Steel, *Steel Res. Int.* 94 (2023) 2200952. <https://doi.org/10.1002/srin.202200952>.
- [11] R.L. Miller, Ultrafine- grained microstructures and mechanical properties of alloy steels, *Met Trans.* 3 (1972) 905–912. <https://doi.org/10.1007/bf02647665>.
- [12] R. Wei, M. Enomoto, R. Hadian, H.S. Zurob, G.R. Purdy, Growth of austenite from as-quenched martensite during intercritical annealing in an Fe-0.1C-3Mn-1.5Si alloy, *Acta Mater.* 61 (2013) 697–707. <https://doi.org/10.1016/j.actamat.2012.10.019>.
- [13] H. Luo, J. Shi, C. Wang, W. Cao, X. Sun, H. Dong, Experimental and numerical analysis on formation of stable austenite during the intercritical annealing of 5Mn steel, *Acta Mater.* 59 (2011) 4002–4014. <https://doi.org/10.1016/j.actamat.2011.03.025>.
- [14] H. Luo, H. Dong, M. Huang, Effect of intercritical annealing on the Lüders strains of medium Mn transformation-induced plasticity steels, *Mater. Des.* 83 (2015) 42–48. <https://doi.org/10.1016/j.matdes.2015.05.085>.
- [15] S. Zhang, K.O. Findley, Quantitative assessment of the effects of microstructure on the stability of retained austenite in TRIP steels, *Acta Mater.* 61 (2013) 1895–1903. <https://doi.org/10.1016/j.actamat.2012.12.010>.
- [16] H. Luo, J. Liu, H. Dong, A Novel Observation on Cementite Formed During Intercritical Annealing of Medium Mn Steel, *Metall. Mater. Trans. A.* 47A (2016) 3119–3124. <https://doi.org/10.1007/s11661-016-3448-0>.
- [17] J.J. Mueller, X. Hu, X. Sun, Y. Ren, K. Choi, E. Barker, J.G. Speer, D.K. Matlock, E. De Moor, Austenite formation and cementite dissolution during intercritical annealing of a medium-

manganese steel from a martensitic condition, *Mater. Des.* 203 (2021) 109598. <https://doi.org/10.1016/j.matdes.2021.109598>.

[18] X. Hu, J.J. Mueller, X. Sun, E. De Moor, J.G. Speer, D.K. Matlock, Y. Ren, The In Situ Observation of Phase Transformations During Intercritical Annealing of a Medium Manganese Advanced High Strength Steel by High Energy X-Ray Diffraction, *Front. Mater.* 8 (2021) 1–9. <https://doi.org/10.3389/fmats.2021.621784>.

[19] M. Lamari, S.Y.P. Allain, G. Geandier, J.C. Hell, A. Perlade, K. Zhu, In situ determination of phase stress states in an unstable medium manganese duplex steel studied by high-energy X-ray diffraction, *Metals (Basel)*. 10 (2020) 1335. <https://doi.org/10.3390/met10101335>.

[20] G. Geandier, E. Aeby-Gautier, A. Settefrati, M. Dehmas, B. Appolaire, Study of diffusive transformations by high energy X-ray diffraction, *Comptes Rendus Phys.* 13 (2012) 257–267. <https://doi.org/10.1016/j.crhy.2011.12.001>.

[21] S.Y.P. Allain, G. Geandier, J.C. Hell, M. Soler, F. Danoix, M. Gouné, In-situ investigation of quenching and partitioning by High Energy X-Ray Diffraction experiments, *Scr. Mater.* 131 (2017) 15–18. <https://doi.org/10.1016/j.scriptamat.2016.12.026>.

[22] Z. Tournoud, F. De Geuser, G. Renou, D. Huin, P. Donnadieu, A. Deschamps, In-situ characterization by high-energy x-ray diffraction of the phase transformations leading to transformation-induced plasticity-aided bainitic steel, *Quantum Beam Sci.* 3 (2019) 25. <https://doi.org/10.3390/qubs3040025>.

[23] S.J. Lee, S. Lee, B.C. De Cooman, Mn partitioning during the intercritical annealing of ultrafine-grained 6% Mn transformation-induced plasticity steel, *Scr. Mater.* 64 (2011) 649–652. <https://doi.org/10.1016/j.scriptamat.2010.12.012>.

[24] S.J. Lee, S. Lee, B.C. De Cooman, Martensite transformation of sub-micron retained austenite in ultra-fine grained manganese transformation-induced plasticity steel, *Int. J. Mater. Res.* 104 (2013) 423–429. <https://doi.org/10.3139/146.110882>.

- [25] F. Moszner, E. Povoden-Karadeniz, S. Pogatscher, P.J. Uggowitzer, Y. Estrin, S.S.A. Gerstl, E. Kozeschnik, J.F. Löffler, Reverse  $\alpha' \rightarrow \gamma$  transformation mechanisms of martensitic Fe-Mn and age-hardenable Fe-Mn-Pd alloys upon fast and slow continuous heating, *Acta Mater.* 72 (2014) 99–109. <https://doi.org/10.1016/j.actamat.2014.03.032>.
- [26] K. Steineder, R. Schneider, D. Krizan, C. Béal, C. Sommitsch, Comparative investigation of phase transformation behavior as a function of annealing temperature and cooling rate of two medium-mn steels, *Steel Res. Int.* 86 (2015) 1179–1186. <https://doi.org/10.1002/srin.201400551>.
- [27] J. Rodriguez-carvajal, Recent advances in magnetic structure determination neutron powder diffraction by neutron powder diffraction, *Phys. B.* 192 (1993) 55–69.
- [28] Y. Lu, H. Yu, R.D. Sisson, The effect of carbon content on the c/a ratio of as-quenched martensite in Fe-C alloys, *Mater. Sci. Eng. A.* 700 (2017) 592–597. <https://doi.org/10.1016/j.msea.2017.05.094>.
- [29] N. Maruyama, S. Tabata, H. Kawata, Excess Solute Carbon and Tetragonality in As-Quenched Fe-1Mn-C (C:0.07 to 0.8 Mass Pct) Martensite, *Metall. Mater. Trans. A.* 51A (2020) 1085–1097. <https://doi.org/10.1007/s11661-019-05617-y>.
- [30] L. Xiao, Z. Fan, Z. Jinxiu, Z. Mingxing, K. Mokuang, G. Zhenqi, Lattice-parameter variation with carbon content of martensite. I. X-ray-diffraction experimental study, *Phys. Rev. B.* 52 (1995) 9970–9978. <https://doi.org/10.1103/PhysRevB.52.9970>.
- [31] J.O. Andersson, T. Helander, L. Höglund, P. Shi, B. Sundman, Thermo-Calc & DICTRA, computational tools for materials science, *Calphad.* 26 (2002) 273–312. [https://doi.org/10.1016/S0364-5916\(02\)00037-8](https://doi.org/10.1016/S0364-5916(02)00037-8).
- [32] P.J. Jacques, S. Allain, O. Bouaziz, A. De, A.F. Gourgues, B.M. Hance, Y. Houbaert, J. Huang, A. Iza-Mendia, S.E. Kruger, M. Radu, L. Samek, J. Speer, L. Zhao, S. Van der Zwaag, On measurement of retained austenite in multiphase TRIP steels results of blind round robin test involving six different techniques, *Mater. Sci. Technol.* 25 (2009) 567–574. <https://doi.org/10.1179/174328408X353723>.

- [33] X. Zhang, G. Miyamoto, T. Kaneshita, Y. Yoshida, Y. Toji, T. Furuhashi, Growth mode of austenite during reversion from martensite in Fe-2Mn-1.5Si-0.3C alloy: A transition in kinetics and morphology, *Acta Mater.* 154 (2018) 1–13. <https://doi.org/10.1016/j.actamat.2018.05.035>.
- [34] H.W. Luo, C.H. Qiu, H. Dong, J. Shi, Experimental and numerical analysis of influence of carbide on austenitisation kinetics in 5Mn TRIP steel, *Mater. Sci. Technol.* 30 (2014) 1367–1377. <https://doi.org/10.1179/1743284713Y.0000000447>.
- [35] O. Dmitrieva, D. Ponge, G. Inden, J. Millán, P. Choi, J. Sietsma, D. Raabe, Chemical gradients across phase boundaries between martensite and austenite in steel studied by atom probe tomography and simulation, *Acta Mater.* 59 (2011) 364–374. <https://doi.org/10.1016/j.actamat.2010.09.042>.
- [36] I. E. Benrabah, Development of compositional-gradient metallic alloys for combinatorial investigation of microstructures, 2021.
- [37] C. Rampelberg, Characterization and modeling of Carbide-Free Bainite transformations along isothermal and anisothermal heat treatments, 2023.
- [38] J. Hu, X.Y. Li, Q.W. Meng, L.Y. Wang, Y.Z. Li, W. Xu, Tailoring retained austenite and mechanical property improvement in Al–Si–V containing medium Mn steel via direct intercritical rolling, *Mater. Sci. Eng. A.* 855 (2022) 143904. <https://doi.org/10.1016/j.msea.2022.143904>.
- [39] D.W. Suh, J.H. Ryu, M.S. Joo, H.S. Yang, K.Y. Lee, Medium – Alloy Manganese – Rich Transformation – Induced Plasticity Steels, *Metall. Mater. Trans. A.* 46A (2013) 286–293.
- [40] R. Schneider, K. Steineder, D. Krizan, C. Sommitsch, Effect of the heat treatment on the microstructure and mechanical properties of medium-Mn-steels, *Mater. Sci. Technol.* 35 (2019) 2045–2053. <https://doi.org/10.1080/02670836.2018.1548957>.
- [41] E. De Moor, D.K. Matlock, J.G. Speera, M.J. Merwin, Austenite stabilization through manganese enrichment, *Scr. Mater.* 64 (2011) 185–188. <https://doi.org/10.1016/j.scriptamat.2010.09.040>.

[42] B. Sun, F. Fazeli, C. Scott, N. Brodusch, R. Gauvin, S. Yue, The influence of silicon additions on the deformation behavior of austenite-ferrite duplex medium manganese steels, *Acta Mater.* 148 (2018) 249–262. <https://doi.org/10.1016/j.actamat.2018.02.005>.

## **5 An *in situ* Study of Austenite Formation During Intercritical Annealing of a Medium-Manganese Steel with Cold-Rolled Starting Microstructure**

Azin Mehrabi, Hatem Zurob, and Joseph R. McDermid

*Draft Manuscript*

### **5.1 Abstract**

Austenite formation from cold-rolled starting microstructure in a prototype Fe-0.15C-5.56Mn-1.1Si-1.89Al medium-Mn third-generation advanced high-strength steel (3G AHSS) was analyzed using *in situ* high-energy X-ray diffraction system (HEXRD). Intercritical annealing was conducted at 665 °C and 710 °C for 120 s and 240 s, followed by cooling to room temperature. The analysis of the HEXRD data was conducted to determine the phase fractions throughout the thermal cycles. The austenite vol% increased to 24% and 40% for the samples annealed for 120 s, and up to 26% and 41% for the samples annealed for 240 s at 665 °C and 710 °C, respectively. Solute partitioning during intercritical annealing was calculated using DICTRA diffusion simulations in order to better understand the distribution of alloying elements within the austenite.

### **5.2 Introduction**

Transportation vehicles should meet strict standards concerning fuel economy, emissions, and safety. Manufacturers are currently working on the development of new lightweight body-in-white assemblies, incorporating advanced high-strength steels (AHSS) to guarantee crashworthiness. Among the promising options for 3G AHSS, medium-Mn (med-Mn) steels with approximately 4 to 10 wt% Mn stand out. A high amount of retained austenite stabilized by increased Mn content, leads to great mechanical performance of this group of 3G AHSS. The required thermal processing path is relatively straightforward, involving a controlled intercritical annealing (IA) treatment. IA parameters not only control the amount of RA but also influence its stability. Therefore, it is essential to study the phase transformation kinetics and the microstructural evolution during IA of med-Mn steels. The primary goal is to identify optimal processing parameters that enhance both the fraction and stability of the retained austenite in the final 3G AHSS products.

It is evident that understanding the phase transformation mechanisms and predicting the kinetics are essential steps in designing and controlling microstructures with specific properties. To study solid–solid phase transformations, numerous characterization methods can be utilized, including X-ray, and electronic microscopy methods. The volume fraction of phases and lattice parameters can be obtained by quantitative analyses of the diffraction patterns. However, achieving accurate determinations requires long acquisition times, restricting investigations for very slow kinetics. The limitations of the lab-based X-ray method can be significantly addressed by synchrotron beam at high energy (60 keV and over). In this method, a considerable volume can be analyzed through X-ray transmission, with acquisition times significantly shortened to a few seconds or less. A high temperature furnace can be connected to the equipment to collect a large number of Debye–Scherrer diffraction patterns during the heat treatment. The volume fraction of phases, and lattice parameters can be precisely obtained during IA to monitor the kinetics of phase transformations.

This research aims to clarify the microstructural evolution during intercritical annealing of a cold-rolled med-Mn 3G steel. Austenite formation kinetics in CR starting microstructure during IA at 665 °C and 710 °C was simulated by Mehrabi et al. [1] using Thermo-Calc's diffusion module, DICTRA. The study presented details on both the volume fraction of austenite and the role of cementite dissolution on the austenite growth kinetics. The standard room temperature XRD results were employed for the validation of the simulation. To overcome the limitations of room temperature XRD and ensure precise validation of the modeling approach, *in situ* measurements of austenite transformation kinetics were carried out. *In situ* HEXRD [2] and dilatometry [3–6] were utilized to assess the austenite volume fraction during intercritical annealing (IA) of a med-Mn steel. Atom Probe Tomography (APT) was used for characterizing solute partitioning and Electron Backscatter Diffraction (EBSD) for assessing morphology and phase distribution. The new experimental results were employed to validate the model of austenite growth during IA.

### **5.3 Materials and Methods**

#### **5.3.1 Starting Material and Heat Treatment Parameters**

The steel, with a composition of 0.15 C-5.56 Mn-1.1 Si-1.89 Al-0.08 Mo-0.01 Ti (wt.%), was supplied by U.S. Steel R&D in Munhall, Pennsylvania. The manufacturing process involved vacuum melting, casting, hot rolling coiling at 665 °C for two hours, edge trimming, surface grinding, and cold rolling to achieve a final thickness of 1.2 mm. Comprehensive information on the manufacture and thermomechanical processing of steel can be found in [7].

The cold-rolled structure microstructure consists of 70% tempered martensite and 30% ferrite (CR). This was used as the starting microstructure for the present study. Ferrite was present owing to the relatively high Al content in the alloy which resulted in a high  $A_3$  temperature. Intercritical annealing temperatures of 665 °C and 710 °C for 120 s and 240 s were used. Both dilatometry and *in situ* HEXRD experiments were conducted to study phase transformation kinetics in a prototype steel with a CR starting microstructure. The heat treatment conditions in the dilatometer were consistent with those used in the *in situ* HEXRD experiments, except for the cooling rates, which were set at 10 °Cs<sup>-1</sup>. The IA temperatures were chosen between the  $A_{e1}$  (625 °C) and  $A_{e3}$  (900 °C) temperatures calculated using Thermo-Calc and the TCFE12 database, with the goal of achieving various volume fractions of intercritical austenite. The selection of intercritical annealing temperatures was based on the findings of Pallisco and McDermid [7], aiming to achieve high strength and ductility in the alloy.

### 5.3.2 Microstructure Analysis

The electron backscatter diffraction (EBSD) technique, conducted on a JEOL 7000F field emission scanning electron microscope (FEG-SEM) with an acceleration voltage of 20 kV and a step size of 50 nm, was employed to characterize the microstructure during IA. The data was collected from an area of 15 × 12 μm and analyzed using Aztec software. Specimens underwent standard metallographic preparation, including colloidal silica oxide polishing for 5 minutes and subsequent cleaning in an ultrasonic bath. To prevent charging, mounted samples were coated with a thin layer of carbon. Detection of the small-scale retained austenite at room temperature was challenging for EBSD due to most austenite phase being below the resolution limit for the specified step size.

3D atom probe tomography (3D APT) was conducted using a Cameca LEAP 4000X HR atom probe (Cameca Instruments) to characterize elemental partitioning between the phases. The

sample preparation details are reported in our previous study [8]. Data reconstruction and analysis were conducted using IVAS v3.8.2 software. APT analysis was specifically applied to the sample subjected to intercritical annealing at 665 °C for 120 s. This particular condition was chosen due to its association with optimal mechanical properties, as indicated by prior assessments [7].

### 5.3.3 Dilatometry

Dilatometry experiments were conducted using the Quench/Deformation BÄHR Dilatometer DIL 805A/D, configured in Quench mode. Specimens were heated using an induction copper coil, and the length change of the specimen was measured using a linear voltage displacement transducer (LVDT) connected to quartz push rods attached to the specimen ends. Temperature measurements were obtained with K-type thermocouples (0.1 mm diameter) spot-welded at the center of the specimens. The specimens, flat rectangular pieces approximately 1.2 mm thick, 5 mm wide, and 10 mm long, were cut from the industrial sheet using electric discharge machining (EDM) to prevent potential sample deformation to martensite. The dimensions of the samples were measured using a Mitutoyo micrometer with a resolution of  $\pm 0.001$  mm, involving five measurements for each specimen to determine an average. The volume fraction of austenite in the samples subjected to annealing at 665 °C and 710 °C for 120 s and 240 s was estimated through the method detailed in [3,9].

### 5.3.4 High Energy X-ray Diffraction (HEXRD)

*In situ* HEXRD experiments were carried out at the Canadian light source (CLS) on the BXDS (Brockhouse X-ray Diffraction Sector) beamline, operated in transmission mode under powder diffraction conditions. The technical details of a synchrotron high-energy X-ray test, including information on energy, wavelength, sample dimensions, heat treatment conditions as well as a high-temperature furnace feature, and detector characteristics, are provided in our previous study [8].

The HEXRD data analysis involved using PYFAI (Python library) to integrate the 2D images into 1D diffractograms. Subsequently, the 1D diffractograms were analyzed employing a full Rietveld refinement procedure. Pseudo-Voigt functions within the FullProf code [10] were

employed with 16 degrees of freedom to fit the diffraction peaks, enabling the determination of both phase fractions and lattice parameters. The microstructure was found to consist primarily of two phases: a face-centered cubic phase (FCC), corresponding to austenite, and a body-centered cubic phase (BCC), corresponding to ferrite. The latter could be either body-centered cubic corresponding to ferrite (BCC-ferrite) or body-centered tetragonal, corresponding to martensite (BCT-martensite). When carbon content is low, distinguishing between martensite and ferrite based solely on tetragonality is not feasible [11–13]. Consequently, the lattices of the two phases were assumed to be cubic during the Rietveld refinement processes, with the  $Fm\bar{3}m$  space group for austenite and  $Im\bar{3}m$  for ferrite.

### 5.3.5 DICTRA Simulations

The DICTRA module of Thermo-Calc [14] was utilized to model the kinetics of austenite growth for an as-received cold rolled (CR) starting microstructure. The models employed the TCFE12 and MOBFE5 databases [14], taking into account the diffusion of C, Mn, Si, and Al in the simulation. Austenite nucleated at ferrite grain boundaries at both 665 °C and 710 °C [1]. The model simulates austenite growth from the spherical geometry, because the globular morphology was experimentally observed in previous studies on this family of alloys [1,7,15].

In CR-665 °C, austenite formed away from the cementite, where the ferrite facilitate the C diffusion. The cell consists of austenite and cementite isolated from one another by ferrite (martensite). Spherical configuration was employed with a cementite particle positioned at the center of a ferrite sphere. The austenite was introduced as an inactive phase on the outer shell of the ferrite sphere. The width of the initial cementite region in the simulation was determined based on the estimated volume fraction of cementite, which was calculated to be 0.02 using the TCFE12 database of Thermo-Calc at 640 °C, where austenite is suspended. The size of cementite was selected as 30 nm based on TEM observations [1,7,16] and the size of ferrite was set based on the mass balance. The C concentration in ferrite was determined to be 0.015 wt% by mass balance, while that of cementite was 6.7 wt% [1]. The Mn content in cementite was set to 10 wt%, which was the average value measured by TEM-EDX [1]. The cell size for the DICTRA simulations for the 665 °C IAT was approximated as 110 nm [1].

In CR-710 °C, cementite dissolution takes place rapidly. As a result, the cementite particles were not considered in the simulation. The simulation was based on a spherical

austenite nucleus within a ferrite matrix. The cell size for the DICTRA simulations for the 710 °C IAT was approximated as 440 nm [1]. The larger cell size at the higher IA temperatures reflects the coarsening of the microstructure with higher IA temperatures.

## 5.4 Results

### 5.4.1 Microstructural Analysis

Figure 5.1 shows typical SEM-EBSD maps of the microstructure after intercritical annealing at 665 °C and 710 °C for 120 s. In the EBSD maps, the FCC retained austenite is indicated in red, while BCC ferrite is represented in green. Un-indexed areas and grain boundaries are shown in black. The starting microstructures comprised globular-shaped ferrite and austenite grains, being consistent with the literature [1,7,16]. It appears that retained austenite mostly forms along the high-angle grain boundaries of ferrite. By increasing IA temperature, the volume fraction of austenite increases. The total volume fraction of retained austenite phase measured by EBSD is about 4.4 % and 20.2% after IA at 665 °C and 710 °C, respectively. This is lower than that of 25% and 27% measured by XRD measurement at room temperature using the standard ASTM E975-13 approach employed by [1,7]. The reason for this discrepancy may be caused by the small size or thickness (<50nm) of retained austenite, which could not be measured by EBSD, particularly after IA at 665 °C [17].

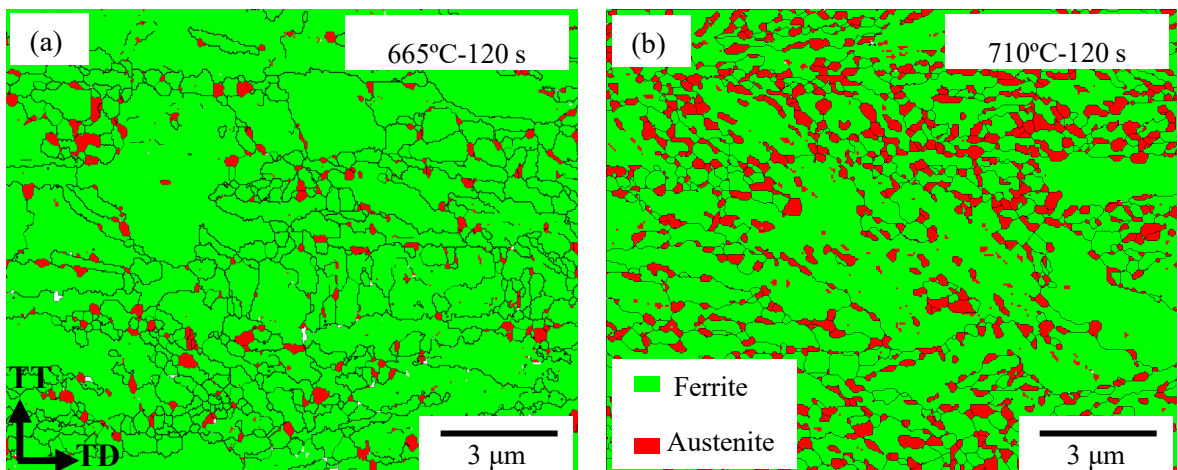


Figure 5.1: EBSD phase maps of the reference steel intercritically annealed during isothermal holding up to 120 s at (a) 665 °C and (b) 710 °C.

Figure 5.2 shows an APT result after intercritical annealing at 665 °C for 120 s. In Figure 5.2a, C atoms are shown in green and Mn atoms in blue. The orange and purple iso-surfaces were set at 3 at. % C and 8.5 at. % Mn, respectively. Additionally, an interface is observed in the Figure 5.2a, with the phases consisting of ferrite, retained austenite, and cementite. Figure 5.2b indicates the alloying element distribution in the austenite layer and surrounding ferrite and cementite. The region near the interfaces is believed to be retained austenite because C and Mn are enriched whilst Al, Si are depleted. This is expected to be due to the partitioning of C and Mn from ferrite to austenite. Similarly, Al and Si partition from austenite to ferrite. Also, in the C and Mn enriched area, no particles emerge. So, it can be suggested that this area is retained austenite, while the surrounding areas with particles are ferrite. From these results, it can be concluded that the area investigated by APT comprised a globular-like austenitic grain with ferritic grains surrounded by C-rich particles (Figure 5.2b). Besides the C atoms, higher amounts of Mn were also detected in these particles. TEM results confirm the idea that the cementite particles that are enriched in C, Mn, formed in the ferritic microstructure while the retained austenite was particle-free [1]. The chemical characterization of the austenite/ferrite interface, depicted in Figure 5.2c, involved one-dimensional concentration profiles extracted perpendicular to the interface. These profiles were obtained along the arrow marked in Figure 5.2a, utilizing the proxigram technique. An increase in Mn up to 14 at. % was observed at the interface. The concentration of Mn in the austenite far from the interface was slightly less than 11 at. %. Within the ferritic matrix the concentration of Mn was approximately 5 at. % which is close to the nominal composition of the alloy. Other elements, Al and Si, show partitioning between the ferrite and austenite phases.

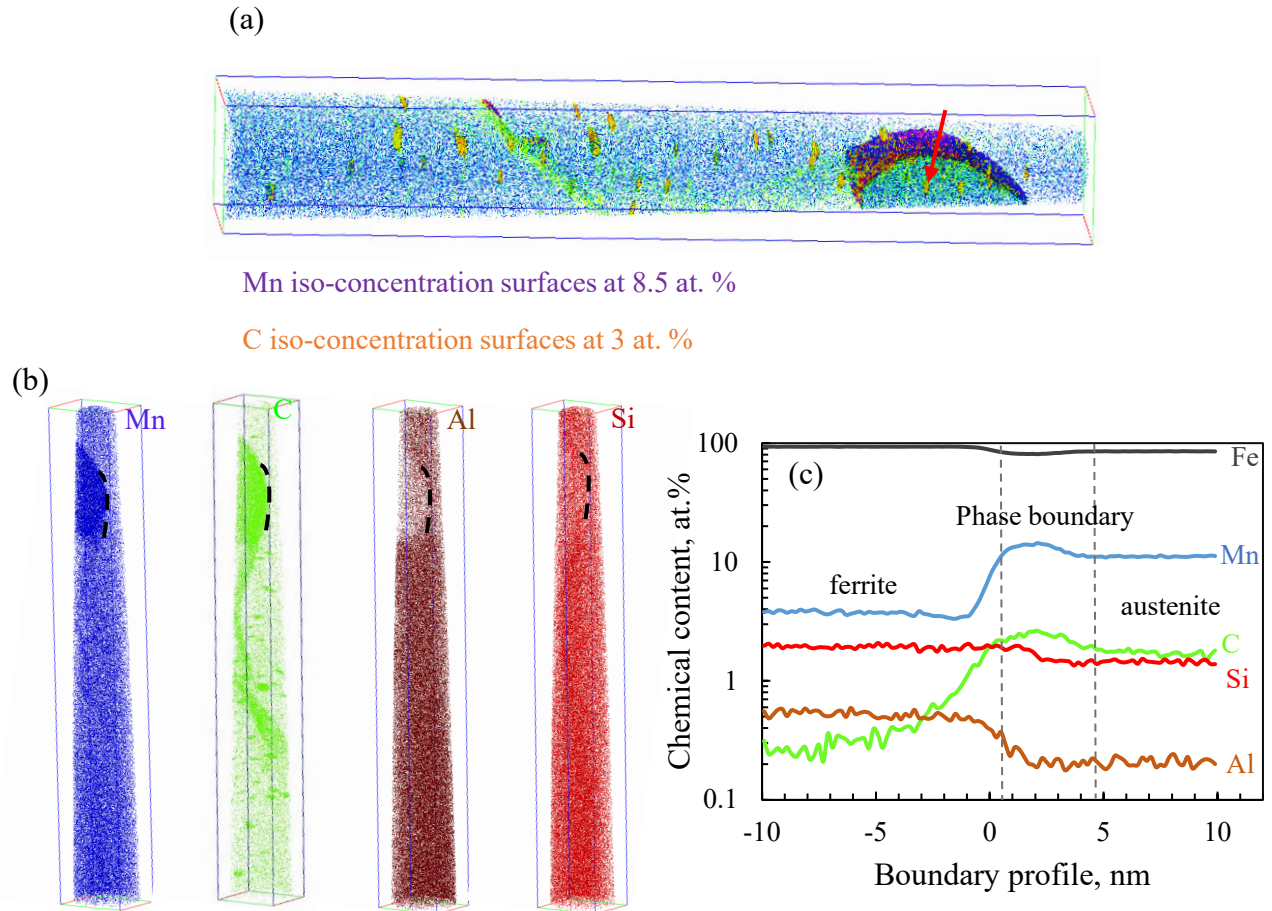


Figure 5.2: Experimental APT of an intercritically annealed sample after 665 °C for 120s. (a) atomic map section showing ferrite, austenite, and cementite regions, where C atoms are given in green and Mn atoms in blue. The orange and purple iso-surfaces indicated 3 at. % C and 8.5 at. % Mn, respectively. (b) experimental APT results show an interface through the APT reconstruction. C atoms (green) are enriched in precipitates in the ferrite. Precipitate-free austenite is bordered by a plate-like zone that is characterized by strong C and Mn enrichment (blue) and Al (brown) and Si (red) depletion. Black dotted lines indicate the suggested position of the phase boundary between ferrite and austenite. (c) concentration profiles for all elements across the ferrite/austenite phase boundaries.

#### 5.4.2 Dilatometry

The dilatometric plots for the two IA treatments at 665 °C and 710 °C for 240 s are presented in Figure 5.3. In the intercritical region, a noticeable strain contraction is observed, indicating the formation of intercritical austenite within the ferritic matrix during isothermal

holding. It should be noted that this contraction becomes more pronounced with increasing intercritical annealing temperature (IAT). Upon analyzing Figure 5.3 a and Figure 5.3b, it becomes evident that austenite formation occurs during heating, marked by deviations from linear behavior in the heating range. Consequently, the austenite vol% has been calculated based on extrapolated dashed lines originating from lower-temperature segments. This approach aimed to provide a more accurate estimation of the total austenite volume fraction [9]. After the isothermal hold, the sample was quenched at  $10\text{ }^{\circ}\text{C}\cdot\text{s}^{-1}$ . The measured austenite vol % during isothermal holding at  $665\text{ }^{\circ}\text{C}$  and  $710\text{ }^{\circ}\text{C}$  are discussed in § 5.4.3 along with the predicted amount of austenite by DICTRA.

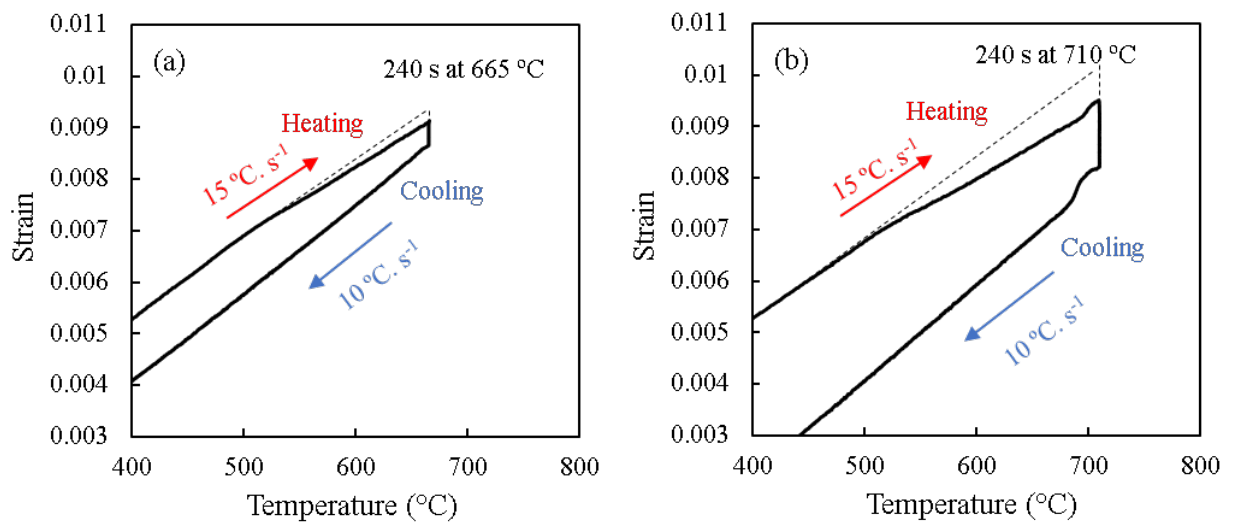


Figure 5.3: Dilatometric strain variations in austenite after a 240 s intercritical annealing at (a)  $665\text{ }^{\circ}\text{C}$  and (b)  $710\text{ }^{\circ}\text{C}$ .

### 5.4.3 HEXRD

#### 5.4.3.1 *Austenite Transformation Kinetics*

Examples of diffraction patterns obtained during the thermal cycle are presented in Figure 5.4. In all the experiments, only two phases were detected in the diffraction patterns: an FCC phase corresponding to austenite, and a BCC phase corresponding to either martensite or ferrite. Due to the relatively small c-axis distortion associated with low C steels, ferrite and martensite are difficult to distinguish. It is also important to note that no peaks from cementite were detected on the diffractograms due to the low volume fraction of cementite. As illustrated in Figure 5.4b,

the austenite fraction is relatively small during heating, but it significantly increases during isothermal holding. In contrast, a substantial amount of austenite remains during cooling, highlighting the chemical stability of the RA.

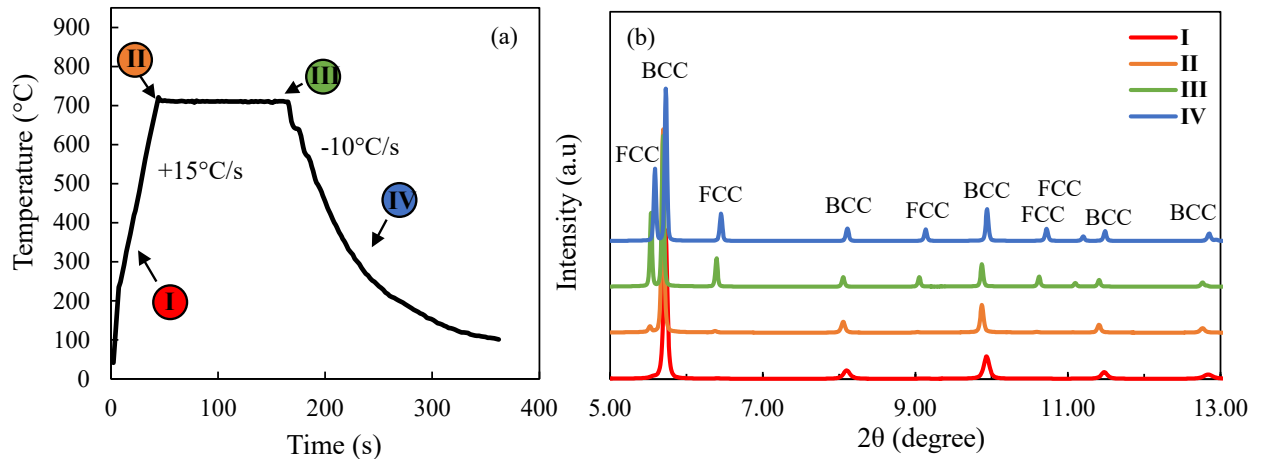


Figure 5.4: The changes over time of (a) experimental thermal cycle (b) and 1D diffractograms obtained at the selected times during heating (time=11 s), at the start of isothermal holding, end of isothermal holding, cooling (just above the  $M_s$  temperature of 300 °C) for intercritical annealing at 710 °C for 120 s.

Figure 5.5 shows the change in austenite vol % with temperature and time for samples subjected to IATs of 665 °C and 710 °C. Each figure shows a comprehensive thermal cycle, commencing from room temperature at the start time of 0 s, progressing through heating towards the isothermal hold temperatures, and ending with cooling to room temperature. This thermal cycle is highlighted by arrows in Figure 5.5a. As can also be seen in Figure 5.5b, the cooling rate was not constant due to furnace limitations. From IAT to 400 °C, the cooling rate was close to 10 °Cs<sup>-1</sup> and then gradually decreased. From Figure 5.5a and Figure 5.5b, it is evident that continuous heating to the IAT did not result in a significant increase in austenite vol%. The austenite vol % exhibits a rise during intercritical annealing (IA), reaching a maximum value of 26% at 665 °C and 41% at 710 °C after isothermal holding for 240 s (Figure 5.5). For the 665 °C IAT, the austenite fraction steadily increases with time, whereas at 710 °C, it reaches a plateau at approximately 180 s, displaying saturation (Figure 5.5b). After cooling to room temperature, the amount of austenite was reduced to approximately 22% and 36% for the 665 °C and 710 °C samples, respectively. The equilibrium vol% predicted using Thermo-Calc and the TCFel2

database is indicated as dotted lines in Figure 5.5b, stand at 34% for the 665 °C IAT and 41% for the 710 °C IAT. The calculated equilibrium value at 710 °C closely aligns with the measured IA austenite value at 240 s, while the measured IA austenite value at the 665 °C IAT did not reach the calculated equilibrium value.

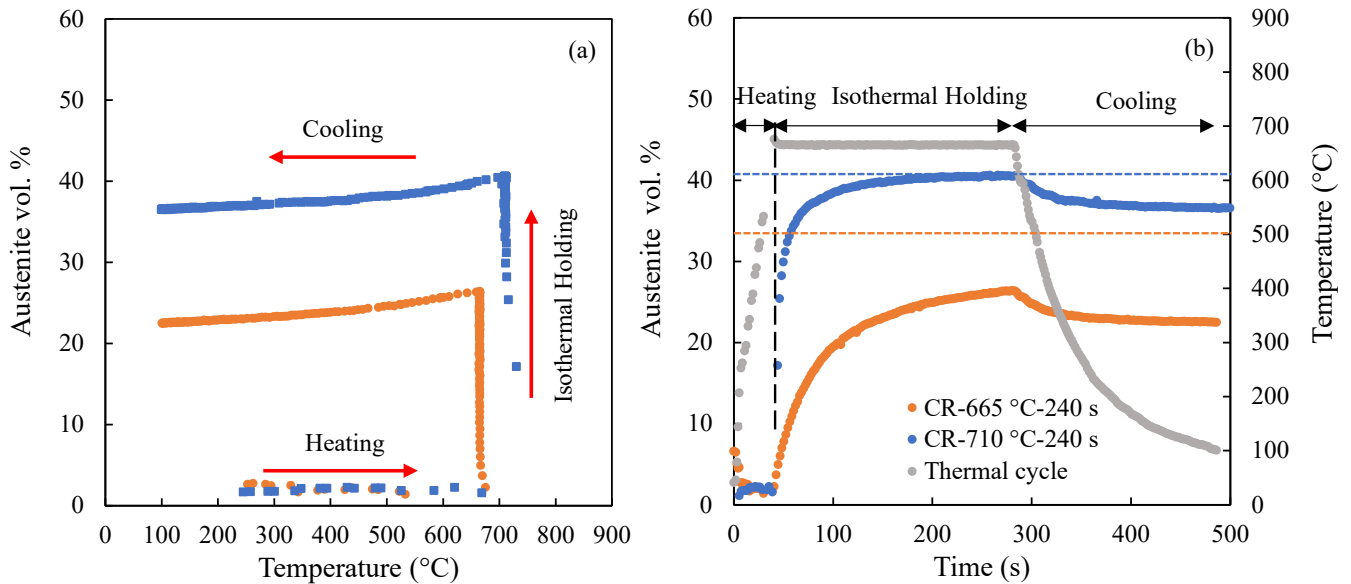


Figure 5.5: Measured HEXRD austenite vol % as a function of (a) temperature and (b) time. The arrows indicate data obtained through the thermal cycle from heating, isothermal holding, and cooling. Dotted lines in (b) show the equilibrium vol % of austenite during IA at 665 °C and 710 °C.

Figure 5.6 compares the predicted austenite vol % (dotted lines) as a function of time at 665 °C (orange) and 710 °C (blue), with the experimentally determined austenite vol % measured by HEXRD (solid lines) and dilatometry (dashed lines). The DICTRA simulation results exhibit good quantitative agreement with the measured austenite vol.% at 665 °C and 710 °C IATs. As depicted in the Figure 5.6, the DICTRA simulation results are within 5% of the measured values. The simple diffusion model in DICTRA has been utilized to predict the overall kinetics without modifying the diffusion coefficient of substitutional alloying elements in ferrite.

Furthermore, both dilatometry-measured and DICTRA-calculated values exhibit similar trends (shape of the curve) for the austenite vol % at 665 °C and 710 °C IATs with respect to isothermal holding time. However, a slight difference is observed between the dilatometry and HEXRD analyses performed regarding the level of austenite present at 710 °C IAT.

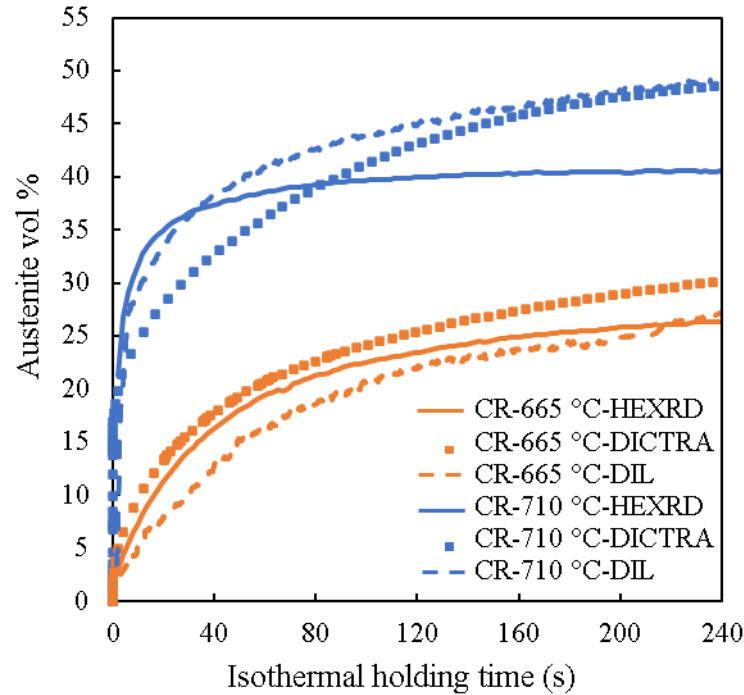


Figure 5.6: Austenite vol % during isothermal holding at 665 °C and 710 °C as determined using *in situ* HEXRD (solid lines) compared to DICTRA simulations (dotted lines) and dilatometry results (dashed lines) up to 240 s.

#### 5.4.3.2 Austenite Lattice Parameter

Figure 5.7 represents the measured austenite lattice parameter normalized by the value determined at the beginning of heating as a function of time at 665 °C and 710 °C. It shows that, during heating, the lattice constant of austenite increases approximately linearly due to thermal expansion. The lattice parameter of austenite exhibits a decrease throughout the holding period at 665 °C and 710 °C. The decrease in lattice parameter during holding is particularly noticeable at 710 °C. The normalized lattice parameter of austenite decreases from 1.014 at the beginning of the isothermal hold to 1.011 during the 665 °C hold and from 1.015 to 1.013 during isothermal holding at 710 °C. Upon cooling to room temperature, the lattice parameter decreases as a result of thermal contraction. At 665 °C, the austenite lattice parameter does not exhibit a saturated value by the end of holding, aligning with the transformation kinetics (Figure 5.5b). Transformations persist throughout the entire duration without attaining a real stasis. In contrast, for the 710 °C IAT, saturation becomes evident as the austenite lattice parameter becomes

constant at approximately 180 s. The normalized lattice parameter of austenite during holding at 665 °C is higher compared to that at 710 °C. This difference is attributed to less C enrichment in intercritical annealed austenite at 710 °C, as C partitioning occurs more rapidly at higher temperatures.

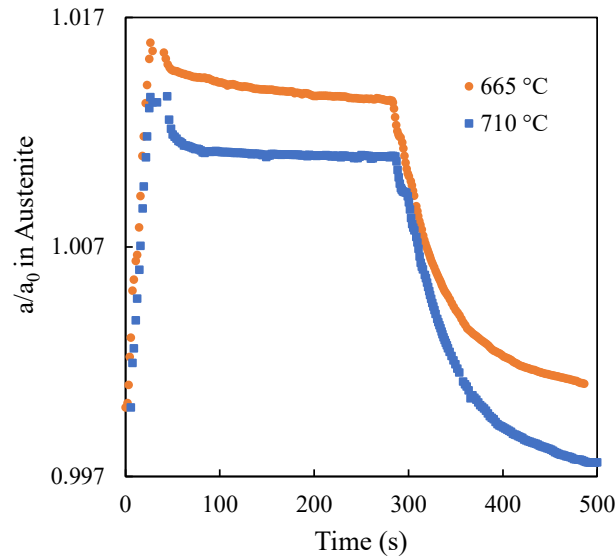


Figure 5.7: Normalized lattice parameters as a function of time during the heating and isothermal holdings at 665 °C and 710 °C: (a) austenite and (b) ferrite/ martensite. The rescaled versions are added to the plots to show a clearer trend of lattice constant change during holding.

#### 5.4.4 Concentration Profile Simulations by DICTRA

Concentration profiles for the different alloying elements across the Cementite/ferrite/austenite interfaces, after annealing at 665 °C for time increments of 0.1 s, 10 s, 120 s and 240 s are shown in Figure 5.8. For each profile, the vertical line shows the interface position of the cementite-ferrite and ferrite-austenite from left to right. The enrichment of C and Mn and the depletion of Al at the austenite interface (Figure 5.8) are in good agreement with the experimentally measured APT concentration profiles presented in Figure 5.2c.

The C profiles at four different time steps during isothermal holding at 665 °C are depicted in Figure 5.8a, showing the distribution in cementite, ferrite, and austenite. To better visualize the gradient of carbon in ferrite and austenite, wide views of the C concentration profile are provided in Figure 5.9a and b, respectively. As the holding time increases, the width of

austenite expands. Additionally, there are variations in the C content of ferrite and austenite over time or position, as depicted in Figure 5.9 a and b, respectively. It's important to note that the dissolution of cementite plays a crucial role in accelerating the growth rate of austenite. The required C content for austenite growth is provided by cementite dissolution, diffusing through ferrite into austenite.

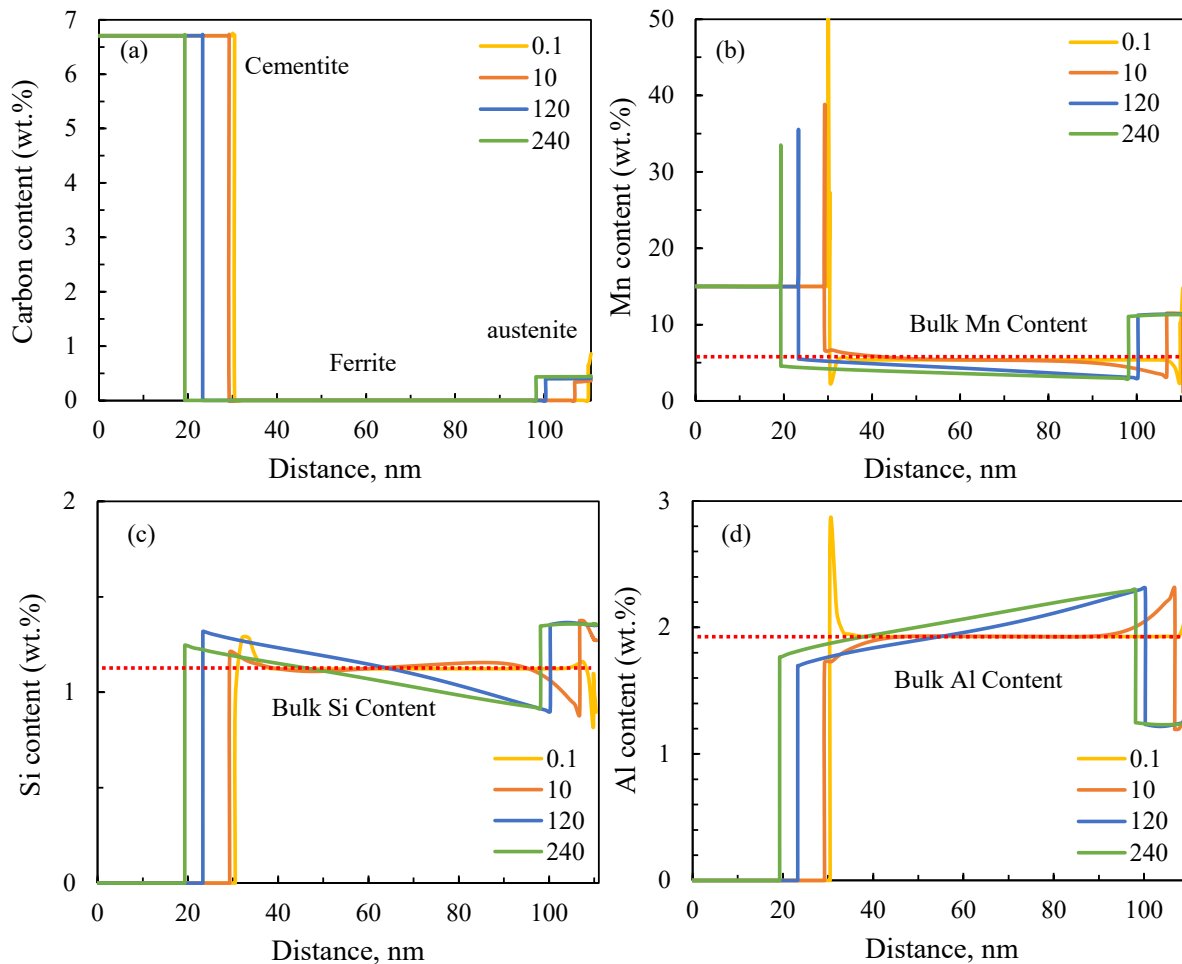


Figure 5.8: Concentration profiles of (a) C, (b) Mn, (c) Si, and (d) Al at various time-steps during isothermal holding at 665 °C.

Wide views of the Mn concentration profile near the  $\theta$ - $\alpha$  interface are shown in Figure 5.9c and near the  $\alpha$ - $\gamma$  interface in Figure 5.9d. Figure 5.9d indicates an enrichment of Mn in austenite. , Figure 5.9c shows that Mn enrichment is also happening in cementite. Between the timesteps of 120 s and 240 s, Figure 5.9d indicates a significant increase in the austenite layer, which also correlate with a decrease in the cementite width shown in Figure 5.9c, indicating how

cementite dissolution has a significant effect on the austenite growth. The Mn distribution in Figure 5.9d illustrates the Mn partitioning to cementite. Because Mn diffusivity is lower in cementite than ferrite, partitioning of Mn causes an increase in the Mn concentration in cementite near the cementite-ferrite interface.

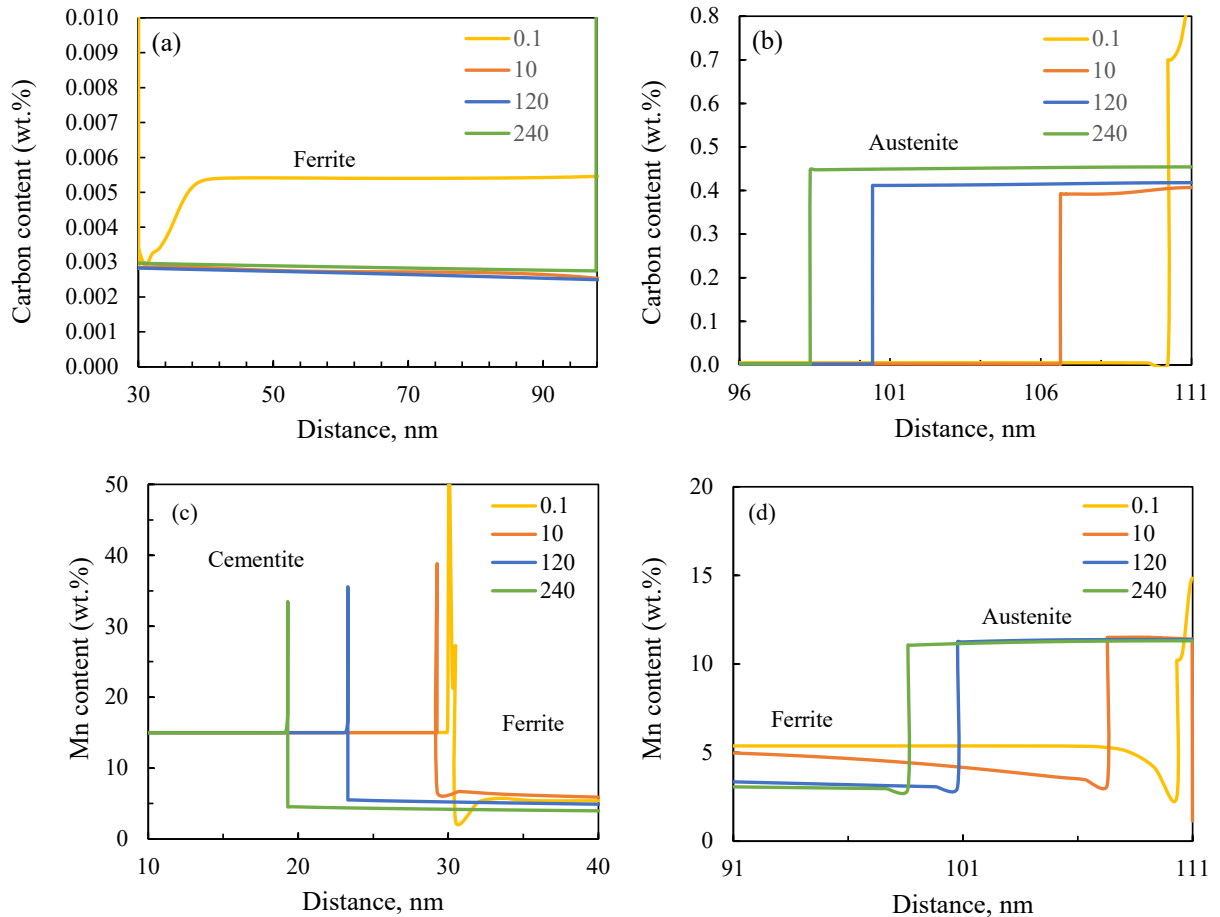


Figure 5.9: Wide distribution of (a) C in  $\alpha$  and (d) C in  $\gamma$ , and (c) Mn near the  $\theta$ - $\alpha$  interface and (d) Mn near the  $\alpha$ - $\gamma$  interface at different time-steps at 655 °C.

Concentration profiles for the different alloying elements across the austenite/ferrite interface, after annealing at 710 °C for time increments of 0.1 s, 10 s, 120 s and 240 s are shown in Figure 5.10, respectively. The enrichment of C and Mn and the depletion of Al at the austenite interface can be seen in Figure 5.8 and Figure 5.10. The Mn profile (Figure 5.8b, Figure 5.10b) at 0.1 s shows negligible partitioning of Mn in the austenite associated with non-partitioning local equilibrium (NPLE) austenite growth. Under NPLE, the concentration spike of Mn can be seen across the interface. As a result of the negligible partitioning of Mn, the Mn concentration

in austenite and ferrite is constant, apart from Mn spike caused by the local equilibrium conditions. These Mn spikes have been observed [8,18,19] in steels with 2, 5, and 6 wt. % Mn, respectively. The Al profiles show negative spike/solute depletion at 665 °C and 710 °C, as shown in Figure 5.8d, 10d. It can be seen that C content of austenite decreases by half as the holding time increases (Figure 5.10a). As the C content in austenite decreases, the lattice parameter is expected to decrease accordingly (Figure 5.7) [8].

The austenite growth is controlled by the diffusion of the substitutional elements in ferrite/martensite for longer times ( $\geq 10$ s). In Figure 5.8 and Figure 5.10, the partitioning of Mn from ferrite to austenite and Al from austenite to ferrite can be observed, aligning with expectations. Unexpectedly, Si appears to be enriched in austenite, a result attributed to the thermodynamic database (TCFE12), which predicts Si partitioning into austenite for this particular alloy composition and temperature. Similar trend was observed during intercritical annealing at 710 °C in the same alloy composition [8].

At the longest holding time (240 s), the substitutional solute profiles in austenite overlap. It was observed that the austenite volume percentage reaches equilibrium after intercritical annealing at 710 °C for 240 seconds (Figure 5.5b). Therefore, there is no shrinkage in the austenite phase, and its growth occurs in only two stages.

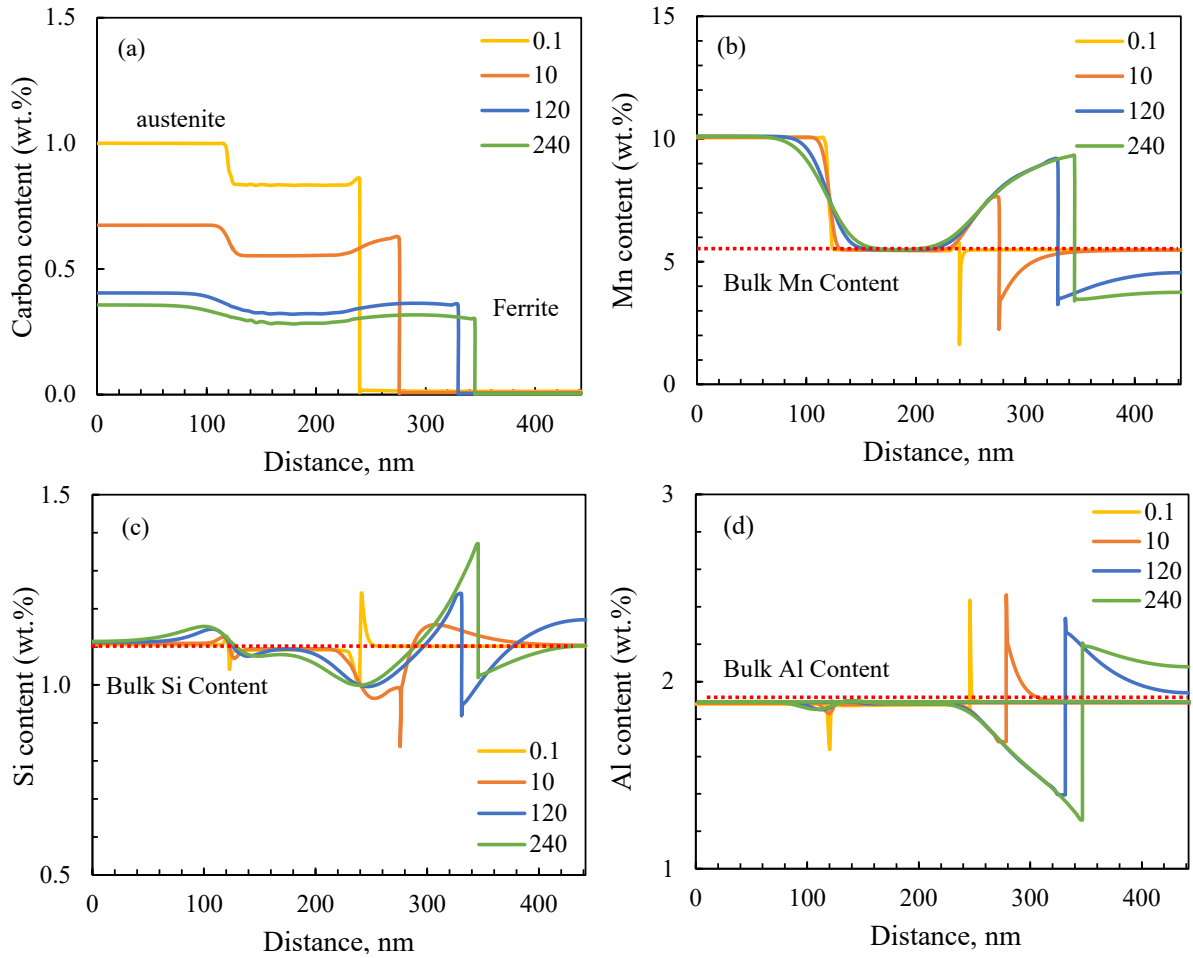


Figure 5.10: Concentration profiles of (a) C, (b) Mn, (c) Si, and (d) Al at various time-steps during isothermal holding at 710 °C.

## 5.5 Discussion

The *in situ* HEXRD methods were performed on med-Mn steel with a cold-rolled starting microstructure to determine the austenite vol % and lattice parameter during isothermal holding at 665 °C and 710 °C. The results are shown in Figure 5.6 in comparison to DICTRA simulations (represented as dashed lines) and dilatometer tests (represented as dotted lines). The transformation from Cementite/ferrite to austenite at IAT of 665 °C and from ferrite at IAT of 710 °C was examined. Figure 5.6 illustrates that the overall kinetics obtained from HEXRD, dilatometry, and DICTRA are in qualitative agreement at 665 °C and 710 °C. The simple diffusion model in DICTRA has been utilized to predict the overall kinetics without modifying the diffusion coefficient of substitutional alloying elements in ferrite. The mobility factor of

substitutional alloying elements remained unchanged. However, in other studies comparing DICTRA simulations to experimental results [20], a mobility factor of 45 was found to provide good agreement between simulation and experimental data.

The vol % of RA at room temperature was measured to be 22% and 36% at 665 °C and 710 °C IAT, respectively. On the other hand, the vol % of austenite was 26% and 41% at 240 s for the 665 °C and 710 °C IATs, respectively, prior to cooling (Figure 5.5). This implies that only ~4% and ~5% of the austenite underwent transformation during quenching. Additionally, while the measured IA austenite vol % reached the calculated equilibrium at 710 °C, it did not attain the equilibrium value at the 665 °C IAT. In another study [21] that conducted detailed kinetic studies of austenite formation from cementite-ferrite microstructures in a range of Fe-C-Mn-Si/Al alloys, similar observations were reported. The study highlighted that the incomplete dissolution of cementite may lead to the plateauing of austenite fraction below equilibrium, while the rapid dissolution of cementite could result in an austenite fraction plateau at or above equilibrium.

From Figure 5.7, it is evident that the lattice parameter of austenite decreases during holding at 665 °C and 710 °C. The decrease in the lattice parameter during isothermal holding is attributed to the decrease in the C content of austenite. As the average C content of austenite decreases, the lattice parameter would also decrease, as shown in Figure 5.8a and Figure 5.9b.

Microstructural observations of this alloy [1] showed the presence of cementite in the cold-rolled sample annealed at 665 °C for 120 s, suggesting that some cementite formed during heating. The dissolution of cementite was observed to be slow at 665 °C [1]. As a result, cementite dissolution had to be considered when modeling the growth of austenite at this temperature. Consequently, the employed model configuration at 665 °C involves a single cementite particle that dissolves into ferrite, providing C for the growth of austenite grains. Additionally, all of the cementite particles examined by TEM were found to be enriched in Mn [1]. The concentration profile in Figure 5.8b demonstrates that the nucleation and growth of austenite are predominantly controlled by Mn partitioning, aligning with simulation predictions for Mn enrichment in austenite. These findings suggest that the transformation is almost immediately controlled by the diffusion of substitutional elements in ferrite. Similar behavior in austenite growth has been reported in a study on intercritical annealing of Fe-0.19C-4.39Mn steel

[2], indicating that the presence of cementite results in austenite growth with a more uniform Mn concentration as cementite gradually dissolves, as depicted in Figure 5.8b.

On the other hand, very little cementite is present at 710 °C, indicating that the cementite particles dissolve quickly at this temperature. The simulations focused primarily on the growth of austenite into supersaturated ferrite. The austenite growth kinetics contains an initial stage which is controlled by carbon diffusion, followed by a second stage which is controlled by the diffusion of the substitutional elements in ferrite (Figure 5.10) [1].

Finally, it is worth commenting on the Si concentration profiles that were calculated using DICTRA. Figure 5.8c and Figure 5.10c indicate that the Si profile shows Si depletion in ferrite. Although Si is known to be a ferrite stabilizer [20,22,23], the TCFE12 database predicts that for some conditions and temperatures, Si can partition to austenite. Mehrabi et al. [8] evaluated the accuracy of the database through direct experimental measurements of the Si profile after intercritical annealing at 710 °C for nearly a year. The findings indicated weak Si enrichment in ferrite. The non-significant effect of Si on austenite growth kinetics was reported, as there was no notable gradient of Si in either ferrite or austenite.

## 5.6 Conclusions

Advanced *in situ* HEXRD analyses were performed on a med-Mn steel with a cold-rolled starting microstructure to monitor austenite growth during intercritical annealing. Austenite growth and solute partitioning during intercritical annealing were modeled using DICTRA™ and compared to *in situ* HEXRD and dilatometry measurements. The study results lead to the following conclusions:

- 1) The simulation with cementite showed that austenite formation began with Mn diffusion through ferrite and proceeded with cementite dissolution. This finding supports the idea that the presence of cementite results in austenite growth with a more uniform Mn concentration as cementite gradually dissolves.
- 2) Austenite growth exhibits two stages: initially controlled by rapid C diffusion, followed by Mn diffusion in ferrite.
- 3) With the exception of Si, the APT measurement aligns with thermodynamic predictions for the partitioning of the substitutional alloying elements at the interface.
- 4) The simple diffusion model in DICTRA has been employed to predict the overall kinetics without

enhancing the diffusion coefficient of substitutional alloying in ferrite.

- 5) The overall kinetics from HEXRD, dilatometry, and DICTRA are qualitatively consistent at 665 °C and 710 °C.
- 6) At the end of the intercritical annealing cycle, the vol % of RA in the microstructures was measured as 22% and 36% for the 665 °C and 710 °C IAT, respectively. Before cooling, the vol % of austenite stood at 26% and 41% at 240 s for the 665 °C and 710 °C IATs, respectively. This suggests that only ~4 vol % and ~5 vol % of the intercritical austenite transformed to fresh martensite during quenching.

### **5.7 Acknowledgements**

The authors express their gratitude to the Canadian Light Source (CLS), Canada's national synchrotron light source facility in Saskatoon, Saskatchewan. Special thanks to Drs. King and Rahemtulla, scientists at the Brockhouse Diffraction Sector, for their valuable assistance with HEXRD experiments, and to Dr. Imed-Eddine Benrabah for his valuable assistance with HEXRD data analysis.

This work received financial support from the International Zinc Association Galvanized Autobody Partnership (IZA-GAP) and the Natural Sciences and Engineering Research Council of Canada (NSERC grant CRDPJ 522309 – 17). The experimental steel was provided by U.S. Steel Research and Development (Munhall, PA, USA). Atom probe tomography and EBSD were conducted at the Canadian Centre for Electron Microscopy (CCEM), a core research facility of McMaster University (also supported by NSERC and other government agencies).

### **5.8 References**

- [1] A. Mehrabi, J.R. McDermid, X. Wang, H. Zurob, Austenite Nucleation and Growth as a Function of Starting Microstructure for a Fe–0.15C–5.56Mn–1.1Si–1.89Al Medium-Mn Steel, *Steel Res. Int.* 94 (2023) 2200952. <https://doi.org/10.1002/srin.202200952>.
- [2] J.J. Mueller, X. Hu, X. Sun, Y. Ren, K. Choi, E. Barker, J.G. Speer, D.K. Matlock, E. De Moor, Austenite formation and cementite dissolution during intercritical annealing of a medium-manganese steel from a martensitic condition, *Mater. Des.* 203 (2021) 109598. <https://doi.org/10.1016/j.matdes.2021.109598>.

- [3] S.J. Lee, S. Lee, B.C. De Cooman, Mn partitioning during the intercritical annealing of ultrafine-grained 6% Mn transformation-induced plasticity steel, *Scr. Mater.* 64 (2011) 649–652. <https://doi.org/10.1016/j.scriptamat.2010.12.012>.
- [4] S.J. Lee, S. Lee, B.C. De Cooman, Martensite transformation of sub-micron retained austenite in ultra-fine grained manganese transformation-induced plasticity steel, *Int. J. Mater. Res.* 104 (2013) 423–429. <https://doi.org/10.3139/146.110882>.
- [5] F. Moszner, E. Povoden-Karadeniz, S. Pogatscher, P.J. Uggowitzer, Y. Estrin, S.S.A. Gerstl, E. Kozeschnik, J.F. Löffler, Reverse  $\alpha' \rightarrow \gamma$  transformation mechanisms of martensitic Fe-Mn and age-hardenable Fe-Mn-Pd alloys upon fast and slow continuous heating, *Acta Mater.* 72 (2014) 99–109. <https://doi.org/10.1016/j.actamat.2014.03.032>.
- [6] K. Steineder, R. Schneider, D. Krizan, C. Béal, C. Sommitsch, Comparative investigation of phase transformation behavior as a function of annealing temperature and cooling rate of two medium-mn steels, *Steel Res. Int.* 86 (2015) 1179–1186. <https://doi.org/10.1002/srin.201400551>.
- [7] D.M. Pallisco, J.R. McDermid, Mechanical property development of a 0.15C–6Mn–2Al–1Si third-generation advanced high strength steel using continuous galvanizing heat treatments, *Mater. Sci. Eng. A.* 778 (2020) 139111. <https://doi.org/10.1016/j.msea.2020.139111>.
- [8] A. Mehrabi, H. Zurob, I. E. Benrabah, J. R. McDermid, Austenite formation in a medium-Mn steel during intercritical annealing via in situ high-energy X-ray diffraction, *J. Mater. Res. Technol.* (2024).
- [9] R. Wei, M. Enomoto, R. Hadian, H.S. Zurob, G.R. Purdy, Growth of austenite from as-quenched martensite during intercritical annealing in an Fe-0.1C-3Mn-1.5Si alloy, *Acta Mater.* 61 (2013) 697–707. <https://doi.org/10.1016/j.actamat.2012.10.019>.
- [10] J. Rodriguez-carvajal, Recent advances in magnetic structure determination neutron powder diffraction by neutron powder diffraction, *Phys. B.* 192 (1993) 55–69.

- [11] Y. Lu, H. Yu, R.D. Sisson, The effect of carbon content on the c/a ratio of as-quenched martensite in Fe-C alloys, *Mater. Sci. Eng. A.* 700 (2017) 592–597. <https://doi.org/10.1016/j.msea.2017.05.094>.
- [12] N. Maruyama, S. Tabata, H. Kawata, Excess Solute Carbon and Tetragonality in As-Quenched Fe-1Mn-C (C:0.07 to 0.8 Mass Pct) Martensite, *Metall. Mater. Trans. A.* 51A (2020) 1085–1097. <https://doi.org/10.1007/s11661-019-05617-y>.
- [13] L. Xiao, Z. Fan, Z. Jinxiu, Z. Mingxing, K. Mokuang, G. Zhenqi, Lattice-parameter variation with carbon content of martensite. I. X-ray-diffraction experimental study, *Phys. Rev. B.* 52 (1995) 9970–9978. <https://doi.org/10.1103/PhysRevB.52.9970>.
- [14] J.O. Andersson, T. Helander, L. Höglund, P. Shi, B. Sundman, Thermo-Calc & DICTRA, computational tools for materials science, *Calphad.* 26 (2002) 273–312. [https://doi.org/10.1016/S0364-5916\(02\)00037-8](https://doi.org/10.1016/S0364-5916(02)00037-8).
- [15] K.M.H. Bhadhon, X. Wang, E.A. McNally, J.R. McDermid, Effect of Intercritical Annealing Parameters and Starting Microstructure on the Microstructural Evolution and Mechanical Properties of a Medium-Mn Third Generation Advanced High Strength Steel, *Metals (Basel).* 12 (2022) 356. <https://doi.org/10.3390/met12020356>.
- [16] K.M.H. Bhadhon, X. Wang, J.R. McDermid, Effects of CGL-compatible thermal processing, starting microstructure, and Sn micro-alloying on the mechanical properties of a medium-Mn third generation advanced high strength steel, *Mater. Sci. Eng. A.* 833 (2022) 142563. <https://doi.org/10.1016/j.msea.2021.142563>.
- [17] P.J. Jacques, S. Allain, O. Bouaziz, A. De, A.F. Gourgues, B.M. Hance, Y. Houbaert, J. Huang, A. Iza-Mendia, S.E. Kruger, M. Radu, L. Samek, J. Speer, L. Zhao, S. Van der Zwaag, On measurement of retained austenite in multiphase TRIP steels results of blind round robin test involving six different techniques, *Mater. Sci. Technol.* 25 (2009) 567–574. <https://doi.org/10.1179/174328408X353723>.

- [18] X. Zhang, G. Miyamoto, T. Kaneshita, Y. Yoshida, Y. Toji, T. Furuhashi, Growth mode of austenite during reversion from martensite in Fe-2Mn-1.5Si-0.3C alloy: A transition in kinetics and morphology, *Acta Mater.* 154 (2018) 1–13. <https://doi.org/10.1016/j.actamat.2018.05.035>.
- [19] H.W. Luo, C.H. Qiu, H. Dong, J. Shi, Experimental and numerical analysis of influence of carbide on austenitisation kinetics in 5Mn TRIP steel, *Mater. Sci. Technol.* 30 (2014) 1367–1377. <https://doi.org/10.1179/1743284713Y.0000000447>.
- [20] O. Dmitrieva, D. Ponge, G. Inden, J. Millán, P. Choi, J. Sietsma, D. Raabe, Chemical gradients across phase boundaries between martensite and austenite in steel studied by atom probe tomography and simulation, *Acta Mater.* 59 (2011) 364–374. <https://doi.org/10.1016/j.actamat.2010.09.042>.
- [21] Y.X. Wu, L.Y. Wang, W.W. Sun, M.J. Styles, A.J. Studer, Y. Bréchet, A. Arlazarov, C.R. Hutchinson, Austenite formation kinetics from multicomponent cementite-ferrite aggregates, *Acta Mater.* 196 (2020) 470–487. <https://doi.org/10.1016/j.actamat.2020.07.001>.
- [22] Z. Dai, H. Chen, R. Ding, Q. Lu, C. Zhang, Z. Yang, S. van der Zwaag, Fundamentals and application of solid-state phase transformations for advanced high strength steels containing metastable retained austenite, *Mater. Sci. Eng. R.* 143 (2021) 100590. <https://doi.org/10.1016/j.mser.2020.100590>.
- [23] B. Sun, F. Fazeli, C. Scott, N. Brodusch, R. Gauvin, S. Yue, The influence of silicon additions on the deformation behavior of austenite-ferrite duplex medium manganese steels, *Acta Mater.* 148 (2018) 249–262. <https://doi.org/10.1016/j.actamat.2018.02.005>.

## **6 Process Maps for Predicting Austenite Fraction in Medium-Mn Third-Generation Advanced High Strength Steels**

Azin Mehrabi, Hatem S. Zurob \* and Joseph R. McDermid

Department of Materials Science and Engineering, McMaster University, 1280 Main Street West, Hamilton, Ontario, Canada, L8S 4L8

*Materials*, 2024, vol. 17, 993.

### **6.1 Abstract**

Process maps were developed using a combination of microstructural analysis and DICTRA-based modeling to predict the austenite vol.% as a function of the intercritical annealing parameters and starting microstructure. The maps revealed a strong dependence of the calculated austenite fraction (vol.%) on the Mn content (4–12 wt.%) and intercritical annealing temperatures (600 °C to 740 °C). The calculations were carried out for constant carbon, Al, and Si contents of 0.2 wt.%, 1.5 wt.%, and 1.0 wt.%, respectively. A modified empirical equation proposed by Koistinen and Marburger was employed to calculate the room-temperature retained austenite vol.% as a function of the intercritical annealing temperature, including the effect of the austenite composition. The process maps offer valuable insights for designing intercritical treatments of medium-Mn steels, aiding in the optimization of steel properties for automotive applications.

### **6.2 Introduction**

There is an increasing demand for high-strength steels in the automotive industry in order to enable weight reduction and improved collision resilience [1]. This has led to the development of advanced high-strength steels (AHSS) with excellent strength and formability characteristics. In recent decades, considerable efforts have been dedicated to enhancing the mechanical properties of these steels by optimizing the composition and thermomechanical processing [2,3]. Austenitic, second-generation steels with Mn contents in the range of 17 to 30%, received a lot of attention in the 1990s and 2000s due to their superior balance of strength and elongation.

However, their engineering applications have been limited owing to high alloying costs and production problems [4].

More recently, much attention has been paid to AHSS with medium Mn (med-Mn) addition [5–7]. Med-Mn steels generally contain 0.05–0.4 wt.% C, 4–12 wt.% Mn, 0.5–3 wt.% Al, 0.5–2 wt.% Si, and small amounts of micro-alloying elements, such as Mo, Ti, V, and Nb [8–10]. Med-Mn steels typically have a complex microstructure consisting of ferrite and/or martensite, and 20–50 vol.% retained austenite (RA). The presence of retained austenite is important for enhancing the mechanical properties of med-Mn steel due to the transformation-induced-plasticity (TRIP) effect. In these steels, the higher concentrations of Mn result in retaining a considerable fraction of intercritical austenite and by consequence a desirable strength–ductility balance [11–14]. One of the first reported results on the effect of increasing alloy Mn concentration is attributed to Miller in the 1970s [15]. It was reported that a high UTS of 1150 MPa with a uniform elongation over 25% could be achieved for a cold rolled 0.1C-6Mn alloy after annealing at 640 °C for 1 h. This was attributed to the high fractions of metastable RA which transformed to martensite during deformation.

In the processing of med-Mn TRIP steels, the formation of austenite primarily occurs through intercritical annealing (IA). During IA, the controlled partitioning of C and Mn into the austenite increases its chemical stability, leading to the partial retention of austenite at room temperature. The volume fraction of intercritical austenite increases with increasing annealing temperature. Increasing the intercritical temperature, however, decreases the average C and Mn contents of the intercritical austenite and, as a result, reduces its chemical stability. As a result, significant fractions of the austenite formed at higher intercritical temperatures transform to martensite during cooling [16–18]. The optimum annealing temperature is determined by achieving the desired balance between the volume fraction and the stability of the austenite [19]. Designing precise alloying and processing strategies is critical to control the volume fraction of RA and, consequently, the mechanical properties of the steel.

It is important to note that steels destined for automotive applications must be corrosion-resistant as they can be exposed to aggressive environments—e.g., roads with heavy loads of de-icing salts. Continuous galvanizing lines (CGLs) play an important role in providing this

corrosion protection in automotive steel manufacturing due to their high production capacity and cost-effectiveness. It is, therefore, necessary to integrate med-Mn steels into the automotive industry with thermal processing parameters compatible with industrial CGL processing windows. The continuous galvanizing process is described in detail in [20]. The steel undergoes a short thermal treatment, typically lasting 3–5 min depending on the line speed, in the radiant tube heating and soaking sections of the CGL. To meet the CGL's productivity targets, the annealing parameters must fall within this time range while achieving the desired microstructures and mechanical properties. Although several studies [21–25] have found that med-Mn steels can achieve 3G AHSS properties through intercritical annealing, the long thermal treatments employed in these studies are not compatible with the industrial CGL. For the present experimental alloy, significant volume fractions of chemically stable retained austenite were obtained after annealing at 710 °C for 120 s, which corresponds to continuous galvanizing industrial practices [26].

In the present study, we focus on developing process maps for the formation of austenite during IA. The maps were constructed using a combination of microstructural analysis and DICTRA-based modeling for different starting microstructures. The process maps are essential for determining the optimal IA parameters for med-Mn steels with specific chemical compositions. This knowledge is crucial for further development of the steel properties to meet the requirements of automotive applications. Also, a modified calculation method [27] is used to predict the room temperature retained austenite fraction as a function of the IA temperature. Additionally, the optimal annealing temperature range to achieve the desired balance between the volume fraction and the stability of the retained austenite in med-Mn steels has been suggested.

## **6.3 Overview of Models**

### **6.3.1 DICTRA-Based Model**

The DICTRA module of Thermo-Calc was used to model the austenite growth kinetics for both the as-cold-rolled condition with a tempered martensite (TM) microstructure and a fully austenitized and as-quenched martensite (M) starting microstructure, which is known to have more rapid austenite reversion kinetics [26,28] DICTRA is an engineering tool for diffusion-

based simulations in multicomponent alloys [29,30]. The software uses the Thermo-Calc thermodynamic (TCFE12) and mobility (MOBFE5) databases [29], which have been derived from assessed experimental data in the literature. The simulations are one-dimensional. DICTRA can accommodate planar, cylindrical, and spherical geometries, all of which can be reduced to a single space variable. In order to set up the simulations of austenite growth, the morphology, compositions, and size of phases are required. The diffusion of C, Mn, Si, and Al was considered in the simulation. The size of the simulation cell was based on the observed length scales within the TEM micrographs reported previously [26,28,31].

Two initial configurations were considered for the DICTRA simulation. In the case of the TM starting microstructure, austenite ( $\gamma$ ) nucleated at ferrite ( $\alpha$ ) grain boundaries, after cementite dissolution had taken place (Figure 6.1a) [31]. A total of 50 and 150 grid nodes were distributed in austenite and ferrite, respectively. In the case of the M starting microstructure, austenite grew from the existing inter-lath RA in martensite (Figure 6.1b) [31]. The selection of the simulation cell was guided by the half-width of a representative martensite lath from the initial microstructure. A total of 150 and 500 grid nodes were distributed in austenite and ferrite, respectively. Based on the experimental results, the concentration of C in austenite was determined to be 1.5 wt.% [32]. The Al and Si contents in austenite were assumed to align with the nominal alloy composition. The composition of ferrite was then determined based on the mass balance.

Martensite is not categorized as a separate phase in DICTRA. Thus, in common with others in the literature [33–37], the BCC phase with a high carbon content is utilized to represent martensite in the model. Throughout this study, both phases will be identified as  $\alpha$ .

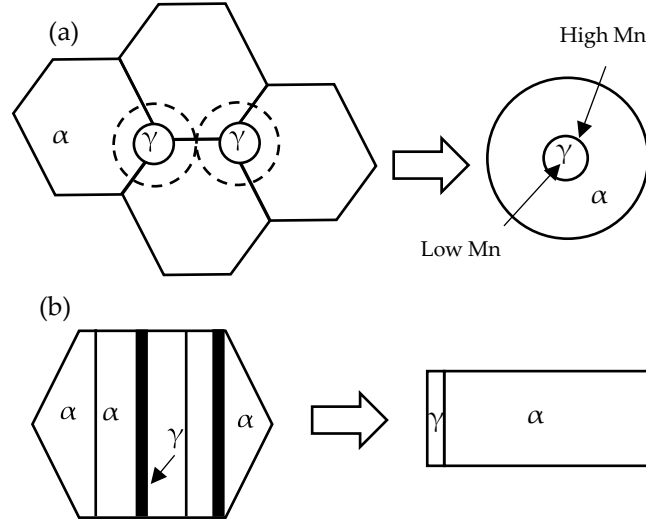


Figure 6.1: Schematic of initial microstructural configuration and resultant DICTRA geometry for austenite formation during heating: (a) TM starting microstructure— austenite nucleation on ferrite with dissolved cementite; and (b) M starting microstructure— austenite growth on ferrite (martensite) lath boundaries ( $\gamma$  = austenite,  $\alpha$  = ferrite). The arrows indicate regions containing high and low Mn contents. Dashed lines surrounding the  $\gamma$  phase represent the growth of austenite.

### 6.3.2 Koistinen–Marburger Model

The Koistinen and Marburger empirical formula [38] was used for calculating the volume fraction of RA:

$$f_y = \exp [-m(M_s - T)^n] \quad [1]$$

where  $f_y$  is the volume fraction of RA and  $T$  denotes the lowest temperature reached during quenching (in the present case, room temperature).  $m$  and  $n$  are coefficients linked to transformation kinetics.  $M_s$  is the martensite start temperature. The parameters  $m$  and  $n$  were adjusted as a function of the Mn and C content of the austenite in wt.% [39].

$$m = 0.0076 + 0.0182C - 0.00014Mn \quad [2]$$

$$n = 1.4609 + 0.4483C - 0.0545Mn \quad [3]$$

The martensite start ( $M_s$ ) temperature is determined by applying the following equation [39,40]:

$$M_s(^{\circ}C) = 545 - 423C - 30.4Mn - 7.5Si + 30Al - 60.5V_y^{-1/3} \quad [4]$$

where  $V_\gamma$  is the average grain volume of austenite in  $\mu\text{m}^3$ . The Mn, C, Si, and Al contents in wt.% were identified with those present on the austenite side of the interface after holding for 120 s at the intercritical annealing temperature.

Based on the experimental observations conducted on med-Mn steels [31], a fixed austenite grain size of 1  $\mu\text{m}$  was considered for the simulations.

The composition of the intercritical austenite at 120 s was calculated using the DICTRA module of Thermo-Calc. This composition was used to determine the values of  $m$ ,  $n$ , and the  $M_s$  temperature. The DICTRA simulations also provided the volume fraction of austenite as a function of IAT and holding time. The room temperature austenite fraction after quenching is expressed using:

$$f_{ret\ \gamma} = f_\gamma \times f_{D\ \gamma} \quad [5]$$

where  $f_{ret\ \gamma}$  is the retained austenite volume fraction at room temperature,  $f_\gamma$  is the volume fraction of austenite after quenching, as calculated by Eq. [1], and  $f_{D\ \gamma}$  is the austenite volume fraction at the IA temperature, as calculated by DICTRA.

The Mn, C, Si, and Al contents were determined using the DICTRA software version 2023.2.119013-24 and the MOB-FE5 mobility database. The composition of the austenite after annealing for 120 s was estimated. The diffusion of Mn, C, and Al resulted in the formation of a Mn and C-enriched region and an Al-depleted region on the austenite side of the interface. DICTRA predicted very limited partitioning of Si between the austenite and ferrite. The carbon and Mn content in the intercritical austenite increased to ranges of 0.3–0.5 wt.% and 7–11 wt. % in both starting microstructures, respectively, due to solute partitioning during the transformation. The calculation results are in good agreement with measured values reported in [26]. The Al content near the interface of the intercritical austenite also decreased to a range of 1–1.4 wt.%.

## 6.4 Results

A set of process maps were developed for a prototype med-Mn steel with the generic composition of 0.2C- $x$ Mn-1.0Si-1.5Al wt.% ( $x = 4$ –12 wt.%). These maps predict the vol.% of austenite formed during IA, based on the intercritical annealing temperature (IAT), IA time, and the initial microstructure.

The process maps were developed for an IAT range of 600–740 °C, while the Mn content was varied between 4 and 12 wt.%. Notably, the process map specifically demonstrated the austenite vol.% resulting from an IA holding time of 120 s, which is compatible with industrial continuous galvanizing practices and had been shown to produce significant volume fractions of chemically stable RA and attractive 3G properties [26,28,41]. It should be recalled that the vol.% of RA at room temperature was calculated as a function of IAT and Mn content using Eqs. [1]-[5].

#### 6.4.1 Tempered Martensite Starting Microstructure

##### 6.4.1.1 *Intercritical Austenite vol.% Calculation using DICTRA*

The TM starting microstructure model simulates austenite growth in a globular microstructure, as shown in Figure 6.1a. Based on the equiaxed microstructure, a spherical geometry was considered [42]. Figure 6.2 depicts an isopleth of the Fe-0.2C- $x$ Mn-1.0Si-1.50Al (wt.%, where  $x = 0$ –12 wt.%) phase diagram showing the temperature range over which cementite is dissolved. The TM starting microstructure simulations were conducted in the temperature and Mn concentration range in which cementite dissolution had been completed. For this reason, IA temperatures greater than 680 °C were used. The total cell size changed from 330 nm to 440 nm in the TM starting microstructure as the IA temperatures increased from 680 °C to 710–720–740 °C, respectively. This change was introduced in an attempt to capture the coarsening of the microstructure with increasing temperatures and was guided by earlier experimental observations [26,28,31].

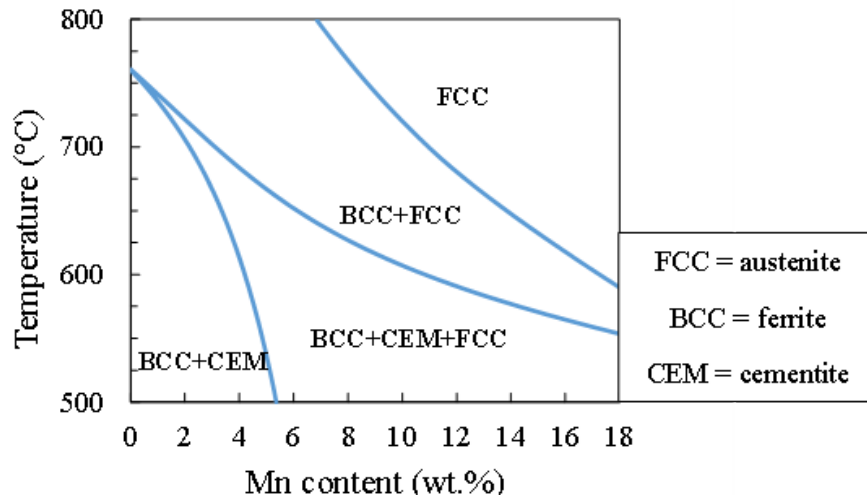


Figure 6.2: Section of the Fe-0.2C-xMn-1.0Si-1.50Al (wt.%) phase diagram, where Mn is varied from 0 – 12 wt.%. Diagram generated using the Thermo-Calc TCFE12 database.

Figure 6.3b shows the intercritical austenite vol.% calculated for the TM starting microstructure as a function of the Mn content of the alloy and IAT for an IA time of 120 s. Throughout the analysis, the bulk C, Al, and Si contents were held constant at 0.2 wt.%, 1.5 wt.%, and 1.0 wt.%, respectively, while the Mn content increased from 4 to 12 wt.%. As expected, an increasing trend in austenite vol.% was observed with increasing IAT from 680 °C to 740 °C. For IATs of 720 °C and 740 °C, for alloy Mn contents of 10 wt.% and 9 wt.%, respectively, the amount of austenite reached nearly 100% after a 120 s holding period.

As a reference point, the equilibrium vol.% of austenite as a function of IAT predicted using Thermo-Calc is shown in Figure 6.3a. The calculated vol.% of austenite after an IA of 120 s (and prior to quenching) is shown in Figure 6.3b. A comparison of the two maps shows that there is a significant difference between the equilibrium values and the modelled values for an IA of 120 s. The difference will likely be even greater for shorter holding times. Differences are smaller at higher IATs, while they are greater at lower IATs. The calculated vol.% of intercritical austenite after 120 s is higher than the predicted equilibrium values at 720 °C and 740 °C. This highlights that equilibrium calculations cannot be used to calculate the amount of austenite formed during intercritical annealing.

In situ high-energy XRD measurements were conducted to compare the intercritical austenite vol.% during a 120 s IA at 710 °C for a 0.15C–5.56Mn–1.89Al–1.1Si steel. The results

in Table 6.1 show that the measured intercritical austenite vol.% was approximately 40% at 710 °C, which is in good agreement with the calculated data.

Table 6.1: Comparison of experimental measurements with calculated values for intercritical annealing austenite vol.% versus the final vol.% of retained austenite for several med-Mn steels. Note that all intercritical annealing treatments are for 120 s at the stated IAT.

Composition	Starting microstructure	IAT (°C)	Measured $\gamma$ (vol%)	Calculated $\gamma$ (vol%)	Measured RA (vol%)	Calculated RA (vol%)
0.18 C–5.91 Mn–1.5 Si–0.4 Al–0.6Cr [28]	TM	675			15.0	19.6
0.15C–5.56Mn–1.89Al–1.1Si [31]	TM	710	40.0	41.8	27.0	30.5
0.18 C–5.91 Mn–1.5 Si–0.4 Al–0.6Cr [28]	TM	710			25.0	23.3
0.15C–5.56Mn–1.89Al–1.1Si [26,32]	M	665	30.8	25.0	21.0	22.3
0.15C–5.56Mn–1.89Al–1.1Si [26,32]	M	710	45.0	42.0	31.0	32.5
0.18 C–5.91 Mn–1.5 Si–0.4 Al–0.6Cr [28]	M	675			25.0	28.4
0.18 C–5.91 Mn–1.5 Si–0.4 Al–0.6Cr [28]	M	690			33.0	32.6
0.18 C–5.91 Mn–1.5 Si–0.4 Al–0.6Cr [28]	M	710			37.0	35.9

#### 6.4.1.1 Retained Austenite Calculation

In Figure 6.3c, the calculated room temperature retained austenite vol.% is plotted for intercritical annealing temperatures of 680, 700, 720, and 740 °C. It is worth noting that the maximum value of the room temperature retained austenite vol.% is achieved at an IAT temperature of 680 °C. At 680 °C, the vol.% of RA closely corresponds to that of intercritical austenite within the Mn content range of 5 to 6.5 wt.% (Figure 6.3b and Figure 6.3c).

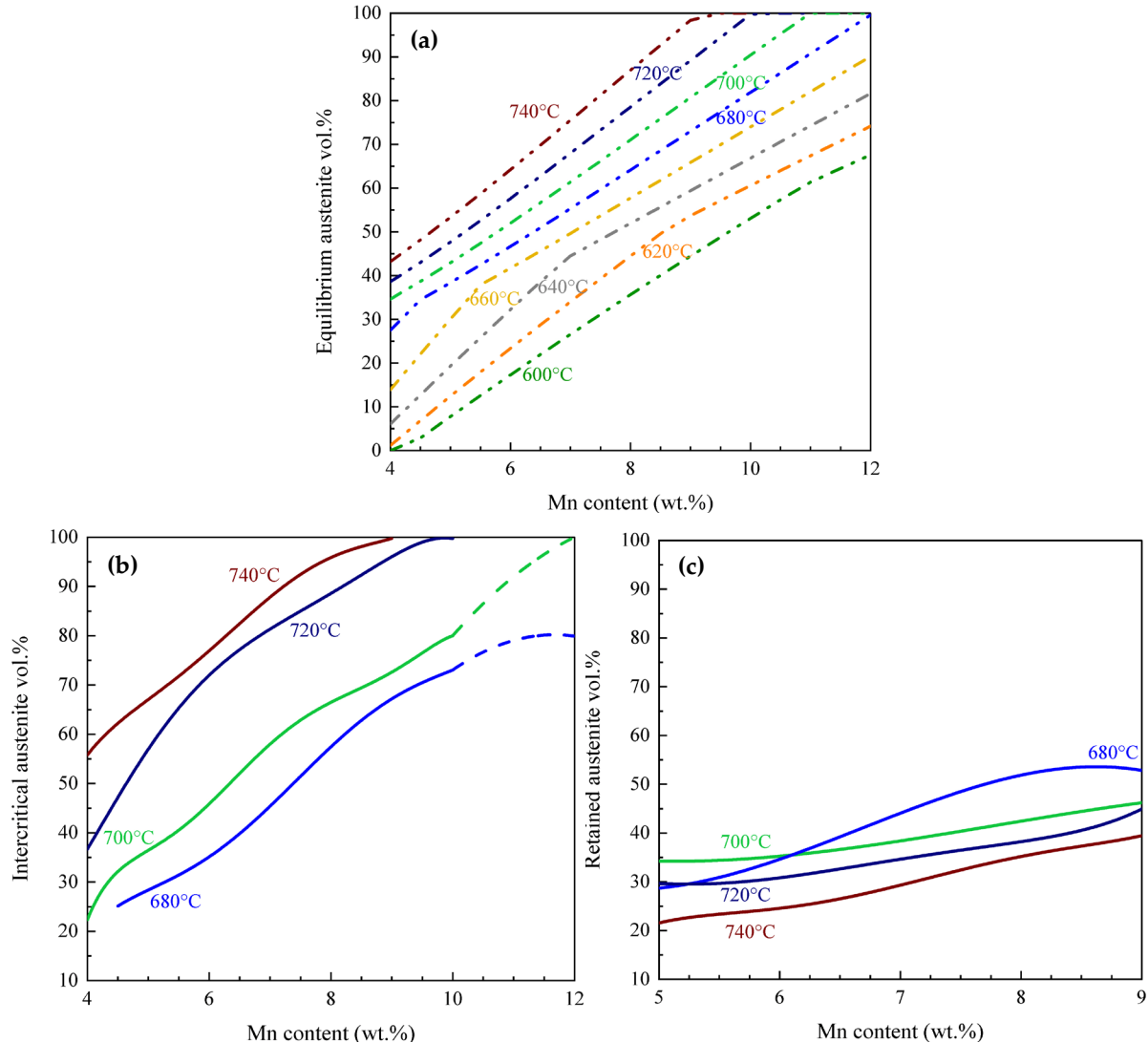


Figure 6.3: (a) Equilibrium austenite vol.%, (b) intercritical austenite, and (c) calculated RA fraction (vol.%) for Fe-0.2C-xMn-1.5Al-1Si wt.% steels ( $x = 4\text{--}12$  wt.%) as a function of IAT from 680 °C to 740 °C for the TM starting microstructure, and assuming an austenite grain size of 1 μm. Note that the dotted lines are related to higher Mn contents as the starting microstructures may be duplex.

## 6.4.2 Martensite Starting Microstructure

### 6.4.2.1 *Intercritical Austenite vol.% Calculation using DICTRA*

The M starting microstructure model simulates austenite growth from the lamellar geometry illustrated in Figure 6.1b. A planar geometry originates from the inter-lath RA geometry observed in previous work on this family of alloys [26,28,31,41]. The cell size for the

DICTRA simulations for the 600–660 °C and 680–740 °C IATs were approximated as 200 nm and 300 nm in the M starting microstructure, respectively. The larger cell size at the higher IAT temperatures reflects the coarsening of the microstructure with higher IA temperatures. The simulation cell sizes were chosen based on the microstructural observations that have previously been made [26,28,31]. Figure 6.4a shows the calculated intercritical austenite vol.% as a function of IAT and Mn content. The simulation predicts 12 to 20 vol.% intercritical austenite at an IAT of 600 °C with increasing alloy Mn, and 55 to approximately 100% at 740 °C.

The austenite vol.% measured using *in situ* high-energy XRD during IA at 665 °C and 710 °C for 120 s for the 0.15C–5.56Mn–1.89Al–1.1Si steel are shown in Table 6.1 for comparison. The results show that the measured intercritical austenite vol.% was roughly  $31\% \pm 2$  at 665 °C and  $45\% \pm 2$  at 710 °C, which is in good agreement with the simulation results [32].

#### 6.4.2.1 Retained Austenite Calculation

Figure 6.4b illustrates the predicted RA vol.% obtained using Eq. [1] for the Fe-0.2C-xMn-1.5Al-1Si wt.% steels ( $x = 4\text{--}12$  wt.%) with a martensitic starting microstructure from 680 °C to 740 °C. The effect of alloying on the austenite transformation kinetics is also clearly expressed in the values for  $m$  and  $n$  (Eqs. [1] and [2]). With increasing Mn content, the kinetics of the austenite transformation are accelerated as Mn is a strong austenite stabilizer [11]. At 680 °C, the intercritically annealed austenite is fully retained after quenching to room temperature, provided that the alloy Mn content is between 5 and 7.5 wt.% (Figure 6.4).

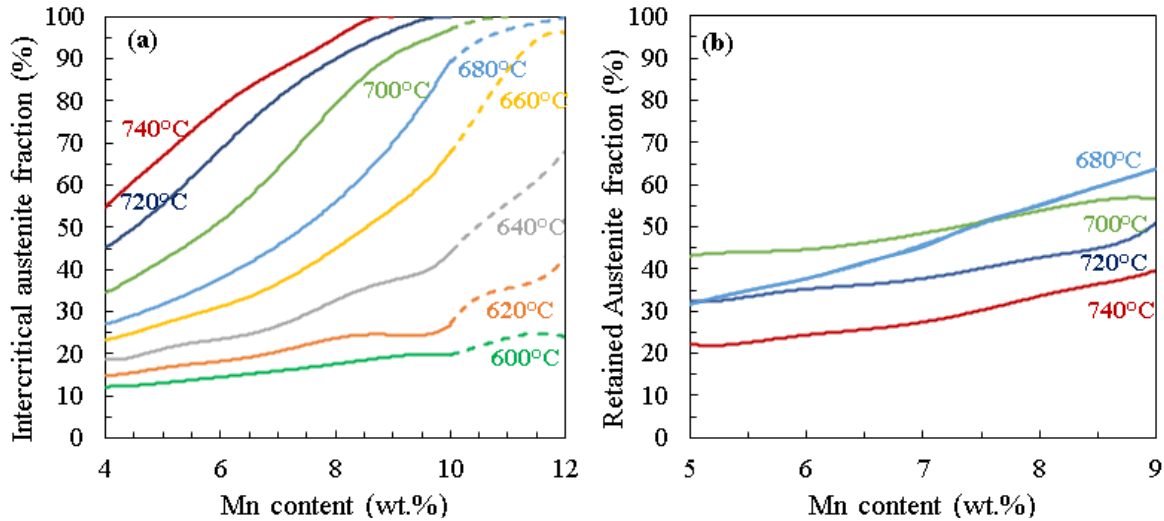


Figure 6.4: Effects of chemical composition on (a) the intercritical austenite and (b) calculated RA fraction (vol.%) for Fe-0.2C-xMn-1.5Al-1Si wt.% steels ( $x = 4\text{--}12$  wt.%) as a function of IATs from 600 °C to 740 °C for the M starting microstructure, and assuming an austenite grain size of 1  $\mu\text{m}$ . Note that the dotted lines are related to higher Mn contents as the starting microstructures may be duplex.

#### 6.4.3 Comparing the Model with the Literature

The process maps for intercritical austenite and RA provide the overall trends for the evolution of austenite vol.% as a function of steel composition and intercritical temperature. There is limited research that matches the exact conditions used to create the maps (for example, some data will match the composition, but not the temperature or the holding time). In order to validate the model, we carried out simulations that exactly match the experimental compositions and intercritical times/temperatures in the available literature [26,28,31]. Table 6.1 presents a comparison between the measured values of RA vol.% obtained from data in the literature [26,28,31] and the corresponding calculated values derived from both the DICTRA-based model and the Koistinen–Marburger model. Table 6.1 shows the experimentally measured RA austenite after annealing at 665 °C, 675 °C, 690 °C, and 710 °C for two different med-Mn steels [26,28]. The RA calculated using Eq [1] is observed to be in excellent agreement, differing by only  $\pm 4\%$  when compared to the experimental results. It is worth noting that in the calculation of RA using Eq [1], Cr is also taken into account for  $M_s$  determination for the 0.18 C–5.91 Mn–1.5 Si–0.4 Al–0.6Cr steel.

## 6.5 Discussion

A comparison between the calculated intercritical austenite values from DICTRA (Figure 6.3b and Figure 6.4a) and the equilibrium austenite values (Figure 6.3a) reveals that equilibrium (thermodynamic) calculations cannot be used to estimate the vol.% of austenite that forms during intercritical annealing under practical processing conditions. Thus, a comprehensive calculation is indispensable. The DICTRA-based model combined with the Koistinen–Marburger model was utilized to better estimate the austenite vol.% in med-Mn steels with as-quenched martensite and tempered martensite starting microstructures.

The calculations based on DICTRA provide a good prediction of the intercritical vol.% of austenite. In order to validate the maps during IA, high-energy X-ray diffraction (HEXRD) tests were conducted and are reported in Table 6.1 for the  $665\text{ }^{\circ}\text{C} \times 120\text{ s}$  and  $710\text{ }^{\circ}\text{C} \times 120\text{ s}$  IA M samples and the  $710\text{ }^{\circ}\text{C} \times 120\text{ s}$  IA TM sample in 0.15C–5.56Mn–1.89Al–1.1Si steel [32]. From this, it can be seen that the experimental intercritical austenite vol.% for the 0.15C–5.56Mn–2Al–1Si steel is in good agreement with the DICTRA-predicted intercritical austenite vol.%. The effect of the starting microstructure on austenite transformation kinetics during IA can be concluded by comparing the two process maps in Figure 6.3b and Figure 6.4a. . During IA for the M starting microstructure, a significantly larger vol.% of intercritical austenite is formed versus the same IAT combination for the TM starting microstructure. This is due to the presence of a lath-shaped martensite starting microstructure. The Mn diffusivity is much higher in the martensite microstructure, resulting in a higher concentration of Mn in the austenite [43].

Furthermore, the DICTRA-based process maps for intercritical austenite indicate that slight changes in temperature can lead to notable changes in the vol.% of intercritical austenite for both starting microstructures. This finding emphasizes the importance of carefully controlling temperature during the IA process to achieve the desired microstructural characteristics. Although these maps are valuable tools for designing intercritical treatments, they do not provide a complete answer regarding the final vol.% of chemically and mechanically stable RA at room temperature. This is because the quantity and stability of RA are influenced by various factors, including the chemical composition of the austenite (e.g., C/Mn content) [37,44]. The calculated results reflect the vol.% of austenite before quenching to room temperature. However, after quenching, a portion of the intercritical austenite is expected to transform into martensite. In

order to address this limitation, the RA maps have been computed using the Koistinen–Marburger model for the med-Mn steels as a function of the starting microstructure.

The combination of the Koistinen–Marburger model, DICTRA, and X-ray diffractometry (XRD) was employed to determine the amount of retained austenite. It should be mentioned that to calculate the RA using Eqs. [1]-[5], the average grain volume of austenite is needed. Based on the experimental observations conducted on med-Mn steels [31], a constant grain size of 1  $\mu\text{m}$  at all IATs was considered for the austenite. Lee et al. [27] studied the effect of varying grain sizes at annealing temperatures on the calculated  $M_s$  temperature. Their findings indicate that, at high annealing temperatures, grain size does not change the calculated  $M_s$  temperature, and the stability of austenite is no longer controlled by its grain size. For validation, values of experimentally measured RA vol.% via XRD for various prototype med-Mn steels from the literature [26,28,31] are compiled in Table 6.1. The validation data were selected to limit the study to two variables: temperature and Mn content. This required fixing the annealing times to be compatible with CGL thermal treatments and compositions similar to those of the experimental alloy with respect to C, Al, and Si contents. The literature data selected were chosen based on their compatibility with the fixed annealing time and compositional constraints documented in Table 6.1 [26,28,31]. Several studies on austenite growth in med-Mn steels, compatible with industrial CGL thermal treatments, have been conducted [7,45–47], while the intercritical annealing time differed from the model. As shown in Table 6.1, the model values are in good agreement with the experimentally measured vol.% of RA obtained from the literature. The variation in grain size between the experimental results and the calculated RA could be the primary reason for the slight difference. The results reveal that the process maps provide valuable insights into designing intercritical treatments. These maps cover a range of med-Mn steel compositions, including 4–12 wt.% Mn,  $1.5 \pm 0.5$  wt.% Al,  $1 \pm 0.5$  wt.% Si, and 0.15–0.2 wt.% C. Changing the alloy C, Al, and Si content significantly affects both the thermodynamic and kinetic calculations [13]. It should also be mentioned that some caution should be exercised using the process maps for higher Mn grades as the starting microstructures may be duplex in nature. Thus, further development of the process simulations to take into account the chemical stability of the austenite and for higher Mn alloys will be undertaken.

When examining Figure 6.3c and Figure 6.4b, which illustrate the relationship between RA fraction, IAT, and alloy Mn content, it becomes evident that there is much more RA in the M

starting microstructure compared to the TM starting microstructure for a given 120 s IAT. This is attributed to two reasons. The first is the greater fraction of austenite which is formed after 120 s of intercritical annealing in the M starting microstructure compared to the TM microstructure. Secondly, the austenite formed during the intercritical annealing of the as-quenched martensite is more stable than that formed during the intercritical annealing of tempered-martensite. This leads to more retained austenite at room temperature for the steels with the as-quenched martensitic microstructure compared to those with the tempered martensite structure. This finding is consistent with previous research papers [21,28,31,48] and can be linked to C and Mn partitioning from the supersaturated martensitic matrix and the reduction in strain energy connected to the formation of inter-lath austenite films [49]. The presence of inter-lath RA films along the martensite lath boundaries accelerates the start of the reverse transformation by eliminating the incubation time associated with the nucleation step [50]. Upon comparing Figure 6.3c and Figure 6.4b it becomes evident that the RA formed from the M starting microstructure exhibits greater stability compared to that formed from the TM starting microstructures. This increased stability can be attributed to the greater C and Mn enrichment in the RA, a result of the shorter diffusion path in the lath-shaped microstructure compared to the equiaxed microstructure [26,28]. Consequently, this leads to a higher vol.% of RA in the samples with a martensitic starting microstructure.

By contrast, the formation of austenite in the TM starting microstructure is controlled by the kinetics of cementite dissolution and the availability of carbon to enrich the austenite. The IATs applied to the TM starting microstructure correspond to the range where cementite dissolution occurs. In the TM starting microstructure, a nucleation step and greater diffusion distance compared to the M starting microstructure led to a lower vol.% of chemically stable RA. As the annealing temperature rises, the volume of austenite increases. However, when we elevate the intercritical temperature, it leads to a decrease in the average C and Mn content within the austenite, causing a reduction in its chemical stability. As a result, a significant portion of austenite formed at high IAT undergoes a transformation into martensite during the cooling process [16–18]. At the lower IA temperatures, the C content of the intercritical austenite will be higher, resulting in retained austenite at room temperature that aligns reasonably well with the model. The optimal annealing temperature range to achieve the desired balance between the vol.% and the stability of austenite is determined to be 700 °C for both starting microstructures.

It is noticeable that the map remains relatively flat at lower Mn contents, suggesting that varying Mn content between 5 to 7% does not notably impact the amount of RA for either starting microstructure. Therefore, designing med-Mn steels with lower Mn contents, around 5 wt.%, can reduce cost while maintaining the same amount of RA as 7% Mn steel. The main challenge is precise temperature control during the thermal processing of med-Mn steels, as even a 20 °C change significantly affects the amount of RA.

It is noticeable that the predicted amount of intercritical austenite (Figure 6.3b and Figure 6.4a) increased above that predicted at equilibrium (Figure 6.3a) at higher IAT. The formation of intercritical austenite beyond the equilibrium amount is attributed to the significantly slower substitutional diffusion within the growing austenite compared to ferrite. In the final stage of austenite growth, its kinetics are controlled by the diffusion of substitutional elements in austenite for final equilibration, potentially leading to austenite shrinkage [50,51]. This shrinkage becomes more pronounced at higher temperatures and higher Mn content. The diffusivities of alloying elements in the parent and growing phases, the composition of the alloy, and IAT can change the amount of excess austenite [50,52,53]. It is worth noting that in industrial processes, both the IAT and time are restricted, which means that the equilibrium phase fractions, and the equilibrium chemistry cannot be achieved.

## 6.6 Conclusions

The development of process maps through a combination of microstructural analysis and DICTRA-based modeling yielded valuable insights into the behavior of med-Mn steels during intercritical annealing. These maps unveiled significant dependencies on Mn content and intercritical annealing temperatures, providing crucial information for the further development of the steel properties in automotive applications. The utilization of the Koistinen–Marburger model deepened our understanding of RA formation kinetics in different starting microstructures.

Compared to the TM starting microstructure, the M starting microstructure promotes a higher vol.% of intercritical austenite during annealing. Additionally, it leads to a higher RA vol.% after quenching to room temperature. These findings highlight the importance of the M starting microstructure in influencing the microstructural evolution and mechanical properties of the med-Mn steels.

Overall, these findings contribute to a model-based approach to develop a robust process window for the further development of med-Mn steels, aiding in the design of steel properties tailored for automotive applications.

## 6.7 Acknowledgements

This work was financially supported by the International Zinc Association Galvanized Autobody Partnership (IZA-GAP), ArcelorMittal Global R&D, Stelco Inc., Teck Metals, and the Natural Sciences and Engineering Research Council of Canada (NSERC grant CRDPJ 522309-17).

The authors would also like to thank U.S. Steel Research for provision of the prototype substrates used in the experimental portions of this investigation.

## 6.8 References

- [1] O. Bouaziz, H. Zurob, M. Huang, Driving force and logic of development of advanced high strength steels for automotive applications, *Steel Res. Int.* 84 (2013) 937–947. <https://doi.org/10.1002/srin.201200288>.
- [2] C. Lesch, N. Kwiaton, F.B. Klose, Advanced High Strength Steels (AHSS) for Automotive Applications – Tailored Properties by Smart Microstructural Adjustments, *Steel Res. Int.* 88 (2017) 1–21. <https://doi.org/10.1002/srin.201700210>.
- [3] R. Kuziak, R. Kawalla, S. Waengler, Advanced high strength steels for automotive industry: A review, *Arch. Civ. Mech. Eng.* 8 (2008) 103–117. [https://doi.org/10.1016/s1644-9665\(12\)60197-6](https://doi.org/10.1016/s1644-9665(12)60197-6).
- [4] B.C. De Cooman, Y. Estrin, S.K. Kim, Twinning-induced plasticity (TWIP) steels, *Acta Mater.* 142 (2018) 283–362. <https://doi.org/10.1016/j.actamat.2017.06.046>.
- [5] L. Liu, B. He, M. Huang, The Role of Transformation-Induced Plasticity in the Development of Advanced High Strength Steels, *Adv. Eng. Mater.* 20 (2018) 1701083. <https://doi.org/10.1002/adem.201701083>.

- [6] C. Liu, Q. Peng, Z. Xue, S. Wang, C. Yang, Microstructure and mechanical properties of hot-rolled and cold-rolled medium-Mn TRIP steels, *Materials (Basel)*. 11 (2018) 2242. <https://doi.org/10.3390/ma11112242>.
- [7] J.M. Jang, S.J. Kim, N.H. Kang, K.M. Cho, D.W. Suh, Effects of annealing conditions on microstructure and mechanical properties of low carbon, manganese transformation-induced plasticity steel, *Met. Mater. Int.* 15 (2009) 909–916. <https://doi.org/10.1007/s12540-009-0909-7>.
- [8] Y.K. Lee, J. Han, Current opinion in medium manganese steel, *Mater. Sci. Technol.* 31 (2015) 843–856. <https://doi.org/10.1179/1743284714Y.00000000722>.
- [9] B. Hu, H. Luo, F. Yang, H. Dong, Recent progress in medium-Mn steels made with new designing strategies, a review, *J. Mater. Sci. Technol.* 33 (2017) 1457–1464. <https://doi.org/10.1016/j.jmst.2017.06.017>.
- [10] Y. Ma, Medium-manganese steels processed by austenite-reverted-transformation annealing for automotive applications, *Mater. Sci. Technol.* 33 (2017) 1713–1727. <https://doi.org/10.1080/02670836.2017.1312208>.
- [11] D.W. Suh, S.J. Kim, Medium Mn transformation-induced plasticity steels: Recent progress and challenges, *Scr. Mater.* 126 (2017) 63–67.
- [12] M. Soleimani, A. Kalhor, H. Mirzadeh, Transformation-induced plasticity (TRIP) in advanced steels: A review, *Mater. Sci. Eng. A.* 795 (2020) 140023. <https://doi.org/10.1016/j.msea.2020.140023>.
- [13] Z. Dai, H. Chen, R. Ding, Q. Lu, C. Zhang, Z. Yang, S. van der Zwaag, Fundamentals and application of solid-state phase transformations for advanced high strength steels containing metastable retained austenite, *Mater. Sci. Eng. R.* 143 (2021) 100590. <https://doi.org/10.1016/j.mser.2020.100590>.
- [14] Y. Chang, C.Y. Wang, K.M. Zhao, H. Dong, J.W. Yan, An introduction to medium-Mn steel: Metallurgy, mechanical properties and warm stamping process, *Mater. Des.* 94 (2016) 424–432. <https://doi.org/10.1016/j.matdes.2016.01.048>.

- [15] R.L. Miller, Ultrafine- grained microstructures and mechanical properties of alloy steels, *Met Trans.* 3 (1972) 905–912. <https://doi.org/10.1007/bf02647665>.
- [16] D.W. Suh, J.H. Ryu, M.S. Joo, H.S. Yang, K.Y. Lee, Medium – Alloy Manganese – Rich Transformation – Induced Plasticity Steels, *Metall. Mater. Trans. A.* 46A (2013) 286–293.
- [17] H. Luo, H. Dong, M. Huang, Effect of intercritical annealing on the Lüders strains of medium Mn transformation-induced plasticity steels, *Mater. Des.* 83 (2015) 42–48. <https://doi.org/10.1016/j.matdes.2015.05.085>.
- [18] R. Schneider, K. Steineder, D. Krizan, C. Sommitsch, Effect of the heat treatment on the microstructure and mechanical properties of medium-Mn-steels, *Mater. Sci. Technol.* 35 (2019) 2045–2053. <https://doi.org/10.1080/02670836.2018.1548957>.
- [19] E. De Moor, D.K. Matlock, J.G. Speera, M.J. Merwin, Austenite stabilization through manganese enrichment, *Scr. Mater.* 64 (2011) 185–188. <https://doi.org/10.1016/j.scriptamat.2010.09.040>.
- [20] A. R. Marder, The metallurgy of zinc-coated steel, *Prog. Mater. Sci.* 45 (2000) 191–271. <https://doi.org/10.1038/089315a0>.
- [21] H. Luo, H. Dong, New ultrahigh-strength Mn-alloyed TRIP steels with improved formability manufactured by intercritical annealing, *Mater. Sci. Eng. A.* 626 (2015) 207–212. <https://doi.org/10.1016/j.msea.2014.12.049>.
- [22] W.Q. Cao, C. Wang, J. Shi, M.Q. Wang, W.J. Hui, H. Dong, Microstructure and mechanical properties of Fe-0.2C-5Mn steel processed by ART-annealing, *Mater. Sci. Eng. A.* 528 (2011) 6661–6666. <https://doi.org/10.1016/j.msea.2011.05.039>.
- [23] A. Arlazarov, M. Gouné, O. Bouaziz, A. Hazotte, G. Petitgand, P. Barges, Evolution of microstructure and mechanical properties of medium Mn steels during double annealing, *Mater. Sci. Eng. A.* 542 (2012) 31–39. <https://doi.org/10.1016/j.msea.2012.02.024>.
- [24] P.J. Gibbs, E. De Moor, M.J. Merwin, B. Clausen, J.G. Speer, D.K. Matlock, Austenite stability effects on tensile behavior of manganese-enriched- austenite transformation-induced

plasticity steel, *Metall. Mater. Trans. A.* 42A (2011) 3691–3702. <https://doi.org/10.1007/s11661-011-0687-y>.

[25] J. Shi, X. Sun, M. Wang, W. Hui, H. Dong, W. Cao, Enhanced work-hardening behavior and mechanical properties in ultrafine-grained steels with large-fractioned metastable austenite, *Scr. Mater.* 63 (2010) 815–818. <https://doi.org/10.1016/j.scriptamat.2010.06.023>.

[26] D.M. Pallisco, J.R. McDermid, Mechanical property development of a 0.15C–6Mn–2Al–1Si third-generation advanced high strength steel using continuous galvanizing heat treatments, *Mater. Sci. Eng. A.* 778 (2020) 139111. <https://doi.org/10.1016/j.msea.2020.139111>.

[27] S. Lee, B.C. De Cooman, On the selection of the optimal intercritical annealing temperature for medium Mn TRIP steel, *Metall. Mater. Trans. A.* 44A (2013) 5018–5024. <https://doi.org/10.1007/s11661-013-1860-2>.

[28] K.M.H. Bhadhon, X. Wang, J.R. McDermid, Effects of CGL-compatible thermal processing, starting microstructure, and Sn micro-alloying on the mechanical properties of a medium-Mn third generation advanced high strength steel, *Mater. Sci. Eng. A.* 833 (2022) 142563. <https://doi.org/10.1016/j.msea.2021.142563>.

[29] J.O. Andersson, T. Helander, L. Höglund, P. Shi, B. Sundman, Thermo-Calc & DICTRA, computational tools for materials science, *Calphad.* 26 (2002) 273–312. [https://doi.org/10.1016/S0364-5916\(02\)00037-8](https://doi.org/10.1016/S0364-5916(02)00037-8).

[30] A. Borgenstam, A. Engström, L. Höglund, J. Ågren, DICTRA, a tool for simulation of diffusional transformations in alloys, *J. Phase Equilibria.* 21 (2000) 269–280. <https://doi.org/10.1361/105497100770340057>.

[31] A. Mehrabi, J.R. McDermid, X. Wang, H. Zurob, Austenite Nucleation and Growth as a Function of Starting Microstructure for a Fe–0.15C–5.56Mn–1.1Si–1.89Al Medium-Mn Steel, *Steel Res. Int.* 94 (2023) 2200952. <https://doi.org/10.1002/srin.202200952>.

- [32] A. Mehrabi, H. Zurob, I. E. Benrabah, J. R. McDermid, Austenite formation in a medium-Mn steel during intercritical annealing via in situ high-energy X-ray diffraction, *J. Mater. Res. Technol.* (2024).
- [33] O. Dmitrieva, D. Ponge, G. Inden, J. Millán, P. Choi, J. Sietsma, D. Raabe, Chemical gradients across phase boundaries between martensite and austenite in steel studied by atom probe tomography and simulation, *Acta Mater.* 59 (2011) 364–374. <https://doi.org/10.1016/j.actamat.2010.09.042>.
- [34] H. Luo, J. Shi, C. Wang, W. Cao, X. Sun, H. Dong, Experimental and numerical analysis on formation of stable austenite during the intercritical annealing of 5Mn steel, *Acta Mater.* 59 (2011) 4002–4014. <https://doi.org/10.1016/j.actamat.2011.03.025>.
- [35] F. Huyan, J.Y. Yan, L. Höglund, J. Ågren, A. Borgenstam, Simulation of the Growth of Austenite from As-Quenched Martensite in Medium Mn Steels, *Metall. Mater. Trans. A.* 49A (2018) 1053–1060. <https://doi.org/10.1007/s11661-018-4497-3>.
- [36] X. Zhang, G. Miyamoto, T. Kaneshita, Y. Yoshida, Y. Toji, T. Furuhashi, Growth mode of austenite during reversion from martensite in Fe-2Mn-1.5Si-0.3C alloy: A transition in kinetics and morphology, *Acta Mater.* 154 (2018) 1–13. <https://doi.org/10.1016/j.actamat.2018.05.035>.
- [37] H. Luo, J. Liu, H. Dong, A Novel Observation on Cementite Formed During Intercritical Annealing of Medium Mn Steel, *Metall. Mater. Trans. A.* 47A (2016) 3119–3124. <https://doi.org/10.1007/s11661-016-3448-0>.
- [38] D.P. Koistinen, R.E. Marburger, A general equation prescribing the extent of the austenite-martensite transformation in pure iron-carbon alloys and plain carbon steels, *Acta Metall.* 7 (1959) 59–60. [https://doi.org/10.1016/0001-6160\(59\)90170-1](https://doi.org/10.1016/0001-6160(59)90170-1).
- [39] S.J. Lee, S. Lee, B.C. De Cooman, Martensite transformation of sub-micron retained austenite in ultra-fine grained manganese transformation-induced plasticity steel, *Int. J. Mater. Res.* 104 (2013) 423–429. <https://doi.org/10.3139/146.110882>.

- [40] E. Jimenez-Melero, N.H. van Dijk, L. Zhao, J. Sietsma, S.E. Offerman, J.P. Wright, S. van der Zwaag, Martensitic transformation of individual grains in low-alloyed TRIP steels, *Scr. Mater.* 56 (2007) 421–424. <https://doi.org/10.1016/j.scriptamat.2006.10.041>.
- [41] K.M.H. Bhadhon, X. Wang, E.A. McNally, J.R. McDermid, Effect of Intercritical Annealing Parameters and Starting Microstructure on the Microstructural Evolution and Mechanical Properties of a Medium-Mn Third Generation Advanced High Strength Steel, *Metals (Basel)*. 12 (2022) 356. <https://doi.org/10.3390/met12020356>.
- [42] A. Mehrabi, J.R. McDermid, H.S. Zurob, F.E. Goodwin, Austenite Nucleation and Growth as a Function of Starting Microstructure in a Fe-0.15C-5.56Mn-1.1Si-1.89Al Medium- Mn Steel, in: *Proc. 5th Int. High Manganese Steel Conf., Linz, Austria, 2022*.
- [43] N. Nakada, K. Mizutani, T. Tsuchiyama, S. Takaki, Difference in transformation behavior between ferrite and austenite formations in medium manganese steel, *Acta Mater.* 65 (2014) 251–258. <https://doi.org/10.1016/j.actamat.2013.10.067>.
- [44] F. G. Caballero, C. Garcia-Mateo, J. Chao, M. J. Santofimia, C. Capdevila, C. García de Andres, Effects of Morphology and Stability of Retained Austenite on the Ductility of TRIP-aided Bainitic Steels, *ISIJ Int.* 48 (2008) 1256–1262.
- [45] S. Lee, Y. Estrin, B.C. De Cooman, Constitutive modeling of the mechanical properties of V-added medium manganese TRIP steel, *Metall. Mater. Trans. A.* 44A (2013) 3136–3146. <https://doi.org/10.1007/s11661-013-1648-4>.
- [46] S. Lee, S.J. Lee, S. Santhosh Kumar, K. Lee, B.C.D. Cooman, Localized deformation in multiphase, ultra-fine-grained 6 Pct Mn transformation-induced plasticity steel, *Metall. Mater. Trans. A.* 42A (2011) 3638–3651. <https://doi.org/10.1007/s11661-011-0636-9>.
- [47] D. Lee, J.K. Kim, S. Lee, K. Lee, B.C. De Cooman, Microstructures and mechanical properties of Ti and Mo micro-alloyed medium Mn steel, *Mater. Sci. Eng. A.* 706 (2017) 1–14. <https://doi.org/10.1016/j.msea.2017.08.110>.

- [48] J.I. Kim, J.H. Ryu, S.W. Lee, K. Lee, Y.U. Heo, D.W. Suh, Influence of the Initial Microstructure on the Reverse Transformation Kinetics and Microstructural Evolution in Transformation-Induced Plasticity-Assisted Steel, *Metall. Mater. Trans. A*. 47A (2016) 5352–5361. <https://doi.org/10.1007/s11661-016-3672-7>.
- [49] N. Nakada, T. Tsuchiyama, S. Takaki, N. Miyano, Temperature dependence of austenite nucleation behavior from lath martensite, *ISIJ Int.* 51 (2011) 299–304. <https://doi.org/10.2355/isijinternational.51.299>.
- [50] R. Wei, M. Enomoto, R. Hadian, H.S. Zurob, G.R. Purdy, Growth of austenite from as-quenched martensite during intercritical annealing in an Fe-0.1C-3Mn-1.5Si alloy, *Acta Mater.* 61 (2013) 697–707. <https://doi.org/10.1016/j.actamat.2012.10.019>.
- [51] J. Ågren, Computer simulations of the austenite/ferrite diffusional transformations in low alloyed steels, *Acta Metall.* 30 (1982) 841–851. [https://doi.org/10.1016/0001-6160\(82\)90082-7](https://doi.org/10.1016/0001-6160(82)90082-7).
- [52] C.I. Garcia, A.J. Deardo, Formation of Austenite in 1.5 Pct Mn Steels, *Metall. Trans. A*. 12A (1981) 521–530. <https://doi.org/10.1007/BF02648551>.
- [53] P.A. Wycliffe, G.R. Purdy, J.D. Embury, Growth of austenite in the intercritical annealing of Fe-C-Mn dual phase steels, *Can. Metall. Q.* 20 (1981) 339–350. <https://doi.org/10.1179/cmqr.1981.20.3.339>.

## 7 Global Discussion

This chapter will present a summative discussion of the main results from Chapters 3 to 6. The effects of starting microstructure and intercritical annealing temperature on the phase transformation kinetics and microstructural evolution will be discussed first and lead into the development of the process maps using a combination of microstructural analysis and DICTRA-based modeling to predict the intercritical austenite vol.% as a function of the intercritical annealing parameters and starting microstructure.

### 7.1 Phase Transformation Kinetics and Microstructural Evolution

The phase transformation kinetics and microstructural evolution of the experimental alloy in Chapter 3-5 of this Ph.D. thesis was determined as a function of starting microstructure and CGL-compatible intercritical annealing parameters. The vol % of intercritical austenite and retained austenite was estimated in a prototype Fe-0.15C-5.56Mn-1.1Si-1.89Al medium-Mn third-generation advanced high strength steel. The vol % of the RA and its stability as a function of the morphology and chemistry of the intercritical austenite in the microstructure has been predicted.

The vol % of intercritical austenite and RA showed an increase with increasing intercritical annealing temperature (IAT) and intercritical annealing (IA) holding time for both initial microstructures; the as-received cold-rolled (CR) tempered martensite and martensite-ferrite (MF) microstructures (Figure 3.9 and Figure 3.10). Nevertheless, the morphology of the retained austenite, and consequently its chemical and mechanical stability, exhibited variations based on the starting microstructure. A comparison of the TEM micrographs for the CR and MF samples (Figure 3.2 vs. Figure 3.4) clearly illustrates the significant effect of the starting microstructure on the resulting characteristics of the retained austenite after intercritical annealing. Granular retained austenite was found in the CR starting microstructure (Figure 3.2), while lath-like retained austenite was observed in the samples with the MF starting microstructure (Figure 3.4) [1–5]. This is due to the presence of different nucleation sites in the two starting microstructures. In the case of the MF microstructure, the intercritical austenite grows from pre-existing films of RA between the martensite laths, and this leads to lamellar RA morphology [6]. In contrast, cementite and ferrite grain boundaries are preferred nucleation sites for intercritical austenite in the CR microstructure [7–11]. Globular intercritical austenite grains are formed at these

nucleation sites. Interestingly, even after the nucleation of austenite, cementite particles are still present in the CR microstructure which was annealed at 665 °C. The required C for partitioning to intercritical austenite and stabilizing it is provided by cementite dissolution. However, Mn enrichment within the cementite particles led to the slow dissolution of cementite and this reduced the growth rate of austenite [6,9,12,13]. The present results are in agreement with earlier work [11] which has shown that when austenite forms at cementite particles in medium Mn steel, the growth of austenite is controlled by Mn diffusion due to the high Mn content in cementite. The concentration profile in Figure 5.8b, support the concept that the nucleation and growth of austenite is mainly controlled by Mn partitioning for CR samples at 665 °C IAT, aligning with the simulation predictions for Mn enrichment in austenite. Undissolved cementite in the microstructure may also affect the TRIP kinetics because the C content of the RA can be significantly decreased if C is trapped in cementite. A lower retained austenite C content translates into lower chemical stability and can result in lower volume fractions of RA and poor RA mechanical stability [2,14]. Consequently, a reduced amount of retained austenite was noted in the CR sample annealed at the 665 °C IAT (Figure 4.5 vs. Figure 5.5) due to the intercritical austenite exhibiting lower chemical stability, leading to substantial fractions transforming into martensite during final cooling.

The lath-shaped RA is usually present in smaller vol % (Figure 3.4) and contains higher C and Mn than the equiaxed or globular RA (Figure 3.2) [2]. In addition, the lath-shaped retained austenite tends to be surrounded by martensite, imposing a local hydrostatic stress which resists the shape change associated with the  $\gamma \rightarrow \alpha'$  transformation. As a result, lath-shaped retained austenite is generally found to be more mechanically stable during subsequent deformation [1,2,4,6,15–20]. Another aspect to assess the chemical stability of the retained austenite in both starting microstructure is by modeling the chemical composition evolution of intercritical austenite through DICTRA (Figure 4.8 vs. Figure 5.8). The C content in the intercritical austenite was higher in the MF samples than for the CR samples for the 665 °C IAT, which supports the hypothesis that the lath-shaped retained austenite in the MF sample exhibited greater chemical stability attributable to the shorter diffusion distances for C enrichment from the surrounding martensite. The difference in austenite growth kinetics in both starting microstructure is also reported to be due to the absence of a nucleation barrier for intercritical austenite formation from existing inter-lath RA (Figure 3.3), along with the rapid partitioning of C from supersaturated

martensite [2,4,6,21,22]. Consequently, a reduced vol % of retained austenite was noted in the CR sample at 665 °C IAT (Figure 4.5 vs. Figure 5.5) due to the intercritical austenite exhibiting lower chemical stability, leading to substantial fractions transforming into martensite during the final cooling process.

Accelerated austenite reversion kinetics were observed for the MF starting microstructure samples under the same annealing conditions (Figure 4.5 vs. Figure 5.5). This was due to the direct growth of intercritical austenite from preexisting inter-lath RA films and the relatively rapid partitioning of C from the surrounding supersaturated martensitic matrix [2,6]. The difference in austenite growth kinetics is more significant for the 665 °C IAT (Figure 4.5 vs. Figure 5.5). In Figure 7.1, the austenite vol % increased to 26% and 33% when annealed for 240 s at 665 °C for the CR and MF samples, respectively [23]. In the present work, these hypotheses are interpreted using the DICTRA module of Thermo-Calc. The DICTRA module (using the TCFE12 and MOBFE5 databases) was used to model austenite growth kinetics for the CR and MF starting microstructures. It is worth noting that martensite is not a thermodynamically stable phase consequently, the model employs a high-carbon content body-centered cubic (BCC) phase to represent martensite. Simulations comparing the intercritical austenite vol % for the 665 °C and 710 °C intercritical anneal from the CR and MF starting microstructures are shown in Figure 3.11. At 665 °C, the modelling predicts that the initial growth of austenite in the MF starting microstructure is controlled by C diffusion in ferrite (under NPLe), whereas austenite growth in the CR starting microstructure is controlled by Mn diffusion in ferrite since there is not a detectable stage that is controlled by C diffusion (Figure 3.11a). The significant difference between the diffusion rates of C and Mn, thus, explains the difference in austenite growth kinetics in the two starting microstructures [6]. The present results align with earlier findings [11] which has shown that when austenite forms at cementite particles in medium Mn steel, the growth of austenite is controlled by Mn diffusion due to the high Mn content in cementite. It is noteworthy that the high Mn content of cementite, determined to be 10-15% through TEM-EDX analysis, emphasizes the significance of Mn diffusion within ferrite.

On the other hand, at higher IAT, when most of the cementite had dissolved, the difference in intercritical austenite fractions in both starting microstructures was smaller. In Figure 7.1, the intercritical austenite vol % increased to 41% and 46% when annealed for 240 s at 710 °C for the CR and MF samples, respectively [23]. It worth mentioning that the vol % of RA in the microstructures was recorded as 36% and 45% at 710 °C IAT for the CR and MF samples, respectively, at the end of the annealing cycle. This implies that ~5% and ~1% of the austenite underwent the transformation to martensite during quenching to room temperature in the CR and MF samples, respectively (Figure 7.1). These results support the argument that the lath-shaped retained austenite in the MF sample was more chemically stable for the 710 °C IAT. Pallisco and McDermid [1] observed enhanced mechanical properties, with the best balance of strength and ductility, for the MF starting microstructure annealed at 710 °C compared to the CR starting microstructure for the present prototype medium-Mn steel. The key findings in this group of medium-Mn steels indicate that the martensitic starting microstructure exhibits a more robust CGL-compatible processing window, leading to the achievement of target mechanical properties for 3G AHSS [1,2]. The thermal processing route, involving austenitizing and a CGL-compatible IA [1,2].

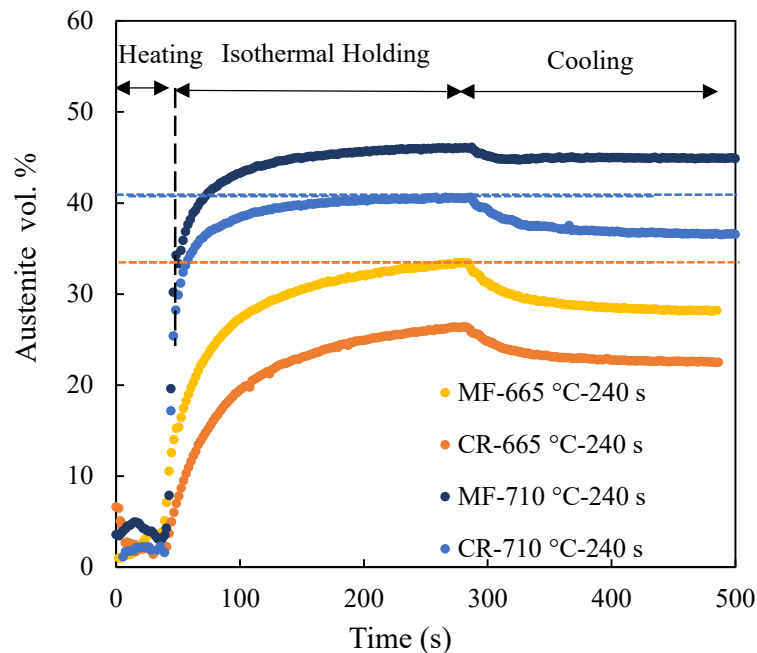


Figure 7.1: Austenite vol. % during isothermal holding at 665 °C and 710 °C for up to 240 s, as determined using *in situ* HEXRD, for the CR and MF starting microstructures.

Concentration profiles for alloying elements across the interface, after annealing at 665 °C and 710 °C are modelled using DICTRA (Figure 4.8 and Figure 4.9, Figure 5.8, and Figure 5.10). The enrichment of C and Mn and the depletion of Al at the austenite interface (Figure 4.8, Figure 4.9, Figure 5.8, and Figure 5.10) are in good quantitative agreement with the experimentally measured APT concentration profiles (Figure 4.2d, and Figure 5.2c). However, there is a discrepancy in the case of Si. While DICTRA predicted Si enrichment in austenite, the experimental data revealed a flat Si profile between ferrite and austenite (Figure 4.10). This suggests that Si does not have a significant effect on austenite growth kinetics, as evidenced by the absence of a substantial Si gradient in either ferrite or austenite. Mn profiles (Figure 4.8b, Figure 4.9b, Figure 5.9d, and Figure 5.10b) at 0.1 s show negligible partitioning of Mn in the austenite associated with non-partitioning local equilibrium (NPLE) austenite growth. The austenite growth is controlled by the diffusion of the substitutional elements in ferrite/martensite for longer times ( $\geq 1$  s). Thus, it can be concluded that austenite growth exhibits two stages: initially controlled by rapid C diffusion, followed by Mn diffusion in ferrite.

The study presented in Chapters 3 – 5 aimed to understand the effects of starting microstructure and intercritical annealing temperature on the phase transformation kinetics and microstructural evolution on Fe-0.19C-4.39 Mn (wt.%) steel. It was shown that the starting microstructure is one of the most important factors affecting the vol.%, stability, morphology, and reversion kinetics of the intercritical and subsequent final RA and the resultant mechanical properties of the med-Mn TRIP steels. Accelerated austenite reversion kinetics were observed for the MF starting microstructure. This was due to the direct growth of intercritical austenite from pre-existing inter-lath RA films and the relatively rapid partitioning of C from the surrounding supersaturated martensitic matrix. It was also shown that lath-shaped retained austenite in the MF sample was more chemically stable at 710 °C IAT.

The overall kinetics, as determined through HEXRD, dilatometry, and as modelled using DICTRA, are in good agreement at 665 °C and 710 °C for both starting microstructures. The slight difference observed between the model and experimental analyses regarding the austenite vol % can be attributed to the limitations of the 1D simulation, which may not precisely capture the complexities in the microstructure. Moreover, the simple geometry for austenite nucleation was considered while the gradual nucleation over time could change the results. In CR starting microstructure cementite particles act as carbon sources for austenite. However, other nucleation

sites for austenite may exist, such as intra-granular austenite grains nucleated on intra-granular cementite particles or austenite nucleation on inter-granular cementite particles present along ferrite grain boundaries. Admittedly, the DICTRA simulations did not account for the presence of 20% ferrite in the microstructure. Instead, it only considered the growth of austenite into martensite. This could explain the discrepancy between the experimental observations and the predictions from the DICTRA simulations. In DICTRA, only the growth of austenite within martensite is considered. However, if an austenite grain were to reach one of the ferrite islands, it is likely that its growth rate will decrease significantly because there is much less carbon in ferrite compared to martensite. This could explain why the DICTRA simulations (which do not account for this effect) over predict the austenite fraction compared to the HEXRD measurements.

Since there is overall agreement between the experimental results and the predictions from the DICTRA simulations, the DICTRA simulation software was employed to develop process maps, predicting the intercritical austenite vol% based on intercritical annealing parameters and starting microstructure for a family of med-Mn steels with the composition Fe-0.2C-xMn-1.0Si-1.50Al (wt.%, where  $x = 4-12$  wt.%). The process maps, detailed in Chapters 6, are further discussed in the following section.

## 7.2 Process Map

The developed process maps presented in chapter 6 sought to predict the intercritical austenite vol % as a function of the intercritical annealing parameters and starting microstructure employing a combination of microstructural analysis and DICTRA-based modeling. The maps highlighted a significant correlation between the calculated intercritical austenite fraction (vol %) and both alloy Mn content (4-12 wt.%) and intercritical annealing temperature (600 °C to 740 °C). The calculations were conducted under constant C, Al, and Si contents of 0.2 wt.%, 1.5 wt.%, and 1.0 wt.%, respectively. It is noteworthy that the process map specifically illustrated the intercritical austenite vol % expected after an IA holding time of 120 s, a duration compatible with industrial continuous galvanizing lines, showcasing significant fractions of chemically stable retained austenite and desirable 3G properties [1,2,24].

A comparison between the predicted intercritical austenite values from DICTRA (Figure 6.3b and Figure 6.4a) and the equilibrium austenite values (Figure 6.3a) indicates that

thermodynamic calculations alone are insufficient for estimating the vol % of austenite formed during intercritical annealing under practical processing conditions. Therefore, a comprehensive calculation becomes essential. The DICTRA-based model, in conjunction with the Koistinen–Marburger model [25–27] was employed to enhance the estimation of RA vol % in med-Mn steels with as-quenched martensite (M) and tempered martensite (TM) starting microstructures. The DICTRA calculations provide a reliable prediction of the intercritical vol.% of austenite. *In situ* HEXRD experiments [23,28], along with complementary microstructural characterization verified the austenite growth model during IA (Table 6.1). The calculated results represent the vol % of intercritical austenite before cooling to room temperature. However, after cooling, a portion of the intercritical austenite is expected to transform into martensite. To address this limitation, the RA maps have been computed using the Koistinen–Marburger model for the med-Mn steels, taking into account the starting microstructure.

The calculation of the room-temperature RA vol % using the modified empirical equation proposed by Koistinen and Marburger considered the IAT and accounted for the effect of the intercritical austenite composition. To validate this method, Table 6.1 compiled experimentally determined RA vol % obtained through XRD for various prototype med-Mn steels documented in the literature [1,2,6]. The values predicted by the model closely correspond with the experimentally measured RA vol % reported in the literature (Table 6.1).

The results highlight that the process maps offer valuable insights for the development of intercritical treatments for a variety of med-Mn steel compositions, ranging from 4-12 wt.% Mn,  $1.5 \pm 0.5$  wt.% Al,  $1 \pm 0.5$  wt.% Si, and 0.15-0.2 wt.% C. The process maps revealed substantial dependencies of the intercritical and retained austenite vol % on alloy Mn content and IAT. This information is crucial for further development of the steel properties in automotive applications. The application of the Koistinen–Marburger model has enhanced our comprehension of RA formation kinetics in different starting microstructures. The M starting microstructure promotes a higher vol % of intercritical austenite during IA. Moreover, it also leads to a higher RA fraction after cooling to room temperature. These findings highlight the importance of the M starting microstructure in influencing the microstructural evolution and mechanical properties of the med-Mn steels. These maps illustrate the compositional range where, under certain conditions, the vol % of intercritical austenite equals the vol % of RA at room temperature. Specifically, this

equivalence occurs at an IAT of 680 °C with low Mn content (5-7 wt.% in the M starting microstructure and 5-6 wt.% in the CR starting microstructure). However, at higher intercritical annealing temperatures and higher Mn content, intercritical austenite becomes very unstable and undergoes transformation during quenching. This highlights the sensitivity of microstructural evolution to variations in IAT and Mn content, emphasizing the need for careful control of these parameters in medium-Mn steel processing. Overall, these findings contribute to a model-based approach to develop a robust process window for further development of med-Mn steels, aiding in the design of steel properties tailored for automotive applications.

### 7.3 References

- [1] D.M. Pallisco, J.R. McDermid, Mechanical property development of a 0.15C–6Mn–2Al–1Si third-generation advanced high strength steel using continuous galvanizing heat treatments, *Mater. Sci. Eng. A.* 778 (2020) 139111. <https://doi.org/10.1016/j.msea.2020.139111>.
- [2] K.M.H. Bhadhon, X. Wang, J.R. McDermid, Effects of CGL-compatible thermal processing, starting microstructure, and Sn micro-alloying on the mechanical properties of a medium-Mn third generation advanced high strength steel, *Mater. Sci. Eng. A.* 833 (2022) 142563. <https://doi.org/10.1016/j.msea.2021.142563>.
- [3] J. Han, S.J. Lee, J.G. Jung, Y.K. Lee, The effects of the initial martensite microstructure on the microstructure and tensile properties of intercritically annealed Fe-9Mn-0.05C steel, *Acta Mater.* 78 (2014) 369–377. <https://doi.org/10.1016/j.actamat.2014.07.005>.
- [4] H. Luo, H. Dong, New ultrahigh-strength Mn-alloyed TRIP steels with improved formability manufactured by intercritical annealing, *Mater. Sci. Eng. A.* 626 (2015) 207–212. <https://doi.org/10.1016/j.msea.2014.12.049>.
- [5] J. Han, A.K. da Silva, D. Ponge, D. Raabe, S.M. Lee, Y.K. Lee, S.I. Lee, B. Hwang, The effects of prior austenite grain boundaries and microstructural morphology on the impact toughness of intercritically annealed medium Mn steel, *Acta Mater.* 122 (2017) 199–206. <https://doi.org/10.1016/j.actamat.2016.09.048>.

- [6] A. Mehrabi, J.R. McDermid, X. Wang, H. Zurob, Austenite Nucleation and Growth as a Function of Starting Microstructure for a Fe–0.15C–5.56Mn–1.1Si–1.89Al Medium-Mn Steel, *Steel Res. Int.* 94 (2023) 2200952. <https://doi.org/10.1002/srin.202200952>.
- [7] M. Kulakov, W.J. Poole, M. Militzer, The effect of the initial microstructure on recrystallization and austenite formation in a DP600 steel, *Metall. Mater. Trans. A.* 44A (2013) 3564–3576. <https://doi.org/10.1007/s11661-013-1721-z>.
- [8] H. Azizi-Alizamini, M. Militzer, W.J. Poole, Austenite formation in plain low-carbon steels, *Metall. Mater. Trans. A.* 42A (2011) 1544–1557. <https://doi.org/10.1007/s11661-010-0551-5>.
- [9] M. Gouné, P. Maugis, J. Drillet, A Criterion for the Change from Fast to Slow Regime of Cementite Dissolution in Fe – C – Mn Steels, *J. Mater. Sci. Technol.* 28 (2012) 728–736. [https://doi.org/10.1016/S1005-0302\(12\)60122-4](https://doi.org/10.1016/S1005-0302(12)60122-4).
- [10] D.Z. Yang, E.L. Brown, D.K. Matlock, G. Krauss, Ferrite recrystallization and austenite formation in cold-rolled intercritically annealed steel, *Metall. Trans. A.* 16A (1985) 1385–1392. <https://doi.org/10.1007/BF02658671>.
- [11] Q. Lai, M. Gouné, A. Perlade, T. Pardoën, P. Jacques, O. Bouaziz, Y. Bréchet, Mechanism of Austenite Formation from Spheroidized Microstructure in an Intermediate Fe-0.1C-3.5Mn Steel, *Metall. Mater. Trans. A.* 47A (2016) 3375–3386. <https://doi.org/10.1007/s11661-016-3547-y>.
- [12] Z. Dai, H. Chen, R. Ding, Q. Lu, C. Zhang, Z. Yang, S. van der Zwaag, Fundamentals and application of solid-state phase transformations for advanced high strength steels containing metastable retained austenite, *Mater. Sci. Eng. R.* 143 (2021) 100590. <https://doi.org/10.1016/j.mser.2020.100590>.
- [13] X. Zhang, G. Miyamoto, T. Kaneshita, Y. Yoshida, Y. Toji, T. Furuhashi, Growth mode of austenite during reversion from martensite in Fe-2Mn-1.5Si-0.3C alloy: A transition in kinetics and morphology, *Acta Mater.* 154 (2018) 1–13. <https://doi.org/10.1016/j.actamat.2018.05.035>.

- [14] H. Luo, J. Liu, H. Dong, A Novel Observation on Cementite Formed During Intercritical Annealing of Medium Mn Steel, *Metall. Mater. Trans. A.* 47A (2016) 3119–3124. <https://doi.org/10.1007/s11661-016-3448-0>.
- [15] H. Luo, H. Dong, M. Huang, Effect of intercritical annealing on the Lüders strains of medium Mn transformation-induced plasticity steels, *Mater. Des.* 83 (2015) 42–48. <https://doi.org/10.1016/j.matdes.2015.05.085>.
- [16] S. Zhang, K.O. Findley, Quantitative assessment of the effects of microstructure on the stability of retained austenite in TRIP steels, *Acta Mater.* 61 (2013) 1895–1903. <https://doi.org/10.1016/j.actamat.2012.12.010>.
- [17] J.R. McDermid, H.S. Zurob, Y. Bian, Stability of retained austenite in high-Al, low-Si TRIP-assisted steels processed via continuous galvanizing heat treatments, *Metall. Mater. Trans. A.* 42A (2011) 3627–3637. <https://doi.org/10.1007/s11661-011-0678-z>.
- [18] P.J. Jacques, J. Ladrière, F. Delannay, On the influence of interactions between phases on the mechanical stability of retained austenite in transformation-induced plasticity multiphase steels, *Metall. Mater. Trans. A.* 32A (2001) 2759–2768. <https://doi.org/10.1007/s11661-001-1027-4>.
- [19] F. G. Caballero, C. Garcia-Mateo, J. Chao, M. J. Santofimia, C. Capdevila, C. García de Andres, Effects of Morphology and Stability of Retained Austenite on the Ductility of TRIP-aided Bainitic Steels, *ISIJ Int.* 48 (2008) 1256–1262.
- [20] J.I. Kim, J.H. Ryu, S.W. Lee, K. Lee, Y.U. Heo, D.W. Suh, Influence of the Initial Microstructure on the Reverse Transformation Kinetics and Microstructural Evolution in Transformation-Induced Plasticity-Assisted Steel, *Metall. Mater. Trans. A.* 47A (2016) 5352–5361. <https://doi.org/10.1007/s11661-016-3672-7>.
- [21] A.K. Chandan, G.K. Bansal, J. Kundu, J. Chakraborty, S.G. Chowdhury, Effect of prior austenite grain size on the evolution of microstructure and mechanical properties of an intercritically annealed medium manganese steel, *Mater. Sci. Eng. A.* 768 (2019) 138458. <https://doi.org/10.1016/j.msea.2019.138458>.

- [22] R. Wei, M. Enomoto, R. Hadian, H.S. Zurob, G.R. Purdy, Growth of austenite from as-quenched martensite during intercritical annealing in an Fe-0.1C-3Mn-1.5Si alloy, *Acta Mater.* 61 (2013) 697–707. <https://doi.org/10.1016/j.actamat.2012.10.019>.
- [23] A. Mehrabi, H. Zurob, I. E. Benrabah, J. R. McDermid, Austenite formation in a medium-Mn steel during intercritical annealing via in situ high-energy X-ray diffraction, *J. Mater. Res. Technol.* (2024).
- [24] K.M.H. Bhadhon, X. Wang, E.A. McNally, J.R. McDermid, Effect of Intercritical Annealing Parameters and Starting Microstructure on the Microstructural Evolution and Mechanical Properties of a Medium-Mn Third Generation Advanced High Strength Steel, *Metals (Basel)*. 12 (2022) 356. <https://doi.org/10.3390/met12020356>.
- [25] D.P. Koistinen, R.E. Marburger, A general equation prescribing the extent of the austenite-martensite transformation in pure iron-carbon alloys and plain carbon steels, *Acta Metall.* 7 (1959) 59–60. [https://doi.org/10.1016/0001-6160\(59\)90170-1](https://doi.org/10.1016/0001-6160(59)90170-1).
- [26] S.J. Lee, S. Lee, B.C. De Cooman, Martensite transformation of sub-micron retained austenite in ultra-fine grained manganese transformation-induced plasticity steel, *Int. J. Mater. Res.* 104 (2013) 423–429. <https://doi.org/10.3139/146.110882>.
- [27] E. Jimenez-Melero, N.H. van Dijk, L. Zhao, J. Sietsma, S.E. Offerman, J.P. Wright, S. van der Zwaag, Martensitic transformation of individual grains in low-alloyed TRIP steels, *Scr. Mater.* 56 (2007) 421–424. <https://doi.org/10.1016/j.scriptamat.2006.10.041>.
- [28] J.J. Mueller, X. Hu, X. Sun, Y. Ren, K. Choi, E. Barker, J.G. Speer, D.K. Matlock, E. De Moor, Austenite formation and cementite dissolution during intercritical annealing of a medium-manganese steel from a martensitic condition, *Mater. Des.* 203 (2021) 109598. <https://doi.org/10.1016/j.matdes.2021.109598>.

## 8 Conclusions and Future Research Directions

### 8.1 Conclusions

The main objective of this Ph.D. was to provide a comprehensive understanding of the phase transformation kinetics and microstructural evolution in a prototype Fe-0.15C-5.56Mn-1.1Si-1.89Al med-Mn third-generation advanced high strength steel (3G AHSS). The study focused on the effects of starting microstructure and intercritical annealing temperature (IAT) on the development of intercritical austenite and its subsequent transformation kinetics during quenching. In that regard, Chapter 3 of this thesis modeled the growth kinetics of austenite from an as-received cold-rolled (CR) microstructure and quenched martensite–ferrite (MF) microstructure during intercritical annealing. The results outlined in Chapter 3 indicated the austenite nucleation sites for the CR and MF starting microstructures and modeled the austenite growth kinetics in both starting microstructures. In order to validate the modelling approach discussed in chapter 3, *in situ* austenite transformation kinetics measurements were conducted as part of this study in chapters 4 and 5. In these chapters, the simulation results were compared and validated with experimental analyses from *in situ* HEXRD and dilatometry. Subsequently, as the predictions aligned well with experimental results, the initial conditions for simulation were considered to develop the process maps.

The major findings of these studies can be summarized as follows:

- 1) The simple diffusion model in DICTRA predicts the overall kinetics without enhancing the diffusion coefficients. The simulation indicates that the presence of cementite extended the time required to achieve the same volume fraction of austenite, as dissolution of cementite was necessary to support austenite growth. Accelerated austenite reversion kinetics were observed for the martensite-ferrite (MF) starting microstructure due to direct intercritical austenite growth from pre-existing inter-lath retained austenite (RA) films and rapid C partitioning from the surrounding martensitic matrix.
- 2) Simulation results were compared and validated with experimental analyses from *in situ* HEXRD and dilatometry, showing good agreement in overall kinetics at 665 °C and 710 °C for both starting microstructures. The slight difference observed between model and

experimental analyses can be attributed to the limitations of the 1D simulation, which may not precisely capture the complexities in the microstructure. Moreover, simplified geometry for austenite nucleation was considered while the gradual nucleation over time could change the results.

- 3) The partitioning of the substitutional alloying elements at the interface, as measured by APT, aligns with thermodynamic predictions, except in the case of Si. DICTRA predicted Si enrichment in austenite, while experimental data revealed a flat Si profile between ferrite and austenite.
- 4) A comparison between intercritical austenite and RA based on HEXRD results revealed that ~1% of austenite transformed into martensite during quenching in the MF, compared to ~5% in the CR sample. These results support the argument that the lath-shaped RA in the MF sample is more chemically stable.
- 5) A set of process maps predict intercritical austenite and RA vol % based on the IAT and Mn content for both starting microstructures. These maps illustrate the compositional range where, under certain conditions (IAT of 680 °C with low Mn content), the vol % of intercritical austenite equals the vol % of RA at room temperature. However, at higher IATs and Mn content, intercritical austenite becomes very unstable and undergoes transformation during quenching. This highlights the importance of precise control over IAT and Mn content in med-Mn steel processing.
- 6) A comparison between process maps of both starting microstructures (M and TM) also highlighted the role of martensite starting microstructure in enhancing the mechanical properties of med-Mn steels. This enhancement is attributed to its ability to promote a higher vol % of intercritical austenite during IA. Additionally, it leads to a higher fraction of RA after quenching.

## 8.2 Future Research Directions

The results of this Ph.D. can serve as a starting point for future research projects. These proposed research projects aim to advance the evolution of emerging 3G AHSS.

- 1) *Effect of secondary alloying elements (Mo, V, Ti, Nb, Cr) on the phase transformation kinetics:* These alloying elements can enhance the strength of med-Mn steels by grain refinement of prior austenite and precipitation strengthening [1–4]. However, the formation of carbides, nitrides, or carbonitrides from these alloying elements may reduce the available C for chemically stabilizing the RA, potentially impacting TRIP kinetics and, consequently, mechanical properties. Therefore, the effect of these alloying elements on both austenite growth kinetics and RA stability should be comprehensively examined either experimentally or DICTRA-based modeling combined with the K-M model, for these med-Mn steels.
- 2) *Influences of microstructural defects like dislocations and precipitates on austenite formation kinetics in med-Mn steels:* Similar to grain boundaries, dislocations can be austenite nucleation sites because of the decreased strain energy and solute segregation [5]. However, it is challenging to model due to lack of understanding and quantification of the effects of microstructural defects like dislocations and precipitates on interface mobility. Moreover, the effects of deformation and recrystallization on the phase transformation are crucial considerations. Recrystallization occurring in a deformed material can profoundly affect the nucleation sites of austenite, thereby influencing both the shape and size of the resulting austenite phases. There exists an interaction between recrystallization and austenite formation; recrystallization may occur either before or after the formation of austenite, thereby impacting its morphology. If recrystallization happens before austenite formation, the austenite tends to be elongated. But if recrystallization happens after, the resulting austenite tends to be more globular.
- 3) *Effect of heating rate on austenite growth kinetics using DICTRA-based model:* In this Ph.D. research, only isothermal holding during intercritical annealing has been considered. Some studies [6–8] have explored the effect of heating rate on austenite growth kinetics and its stability through experiments. However, the developed model was employed to simulate austenite growth kinetics during the isothermal holding process. Furthermore, the heating rate plays a significant role in the processes of recovery and recrystallization during heating. These processes can directly impact the growth of austenite and its nucleation.

### 8.3 References

- [1] M. Cai, Z. Li, Q. Chao, P.D. Hodgson, A Novel Mo and Nb Microalloyed Medium Mn TRIP Steel with Maximal Ultimate Strength and Moderate Ductility, *Metall. Mater. Trans. A.* 45 (2014) 5624–5634. <https://doi.org/10.1007/s11661-014-2504-x>.
- [2] H. Pan, H. Ding, M. Cai, Microstructural evolution and precipitation behavior of the warm-rolled medium Mn steels containing Nb or Nb-Mo during intercritical annealing, *Mater. Sci. Eng. A.* 736 (2018) 375–382. <https://doi.org/10.1016/j.msea.2018.08.055>.
- [3] D. Lee, J.K. Kim, S. Lee, K. Lee, B.C. De Cooman, Microstructures and mechanical properties of Ti and Mo micro-alloyed medium Mn steel, *Mater. Sci. Eng. A.* 706 (2017) 1–14. <https://doi.org/10.1016/j.msea.2017.08.110>.
- [4] B.C. De Cooman, Y. Estrin, S.K. Kim, Twinning-induced plasticity (TWIP) steels, *Acta Mater.* 142 (2018) 283–362. <https://doi.org/10.1016/j.actamat.2017.06.046>.
- [5] A. Kwiatkowski da Silva, G. Leyson, M. Kuzmina, D. Ponge, M. Herbig, S. Sandlöbes, B. Gault, J. Neugebauer, D. Raabe, Confined chemical and structural states at dislocations in Fe-9wt%Mn steels: A correlative TEM-atom probe study combined with multiscale modelling, *Acta Mater.* 124 (2017) 305–315. <https://doi.org/10.1016/j.actamat.2016.11.013>.
- [6] X. Zhang, G. Miyamoto, Y. Toji, T. Furuhashi, Effects of heating rate on formation of globular and acicular austenite during reversion from martensite, *Metals (Basel)*. 9 (2019) 266. <https://doi.org/10.3390/met9020266>.
- [7] J. Han, Y.K. Lee, The effects of the heating rate on the reverse transformation mechanism and the phase stability of reverted austenite in medium Mn steels, *Acta Mater.* 67 (2014) 354–361. <https://doi.org/10.1016/j.actamat.2013.12.038>.
- [8] M. Bellavoine, M. Dumont, M. Dehmas, A. Stark, N. Schell, J. Drillet, V. Hébert, P. Maugis, Ferrite recrystallization and austenite formation during annealing of cold-rolled advanced high-strength steels: In situ synchrotron X-ray diffraction and modeling, *Mater. Charact.* 154 (2019) 20–30. <https://doi.org/10.1016/j.matchar.2019.05.020>.